HAL
open science

Quantum-enhanced sensing and synthetic Landau levels with ultracold dysprosium atoms

Thomas Chalopin

To cite this version:

Thomas Chalopin. Quantum-enhanced sensing and synthetic Landau levels with ultracold dysprosium atoms. Quantum Gases [cond-mat.quant-gas]. Sorbonne Université, 2019. English. NNT : 2019SORUS589 . tel-02495722v2

HAL Id: tel-02495722

https://hal.science/tel-02495722v2

Submitted on 16 Sep 2021

HAL is a multi-disciplinary open access archive for the deposit and dissemination of scientific research documents, whether they are published or not. The documents may come from teaching and research institutions in France or abroad, or from public or private research centers.

L'archive ouverte pluridisciplinaire **HAL**, est destinée au dépôt et à la diffusion de documents scientifiques de niveau recherche, publiés ou non, émanant des établissements d'enseignement et de recherche français ou étrangers, des laboratoires publics ou privés.

THÈSE DE DOCTORAT DE SORBONNE UNIVERSITÉ

préparée par

THOMAS CHALOPIN

QUANTUM-ENHANCED SENSING AND SYNTHETIC LANDAU LEVELS WITH ULTRACOLD DYSPROSIUM ATOMS

SENSIBILITÉ ACCRUE PAR EFFET QUANTIQUE ET NIVEAUX DE LANDAU SYNTHÉTIQUES AVEC DES ATOMES DE DYSPROSIUM ULTRAFROIDS

Spécialité : **Physique quantique**

Soutenue le 12 décembre 2019 devant le jury composé de :

Dr. Caroline CHAMPENOIS ..... Rapporteuse
Dr. Ulrich SCHNEIDER ..... Rapporteur
Pr. Benoît DOUÇOT ..... Président
Pr. Jean DALIBARD ..... Directeur de thèse
Dr. Sylvain NASCIMBENE ..... Membre invité

Travail réalisé au laboratoire Kastler Brossel, au sein du Collège de France

Abstract

THIS THESIS presents several experimental studies based on light-spin interaction in ultracold gases of dysprosium. The complex electronic structure of dysprosium is at the origin of peculiar atomic properties – such as a large magnetic moment, a large angular momentum in the ground state, and narrow optical transitions – which can be used to explore a large variety of physical phenomena.

The manuscript contains three relatively independent parts. In the first part, we give a global description of the apparatus, and of the experimental protocol that leads to the production of degenerate gases of bosonic dysprosium. A key step of our experimental sequence consists in using the intercombination line at 626 nm to perform in-trap Doppler cooling. We show in particular that the strong anisotropy of the corresponding excited state's polarizability is beneficial for the following evaporative cooling scheme.

In the second part, we present experiments that use the strong light-spin coupling associated to this intercombination line to coherently manipulate the internal states of the atoms and to realize non-classical spin states. We focus primarily on the realization of N00N states, which are coherent superpositions of classical states with opposite magnetizations. We experimentally demonstrate that the magnetic field sensitivity of the states that we produce is close to the Heisenberg limit.

The last part is dedicated to the study of quantum Hall physics, which we realize with our system by encoding a synthetic dimension in the internal degree of freedom of the atoms. We show in particular that, using spin-orbit coupling, we realize a system that has the same structure as Landau levels. We probe paradigmatic properties of the lowest Landau level: suppressed dispersion in the bulk, chiral edge modes, cyclotron and skipping orbits, and a Hall response that is characteristic of a non-trivial topology.

Résumé

CETTE THÈSE porte sur plusieurs études expérimentales qui se basent sur les interactions entre photons et atomes ultrafroids de dysprosium. La structure électronique complexe du dysprosium est à l'origine de ses propriétés atomiques singulières – son grand moment magnétique, son grand moment orbital dans l'état fondamental, ses transitions optiques fines – qui donnent accès à une phénoménologie physique riche et diversifiée.

Ce manuscrit est structuré en trois parties relativement indépendantes. Dans la première partie, nous donnons une description globale de notre expérience, et du protocole expérimental qui permet la production de gaz dégénérés de dysprosium bosonique. Une étape importante de notre séquence expérimentale porte sur l'utilisation de la raie d'intercombinaison à 626 nm pour le refroidissement Doppler d'atomes piégés. Nous montrons en particulier que la forte anisotropie de la polarisabilité de l'état excité correspondant est bénéfique pour le refroidissement évaporatif qui suit.

Dans la deuxième partie, nous présentons des expériences qui utilisent le couplage fort entre les photons et le spin, inhérent à cette raie d'intercombinaison, pour manipuler de façon cohérente les états internes des atomes et réaliser des états non-classiques de spin. Nous nous concentrons en particulier sur la réalisation d'états N00N, correspondant à la superposition cohérente d'états classiques ayant des aimantations opposées. Nous démontrons expérimentalement que la sensibilité aux champs magnétiques des états que nous produisons est proche de la limite de Heisenberg.

La dernière partie est dédiée à la physique de l'effet Hall quantique, que nous pouvons étudier avec notre système en encodant une dimension synthétique dans les degrés de liberté internes des atomes. Nous montrons en particulier qu'à l'aide d'un couplage spin-orbite, nous réalisons un système qui a la même structure que les niveaux de Landau. Nous observons les propriétés paradigmatiques du niveau de Landau fondamental : une dispersion supprimée dans le cœur du système, des états de bords chiraux, des orbites cyclotrons et des orbites sautantes, ainsi qu'une réponse de Hall caractéristique d'une topologie non-triviale.

Remerciements

Victoriae mundis et mundis lacrima. Bon, ça ne veut absolument rien dire, mais je trouve que c'est assez dans le ton.

— *François Rollin / Alexandre Astier, Kaamelott*

Le travail et les résultats présentés dans ce manuscrit, et qui résument mes quatre années passées au laboratoire, sont avant tout le produit d'un travail d'équipe. Les quelques lignes qui suivent vont permettre, j'espère, de rendre compte de toute la reconnaissance que j'éprouve envers celles et ceux qui ont pu, de près ou de loin, m'accompagner dans cette aventure.

Je tiens donc avant tout à remercier chaleureusement mes deux encadrants de thèse, Sylvain Nascimbène et Jean Dalibard. Déjà pour m'avoir accueilli sur l'expérience dysprosium, mais surtout pour leur disponibilité et la pertinence de leur nombreux conseils. Je finis cette thèse en ayant appris énormément tant sur le plan technique que théorique, et c'est particulièrement grâce au temps passé par Sylvain à répondre à mes questions – plus ou moins réfléchies – et à me permettre de comprendre les subtilités de la physique des gaz ultrafroids, des manipulations de spin, ou des phases topologiques. Je remercie aussi les membres de mon jury, Caroline Champenois, Ulrich Schneider et Benoît Douçot, pour leur lecture minutieuse de mon manuscrit, leur écoute attentive de ma présentation, et leurs conseils et suggestions de modifications.

J'ai été accueilli au Collège de France début 2016, d'abord en stage de Master, puis ensuite en tant que thésard sur l'expérience dysprosium. Je suis arrivé sur une expérience en fin de construction, et je tiens donc à remercier les personnes qui m'ont confié une machine en état de marche. Je remercie en particulier Davide, Chayma et Leonid, avec qui j'ai partagé les premières années de ma thèse, et qui ont été des collègues – et qui restent des amis – formidables. Gérer la manip avec eux a été particulièrement agréable, et il est clair que la motivation que j'ai conservée pendant ces premières années est largement corrélée à leur présence dans le groupe.

Une thèse est bien entendu l'occasion de voir partir et arriver de nouvelles personnes au fil des années. Ainsi, j'aimerais remercier chaleureusement les personnes avec qui j'ai pu travailler après le départ des 'anciens'. Merci à Vasiliy, Alex, Tanish et Aurélien pour avoir su s'approprier, conserver et confirmer la bonne ambiance (et la motivation !) laissée par leurs prédécesseurs. Je remercie aussi Raphael, d'avoir su mettre à profit son expérience et sa persévérance pour faire progresser nos expériences lorsque nous étions bloqués, et pour passer autant de temps au laboratoire afin de nous faire profiter de son expertise.

Mais je remercie surtout tous mes collègues pour le temps passé en dehors du labo, à la pause déjeuner, pour les dîners dysprosium, en conférence ou autour d'un verre, car c'est

véritablement dans ces moments là que de simples collègues deviennent de véritables amis.

Cette thèse a aussi été l'occasion de côtoyer de nombreuses autres personnes, et notamment les autres membres du groupe *Condensats de Bose-Einstein*. J'aimerais ainsi remercier tous les membres des équipes *rubidium*, *ytterbium* et *sodium*, avec qui j'ai pu interagir au cours de ces années. Je remercie aussi Alexei et son équipe, qui partagent le même étage que nous au Collège de France (et les mêmes thématiques de recherche), et avec qui j'ai pu aussi beaucoup interagir. J'aimerais remercier en particulier Nicolas, les deux Raphaël, Jean-Loup, Manel, Bertrand, Édouard, Alexis, Brice, Chloé et Rémy, pour toutes les discussions, sorties et escapades – au bar, à la salle d'escalade, sur une falaise, ou même en randonnée...

J'aimerais de façon plus générale remercier l'ensemble des membres du LKB et de l'institut de Physique du Collège de France, pour leur accueil et leur aide au quotidien. Je remercie chaleureusement Carmen, pour sa disponibilité, son efficacité et sa gentillesse, et pour toute l'aide qu'elle a pu m'apporter pour l'organisation de la soutenance. Merci aussi à Pascal et l'atelier mécanique pour son travail exceptionnel, Thierry, Audrey, Céline et les gestionnaires du LKB, sans qui tout ce travail de thèse n'aurait pas pu être effectué.

Je remercie par ailleurs l'ensemble de mes amis, qui m'ont accompagné et supporté depuis le début de cette thèse – et même depuis mon entrée à l'université. Merci à Hugo, William, Théo, Corentin et Valentin pour toutes ces soirées, sorties et vacances qui m'ont permis, je pense, de prendre du recul sur ce travail et de me changer les idées lorsque c'était nécessaire.

Enfin, un immense merci à l'ensemble de ma famille, pour le soutien inconditionnel qu'ils m'ont porté au cours de cette thèse. Merci à mes parents, et mes grands parents, pour s'intéresser de près ou de loin à tous mes projets. Merci à Caro pour avoir su égayer nos soirées en toute circonstance, et Chris et Marina, pour leur accueil chaleureux lors de tous ces week-ends à Lille. Je remercie également Véro, Phil et Nat, pour ces soirées et dîners qui ont aussi, en quelque sorte, rythmé ces quatre années de thèse. Pour conclure, je remercie particulièrement Justine, pour avoir su m'accompagner, me soutenir et me supporter – et continuer à le faire – pendant toutes ces années, et pour m'avoir encouragé dans l'ensemble des projets que j'ai pu entreprendre.

Merci.

Contents

Abstract - Résumé i

Remerciements iii

Introduction vii

I **Degenerate dysprosium gases**

1 **Ultracold dysprosium experiment** 3
1.1 Atomic properties 4
1.2 Overview of the experimental setup 6
1.3 Optical dipole traps 8
1.4 Science cell 15
1.5 Outlook 19

2 **Magic polarization for in-trap Doppler cooling** 23
2.1 Anisotropic polarizability 24
2.2 Magic polarization of the intercombination line 26
2.3 Application to Doppler cooling 31
2.4 Conclusion 36

3 **Bose-Einstein condensation of dysprosium** 39
3.1 Condensation of dipolar gases 40
3.2 Evaporation to degeneracy 45
3.3 Degenerate Bose gases 50
3.4 Conclusion 55

II **Quantum-enhanced sensing**

4 **Non-classical spin states: theoretical concepts** 59
4.1 Large spin systems 60
4.2 Quantum-enhanced sensing 66
4.3 One-axis twisting 72
4.4 Conclusion 78

5 **Experimental realization of N00N states** 79
5.1 Experimental implementation of one-axis twisting 80
5.2 N00N state 89
5.3 Tomography and decoherence 92
5.4 Outlook 95

III **Synthetic Landau levels**

6 **Quantum Hall effect in synthetic dimensions: elements of theory** . 101
6.1 Classical and quantum Hall effects 102
6.2 SOC, artificial gauge fields and synthetic dimensions 111
6.3 Implementation with dysprosium 114
6.4 Synthetic Landau levels 121

7 **Experimental realization of synthetic Landau levels** 131
7.1 Experimental implementation 132
7.2 State preparation in the ground band 134
7.3 Cyclotron orbits 139
7.4 Hall conductance and topological markers 142
7.5 Conclusion 145

8 **Summary and outlook** 147
8.1 Summary 147
8.2 Outlook: towards topological many-body states 148

IV **Appendices**

A **Laser system** 159
A.1 Laser at 626 nm 159
A.2 Laser at 421 nm 161

B **Local Chern marker** 163
B.1 Stripe geometry in real dimensions 163
B.2 Synthetic quantum Hall system 166

Publications 167

Bibliography 199

Introduction

QUANTUM MECHANICS is at the heart of our understanding of the world surrounding us, and is at the origin of most modern physics theories. It describes the behavior of light and matter down to their most elementary constituents, with exceptional accuracy. In that regard, the domain of ultracold atoms is particularly adapted for testing such theories, as it allows the study of matter and its interaction with its environment – matter or light – at the scale of these elementary constituents.

At very low energy, when quantum statistics start to play a role, matter do not behave as *ordinary* matter. A spectacular example is the formation of Bose-Einstein condensation: below a critical temperature, bosons accumulate in the ground state of the system and form a collective state described by a single wavefunction, with unintuitive properties such as superfluidity. Its first experimental realization in 1995 [Davis et al. 1995; Anderson et al. 1995], was rewarded the 2001 Nobel prize.

The experimental techniques developed in the past 40 years for trapping, cooling, and detecting ultracold atoms are now such that one can manipulate and image single atoms in a very well controlled environment, including the interactions with the other particles. Such control and versatility is one of the reasons ultracold quantum gases settings are now established in the context of interacting many-body quantum simulation [Bloch et al. 2008; Bloch et al. 2012]. Ultracold atoms platforms are indeed used to study paradigmatic models of condensed matter physics, in a clean, defect-free environment, such as the Bose-Hubbard [Greiner et al. 2002] or Fermi-Hubbard model [Köhl et al. 2005].

Technical advances in ultracold atoms have furthermore brought unprecedented performance in the domain of metrology, and notably for time keeping [Ludlow 2015]. More generally, quantum effects can enhance the performance of a sensor [Giovannetti et al. 2011], through non-classical correlations – entanglement – in the quantum state of the sensor. Ultracold gases, and the general framework of AMO[1] physics, provide convenient tools for engineering quantum-enhanced sensors and testing fundamental limits.

In this introductory chapter, we motivate the use of dysprosium for ultracold atoms experiments, in the context of this thesis. We give a broad introduction on three different aspects that are specifically relevant for this work: the physics of dipolar gases, quantum-enhanced sensing using collective spins, and quantum simulation of topological phases of matter.

[1] Atomic, molecular and optical physics.

Dysprosium: motivation

The first magneto optical trap, Bose-Einstein condensate and degenerate Fermi gases of dysprosium were all obtained in the group of Prof. Lev, in Stanford [Lu et al. 2010; Lu et al. 2011b; Lu et al. 2012]. Similar work was performed in the same period on erbium, which is very similar to dysprosium, in the group of Prof. Ferlaino in Innsbruck [Frisch et al. 2012; Aikawa et al. 2012]. Several other groups have now reached degeneracy with dysprosium or with a mixture involving dysprosium [Kadau et al. 2016; Lucioni et al. 2018; Ravensbergen et al. 2018b; Trautmann et al. 2018].

Dipolar quantum gases

Dysprosium is the most magnetic element of the periodic table[2], with a magnetic moment of $\mu \approx 10\mu_B$ in its electronic ground state. As such, dysprosium is a very good candidate for the study of degenerate dipolar gases.

In conventional dilute, ultracold gases, interactions between particles are dominated by the short range van der Waals interactions, originating from second order interactions between electric dipoles. If the temperature is sufficiently low, one can describe these interactions by low energy collisions. The dominant interaction is then entirely defined by the s-wave scattering length a_s. In dipolar gases such as dysprosium, one also has to include interactions between magnetic dipoles, which are both long range (with a characteristic $1/r^3$ decay of the interacting potential) and anisotropic. The typical length scale associated to the dipolar interaction is [Lahaye et al. 2009]

$$a_{\mathrm{dd}} = \frac{\mu^2 \mu_0 m}{12\pi\hbar^2}, \tag{i}$$

with μ_0 the vacuum permittivity and m the mass of the particles. The dimensionless dipolar parameter $\epsilon_{\mathrm{dd}} = a_{\mathrm{dd}}/a_{\mathrm{s}}$ characterizes whether collisions are dominated by contact interactions ($\epsilon_{\mathrm{dd}} \ll 1$) or dipolar interactions ($\epsilon_{\mathrm{dd}} \gtrsim 1$).

Pioneer experimental work on dipolar degenerate gases was performed on chromium atoms, mostly in the group of Prof. Pfau, in Stuttgart [Griesmaier et al. 2005]. The dipolar parameter of chromium $\epsilon_{\mathrm{dd}} \approx 0.16$ is not large enough for the dipolar interactions to be dominant using the background value of the scattering length, but Feshbach resonances can be used to lower a_{s} and thus enter the strong dipolar regime [Lahaye et al. 2007].

With dysprosium, the dipolar length is sufficiently high to have $\epsilon_{\mathrm{dd}} \approx 1.45$ (*e.g.* for ^{164}Dy, with $a_{\mathrm{s}} = 64(4)a_0$ [Ferrier-Barbut et al. 2018], a_0 being the Bohr radius) making the dipolar interaction naturally dominant. New exotic dipolar phenomena – in the context of quantum gases – can be observed, such as the emergence of quantum droplets stabilized by beyond mean field effects [Kadau et al. 2016; Ferrier-Barbut et al. 2016]. One of the most awaited results was the observation of the roton-maxon spectrum expected from a trapped dipolar gas and predicted in 2003 [Santos et al. 2003]. This particular spectrum was observed very recently with an erbium quantum gas ($\epsilon_{\mathrm{dd}} \approx 1$) [Chomaz et al. 2018], and was followed by a series of studies on the supersolid nature of the system with both erbium and dysprosium atoms [Chomaz et al. 2019; Tanzi et al. 2019; Böttcher et al. 2019b].

On a different topic, the dipolar nature of dysprosium could be used in the context of

[2]Terbium, of atomic number $Z = 65$, is as magnetic as dysprosium, but has not been laser cooled.

quantum simulation, which, as we already mentioned, is a major interest in the domain of ultracold atoms. The Bose-Hubbard model, for instance, can be extended to account for beyond nearest neighbor interactions, in which novel stable phases are expected [Góral et al. 2002]. In particular with dipolar bosons, unusual configuration such as checkerboard patterns (fractional filling insulating phases), or supersolid phases with spatial density modulation which differs from the lattice, should emerge [Trefzger et al. 2011].

Non-classical spin states

In the scope of this thesis, we do not use dysprosium for the dipolar interactions, but rather for its peculiar internal structure, yielding a large spin and narrow optical transitions. These properties are found to be useful for efficient light-spin coupling and spin manipulation.

In the framework of collective spins, a large spin of size $J = N/2$ can be mapped onto the symmetric states of N spin-1/2. Non-classicality, in those many-body systems, essentially stems from entanglement between the elementary constituents. With the techniques provided by the progress of AMO physics, such non-classical collective states of matter have been realized in various settings: ion traps [Sackett et al. 2000], ensembles of cold atoms [Appel et al. 2009], or in Bose-Einstein condensates [Estève et al. 2008]. These realizations come about 20 years after the first experimental production of a squeezed state of light [Slusher et al. 1985]. Such non-classical states are known to provide metrological enhancement, and can be used *e.g.* in atomic clocks [Ludlow 2015], or gravitational waves detectors [Miller et al. 2015; Tse et al. 2019; Acernese et al. 2019]

In the absence of non-classical correlations among the elementary constituents, the performance of a sensor is limited by the so-called *standard quantum limit* [Giovannetti et al. 2004], which is another way to designate classical shot noise. In a shot-noise limited sensor state, each particle acts as an independent measurement, and the precision scales as $1/\sqrt{N}$. If quantum correlations are present, this limit can be overcome, until a fundamental quantum limit is reached, the *Heisenberg limit*, in which the precision of the measurement scales as $1/N$. The aim of quantum metrology is thus to provide sensor states and measurement protocols that allow to beat the standard quantum limit and approach the Heisenberg limit.

Dysprosium naturally comes with a large spin – $J = 8$ in the electronic ground state for bosons. In view of the considerations mentioned above, such a spin can be regarded as an ensemble of $N = 2J = 16$ fictitious particles. A key advantage of using a single particle with a large spin, at least for metrological considerations, lies in the dimension of the Hilbert space: while $2J$ independent particles evolve in a Hilbert space of dimension 2^{2J}, a large spin of size J is solely described by $2J + 1$ states. Engineering non-classical states in such a reduced Hilbert space is greatly facilitated, for the number of decoherence channels is dramatically reduced. Non-classical spin states in particles with a large numbers of internal states – realizing an effective spin – have for instance been realized with Rydberg atoms [Facon et al. 2016; Dietsche et al. 2019], and progress towards the coherent control of molecules [Will et al. 2016] promises even larger numbers of internal states.

Artificial gauge fields

The peculiar internal structure of dysprosium furthermore provides convenient tools for the realization and study of artificial gauge fields and topological phases of matter.

Over the past twenty years, tremendous efforts were made to simulate the physics of gauge fields with ultracold gases – see *e.g.* [Dalibard et al. 2011; Cooper et al. 2019] for reviews. The idea is to study, with neutral atoms, the coupling between a particle and a gauge field $\boldsymbol{\mathcal{A}}(\hat{\mathbf{r}})$, by engineering a Hamiltonian of the type

$$\hat{H} = \frac{(\hat{\mathbf{p}} - \boldsymbol{\mathcal{A}})^2}{2m}. \tag{ii}$$

This is in complete analogy with a charged particle in an external magnetic field $\mathbf{B}$, for which $\boldsymbol{\mathcal{A}} = q\mathbf{A}$ and $\mathbf{B} = \nabla \times \mathbf{A}$, featuring very rich physics related to topological phases, such as in the quantum Hall effect [Halperin 1982].

Topological matter is characterized by the fact that some fundamental properties, such as the existence of gapless edge modes or the quantization of the Hall conductance in the case of the quantum Hall effect, are robust against smooth changes of the system. In two-dimensional systems, different topological phases are distinct from one another by a topological invariant, called the Chern number, which takes integer values. In the context of condensed matter systems, the Chern number is given by the surface integral of the Berry curvature through the Brillouin zone. Such a quantity can also be expressed as a line integral of the Berry phase around a closed loop in momentum space. As such, the Berry phase is considered as a geometric phase, acquired by a state when traveling in a closed loop in phase space, in analogy with the Aharonov-Bohm phase, which is the phase acquired by the state vector of a charged particle traveling in a vector potential.

In the same spirit as for the realization of condensed matter models, ultracold atoms settings can be used to simulate the physics of gauge fields. There are many examples of ultracold atoms experiments that have realized artificial gauge fields. In [Chevy et al. 2000; Engels et al. 2003] for instance, the artificial gauge field emerges from the Coriolis force resulting from a rotation of the atomic gas. As such, one simulates the quantum Hall effect, and the physics of Landau levels. Another possibility is to work with optical lattices: gauge fields emerge from complex tunneling elements between neighboring sites [Jaksch et al. 2003], and can be implemented by shaking the lattice [Aidelsburger et al. 2013] (often referred to as *Floquet* engineering), or by engineering light-assisted tunneling. Optical lattice systems are analogue of condensed matter systems: the optical lattice plays the role of the ionic crystal, while the atoms play the role of the electrons.

In the experiments cited above, the artificial gauge field that is engineered is an Abelian gauge field, characterized by the fact that its cartesian components commute with each other. When the motion of the particle is coupled to its internal state, however, the gauge field may become non-Abelian. Implementing such gauge fields allows to simulate the physics of spin-orbit coupled materials, which is essential *e.g.* for topological insulators [Hasan et al. 2010]. With ultracold atoms, non-Abelian gauge potentials emerge in the presence of spin-orbit coupling, and with dynamics that involve several spin components. Spin-orbit coupling in atomic gases have already been realized in one-dimension [Lin et al. 2011], and more recently in two dimensions [Wu et al. 2016], opening the way towards the implementation of non-Abelian gauge fields with ultracold atoms.

In the past few years, much effort has been put in the direction of the realization of many-body topological phases, which feature rich physics with no single-particle counterpart. A paradigmatic example is the current pursue towards the experimental

production of fractional quantum Hall states, such as the Laughlin state [Laughlin 1983]. Such states carry elementary excitations with fractional charge and with anyonic statistics [Halperin 1984]. Some of these fractional quantum Hall states furthermore feature non-Abelian statistics. As such, those states are considered promising candidates for error-free quantum computing [Nayak et al. 2008]. In this context, information is stored in a non-local many-body state which is protected from decoherence by the underlying global topological order, and unitary operations are performed by the non-trivial braiding properties of the anyons.

In this work, we will focus on an approach that only relies on atom-light interaction to create an artificial gauge potential. The basic idea is to engineer space-dependent energy landscapes in such a way that the equation of motion of an eigenstate of the system contains a new term, interpreted as a gauge field as in eq. (ii) [Dalibard et al. 2011]. This approach has been realized with alkali gases, *e.g.* in [Lin et al. 2009].

A major drawback with alkali atoms, however, lies in their electronic structure, which prevents efficient light-spin coupling. As a result, strong atom-light interaction is usually accessible by tuning the addressing light close to the electronic transition, causing technical problems such as a relatively high heating rate. In that regard, realizing exotic many-body states, which are fundamentally built from interactions between particles, is challenging, because relatively large coherence times are needed. Such technical limitations have prevented, so far, the realization of these states.

Dysprosium has many narrow, isolated transitions in its spectrum that can overcome the heating problem. One can indeed tune the addressing light relatively close to a well chosen transition, but still far enough to limit spontaneous emission – meaning that strong coupling regimes can be reached with limited heating. Dysprosium can be used, for instance, as a platform for engineering strong spin-orbit coupling, with the additional feature that its large spin also leads to a richer phase diagram than for alkali atoms [Cui et al. 2013]. A first step towards the observation of these phases was achieved through the realization of a long-lived spin-orbit coupled degenerate Fermi gas of dysprosium [Burdick et al. 2016]. A spin-orbit coupled Fermi gas of dysprosium has been proposed as a candidate for realizing the Kitaev model [Kitaev 2001], which precisely features topologically protected non-Abelian anyonic excitations in the gap [Nascimbène 2013].

Content of this thesis

This manuscript is arranged in three relatively independent parts. In part I, we describe the experimental setup and the production of degenerate Bose gases of dysprosium. Part II is dedicated to the experimental realization of non-classical spin states, while part III presents the realization of artificial gauge fields, encoding the large spin of dysprosium as a synthetic dimension. We give below a brief summary of each chapter.

I. Degenerate dysprosium gases

Chapter 1 is a presentation of the experimental setup. After a brief introduction about dysprosium's properties, a broad description of the whole system is given. We particularly focus on the optical dipole traps and the science cell configuration.

Chapter 2 is dedicated to the implementation of in-trap Doppler cooling. We detail an experimental determination of the relevant excited state's polarizability, and show that its large anisotropy is convenient for an in-trap cooling scheme.

Chapter 3 provides a description of the forced evaporation process, and the production of a dipolar Bose-Einstein condensate of dysprosium. The characterization of the condensate is given, and the effects of dipolar interactions are highlighted.

II. Quantum-enhanced sensing

Chapter 4 gives general theoretical concepts concerning non-classical spin states. We focus on the definition of a collective spin, the relation between entanglement and non-classicality, and the metrological perspectives that arise. We furthermore describe the model that we use to generate such non-classical spin states in the internal state of dysprosium.

Chapter 5 is dedicated to the implementation of the model described in chapter 4. We particularly focus on the realization of N00N states and show that we reach high metrological gain, close to the Heisenberg limit.

III. Synthetic Landau levels

Chapter 6 introduces the last part of the thesis. We present the quantum Hall effect, and how it can be observed using spin-orbit coupling and synthetic dimensions. The analogy between synthetic systems and standard systems is carried out.

Chapter 7 describes the implementation of the Landau Hamiltonian with bosonic dysprosium, using its internal spin state as a synthetic dimension. We show that we observe all the characteristics of Landau levels in our synthetic system: chiral edge modes and the suppression of kinetic energy in the bulk, the existence of semi-classical cyclotron and skipping orbits and quantization of the conductance. We furthermore probe the topology of the system

Chapter 8 briefly summarizes the thesis, and gives experimental perspectives following the realization of synthetic Landau levels. We show in particular that our system is suitable for the observation of many-body topological phases.

Publications

The following articles were published in the context of this thesis. The asterisks mark the one specifically relevant to the work presented here.

T. Chalopin, C. Bouazza, A. Evrard, V. Makhalov, D. Dreon, J. Dalibard, LA. Sidorenkov, and S. Nascimbene
**Quantum-enhanced sensing using non-classical spin states of a highly magnetic atom*
Nature Communications, **9**, 4955 (2018)

T. Chalopin, V. Makhalov, C. Bouazza, A. Evrard, A. Barker, M. Lepers, J.-F. Wyart, O. Dulieu, J. Dalibard, R. Lopes, and S. Nascimbene
**Anisotropic light-shift and magic-polarization of the intercombination line of Dysprosium atoms in a far-detuned dipole trap*
Phys. Rev. A **98** 040502(R) (2018)

A. Evrard, V. Makhalov, **T. Chalopin**, L. A. Sidorenkov, J. Dalibard, R. Lopes, and S. Nascimbene
Enhanced magnetic sensitivity with non-gaussian quantum fluctuations
Phys. Rev. Lett. **122** 173601 (2019)

V. Makhalov, T. Satoor, A. Evrard, **T. Chalopin**, R. Lopes, and S. Nascimbene
Probing quantum criticality and symmetry breaking at the microscopic level
Phys. Rev. Lett. **123** 120601 (2019)

T. Chalopin, T. Satoor, A. Evrard, V. Makhalov, J. Dalibard, R. Lopes, and S. Nascimbene
**Exploring the topology of a quantum Hall system at the microscopic level*
arXiv:2001.01664 (2020)

I

Degenerate dysprosium gases

1 Ultracold dysprosium experiment

1.1 Atomic properties **4**

1.2 Overview of the experimental setup **6**

1.3 Optical dipole traps **8**

1.3.1 Transport ODT 9

1.3.2 Crossed trap 9

1.4 Science cell **15**

1.4.1 Magnetic field control 15

1.4.2 Imaging 17

1.4.3 Doppler cooling and spin dynamics 18

1.5 Outlook **19**

THIS FIRST CHAPTER is dedicated to a description of the experimental apparatus. We start with a brief description of dysprosium's peculiar atomic properties, which, as mentioned in the introduction, lead to a large magnetic moment, a large spin, and narrow optical transitions.

We then give a sketch of the whole experimental apparatus, briefly discussing each element. We particularly focus on two specific parts: the optical dipole traps and our science cell configuration. On the one hand, we use the dipole traps to transport, hold, and cool down the atoms, making them essential tools to produce the ultracold samples with which we work. A precise and complete characterization is thus needed to fully understand our experiment and optimize it. The glass cell, on the other hand, is where the final stage of the sample preparation is realized. Its environment, essentially made of well controlled magnetic fields and laser beams, is discussed.

We will conclude with an outlook on the potential experimental updates we have planned. The current status of the experiment is such that we have a well functioning setup, which allows to explore some of the topics we have mentioned in the introduction. The additional experiment developments that we describe in the outlook, such as exotic atom-light interactions, high-resolution imaging or a low-noise magnetic environment, would allow to go beyond the studies we have already led (*e.g.* towards the realization of many-body topological phases of matter), and explore new topics and novel physics with ultracold dysprosium.

1.1 Atomic properties

Dysprosium can be found in nature in seven stable isotopes. Among them, four isotopes are relatively abundant: two fermions and two bosons. The bosonic isotopes have a nuclear spin $I = 0$, while $I = 5/2$ for the fermions. The most abundant isotopes are presented in table 1.1. In this work, we only work with bosons, which do not have a hyperfine structure.

Isotope	^{161}Dy	**^{162}Dy**	^{163}Dy	^{164}Dy
Abundance	18.9 %	**25.5 %**	24.9 %	28.2 %
Statistics	Fermion	**Boson**	Fermion	Boson
Nuclear spin	$I = 5/2$	$I = 0$	$I = 5/2$	$I = 0$

Table 1.1 – Dysprosium isotopes. All the work presented in this thesis was performed on bosonic isotopes, mostly with ^{162}Dy, in bold.

Electronic structure

Similarly to many lanthanides, dysprosium has an electronic structure which is said to be in a *submerged shell* configuration. The electron repartition on the different orbitals can be written in the form

$$[\mathrm{Xe}]4f^{10}6s^2, \tag{1.1}$$

meaning that the outer shell $6s$ is filled with two electrons, while the inner shell $4f$ only has 10 electrons (see fig. 1.1). As a consequence, the electronic spin of dysprosium in its ground state is $S = 2$, while the total orbital spin is $L = 6$, giving a total angular momentum $J = 8$. Using the spectroscopic notation $^{2S+1}L_J$, the ground state of dysprosium is written $^5I_8$.

Such an electronic structure gives a very rich energy spectrum, with many available transitions. A part of the energy diagram is given in fig. 1.1, along with the two cooling transitions that we use, which will often be referred as the blue ($\lambda = 421\,\mathrm{nm}$) and red ($\lambda = 626\,\mathrm{nm}$) transitions. In both of these transitions, one of the $6s$ orbital electrons is promoted to a $6p$ orbital. While the blue transition is allowed and quite broad, the red transition involves a forbidden spin flip, which is why it is referred as the *intercombination line*. As a result, it is much narrower. These two transitions are quite convenient for laser cooling schemes. The blue transition is suitable for slowing and cooling the atoms and for imaging. The red transition, on the other hand, is useful to realize cold magneto-optical traps. We give in table 1.2 the relevant parameters for these transitions. The section 1.2 explains how they are used on the experiment.

Magnetic properties

The magnetic moment μ of a single atom is given by

$$\mu = m_J g_J \mu_\mathrm{B}, \tag{1.2}$$

with m_J the spin projection on the quantization axis, g_J the Landé g-factor and μ_B the Bohr magneton. When immersed in an external magnetic field B, the J manifold has its degeneracy lifted, as each of the m_J substates have a different energy. The Zeeman energy

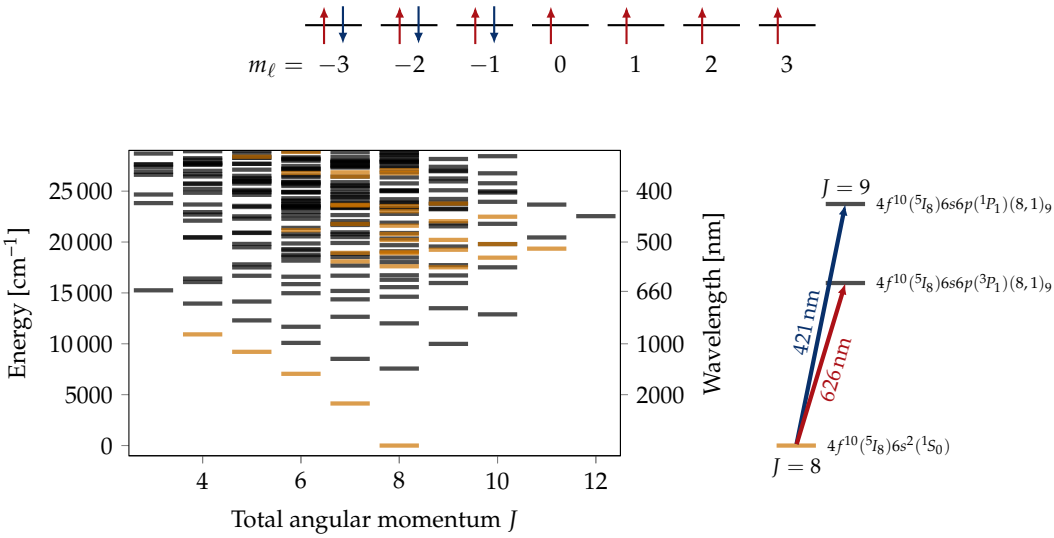

Figure 1.1 – Electronic structure and energy spectrum. (Top) The submerged shell $4f$ has four unpaired electrons, yielding $S = 2$ and $L = 6$ in the ground state. (Left) Energy levels of dysprosium up to $\sim 30\,000\,\mathrm{cm}^{-1}$. Many other lines are present at higher energies, until the ionization limit at $47\,902\,\mathrm{cm}^{-1}$ [Martin et al. 1978]. Even and odd parity levels are depicted in orange and black respectively. (Right) Details of the cooling transitions, along with the corresponding spectroscopic term.

λ	Γ	$\Gamma/2\pi$	I_{sat}	T_{D}	g
421 nm	$2.2 \times 10^2\ \mu\mathrm{s}^{-1}$	32.2 MHz	$56.4\ \mathrm{mWcm}^{-2}$	774 µK	1.22
626 nm	$0.85\ \mu\mathrm{s}^{-1}$	135 kHz	$72\ \mu\mathrm{Wcm}^{-2}$	3.2 µK	1.29

Table 1.2 – Laser cooling parameters. Γ is the transition linewidth and I_{sat} is the saturation intensity. The Doppler temperature is given by $T_{\mathrm{D}} = \hbar k/2k_{\mathrm{B}}$, with $k = 2\pi/\lambda$. The Landé g-factors are also given. These values were measured in [Lu et al. 2011a].

of a given m_J-state is

$$E_{m_J} = \mu_{\mathrm{B}} m_J g_J B. \tag{1.3}$$

The Landé g-factor of the ground state is $g_J = 1.242$ [Martin et al. 1978], giving for a polarized state $m_J = 8$ a high magnetic moment

$$\mu = 9.93 \times \mu_{\mathrm{B}}. \tag{1.4}$$

The g-factors of the excited states corresponding to the blue and red transitions that we use are also indicated in table 1.2.

1.2 Overview of the experimental setup

Our experimental setup is quite typical for a cold atom experiment. There are two essential parts: the ultra high vacuum (UHV) system and the laser system. The overall aim of our machine is to bring a hot vapor of dysprosium to an ultracold cloud at degeneracy. The high vacuum part essentially ensures that the dysprosium atoms that we work with are not perturbed by other particles – better vacuum simply means better lifetimes. The laser system is on its own the core of the experimental setting. Light interacts with the atoms to slow them down, trap them, transport them and cool them down to degeneracy, before it is used to engineer interactions such as the ones mentioned in the introduction.

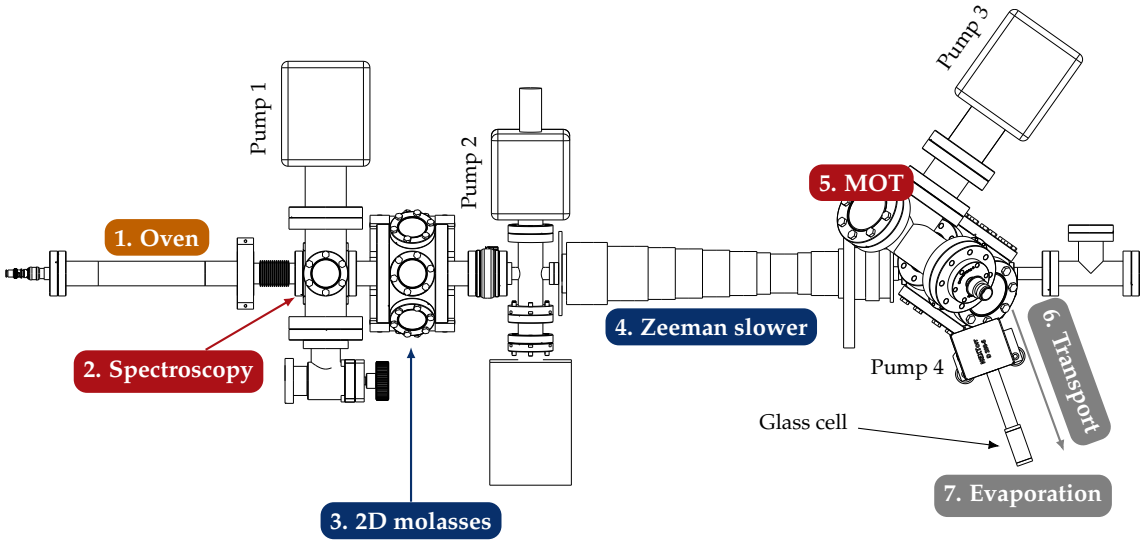

Figure 1.2 – Experimental apparatus. The atoms are ejected by the oven (1). The atomic jet is used for spectroscopy (2) and cooled down in the transverse direction by 2D molasses (3). The atoms are then slowed down by the Zeeman slower (4) before being captured by the MOT (5). Finally, they are transported to the glass cell using an ODT (6), and furthermore cooled down by forced evaporative cooling (7). The four ion pumps are also indicated.

We give an overall diagram of the setup in fig. 1.2. The whole setup has been described in detail in previous Ph.D. theses in our group [Dreon 2017; Bouazza 2018], and we only give here an overview. Details about the laser sources for the blue and red transitions are given in appendix A. In the next sections, we will give additional details about the parts which are specifically relevant to the scope of this thesis: the optical dipole traps and the science cell setup.

1. **Oven.** A non-negligible vapor pressure for dysprosium is achieved for temperatures typically above $\sim 1000\,^{\circ}\mathrm{C}$. Such high temperatures are attained with a commercial double effusion oven made of tantalum, that we fill with metallic dysprosium cut in small pieces. The dysprosium vapor exits the oven through a collimation tube, thus producing an atomic jet that overall goes in the desired direction.

2. **Spectroscopy.** Optical access is granted on the atomic jet right after the oven to

perform Doppler-free spectroscopy. The blue laser is locked using a modulation-transfer spectroscopy technique, and the red laser is locked on the Lamb-dip signal that we obtain from fluorescence spectroscopy.

3. **2D molasses.** The divergence of the atomic jet is still relatively high at the output of the oven, and is reduced using a transverse cooling scheme. We use laser beams tuned to the 421 nm transition and propagating in a direction orthogonal to the atomic jet to reduce the transverse velocity of the atoms, consequently increasing the flux of atoms going to the Zeeman slower. The laser beams have a strong ellipticity in order to optimize the overlap with the atomic jet. We typically dedicate $\sim 50\,\mathrm{mW}$ of blue light to the transverse cooling, which is usually all we can spare. It is worth noting that with such power, we remain well below the saturation intensity of the blue transition (we typically work at $I/I_s \approx 0.1$), and increasing the overall power that we could spare should greatly increase the efficiency of transverse cooling.

4. **Zeeman slower.** The atoms are then slowed down in a Zeeman slower. We typically use $\sim 60\,\mathrm{mW}$ of blue light, sent counter-propagating to the atomic jet. The Zeeman slower is 50 cm long, and allows to bring fast atoms ($\sim 500\,\mathrm{m\,s^{-1}}$) from the output of the oven to the capture velocity of our magneto-optical trap ($\sim 8\,\mathrm{m\,s^{-1}}$).

5. **Magneto-optical trap (MOT).** Our MOT works on the intercombination line at 626 nm, which is considered as a narrow line compared to D_2 lines typically used in alkali setups. MOT loading is achieved in two steps. In the first step, the beam intensity is very large ($I/I_{\mathrm{sat}} \approx 50$), and the line is broadened by means of sideband modulation. It allows to broaden the velocity class captured by the MOT. In the second step, the trapped cloud is compressed to increase the density and reduce the temperature. The laser intensity is lowered, the sideband modulation is turned off, and the MOT beams detuning is reduced. The temperature and density of the cloud are strongly dependent on the MOT parameters (such as the magnetic field, the intensity or detuning of the beams), and a complete study on this matter was published [Dreon et al. 2017]. Typically, our MOT is constituted of about 1×10^8 atoms at $T \approx 15\,\mu\mathrm{K}$. Such a temperature is roughly 5 times larger than the Doppler temperature, but remains sufficiently small for the next experimental step.

6. **Transport.** Once compressed, the atoms in the MOT are loaded in a far-detuned optical dipole trap (ODT). We use a 50 W, multi-mode fiber-amplified laser at 1070 nm[1]. The ODT is initially focused on the MOT, allowing the loading of about 10 % of the atoms into the ODT. The focal point of the ODT is then shifted from the MOT chamber to the science chamber, over a distance of about 30 cm. We use a translation stage to move a corner-cube mirror after the focusing lens. The trapped atoms follow the focal point, and are transported to the science cell.

7. **Evaporation.** Once transported, the atoms are cooled down by means of Doppler cooling in the trap. This process is entirely described in the next chapter. We then switch on two other far-detuned ODTs to form a crossed optical dipole trap (cODT). Each of these new beams are 45 W single-mode 1064 nm fiber-amplified lasers[2]. The loading efficiency is also increased by spatially modulating the position of their

[1] YLR 50 W, IPG Photonics.
[2] Azurlight systems.

focal point, increasing the effective volume of the crossed region. The intensity of the ODTs are then lowered down for forced evaporative cooling, until we reach Bose-Einstein condensation. This step is described in chapter 3.

The original work in this thesis mostly concerns the last step described above. In the next section, we give additional detail about our ODTs. Their precise calibration is indeed quite important for the in-trap cooling and evaporation.

1.3 Optical dipole traps

We consider here the interaction between an atom and a light field which frequency is much lower than any of the transitions of the atoms. The interaction potential between the atom and the light field can be written as [Grimm et al. 2000]

$$U_{\mathrm{dip}}(\mathbf{r}) = -\frac{I(\mathbf{r})}{2\epsilon_0 c}\,\mathrm{Re}(\alpha). \tag{1.5}$$

In this expression, $I(\mathbf{r})$ is the position-dependent light intensity, and $\mathrm{Re}(\alpha)$ designates the real part of the atomic polarizability.

In general, α depends on the internal state of the atom. We will see in the next chapters that these spin-dependent terms are at the origin of the light-spin interactions that we engineer and study. Here, we only focus on the *scalar* part of α, *i.e.* the spin-independent part of the polarizability, which is furthermore positive $\mathrm{Re}(\alpha) > 0$.

The intensity profile of a gaussian beam is written as

$$I(\mathbf{r}) = I(\rho, z) = I_0 \left(\frac{w_0}{w(z)}\right)^2 \exp\left(-\frac{2\rho^2}{w(z)^2}\right). \tag{1.6}$$

In this expression, we assume cylindrical symmetry around the propagation axis z, such that $\rho = \left(x^2 + y^2\right)^{1/2}$ designates the distance from the axis. By convention, $z = 0$ is the position of the focal point, where the $1/\mathrm{e}^2$ radius is equal to the beam waist w_0. The radius of the beam expands in the z direction as

$$w(z) = w_0 \sqrt{1 + \left(\frac{z}{z_{\mathrm{R}}}\right)^2}, \tag{1.7}$$

where $z_{\mathrm{R}} = \pi w_0^2/\lambda$ is the Rayleigh range. The intensity I_0 directly relates to the total optical power P, as

$$I_0 = \frac{2P}{\pi w_0^2}. \tag{1.8}$$

The intensity is maximum and is equal to I_0 at $(z, \rho) = (0, 0)$, which corresponds to a minimum of potential according to eq. (1.5). It is at this point that the atoms are trapped.

An ODT is often characterized by its total depth U_0 and its frequencies ω_i, for $i = x, y, z$. The total depth U_0 is simply given by

$$U_0 = -U_{\mathrm{dip}}(\mathbf{r} = \mathbf{0}) = \frac{I_0}{2\epsilon_0 c}\,\mathrm{Re}(\alpha). \tag{1.9}$$

The frequencies of the trap can be found by expanding eq. (1.6) to the lowest order around its maximum. We obtain for the dipole potential

$$U(\rho,z) = -U_0 \left[1 - 2\left(\frac{z}{z_\mathrm{R}}\right)^2 - 2\left(\frac{\rho}{w_0}\right)^2 + \mathcal{O}\left(\frac{z^4}{z_\mathrm{R}^4}, \frac{\rho^4}{w_0^4}, \frac{z^2}{z_\mathrm{R}^2}\frac{\rho^2}{w_0^2}\right)\right]. \tag{1.10}$$

We recognize the expression of a 3-dimensional harmonic potential

$$U(\rho,z) \approx -U_0 + \frac{m}{2}\left[\omega_\rho^2\rho^2 + \omega_z^2 z^2\right] \quad \text{with} \quad \begin{cases} \omega_\rho = \sqrt{\dfrac{4U_0}{m w_0^2}} \\ \omega_z = \sqrt{\dfrac{2U_0}{m z_\mathrm{R}^2}}. \end{cases} \tag{1.11}$$

Such a trap description is valid in the limiting case where the cloud dimensions are much smaller than the typical trap sizes, given by z_R along the propagation axis and w_0 in the orthogonal plane. This approximation is often verified in practice.

1.3.1 Transport ODT

A complete discussion about our transport apparatus was given in [Bouazza 2018]. Here, we will only focus on the ODT itself, because a good characterization of the trap frequencies will be needed in the next chapter. For reference, we give a scheme of the experimental setup in fig. 1.3.

Trap frequencies

There are two kinds of elementary excitations that we can measure in the trap: the dipole mode and the monopole mode. The former corresponds to a center-of-mass (CoM) displacement of the cloud, and the latter is sometimes called the *breathing* mode, as it corresponds to an oscillation of the size of the cloud. The axial frequency is measured by *kicking* the atoms along the propagation axis, with the translation stage, and exciting the dipole mode. For the radial frequency, the ODT power is lowered and then abruptly increased in order to excite the breathing mode. Results of such measurements are given in fig. 1.4.

The data is fitted by a damped oscillator model, from which we extract the trapping frequency. The damping of the oscillation can be explained by the anharmonicity of the trap explored during the oscillation, as well as the thermal energy distribution of the cloud. We get $\omega_z \approx 2\pi \times 8.5\,\mathrm{Hz}$ and $\omega_\rho \approx 2\pi \times 1.7\,\mathrm{kHz}$ for the axial and radial frequencies respectively, for a trap depth of about $U_0 \approx 0.7\,\mathrm{mK}$. It is worth noting here that the timescales associated to the axial frequency are smaller than the transport time (about 1 s), which allows us to transport in the adiabatic regime, thus quite efficiently.

1.3.2 Crossed trap

We discuss here the characterization of the cODT that we turn on once the atoms are transported in the glass cell. These dipole traps are spatially modulated in order to increase the capture volume and thus improve the loading efficiency from the transport

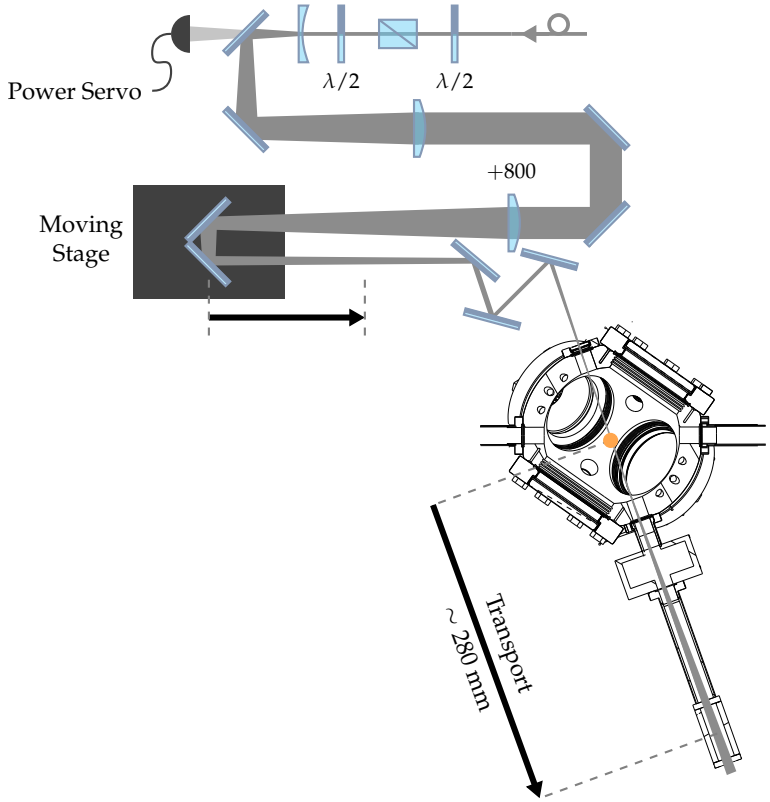

Figure 1.3 – Transport optical setup. The beam goes through a corner-cube mirror right after the last lens, which has a focal length $f = 800\,\mathrm{mm}$. The corner-cube mirror is mounted on a translation stage. Moving the translation stage is equivalent to moving the focal point, and allows to transport atoms from the MOT chamber to the glass cell. This figure is adapted from [Dreon 2017].

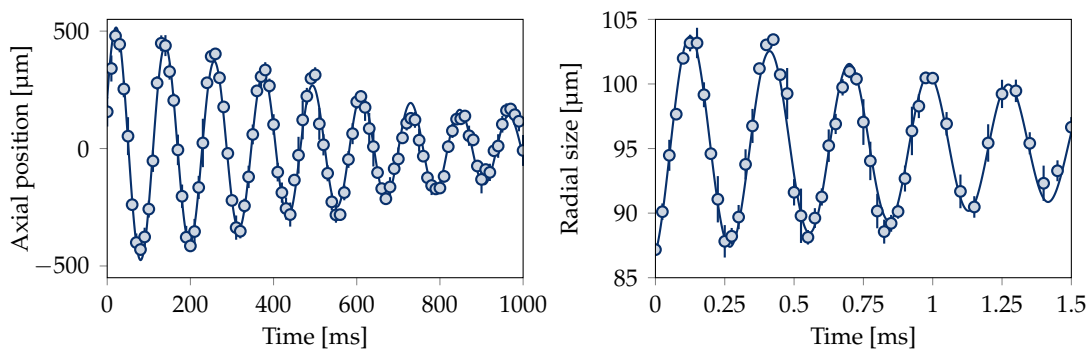

Figure 1.4 – Trap frequency measurements. (Left) The axial frequency is measured by exciting the dipole mode along the propagation axis. (Right) The radial frequency is measured by exciting the monopole mode of the cloud. Solid lines are fits.

ODT to the cODT. In this section, we only discuss the experimental setup and the trapping characteristics. A more complete discussion of the cODT loading and the benefits of

modulation will be given in chapter 3.

The experimental setup is given in fig. 1.5. In this section, we will adopt a more convenient set of coordinates: z is now the vertical coordinate, while X and Y are set by the cODT geometry.

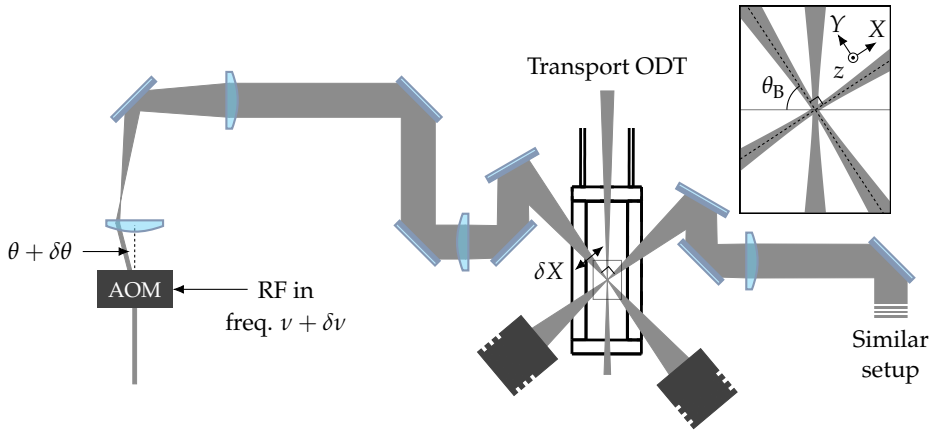

Figure 1.5 – Crossed dipole trap setup. Two ODTs cross each other at their focal point, and overlap with the transport trap at the center of the glass cell. A zoom on the crossing region is given, with a definition of the local coordinate system. The first trap enters the glass cell at the Brewster angle θ_B, and the second trap is orthogonal to the first one. For each of these traps, the final in-plane position can be shifted (δX) by shifting the RF frequency ($\delta\nu$) sent to the AOM. See text for additional details.

Trap geometry

Both ODTs have almost identical setups, and the discussion that follows applies to both of the traps. We use a broad-band acousto-optic modulator (AOM)[3]. To a given frequency ν_0 is associated a given diffraction angle θ_0, such that a shift of the frequency $\delta\nu$ causes a shift of the angle $\delta\theta$ (see fig. 1.5). Our optical setup is designed such that an angle shift $\delta\theta$ gives a position shift δX at the focal point. In that respect, a modulation of the AOM driving frequency results in a modulation of the trap position. If the frequency of the modulation is large enough – typically much larger than the trap radial frequency – the atoms see an average trapping potential with a larger effective size and a smaller trap depth.

Experimentally, the RF is generated from a VCO which we modulate periodically. As such, the frequency received by the AOM is

$$\nu(t) = \nu_0 + \delta\nu_{\max} f_{\mathrm{mod}}(2\pi\nu_{\mathrm{mod}} t), \tag{1.12}$$

where $\delta\nu_{\max}$ is the amplitude of the modulation f_{mod} is a periodic function, and ν_{mod} is the modulation frequency. We can measure the shape of the ODT at the focal point as a function of $\delta\nu_{\max}$, simply by taking pictures of the beam with a CCD camera. The modulation frequency is set to $\delta\nu_{\mathrm{mod}} = 50\,\mathrm{kHz}$, which is much larger than any of the trap frequencies. The central frequency is $\nu_0 = 80\,\mathrm{MHz}$ in our case.

[3] AA Optoelectronics, MCQ80.

Examples of pictures are given in fig. 1.6. As one can see, in the absence of modulation, *i.e.* when the RF contains a single frequency ν_0 (top panels), the beam shape is almost isotropic. The waists w_X and w_z are extracted from gaussian fits of the integrated profiles. When the modulation is turned on (bottom panels), the RF spectrum is effectively much wider, and the trap shape becomes elongated in the horizontal direction. The integrated profile also shows that, along this elongated direction, the beam shape isn't gaussian anymore. We can extract an effective waist by fitting a generalized gaussian distribution[4] to the profile, and define the waist as the $1/e^2$ radius. This model is entirely empirical, and is only meant to give an insight on the evolution of the trap size.

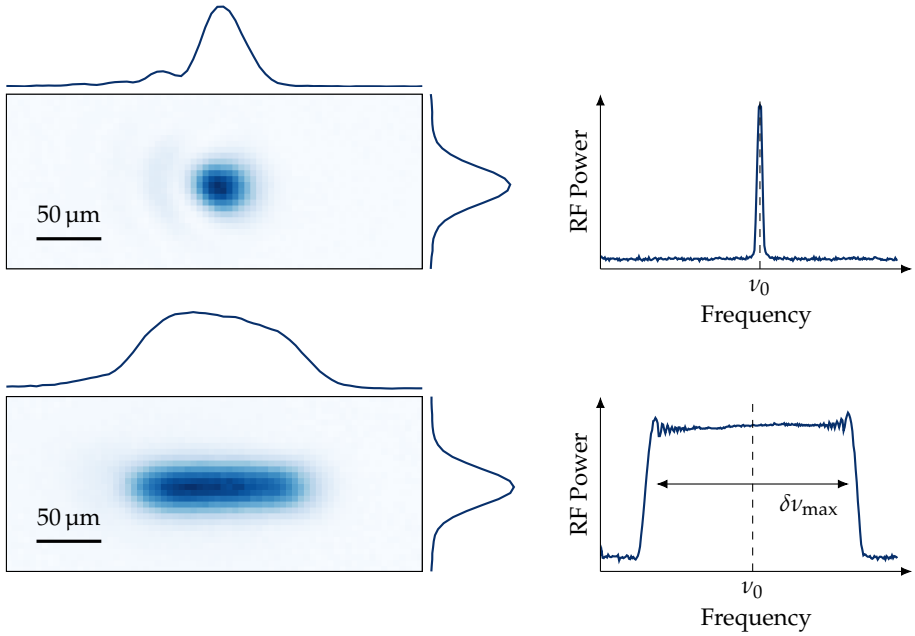

Figure 1.6 – Spatial modulation of the ODT. Pictures of the ODT at the focal point without and with modulation (top and bottom pictures, respectively). The solid lines next to the pictures are the integrated profiles that we use to extract the waist of the beam. On the right, we show the RF spectra sent to the AOM. These pictures were taken in the (Xz) plane, along the propagation axis of the ODT (see fig. 1.5).

These measurements are performed for several values of the modulation amplitude $\delta\nu_{\max}$. The measured waists as a function of the modulation amplitude are given in fig. 1.7. As expected, the horizontal size (w_X, red squares) increases when the modulation amplitude is higher, while the vertical size (w_z, blue circles) remains unchanged. From these measurements, we can see that the trap aspect ratio w_X/w_z can be tuned continuously from ~ 1 to ~ 3 simply by tuning the modulation amplitude.

It is worth noting here that the periodic function f_{mod} completely defines the shape of the average potential. In the example given above, a triangular function was chosen.

[4]This distribution is defined by

$$f(x) \propto \exp\left[-\left|\frac{x-x_0}{\sigma}\right|^{\beta}\right],$$

with β and σ real and positive. The gaussian distribution is recovered for $\beta = 2$. In our case, we fit $\beta > 2$, which gives a flatter distribution with sharper edges.

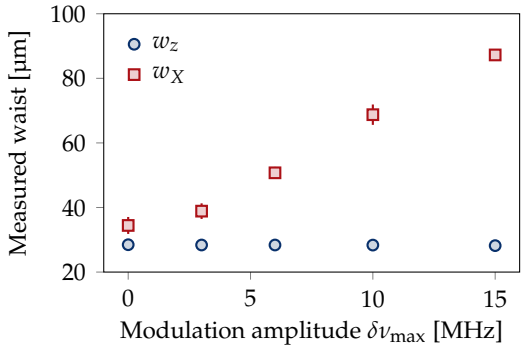

Figure 1.7 – Effective waist of the modulated ODT. The waists are extracted from fits to the integrated profiles of the type shown in fig. 1.6. See text for additional detail.

During one modulation period, the displacement velocity of the trap center is always the same. As such, the trap spends as much time on the edges as in the center, hence a flatter average shape with sharper edges. When using the trap on the atoms, f_{mod} is chosen to be fast on the edges and slow at the center, such that the average potential is closer to the usual gaussian potential.

Trap frequency

The main use of our crossed ODT is to perform forced evaporative cooling to reach degeneracy. Once the atoms are loaded into the cODT, the transport trap is turned off and the evaporation starts. Knowing the trap frequencies at every moment of the evaporation is necessary to quantify the efficiency of the cooling and optimize the whole process. A good calibration is crucially important at low power, when the system is on the verge of condensation and the optical potential is altered by the effects of gravity.

Let us first consider the vertical trapping frequency. The total vertical potential at $X = Y = 0$, taking into account gravity, can be written as

$$U_{\text{tot}}(z) = U_1(z) + U_2(z) - mgz, \tag{1.13}$$

where U_1 and U_2 are the potential induced by each ODT and mgz is the gravity contribution. We suppose here for simplicity that both dipole traps have similar waists $w_{z,0}$ along the vertical direction, such that the total trap can be described by an effective gaussian potential

$$U_{\text{tot}}(z) = -U_0 \exp\left(-\frac{2z^2}{w_0^2}\right) - mgz, \tag{1.14}$$

where $U_0 = U_1(0) + U_2(0)$ is the total trap depth and w_0 is an effective waist. We now introduce the dimensionless tilt parameter $\alpha = mgw_0/U_0$, which quantifies the relative strength of gravity with respect to the trap depth. Our problem is recast in

$$U_{\text{tot}}(z) = -U_0 \left[\exp\left(-2\zeta^2\right) + \alpha\zeta\right], \tag{1.15}$$

with $\zeta = z/w_0$. Above a critical value $\alpha > \alpha_c = 2e^{-1/2}$, the expression (1.15) does not feature a minimum anymore, and trapping is not possible. For $\alpha < \alpha_c$, the minimum exists,

and its position ζ_0 is shifted from $\zeta = 0$. The trapping frequency ω, which is related to the curvature of the trap around ζ_0, is also reduced by the tilt. We give in figure 1.8 examples of trapping potential for different values of α, along with the frequency reduction and the shift of the position of the minimum.

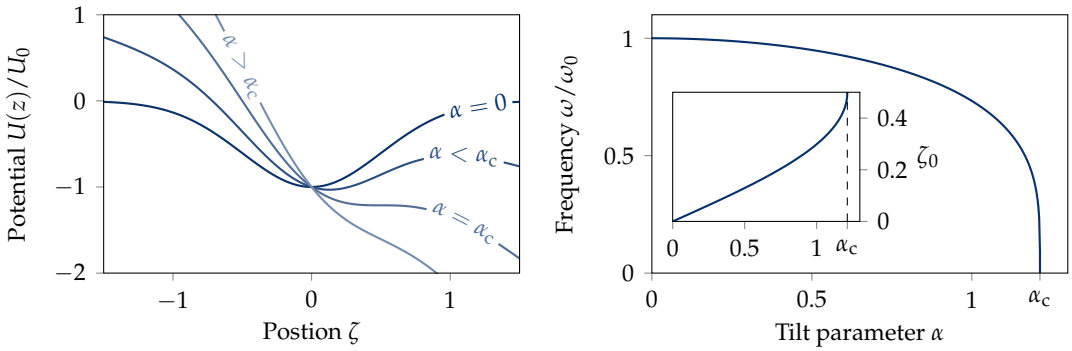

Figure 1.8 – Effects of gravity. (Left) potential profiles for different values of $\alpha = mgw_0/U_0$. For $\alpha > \alpha_c$, the profile does not feature a minimum and atoms cannot be trapped. (Right) Reduction of the trapping frequency. In the absence of tilt, $\omega = \omega_0$. When $\alpha > 0$, the frequency is reduced until it reaches 0 for $\alpha = \alpha_c$. (Inset) The position of the minimum is shifted away from $z_0 = 0$ by the tilt.

Both our ODTs have a similar waist $w_0 \approx 25\,\mu$m, and the above discussion applies to our experiment. We measure the vertical frequency of the cODT for different values of P_1 and P_2, with P_i the optical power of the ith trap. Results are given in fig. 1.9 (left).

The fitting model that we use is deduced from the trap depth model described above, using the relations in eq. (1.11). The total trap depth U is assumed to be proportional to an effective power $P = \beta P_1 + P_2$, where β accounts for geometrical differences between the two traps. The frequency is then $\omega_z \propto \eta(\alpha)\sqrt{U}$, where η is the reduction factor given by the right panel of fig. 1.8 and $\alpha \propto 1/U$.

The effects of gravity are obvious when comparing the measured frequency with the one expected in the absence of gravity (*e.g.* by compensating it) which is given by the red dashed line in the left panel of fig. 1.9. As one can see, the measured frequencies are significantly reduced, exhibiting a minimal required optical power for holding the atoms.

The same measurements are realized for the transverse frequencies ω_X and ω_Y. In our case, the traps are orthogonal to each other, which means that the contribution to ω_X mostly comes from the first trap and the contribution to ω_Y mostly comes from the second trap. This is well verified by the data in fig. 1.9 (right). In this graph, each point corresponds to a frequency measurement for a given set (P_1, P_2). For the fit, we simply assume $\omega_X \propto \sqrt{P_1}$ and $\omega_Y \propto \sqrt{P_2}$, which agrees reasonably well with our data.

For both the vertical and in-plane frequencies, our models fit well to the data, which allows us to extrapolate the trap frequencies for any power P_1, P_2.

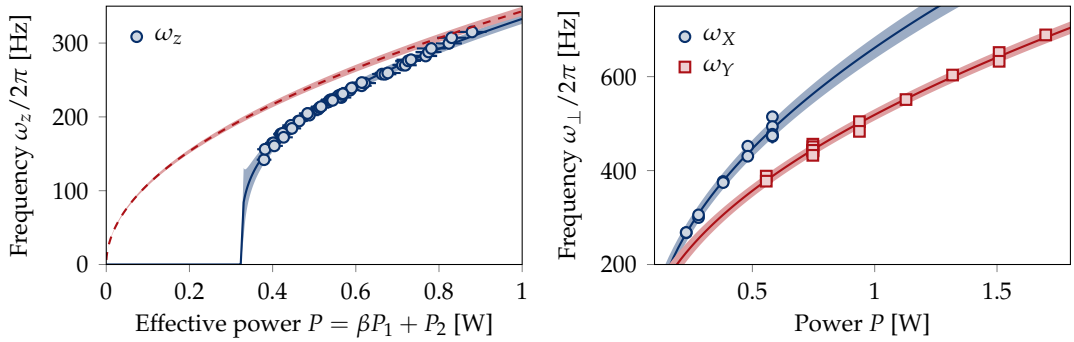

Figure 1.9 – Frequency measurements of the cODT. (Left) Vertical frequency ω_z as a function of an effective power. The blue solid line is a fit which takes into account the effects of gravity. The red dashed line is the gravity-compensated expected frequency, computed from the results of the fit but removing the effects of gravity. (Right) Transverse frequencies ω_X and ω_Y as a function of the trap power $P = P_i$, where $i = 1, 2$ for ω_X, ω_Y respectively. The solid lines are fits.

1.4 Science cell

The science cell to which the atoms are transported is the central part of the experiment. As described in section 1.2, the glass cell is where the Bose condensate is created and where the physics we aim at studying is realized. The main advantage of having a glass cell separated from the MOT chamber is mainly about practical optical access. We will see indeed that many laser beams are sent on the atoms, and a separated chamber gives more space and more options for the optical setups. A differential pumping stage in the transport path also allows to improve the vacuum between the MOT chamber and the glass cell.

In this section, we give a more detailed overview of our science cell setup. The dipole traps were already described in section 1.3, so we rather give here additional information about the control of the magnetic fields and the additional laser light that we use to address and detect the atoms. Those two aspects of the experimental setup are fundamental for all the experiments we describe in this work.

A global scheme of the glass cell is given in fig. 1.10. The coordinate system that we use in this section is given as follows: the vertical direction remains labeled z, the x direction coincides with the transport ODT propagation axis, and the y direction completes this orthonormal set. In this figure, we have represented the glass cell itself, surrounded by the coils that we use to generate uniform and gradient magnetic fields at the atom position. We also give the main laser beams entrance directions.

1.4.1 Magnetic field control

A precise control of the bias magnetic field (or B-field) is in general necessary for any cold atom experiment, because it defines the quantization axis. It is particularly true with dysprosium, which is highly magnetic, as described in section 1.1. Well controlled B-fields are used to work with Feshbach resonances, which, in the case of dysprosium, are usually quite narrow [Maier et al. 2015]. As mentioned in section 1.1, Feshbach resonances are

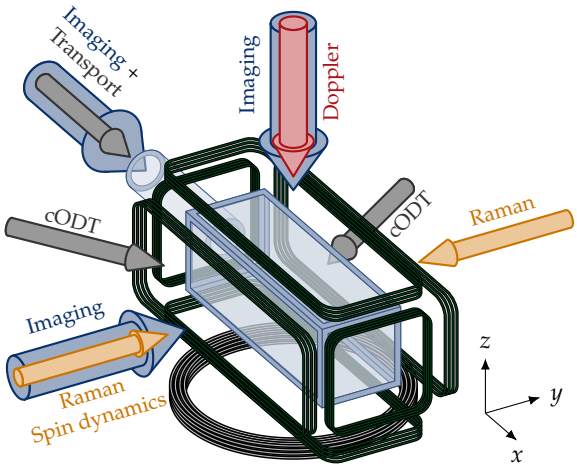

Figure 1.10 – Science cell. At the end of the experimental sequence, the dysprosium atoms are held at the center of this glass cell. It is surrounded by three pairs of coils (green rectangular shapes), which are used to control the magnetic field seen by the atoms. An additional coil is also present below all the others (gray circular shape), used to create strong magnetic gradients. The main laser beams addressing the atoms are the ODTs (gray), the imaging beams (blue), the Doppler cooling beam (red) and the spin dynamics beam (orange in the figure for clarity, although it has the same wavelength as the Doppler beam).

commonly used to tune the interaction strength between particles, and choose between strong and weak dipolar regimes. We also use B-fields to perform arbitrary spin rotations and to realize strong magnetic field gradients for Stern-Gerlach detection. Additional details about spin rotations and Stern-Gerlach detection will be given in chapter 5.

Field calibration

The magnetic field is controlled by the current passing through the coils, but the precise value of the field seen by the atoms as a function of the current is *a priori* unknown. Experimentally, we calibrate the B-field by a loss spectrum. The idea is to measure the energy difference between two Zeeman sublevels. The unknown B-field that we wish to measure indeed lifts the degeneracy of the ground state, such that, as introduced in section 1.1, the energy difference between two adjacent sublevels m_J and $m_J + 1$ is

$$\Delta E_{m_J,m_J+1} = h\nu_{m_J,m_J+1} = h \times \frac{g_J \mu_B}{h} \times |\mathbf{B}|\,, \tag{1.16}$$

with $\Delta\nu_{m_J,m_J+1}$ the frequency difference and $g_J\mu_B/h \approx 1.737\,\mathrm{MHz\,G^{-1}}$. When subjected to a RF radiation which is resonant with the splitting, an atom in the absolute ground state $m_J = -J$ can be transferred to the next Zeeman sublevel $m'_J = -J + 1$. This new state can decay back to the absolute ground state by means of dipolar relaxation [Burdick et al. 2015], which is a collisional process that converts the Zeeman energy into kinetic energy,

$$\mathrm{Dy}_{m_J} + \mathrm{Dy}_{m'_J} \rightarrow 2\mathrm{Dy}_{m_J} + \Delta E_{m_J,m'_J}, \tag{1.17}$$

and causes heating and losses, if the trap depth is smaller than the acquired kinetic energy. On the experiment, the radiation is produced by a small antenna placed close to the atoms.

Atom losses are measured as a function of the RF frequency after a few hundreds of ms of radiation. An example of a loss spectrum are given in fig. 1.11.

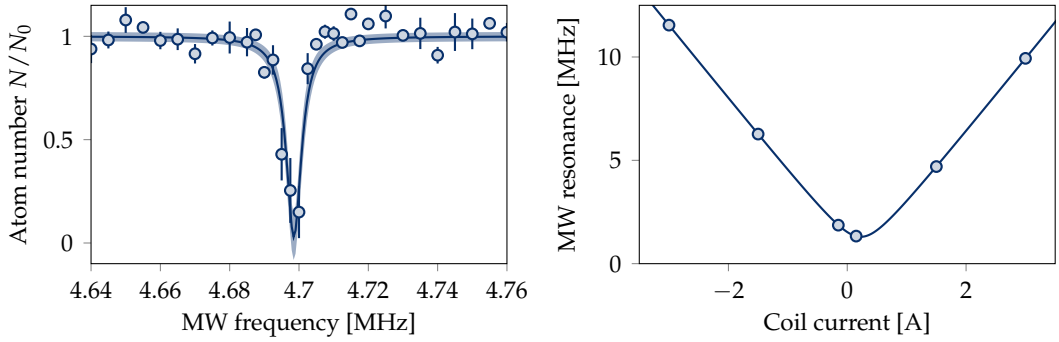

Figure 1.11 – Magnetic coil calibration. (Left) Typical loss spectrum obtained after shining the RF radiation on the atoms. The resonance frequency is extracted from a lorentzian fit (solid line). (Right) Resonance frequencies measured as a function of the current flowing through the vertical coil pair. Negative currents mean an inverted polarity. The solid line is a fit which takes into account stray fields.

The resonances are probed for different values of the coil current, and a fit of the form of eq. (1.16) allows to infer the value of the B-field for any current. This procedure is repeated in all three directions of space, granting full control on the strength and direction of the field.

We also have compensation coils in all three directions surrounding the whole experimental setup, that we use to cancel stray fields. We use them to ensure that the magnetic field vanishes on the atoms when the current flowing through the glass cell coils is set to 0 A.

1.4.2 Imaging

Our principal measurement tool is absorption imaging of the atomic sample. The idea is fairly simple, and consists in sending a large resonant beam on the sample. Photons are absorbed by the atoms, and are re-emitted in all directions through spontaneous emission. An image of the beam is then recorded on a CCD camera, and the atomic cloud is seen as a shadow on the beam.

Imaging is performed with the broad $\lambda = 421$ nm transition. Such a broad transition gives fast imaging cycles: on resonance and for $I \approx I_s$, an atom will absorb and re-emit a photon every 30 ns approximately. This imaging technique thus comes at a cost – scattered photons causes heating and destruction of the sample.

Here, we simply describe the basics of the imaging setup. More subtle effects related to spin-dependent cross-sections will be shortly discussed in chapter 5, where details about our spin-resolved imaging setup are given. The absorption of the atomic cloud is given by the Beer-Lambert law, which, in the limit of low intensity $I \ll I_{\text{sat}}$, reads

$$I(x,y) = I_0(x,y)\mathrm{e}^{-\bar{n}(x,y)\sigma_0} = I_0(x,y)\mathrm{e}^{-\mathrm{OD}(x,y)}, \tag{1.18}$$

where $\sigma_0 = 3\lambda^2/2\pi$ the resonant cross-section, and $\bar{n}$ the integrated density distribution

along the propagation axis

$$\bar{n}(x,y) = \int \mathrm{d}z\, n(x,y,z). \tag{1.19}$$

The optical depth (OD) of the sample is experimentally computed by comparing the intensities I and I_0, which amounts to comparing two pictures: a picture with the atoms and a picture without the atoms,

$$\mathrm{OD}(x,y) = -\log\left(\frac{I(x,y)}{I_0(x,y)}\right). \tag{1.20}$$

The optical depth is used to compute the total atom number

$$N = \int \mathrm{d}x\mathrm{d}y\mathrm{d}z\, n(x,y,z) = \frac{1}{\sigma_0}\int \mathrm{d}x\mathrm{d}y\, \mathrm{OD}(x,y). \tag{1.21}$$

A typical imaging setup is given in fig. 1.12.

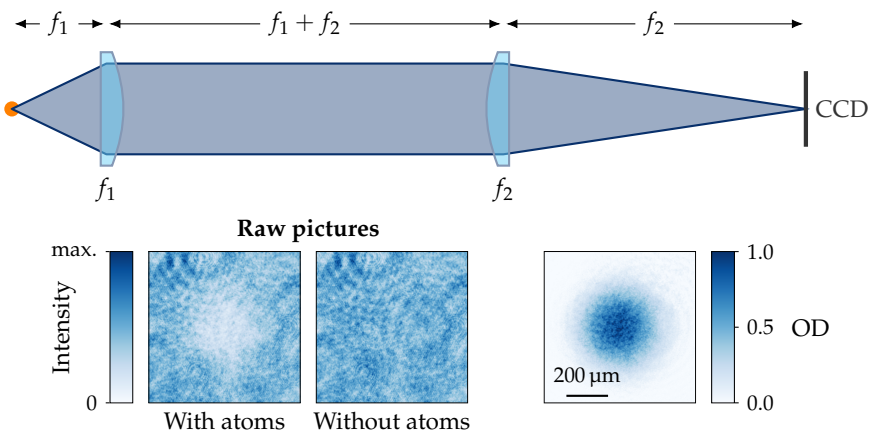

Figure 1.12 – Absorption imaging. (Top) Typical imaging setup. Two lenses of focal f_1 and f_2 are placed to image the atoms on a CCD camera. The magnification is given by f_2/f_1, and is typically calibrated by measuring free fall times of the atomic cloud, when possible. (Bottom) Typical images of the atoms, taken after free flight expansion. The raw pictures correspond to the maps $I(x,y)$ and $I_0(x,y)$ of the light intensity in the presence or in the absence of the atoms respectively. The optical depth is computed according to eq. (1.20).

1.4.3 Doppler cooling and spin dynamics

The atoms are also addressed with laser beams tuned to the MOT transition. On the vertical axis, we have installed a Doppler cooling beam, which we use to cool down the atoms in the transport trap before loading in the cODT. This process will be extensively described in chapter 2.

We also use the same transition to induce spin dynamics and spin-orbit coupling. These two processes are generated by beams propagating along the y axis (see fig. 1.10), and constitute the main tools for the experiments described in parts II and III. The technical characteristics of the optical setup regarding these experiments will be introduced in the

relevant sections of this manuscript.

1.5 Outlook

The experimental setup described in this chapter allows us to bring bosonic dysprosium to degeneracy, and to realize the experiments realized in the scope of this thesis. There are nonetheless a few updates that are intended to be implemented in the near future. These updates will give, in principle, better control on the atomic sample. In this section, we give a quick overview of these updates. Not all of them are operational nor ready to be installed, but an initial characterization, which required a non-negligible time in the lab, has been performed.

Optical transitions

In this work, only two transitions are used: the 421 nm and the 626 nm lines. There are however many more transitions which could be used to address the atoms, as described in section 1.1.

In the red and near infrared part of the optical spectrum specifically, there are several transitions with linewidths expected to be quite narrow, giving the possibility to engineer strong spin-dependent potentials with reduced spontaneous emission. Already with the MOT transition, which is 135 kHz wide, we will see in part II that we can realize strong light-spin coupling with limited heating.

These additional lines also grant us a choice regarding the nature of the spin coupling. Indeed, the 626 nm transition is a $J = 8 \rightarrow J' = 9$ transition, but we can also find $J' = 8$ and $J' = 7$ transitions, which have different algebra of light-spin couplings than the $J' = 9$. The 584 nm transition, for instance, is a $J' = 8$ transition that was characterized in the group of Prof. Pfau [Schmitt et al. 2013] and is thought to be a good candidate for demagnetization cooling

Experimentally, we can address some of these transitions with a Ti-Sapph laser which can be continuously tuned between 695 nm and 1005 nm. In this range, there are 5 known lines with the absolute ground state $^5I_8$ as the lower state, as shown in fig. 1.13.

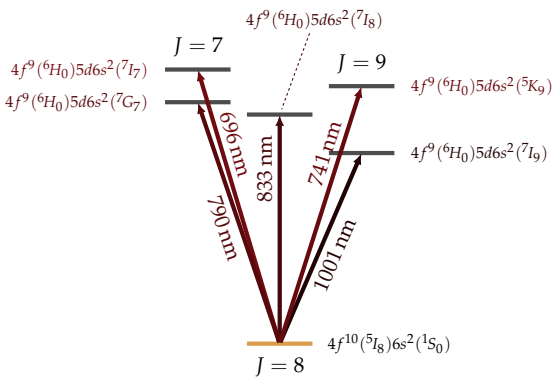

Figure 1.13 – Alternative transitions. These transitions are in principle addressable by our Ti-Sapph laser. The $J = 8 \rightarrow J' = 9$ transitions are cycling transitions that can potentially be used for laser cooling.

The 741 nm, which has a linewidth $\Gamma = 11.2\,\mathrm{ms}^{-1} = 2\pi \times 1.78\,\mathrm{kHz}$ is used in practice in the Stanford group for a narrow-line MOT [Youn et al. 2010]. The 1001 nm transition can be considered as a clock transition: a recent experiment [Petersen et al. 2019] measured the exited state lifetime to be above 87 ms, yielding a linewidth on the order of one Hz.

Precise experimental determinations of the other transitions shown in fig. 1.13 have not been realized to our knowledge. Yet, theoretical values allow to estimate their linewidths, and each of them should be in the kHz range [Dzuba et al. 2011].

High resolution imaging

Imaging setups such as the one presented in 1.12 are fundamentally limited by the numerical aperture (NA) of the first lens f_1. In theory, the size d of the smallest object that can be resolved is given by the diffraction limit $d \approx \lambda/2\,\mathrm{NA}$. If our current imaging setups were perfect[5], we still could not resolve details smaller than typically 1 µm.

Some of the experiments we plan on doing require to image small sub-micron objects, *e.g* vortices (see chapter 8). It is thus planned to install a high-NA microscope objective to replace the first lens f_1 mentioned above. The objective is ready to be mounted and has a numerical aperture $\mathrm{NA} = 0.65$, which provides a resolution below 0.5 µm at $\lambda = 421$ nm.

The objective is also designed to work with red and near infrared light. As mentioned above, this part of the spectrum contains many optical transitions that are of interest. Having a microscope objective at these wavelengths can thus also be used to project the addressing light locally. In combination with a digital micromirror device (DMD), which is also ready to be installed, the objective will allow the projection of arbitrary potentials and potentially single atom imaging and addressing [Ma 2014].

The imaging quality also strongly depends on the quality of the camera, which collects the light. The signal to noise ratio of the pictures indeed depends on parameters such as the quantum efficiency of the CCD and its electronic noise. For absorption imaging specifically, two pictures are taken. The time delay between these two pictures should be as short as possible, to reduce the effects of drifts of the imaging light. All these issues are addressed with an electron multiplier camera, which combine good quantum efficiency with fast repetition rate and low electronic noise.

Magnetic shielding

We already mentioned that a good magnetic control is necessary to perform our experiments. In some cases however, the magnetic field needs to be as small as possible. A typical example is the realization of topological interacting states, for which the sample is constituted of several spin states [Cui et al. 2013]. The timescales associated to the formation of these states are given by the interaction energy between particles, and are typically on the order of seconds [Yao et al. 2013]. We have seen however that the sample is also subjected to spin relaxation, causing heating and potentially destroying the system in faster timescales.

One solution is to work at zero field, which is equivalent of having zero Zeeman energy. In practice, the field still needs to be much bigger than the uncontrolled field fluctuations. Experimentally, we measure rms fluctuations on the order of 0.5 mG, meaning

[5] Putting aside any form of aberration or misalignment.

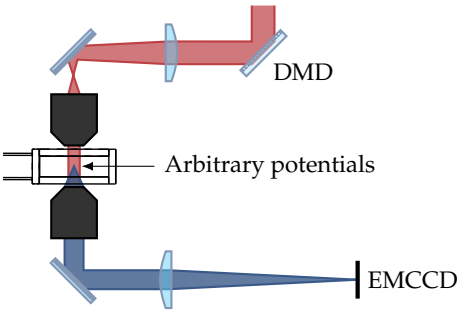

Figure 1.14 – Future high resolution optical setup. Two microscope objectives are placed on both sides of the glass cell. One of them is used for projecting arbitrary potentials, by imaging arbitrary patterns shaped by a DMD (red beam). The other objective is used in combination of the EMCCD camera for high resolution imaging (blue beam).

that the magnetic field cannot be lowered below than $\sim 10\,\mathrm{mG}$ to maintain a well defined orientation of the magnetic field. Already at these values, spin relaxation prevents the target topological states to be realized. Indeed, such fluctuations give energy scales in the kHz range, which is the same order of magnitude as the typical chemical potential of the degenerate gases we work with.

In order to explore interaction-related physics, the field fluctuations need to be much smaller than the typical interaction energy scale, which corresponds to a few hundreds of µG. It is thus planned to implement a magnetic shielding around the glass cell, constituted of µ-metal. The fluctuations are expected to be reduced by a few orders of magnitude, allowing to reduce the quantization by a similar ratio, and hence drastically reduce dipolar relaxation.

2 Magic polarization for in-trap Doppler cooling

2.1 Anisotropic polarizability **24**

2.2 Magic polarization of the intercombination line **26**

2.2.1 Differential polarizability 26

2.2.2 Differential light-shift measurement 27

2.2.3 Magic polarization 29

2.3 Application to Doppler cooling **31**

2.3.1 Doppler cooling at the magic angle 32

2.3.2 Non-zero differential light-shift: selective cooling 34

2.4 Conclusion **36**

In this chapter, we describe how we can make use of the strong anisotropic polarizability of dysprosium to implement efficient cooling of the atoms, trapped in a far-detuned optical dipole trap (ODT). Our approach is based on previous works for trapped atoms: Doppler cooling was implemented on magnetic traps [Newbury et al. 1995; Schmidt et al. 2003] and optical traps [Ido et al. 2000; Chalony et al. 2011]. More recently, such techniques were used to reach degeneracy [Stellmer et al. 2013], and even to cool down trapped molecules [Anderegg et al. 2018]. Experimentally, we realized that this intermediate step, which comes after transport and before evaporation, was necessary to have efficient loading of the crossed dipole trap, and ultimately to reach quantum degeneracy.

The anisotropy of the electronic orbitals in dysprosium leads to a weak, yet measurable tensorial contribution in its polarizability in the infrared domain [Li et al. 2017]. Close to the 741 nm transition, for example, the tensorial contribution leads to a significant polarization-dependent shift of the tune-out wavelength[1] [Kao et al. 2017]. In a far-detuned ODT, this effect translates to a polarization-dependent trapping potential. Theoretical predictions of the polarizability are challenging, as one has to consider all the details of the atomic spectrum. A quantitative determination of the ground state's scalar and tensorial polarizabilities at 1064 nm was recently realized in the group of Prof. Grimm in Innsbruck [Ravensbergen et al. 2018a]. In our experimental setup, we implement Doppler cooling on the 626 nm optical transition, and the polarizability of the corresponding excited state must

[1] Defined as the wavelength for which the ground state light-shift is canceled

be taken into account. More precisely, it is the *differential polarizability*, which measures the difference in trap depth between the ground and excited states, that is of importance.

We first give a brief theoretical description of the atom-light interaction, in order to outline the influence of the scalar and tensorial contributions on the trapping potential. We then describe our experimental measurement of the differential polarizability, and the determination of a *magic polarization* of the ODT, at which both states have equal polarizabilities. The last part of this chapter will be dedicated to the Doppler cooling scheme that we have implemented on the trapped atoms. We describe how the existence of the magic polarization provides a convenient knob for tuning the cooling procedure.

Most of the results presented in this chapter were published in [Chalopin et al. 2018a].

2.1 Anisotropic polarizability

The notion of polarizability was introduced in chapter 1, in order to characterize the trapping potential of our ODTs. Here, we go into a bit more detail on the nature of the atom-light interaction. An atom's polarizability basically measures the strength of the AC Stark shift resulting from its interaction with an oscillating electric field. Usually, the oscillating field $\mathbf{E}$ is produced by a laser beam,

$$\mathbf{E} = \frac{1}{2}\mathcal{E}\mathbf{u}\mathrm{e}^{-\mathrm{i}\omega t} + \text{c.c.}. \tag{2.1}$$

Here, ω is the angular frequency of the oscillating field, $\mathcal{E}$ is the complex amplitude and $\mathbf{u}$ is the unit polarization vector. For off-resonant light, and in second-order perturbation theory, the atom-light interaction can be decomposed as the sum of tensors of ranks 0, 1 and 2 [Kien et al. 2013]. As such, the interaction can be written in the form of a light-shift operator

$$\hat{V} = -\frac{|\mathcal{E}|^2}{4}\left[\alpha^{\mathrm{s}}_{nJ}\hat{\mathbb{1}} - \mathrm{i}\alpha^{\mathrm{v}}_{nJ}\frac{(\mathbf{u}^*\times\mathbf{u})\cdot\hat{\mathbf{J}}}{2J} + \alpha^{\mathrm{t}}_{nJ}\frac{3[(\mathbf{u}^*\cdot\hat{\mathbf{J}})(\mathbf{u}\cdot\hat{\mathbf{J}}) + (\mathbf{u}\cdot\hat{\mathbf{J}})(\mathbf{u}^*\cdot\hat{\mathbf{J}})] - 2\hat{\mathbf{J}}^2}{2J(2J-1)}\right]. \tag{2.2}$$

Here, we only consider the atom-light interaction which shifts the fine-structure levels of the atom, labeled $|nJ\rangle$[2]. The coefficients α^{s}_{nJ}, α^{v}_{nJ} and α^{t}_{nJ} are respectively the scalar, vectorial and tensorial polarizabilities, and depend on the frequency ω of the oscillating field. It is possible, in principle, to compute them, but a practical *ab initio* determination requires the full knowledge of the atomic spectrum and remains challenging for dysprosium, due to the complexity and large number of electronic shells involved [Dzuba et al. 2011; Li et al. 2017].

In the case of a linearly polarized laser light, the vectorial contribution is canceled, and the light-shift operator becomes

$$\hat{V} = V_0(\mathbf{r})\left[\alpha^{\mathrm{s}}_{nJ}(\omega)\hat{\mathbb{1}} + \alpha^{\mathrm{t}}_{nJ}(\omega)\frac{3(\mathbf{u}\cdot\hat{\mathbf{J}})^2 - \hat{\mathbf{J}}^2}{J(2J-1)}\right], \tag{2.3}$$

where the frequency dependence of the polarizabilities is now explicitly written, and

[2] This is valid for bosonic dysprosium, for which the absence of a nuclear spin leads to the absence of hyperfine coupling.

where we introduced a position-dependent amplitude, given by the laser beam intensity profile $I(\mathbf{r})$,

$$V_0(\mathbf{r}) = -\frac{1}{4}\left|\mathcal{E}(\mathbf{r})\right|^2 = -\frac{I(\mathbf{r})}{2\epsilon_0 c}. \tag{2.4}$$

As such, we recover the trapping potential of eq. (1.5).

In the presence of an external magnetic field $\mathbf{B}$, the $|nJ\rangle$ manifold of the atom is submitted to a Zeeman splitting. Introducing the corresponding Landé factor g_{nJ} and the Bohr magneton μ_B, this interaction is described by the Hamiltonian $\hat{H}_\mathrm{Z} = g_{nJ}\mu_\mathrm{B}\mathbf{B}\cdot\hat{\mathbf{J}}$. In the absence of light-shift, and when $g_{nJ} > 0$, this magnetic field polarizes the atom into the lowest Zeeman state $|nJ, m_J = -J\rangle$, with m_J labeling the total angular momentum (spin) projection. In the general case, the total Hamiltonian of our problem is

$$\hat{H}_{nJ} = \hat{H}_\mathrm{Z} + \hat{V} = g_{nJ}\mu_\mathrm{B}\mathbf{B}\cdot\hat{\mathbf{J}} + V_0(\mathbf{r})\left[\alpha^\mathrm{s}_{nJ}(\omega)\hat{\mathbb{1}} + \alpha^\mathrm{t}_{nJ}(\omega)\frac{3(\mathbf{u}\cdot\hat{\mathbf{J}})^2 - \hat{\mathbf{J}}^2}{J(2J-1)}\right]. \tag{2.5}$$

The scalar contribution of the light-shift has no effect on the angular momentum of the atom, and the energy shifts of all the different $|nJ, m_J\rangle$ substates are equal. The energy shifts resulting from the tensorial contribution, however, are not equal for each of these substates. In the case where this tensorial shift can be treated as a first order perturbation to $\hat{H}_\mathrm{Z}$, the atom remains in the lowest Zeeman state, and the light-shift is now simply given by

$$\delta E_{nJ,-J} = \langle nJ, -J|\hat{V}|nJ, -J\rangle\,. \tag{2.6}$$

For the discussion that follows, we will assume that this approximation is valid. Experimentally, it amounts to choosing a quantization magnetic field that produces a Zeeman splitting bigger than the tensorial light-shift.

Let us introduce the angle θ between the external field $\mathbf{B}$ and the light polarization $\mathbf{u}$. The total light-shift of the lowest Zeeman state, calculated from eq. (2.6), now reads

$$\delta E_{nJ,-J} = V_0(\mathbf{r})\left[\alpha^\mathrm{s}_{nJ}(\omega) + \alpha^\mathrm{t}_{nJ}(\omega)\frac{3\cos^2\theta - 1}{2}\right], \tag{2.7}$$

and explicitly depends on θ. For far-detuned ODTs in general, the anisotropy remains a small correction to the total light-shift of the ground state, because the tensor polarizabilty is small compared to the scalar one, even for highly magnetic elements such as dysprosium and erbium [Lepers et al. 2014; Li et al. 2017]. A schematic view of the total light shift is given in fig. 2.1.

It is worth noting that if the tensor contribution is large enough, it is possible to go from trapping to anti-trapping by simply tuning the polarization of the trapping light. Namely,

$$\text{if} \quad \left|\frac{\alpha^\mathrm{t}_{nJ}}{\alpha^\mathrm{s}_{nJ}} - \frac{1}{2}\right| \geq \frac{3}{2}, \qquad \text{then} \quad \delta E_{nJ,-J} = 0 \quad \text{for} \quad \theta = \arccos\sqrt{\frac{1}{3}\left(1 - \frac{2\alpha^\mathrm{s}_{nJ}}{\alpha^\mathrm{t}_{nJ}}\right)}. \tag{2.8}$$

In 2018, the ground state's scalar and tensor polarizabilities of dysprosium were precisely measured in the group of Prof. Grimm [Ravensbergen et al. 2018a], for a far-detuned ODT at 1064 nm. They report a scalar polarizability $\alpha^\mathrm{s}_0 = 184.4(24)$ at.u. and a

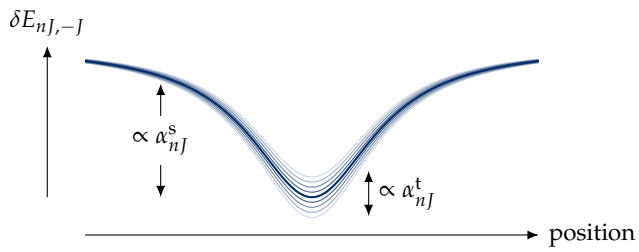

Figure 2.1 – Total light-shift created by a far-detuned ODT. The scalar contribution α^{s}_{nJ} essentially sets the total amplitude of the energy shift (solid blue line), and is polarization independent. The tensorial contribution α^{t}_{nJ}, chosen here to be smaller than the scalar component, sets how much the total shift can be tuned when varying the polarization, and is represented here with the light blue curves.

tensor polarizability $\alpha^{t}_{0} = 1.7(6)$ at.u., where at.u. stands for *atomic unit of polarizability*[3].

2.2 Magic polarization of the intercombination line

The analysis described in the previous section holds for any of the electronic states of the atoms. The excited states are also shifted in the presence of the light field, with shift amplitudes that can be quantitatively different from the ground state. As a result, the transition frequencies of trapped atoms generally depend on the intensity of the ODT, because of a differential light-shift.

In some cases and for a given transition, there are singular ODT wavelengths for which the ground and excited states experience the same energy shift. Such wavelengths are commonly called *magic wavelengths*, and are used, for example, in optical lattice clocks to cancel systematic shifts [Ludlow 2015]. On the other hand, one can also find wavelengths for which the excited state is light-shifted with an opposite sign, and is anti-trapped by the trapping light field. Those wavelength can be used *e.g.* to engineer state-dependent lattice potentials [Yi et al. 2008; Gerbier et al. 2010].

In our experimental setup, we used a far-detuned ODT operating at 1070 nm[4]. We do not expect a significant difference in the ground state polarizabilities at this wavelength compared to the one reported at 1064 nm mentioned above. However, the excited states polarizabilities remain unknown. When the differential light-shift becomes on the order of the transition linewidth, it needs to be taken into account when addressing the trapped atoms with resonant laser light – a typical example is the loading of a narrow-line MOT into an ODT [Duarte et al. 2011]. In this section, I detail our experimental determination of the differential light-shift of the intercombination line at $\lambda = 626$ nm in our ODT.

2.2.1 Differential polarizability

In the presence of a quantization magnetic field B, the ground and excited states of this $J = 8 \rightarrow J' = 9$ transition experience a Zeeman splitting. We will denote $|g\rangle$ and $|e\rangle$

[3]Defined as 1 at.u. $= 4\pi\epsilon_0 a_0^3$, with a_0 the Bohr radius.
[4]YLR 50 W, IPG Photonics

the lowest energy substates of the ground and excited state manifolds respectively. The energy difference between these states can be cast in

$$\Delta E_{eg} = E_e - E_g = \langle e|\hat{H}_e|e\rangle - \langle g|\hat{H}_g|g\rangle\,, \tag{2.9}$$

where $\hat{H}_{e,g}$ are given by eq. (2.5).

If we continue with the assumption that the light-shift can be treated as a first order perturbation to the Zeeman splitting, then $|g\rangle = |J, -J\rangle$ and $|e\rangle = |J', -J'\rangle$[5]. The energy difference becomes

$$\Delta E_{eg} = -\Delta g_{J,J'}\mu_{\mathrm{B}}B + V_0(\mathbf{r})\left[\Delta\alpha^{\mathrm{s}} + \frac{\Delta\alpha^{\mathrm{t}}}{2}(3\cos^2\theta - 1)\right]. \tag{2.10}$$

In this expression, $\Delta\alpha^{\mathrm{s,t}} = \alpha_e^{\mathrm{s,t}} - \alpha_g^{\mathrm{s,t}}$ are the differential polarizabilities, and $\Delta g_{J,J'} = J' g_{J'} - J g_J \approx 1.67$ is the weighted Landé factor difference. Consequently, the transition frequency ν is shifted from the bare resonance frequency ν_0 as a function of the magnetic field and of the trapping potential

$$\nu = \nu_0 - \frac{\Delta g_{J,J'}\mu_{\mathrm{B}}B}{h} + \frac{V_0(\mathbf{r})\Delta\alpha(\theta)}{h}, \tag{2.11}$$

where $\Delta\alpha(\theta) = \Delta\alpha^{\mathrm{s}} + \Delta\alpha^{\mathrm{t}}(3\cos^2\theta - 1)/2$ accounts for the total anisotropic differential polarizability. By measuring the transition frequency as a function of θ and for a given quantization field, we extract the differential polarizability. This method still holds even when the light-shift cannot be treated as a perturbation.

2.2.2 Differential light-shift measurement

We start with about 10^7 atoms of ^{162}Dy in our transport ODT (see chapter 1 for details on the optical setup). The ODT is linearly polarized, at about 60° with respect to the vertical direction. The quantization field $B = 2\,\mathrm{G}$ is initially aligned in the vertical direction.

The resonance frequency is probed by shining, for a time τ, a circularly-polarized (σ_-) laser beam of intensity I and frequency ν_{L}, aligned along the z-axis and close to the 626 nm transition. The beam diameter is chosen to be much larger than the cloud size (typically a few mm in the elongated direction), such that the atom-light interaction is homogeneous. A scheme of the experimental implementation is given in fig. 2.2.

Every trapped atom is subjected to a frequency-dependent radiative force which reads

$$\mathbf{F}(\Delta\nu, \mathbf{v}) = \frac{\hbar\mathbf{k}\Gamma}{2}\frac{s}{1 + s + 4\left(2\pi\Delta\nu - \mathbf{k}\cdot\mathbf{v}\right)^2/\Gamma^2}. \tag{2.12}$$

In this expression, $\mathbf{k} = -(2\pi/\lambda)\mathbf{e}_z$ is the laser wave vector, $\Gamma = 0.85\,\mu\mathrm{s}^{-1}$ is the transition linewidth, $s = I/I_{\mathrm{sat}}$ is the saturation parameter on resonance (we chose $s = 2$ in the following), and $\Delta\nu = \nu_{\mathrm{L}} - \nu$ is the detuning of the laser to the light-shifted resonance frequency. We also introduce the velocity $\mathbf{v}$ of the atom, which causes a Doppler shift in the resonance frequency.

[5] The Landé factor of the excited state has the same sign as for the ground state ; both states are low-field seeker.

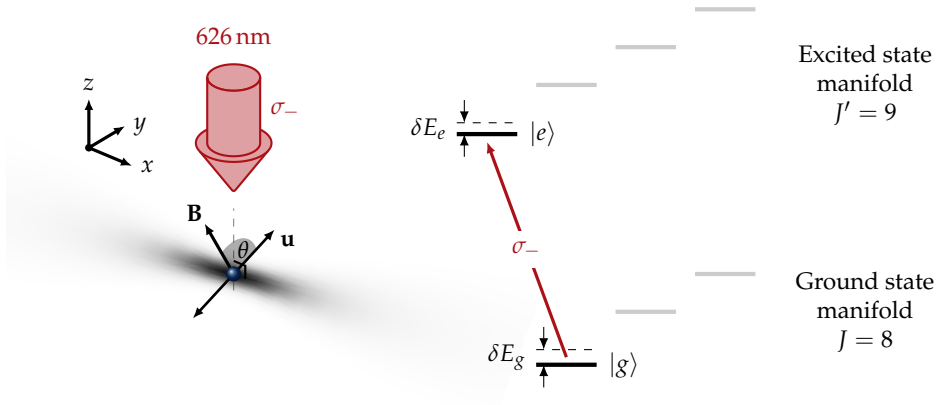

Figure 2.2 – Experimental setup. (Left) The atoms are trapped at the focal point of an ODT (shaded region) propagating in the x direction. The magnetic field $\mathbf{B}$, orthogonal to the propagation axis, forms an angle θ with the polarization vector $\mathbf{u}$ of the ODT. The probe beam (red arrow), whose frequency is close to the 626 nm transition, is propagating along $-z$, and is circularly polarized. (Right) Energy levels taken in consideration here. The ground and excited states manifold have their degeneracy lifted by the Zeeman term and we designate by $|g\rangle$ and $|e\rangle$ their respective lowest energy states. These states are furthermore shifted from their Zeeman-shifted position (dashed lines) in the presence of an ODT. The amplitude of this shift is given by eq. (2.6). The transition frequency is probed by shining a σ_- laser near resonance.

Upon the application of such a force, the atoms are kicked and acquire a velocity v_z in the vertical direction. In the limit of short τ, we can neglect the displacement of the atom during the kick, such that v_z is simply written

$$v_z = \frac{\tau}{m} F_z(\Delta\nu, \mathbf{v}), \tag{2.13}$$

where m is the atomic mass and $F_z = \mathbf{F} \cdot \mathbf{e}_z$ is the vertical component of $\mathbf{F}$.

In the experiment, we measure the center-of-mass (CoM) displacement δz of the atomic cloud after turning-off the trapping potential and letting the atoms fall for a time-of-flight (ToF) duration t_{ToF}. This displacement can be calculated by averaging the acquired velocity v_z over the position and velocity distribution in trap $\rho(\mathbf{r}, \mathbf{v})$, to get

$$\delta z = t_{\mathrm{ToF}} \int \mathrm{d}\mathbf{r}\mathrm{d}\mathbf{v}\, v_z(\Delta\nu(\mathbf{r}), \mathbf{v})\rho(\mathbf{r}, \mathbf{v}), \tag{2.14}$$

where the position dependence of $\Delta\nu$ is now explicitly written. Our method is similar to the one used for measuring the excited state polarizability of the 583 nm transition in erbium by [Becher et al. 2018][6].

In all the experiments described in this section, the strength of the quantization field is

[6] Their experimental setup is almost identical, but they measure resonant atom losses instead of displacement.

kept constant. As such, we introduce the bare, Zeeman-shifted resonance frequency

$$\nu_Z = \nu_0 - \frac{\Delta g_{J,J'} \mu_B B}{h}. \tag{2.15}$$

which is also constant throughout all our measurements, and which is determined by measuring the resonance frequency in the absence of trap. The detuning $\Delta\nu^* = \nu_L - \nu_Z$ then conveniently represents the detuning to the bare, Zeeman-shifted resonance.

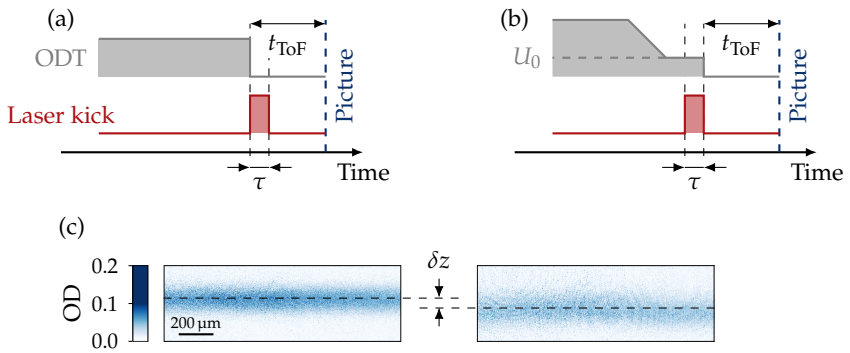

Figure 2.3 – Experimental sequence for measuring the resonance frequency. (a) The bare, Zeeman-shifted resonance is measured by applying the kicking pulse for a duration τ after the trap is turned off, and measuring the center-of-mass displacement after a time-of-flight t_{ToF}. (b) The light-shifted resonance is measured by kicking the atoms in-trap. Before the kick, the trap depth is adjusted to its final value U_0. Experimentally, the resonance is measured for several values of U_0. In both cases, we have $\tau = 30\,\mu\mathrm{s}$ and $t_{\mathrm{ToF}} = 1.5\,\mathrm{ms}$. (c) Example of cloud pictures. When the light is off-resonant (left), the cloud is not displaced. On resonance (right), the cloud is kicked and the displacement δz can be measured.

A scheme of the experimental sequence is given in fig. 2.3. The bare resonance frequency, which defines $\Delta\nu^* = 0$, is measured by kicking the atoms right after the ODT is turned off. The light-shifted resonance frequency is measured by kicking the atoms in-trap. The measurement is repeated for several values of θ and for several values of the ground state trap depth $U_0 = V_0(\mathbf{0})\alpha_g(\theta)$, where $\alpha_g(\theta)$ is the total ground state polarizability. The value of θ is tuned by changing the orientation of the quantization field. The measured resonances are given in fig. 2.4.

We can distinguish two broadening mechanisms. The position distribution in the trap causes an inhomogeneous broadening (intuitively, there are more atoms at the bottom of the trap, where the light-shift is stronger, than on the wings). The velocity distribution furthermore causes an homogeneous Doppler broadening. These two mechanisms have a strong impact on the measured line shapes, and are taken into account in our fitting model. The cloud's temperature and the trap depth, which play a significant role in these broadening mechanisms, are measured independently.

2.2.3 Magic polarization

As one can see in fig. 2.4, the presence of a trap causes a shift in the resonance frequency. From eq. (2.11), we expect this shift to be linear in the potential strength as long as θ is

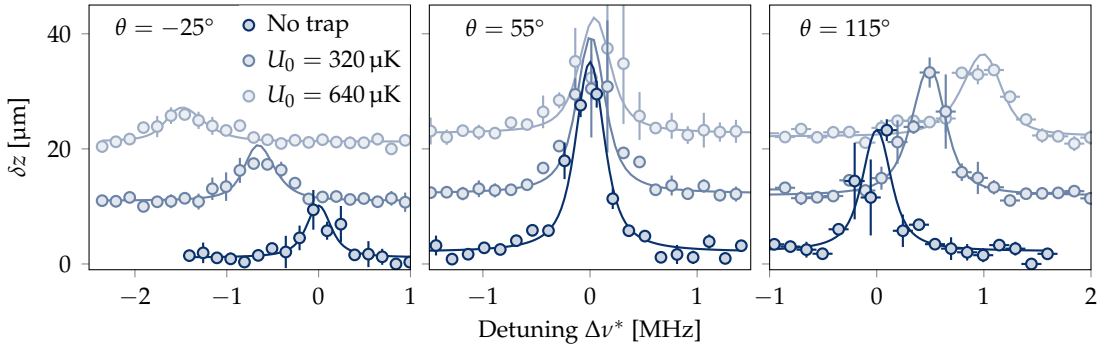

Figure 2.4 – Resonance measurements. Center-of-mass displacement δz of the atomic cloud after a time-of-flight $t_{\mathrm{ToF}} = 1.5\,\mathrm{ms}$ as a function of the detuning $\Delta\nu^*$, for different trap depth and different angles θ. The dark blue data correspond to the bare, Zeeman-shifted resonance measured in the absence of the trap, and sets by definition $\Delta\nu^* = 0$. The lighter colors indicate stronger trap depths. Solid lines are fits of the model given by eq. (2.14). The different curves are shifted from one-another for clarity. Error bars represent the 1σ statistical error.

kept constant. In fig. 2.5 we plot the differential trap depth extracted from the resonance frequency as a function of U_0. We then extract the differential polarizability from a linear fit.

The total differential polarizability $\Delta\alpha$ as a function of θ is given in fig. 2.5. The scalar and tensorial differential polarizabilities are extracted from a fit to our data. The fitting procedure does not rely on the approximation that leads to eq. (2.10), in which we assume the magnetic field to be sufficiently strong to consider the light-shift as a perturbation, but rather uses eq. (2.9), without any assumption on the relative strength of the Zeeman term. The only free parameters are $\Delta\alpha^{\mathrm{s}}$ and $\Delta\alpha^{\mathrm{t}}$.

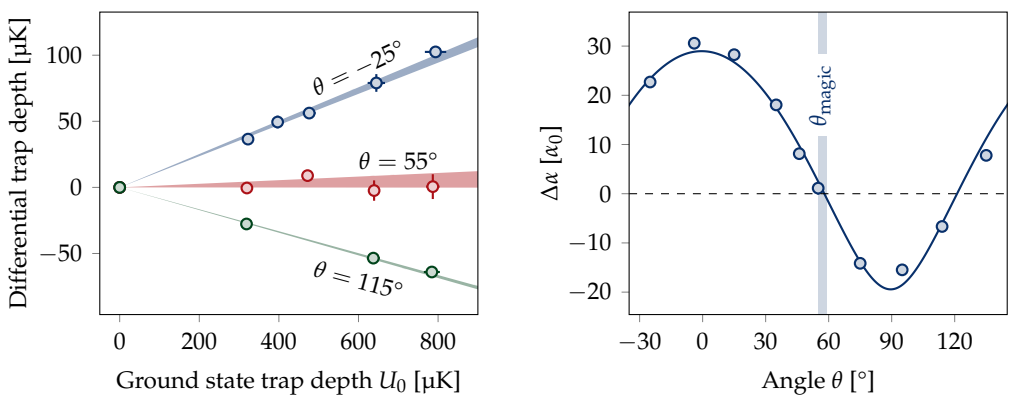

Figure 2.5 – Measurement of the differential polarizabilities. (Left) Differential trap depth as a function of the ground state trap depth. The differential polarizability is extracted from a linear fit to the data. The three data sets given here correspond to the data presented in fig. 2.4. (Right) Differential polarizability $\Delta\alpha$ as a function of the angle θ. The solid line is a fit, using eq. (2.9) as a model. The *magic angle* θ_{magic}, defined as the angle for which $\Delta\alpha = 0$, is also represented.

We find $\Delta\alpha^{\mathrm{s}} = -5(2)\alpha_0$ and $\Delta\alpha^{\mathrm{t}} = 33(2)\alpha_0$. The uncertainties are extracted from a bootstrap fitting procedure.

At 1070 nm, we expect the ground state polarizabilities to be close to the one measured at 1064 nm, but not necessarily equal. Theoretical estimations, using the data of [Li et al. 2017], give $\alpha_g^{\mathrm{s}} = 193(10)\alpha_0$ and $\alpha_g^{\mathrm{t}} = 1.3(10)\alpha_0$. From these values and our measurements, we can give an estimate to the excited state polarizabilities, $\alpha_e^{\mathrm{s}} = 188(10)\alpha_0$ and $\alpha_e^{\mathrm{t}} = 34(2)\alpha_0$.

Although the scalar contributions to the polarizabilities are similar for the ground and excited states, the tensorial component is much bigger for the excited state than for the ground state. This implies the existence of a *magic angle* θ_{magic}, for which the differential light-shift is canceled, and which is clearly visible in fig. 2.5. Our measurements yield $\theta_{\mathrm{magic}} = 57(2)^\circ$. It is worth noting that neither the ground nor the excited states have polarizabilities that fulfill the condition of eq. (2.8), *i.e.* there are no angles for which the total light-shift of either of these states is canceled, at the near-infrared wavelength of our ODT.

2.3 Application to Doppler cooling

As described in the previous chapter, our atomic cloud, once transported to the glass cell, is loaded in a cross dipole trap (cODT) before evaporative cooling. The evaporation efficiency crucially depends on the initial density of the cloud – a higher collision rate leads to faster evaporation. It is thus important, before evaporation, to optimize the loading in the cODT.

Several factors influence the cODT loading efficiency. The trap depth needs to be large enough to load even hotter atoms, and the trap volume needs to be small enough to have larger densities. However, if the volume is too small, fewer atoms are likely to explore the crossed region and become trapped.

Experimentally, we have adopted two strategies that help us improving the cODT loading efficiency. On the one hand, as already introduced in chapter 1 the trap volume can be adjusted by a fast modulation of the individual ODTs, allowing to choose between large volume (loading phase) and small volume (compression phase). On the other hand, inspired by the dysprosium experiment of the Stuttgart group [Maier 2015], we implement a Doppler cooling stage in the ODT before crossing. We make use of the same 626 nm beam introduced in the previous section to cool down the atoms. In fig. 2.4, we saw that the shift in the resonance frequency can be of a few MHz, which is several times the linewidth Γ of the transition. We thus expect the angle θ to be an important parameter in the implementation. In this section, we discuss the experimental optimization of this technique, how far we can cool the atoms, and how the magic angle θ_{magic} can be helpful.

There are essentially four parameters to play with in order to optimize the cooling efficiency: the angle θ between the quantization field and the ODT polarization, the frequency ν_{L} of the cooling beam, its saturation parameter $s = I/I_{\mathrm{sat}}$ and the cooling step duration t_{D}.

In the one-particle picture, the situation is expected to follow the textbook Doppler cooling mechanism[7]: the resonance frequency ν depends on θ as described by eq. (2.11),

[7] Our cooling beam is oriented along the vertical axis, which corresponds to an eigen-axis of the dipole

and optimal cooling is reached when $\Delta\nu = \nu_L - \nu = -\Gamma/2$, for which the lowest temperature is the Doppler temperature $T_D = \hbar\Gamma/2k_B \approx 3.2\,\mu K$. In the limit of low intensity $s \ll 1$, the typical cooling time is given by $t_D^{-1} \sim \hbar k^2 s/2m$, which is on the ms timescale.

In the case of a trapped, interacting atomic cloud, the situation is much more complicated. The timescales are strongly impaired by the trapping dynamics and the collision rates, and light-assisted losses limit the lowest possible temperature. In the following, we explore the cooling mechanisms after varying some of these parameters. We do not aim to give a full quantitative description of the cooling processes and its limits, but rather empirically find a situation which is beneficial for the subsequent steps of the experiment.

2.3.1 Doppler cooling at the magic angle

We start by investigating the cooling dynamics for $\theta = \theta_{magic}$, and for a saturation parameter $s = 0.5$. The Doppler cooling beam is shone on the trapped atoms, and an absorption picture of the atomic cloud is taken after 1.5 ms of ToF. The experiment is repeated for several values of the laser detuning $\Delta\nu$ and for several cooling durations t_D. The temperature and atom number are computed from the ToF pictures and the trap frequencies. Results are given in fig. 2.6.

The overall behavior observed agrees qualitatively with a textbook Doppler cooling mechanism. Far from resonance, the atoms do not see the cooling light and are not affected. When the laser frequency gets closer to resonance, we either observe cooling (negative detunings) or heating (positive detunings). For longer times, we also observe atom losses close to resonance, which are specifically strong for positive detunings.

To be more quantitative, we see from fig. 2.6(a) that the temperature of the cloud can be significantly reduced. We can *e.g.* cool it from 100 µK to about 30 µK in about 200 ms. This strong cooling however goes along with a significant atom loss – about a factor 4 from fig. 2.6(b). As already mentioned, we aim for optimizing the initial condition for evaporative cooling, the relevant quantity to consider is thus the elastic collision rate [Wu et al. 1997]

$$\gamma = n\sigma\bar{v}. \tag{2.16}$$

In this expression, n is the particle density, σ is the scattering cross-section and $\bar{v}$ is the average thermal velocity. We choose $n = n_0$ the peak density at the center of the trap, and plot the result[8] in fig. 2.6(c). As we can see, cooling is in general accompanied by an increase in the collision rate, at least for relatively short times. For longer times, atom losses are too great to have a significant impact on the collision rate, even though the temperature is strongly reduced.

This situation is quantitatively investigated in fig. 2.7. We extract[9] from the data of fig. 2.6 the minimal temperature T_{min} and the maximum collision rate γ_{max}, along with the

trap. Strictly speaking, the beam can thus only cool down the vertical motional degree of freedom of the trapped atoms. The other directions are cooled down via collisions, similarly to sympathetic cooling in ion traps (see *e.g.* [Larson et al. 1986]). As such, we already know that the single-particle picture cannot describe our situation.

[8] In the case of dysprosium, the scattering cross-section must include the anisotropic dipole-dipole term, such that the overall collision rate depends on the trap geometry. The values we give here are only rough estimates of the absolute value of the collision rates. The relative values however, still provide useful information.

[9] We perform a quadratic fit around the visible extrema.

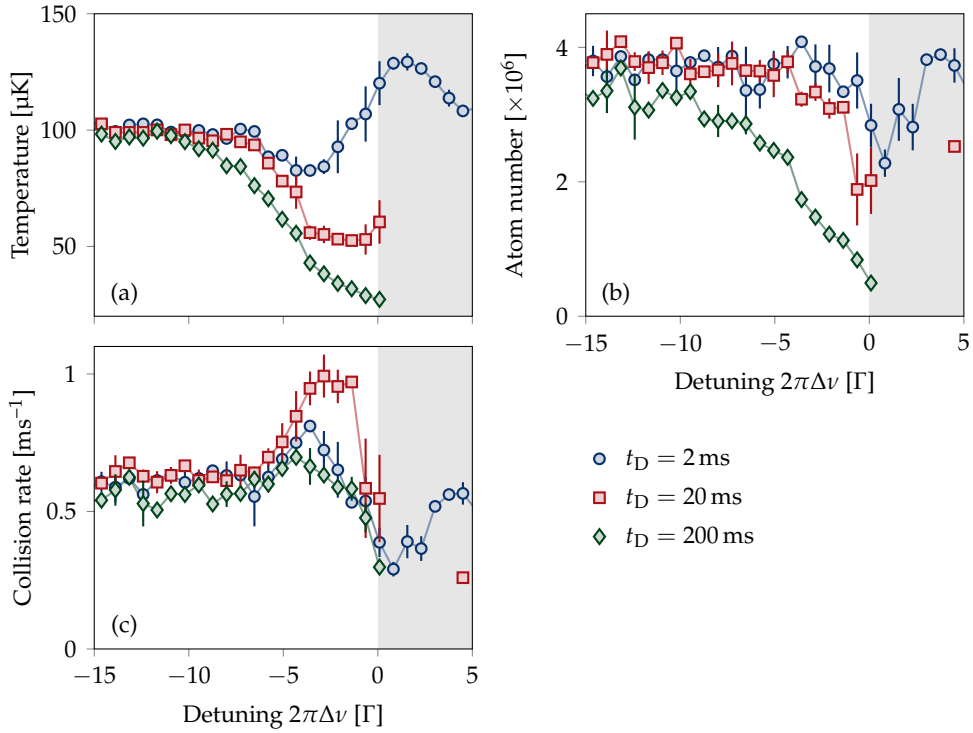

Figure 2.6 – Doppler cooling in trap for different durations t_D. (a) Temperature of the cloud as a function of laser detuning. The temperatures are inferred from the cloud size after a 1.5 ms ToF, taking into account the trap frequencies (see chapter 1 for their measurement). (b) Atom number in trap. When the detuning is positive (shaded region), the atoms are heated and are lost. (c) Collision rate at the center of the trap.

detunings at which they are reached.

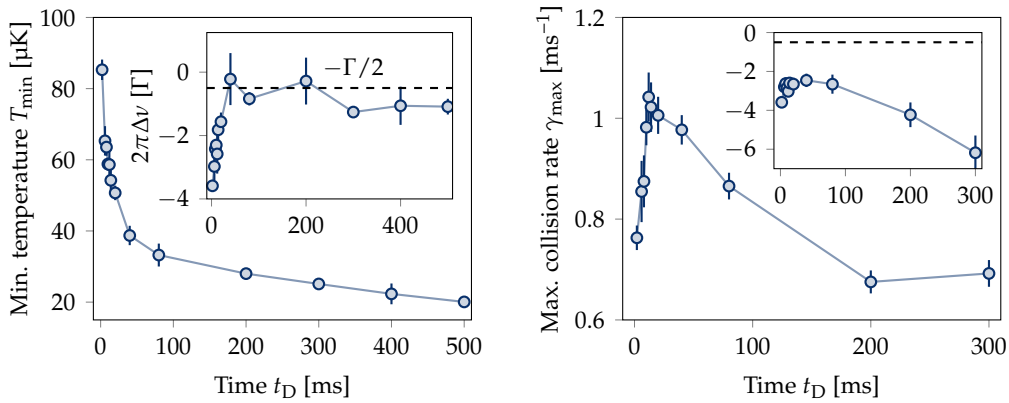

Figure 2.7 – Cooling dynamics. Minimal temperature T_{min} (left) and maximal collision rate γ_{max} (right) reached as a function of the cooling time t_D. (Insets) Detunings at which the T_{min} (left) and γ_{max} (right) are measured. The dashed lines marks the textbook expected detuning $-\Gamma/2$.

The data of fig. 2.7 clearly exhibits two different timescales. We see a fast and efficient

cooling during the first few tens of ms, associated to an increase of the collision rate. We also see that the value of the detuning at which T_{min} is measured rapidly saturates close to the textbook value $2\pi\Delta\nu = -\Gamma/2$. This detuning, however, does not correspond to the one with the highest collision rate, because of strong atom losses at this value, associated to light assisted inelastic collisions. By going further away from resonance, although the temperature is a bit higher, the lower atom losses lead to a higher collision rate.

For longer times $t_{\text{D}} \gtrsim 50$ ms, the cooling rate is reduced, and the collision rate decreases. Even though the temperature keeps decreasing, it cannot overcome the atom losses. As a result, γ_{max} is reached much further away from resonance, where essentially nothing happens.

2.3.2 Non-zero differential light-shift: selective cooling

The measurements performed above were repeated for different values of θ. When $\theta \neq \theta_{\text{magic}}$, the resonance frequency depends on the position in the trap. From now on, $\Delta\nu$ will designate the detuning from the resonance frequency at the center of the trap, *i.e.* defined by eq. (2.11) at $\mathbf{r} = \mathbf{0}$. We show in fig. 2.8 examples of such measurements away from the magic angle.

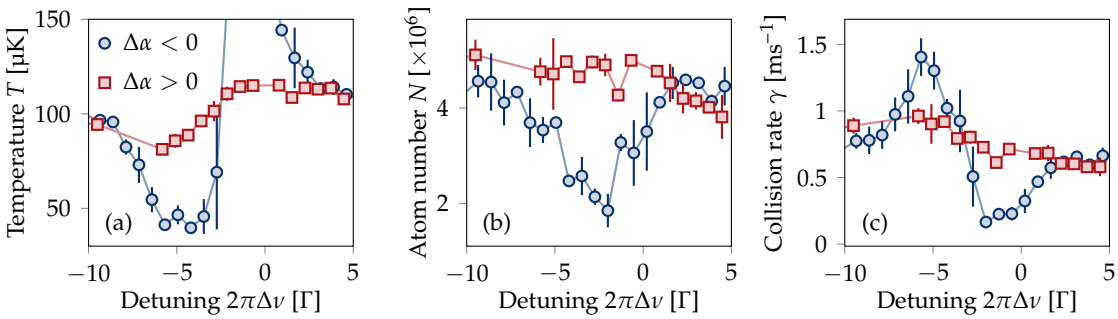

Figure 2.8 – Angle dependence for Doppler cooling. (a) Temperature, (b) atom number and (c) collision rate as a function of the detuning $\Delta\nu$. The data for $\Delta\alpha < 0$ (blue circles) was taken at $\theta = \theta_{\text{magic}} + 10°$, after $t_{\text{D}} = 6$ ms of cooling. The data for $\Delta\alpha > 0$ (red squares) was taken at $\theta = \theta_{\text{magic}} - 10°$, after $t_{\text{D}} = 20$ ms of cooling.

The difference between $\theta > \theta_{\text{magic}}$ ($\Delta\alpha < 0$) and $\theta < \theta_{\text{magic}}$ ($\Delta\alpha > 0$) is striking. In the former case, we see that cooling is fast and efficient. The cloud is cooled down to ~ 30 μK in 6 ms with limited atom losses. As a result, the collision rate increases to a relatively high value. We furthermore notice that the peak in γ occurs around $2\pi\Delta\nu = -5\Gamma$, relatively far away from resonance. On the contrary, when $\theta < \theta_{\text{magic}}$, the cooling is almost non-existent on the timescale we consider here. For longer times, we experimentally observe stronger atom losses, and almost no gain in the collision rate.

This behavior is explained by the trap-dependent resonance frequency. A sketch of the situation is given in fig. 2.9, in which we have three distinct behaviors.

- When $\theta < \theta_{\text{magic}}$, we have $\Delta\alpha > 0$ (fig. 2.9, left). The energy difference between the ground and excited states is smaller at the center of the trap than over the wings. In

order to cool down the atoms, the Doppler cooling beam needs to be red-detuned with all the atoms. Consequently, the detuning seen by the atoms in the wings is bigger than those at the trap center. Overall, only the regions of high atomic density see the cooling light.

– For $\theta = \theta_{\text{magic}}$, the differential light-shift is canceled (fig. 2.9, middle). Every atom in the trap sees the same detuning, and the lowest temperatures are reached when $2\pi\Delta\nu \approx -\Gamma/2$ (fig. 2.7, left).

– When $\theta > \theta_{\text{magic}}$, then $\Delta\alpha < 0$ (fig. 2.9, right). Here, the energy difference between the ground and excited states is bigger in the trap center. When setting the cooling beam close to resonance on the wings, the atoms at the trap center are further red-detuned and don't see the cooling light. As a result, Doppler cooling is effective on the wings, where the density is lower.

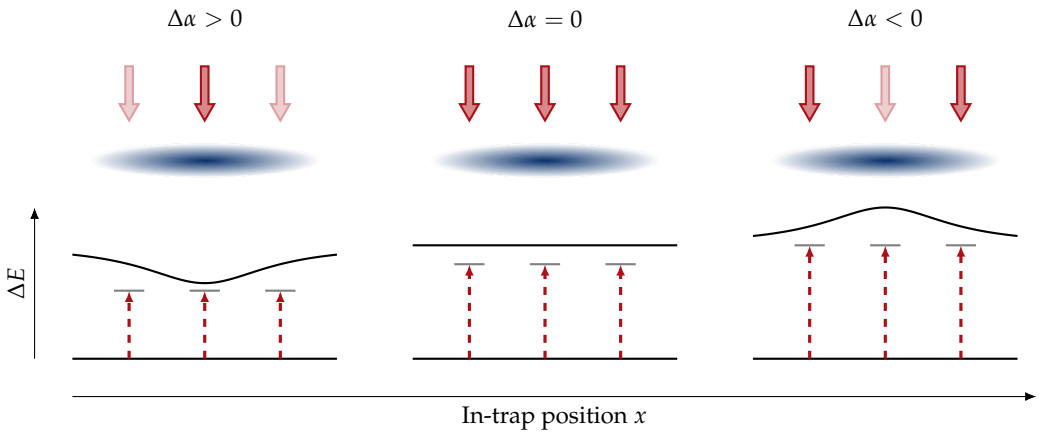

Figure 2.9 – Differential light-shift effects on Doppler cooling. Sketch of the situations for $\Delta\alpha > 0$ (left), $\Delta\alpha = 0$ (middle) and $\Delta\alpha < 0$ (right). (Bottom) The plots represent the energy difference ΔE_{eg} as a function of the trap position. The red dashed arrows denote the transition used for Doppler cooling. (Top) The diagrams represent the position dependent interaction. The faded red arrows represent weaker interaction than the bright ones. The blue, shaded areas represent the atomic cloud.

The qualitative explanation given above is confirmed by the maximum measured collision rate γ_{max} as a function of θ. The results are given in fig. 2.10.

We can see that our Doppler cooling implementation is more efficient for $\theta > \theta_{\text{magic}}$, which corresponds to $\Delta\alpha < 0$. Globally, cooling is inefficient when the density is too high. This is the case for $\theta < \theta_{\text{magic}}$ of course, where the regions of high density are the only ones that are addressed by the cooling beam. This situation is also valid at the magic angle. For $\theta > \theta_{\text{magic}}$ however, the high-density region is not addressed at all. Atoms in the wings are cooled efficiently, and ultimately, when their energy has been sufficiently lowered, end-up in the central region. The density keeps increasing, but atom losses are limited, and we observe a relatively large increase (almost a factor of 3) in the collision rate.

The detuning at which γ_{max} is measured is also consistent with our scenario (see inset of fig. 2.10). For $\theta < \theta_{\text{magic}}$, 'efficient' cooling is measured far from resonance, where

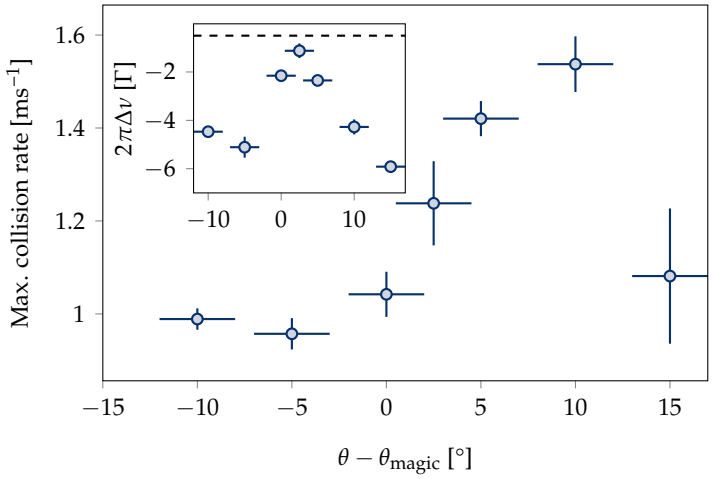

Figure 2.10 – Doppler cooling optimization. Maximal collision rate γ_{max} measured as a function of θ. (Inset) Detuning at which γ_{max} is measured. The dashed line marks the textbook result $-\Gamma/2$.

light-assisted losses are limited. Around $\theta \approx \theta_{\text{magic}}$, we get closer to $2\pi\Delta\nu \approx -\Gamma/2$. As discussed in section 2.3.1, we see that this theoretical value is not reached because of the strong atom losses observed – which are now attributed to light-assisted collisions. For $\theta > \theta_{\text{magic}}$, efficient cooling is performed on the wings, which corresponds to having a beam further detuned from the trap center.

2.4 Conclusion

The implementation of a Doppler cooling stage in the ODT was the primary goal of this study. It turns out that in the case of dysprosium, using a relatively narrow transition and having strong spin-dependent light-shifts results in a non-trivial optimization procedure for the cooling parameters.

We observed that the differential light-shift $\Delta\alpha$ caused by an ODT at 1070 nm on the intercombination line at 626 nm can be tuned by changing the angle between the beam polarization and the external quantization magnetic field. More importantly, we observed that it can be completely canceled when choosing the specific angle $\theta = \theta_{\text{magic}}$. This total cancellation is quite convenient, especially since the typical differential light-shift is large compared to the transition linewidth.

We use this feature to implement and optimize a Doppler cooling stage. The existence of a magic angle gives us a convenient tool for selectively cooling regions of the ODT. By carefully choosing θ such that $\Delta\alpha$ is small and negative, we achieve cooling on the wings of the ODT, limiting the light-assisted losses that occur in regions of high density. In a sense, a small and negative $\Delta\alpha$ allows to realize the analog of a dimple trap, such as in [Stellmer et al. 2013], where high density regions are pushed away from resonance by the application of an additional, tightly focused ODT.

The figure of merit we chose to use is the collision rate γ at the trap center, which is the relevant parameter to consider for forced evaporation. Our scheme allows us to

significantly increase the collision rate, and we will see in the next chapter that it provides a good starting point for the forced evaporation in the cODT.

The efficiency of a cooling mechanism can also be quantified by computing the quantity

$$\chi = -\frac{\mathrm{d}\log\mathcal{D}}{\mathrm{d}\log N}, \tag{2.17}$$

where $\mathcal{D}$ is the phase space density (PSD) and N the atom number. Using our optimum point, obtained for $\theta = \theta_{\text{magic}} + 10°$, we measure an efficiency $\chi = 6.0(4)$.

3 Bose-Einstein condensation of dysprosium

3.1 Condensation of dipolar gases **40**
3.1.1 Bose-Einstein condensation in a harmonic trap 40
3.1.2 Stability of a dipolar BEC 42
3.2 Evaporation to degeneracy **45**
3.2.1 Loading the crossed dipole trap 46
3.2.2 Forced evaporative cooling 48
3.3 Degenerate Bose gases **50**
3.3.1 Expansion of a dipolar BEC 51
3.3.2 Calibration of the atom number 52
3.4 Conclusion **55**

We describe in this chapter the experimental production of degenerate dysprosium Bose gases. Condensation was predicted by Bose and Einstein in 1924 [Bose 1924; Einstein 1924] and was achieved more than 70 years later with rubidium atoms [Anderson et al. 1995] and sodium atoms [Davis et al. 1995]. Since then, numerous experiments use degenerate gases to explore the physics of ultracold quantum matter.

Section 3.1 is dedicated to the physical phenomena related to Bose-Einstein condensation. We first discuss simple notions of non-interacting gases, in order to set the basics and introduce the notations that will be used throughout this chapter. The role of interactions is also discussed, and particularly the consequences of the anisotropic and long-range dipolar interactions, which have both a qualitative and quantitative impact on the shape and stability of a degenerate dysprosium Bose gas. As we will see, these consequences need to be considered beforehand in the design of the experiment and on the choice of the isotope.

Experimentally, we reach condensation by means of forced evaporative cooling in a crossed optical dipole trap (cODT). The optical setup of the cODT, and specifically the implementation of a spatial modulation of the individual traps, was already introduced in chapter 1. Here, in section 3.2, we discuss instead the impact of such an apparatus on the loading of the cODT. Along with the Doppler cooling apparatus, discussed in chapter 2, modulation allows to bring the experiment to acceptable conditions for evaporative cooling. Our evaporation is efficient enough to reach condensation in a few seconds.

The last section is dedicated to brief studies and calibrations of our condensate. The typical signature of condensation is observed, namely the emergence of a condensed anisotropic peak on top of the isotropic gaussian velocity distribution of thermal atoms. The effects of dipolar interactions are also visible in the evolution of the density distribution after time-of-flight, as we observe an enhanced elongation of the cloud in the direction of the dipoles. Finally, we show how we use the condensation transition to estimate the efficiency of our imaging system and calibrate the difference between the measured and real atom number.

3.1 Condensation of dipolar gases

In this section, we review the specificities of dipolar interactions in the formation and stabilisation of a Bose-Einstein condensate (BEC). We start briefly with conventional BECs in harmonic traps, before discussing the role of the dipolar interactions.

3.1.1 Bose-Einstein condensation in a harmonic trap

We do not aim, here, at giving a detailed and quantitative description of the condensation, but we rather give a qualitative overview of the physics. The equations and results presented here are derived in details in review papers and books (see *e.g.* [Pitaevskii et al. 2016; Dalfovo et al. 1999]), or even lectures (*e.g.* [Cohen-Tannoudji 1997; Cohen-Tannoudji 1998]).

The main idea behind the process of condensation is illustrated in fig. 3.1. In bosonic statistics, the chemical potential is constrained to be smaller than the energy of the ground state of the system, $\mu \leq \epsilon_0$. When μ approaches ϵ_0, the occupation number of the ground state increases, while the number of particles in the excited states remains bounded. At $\mu = \epsilon_0$, the number of atoms in the ground state diverges, and the system forms a Bose-Einstein condensate.

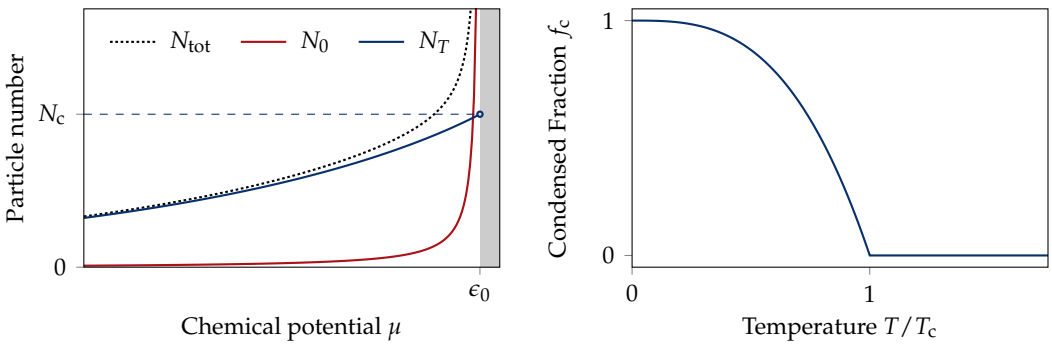

Figure 3.1 – Bose-Einstein condensation. (Left) In the grand canonical point of view, when the chemical potential μ gets close to the ground state energy ϵ_0, the occupation number N_0 of the ground state diverges, while the occupation number N_T of the excited states saturates. Given a total atom number N_{tot}, a BEC exists if $N_{\text{tot}} > N_c$. Experimentally, such a condition is always achievable when the temperature is low enough. (Right) Condensed fraction as a function of the temperature for a 3D harmonic trap.

Throughout this chapter, the total particle number N in our system will be decomposed as

$$N = N_0 + N_T, \tag{3.1}$$

with N_0 the number of particles in the ground state – *the condensate* – and N_T the number of particles in the excited states – *the thermal component*. As we can see in figure 3.1, the thermal component is bounded: $N_T(\mu \to \epsilon_0) = N_c$, with N_c the temperature-dependent critical atom number. Physically, if the number of particles in the system is bigger than N_c, the thermal component will be saturated and the excess number of particles constitutes the condensate. In practice, for a given total number of particles N, one always finds a temperature low enough such that $N_c(T) < N$. In the case of a harmonic trap, one has

$$N_c \left(\frac{\hbar\omega_{ho}}{k_B T_c}\right)^3 = \zeta(3) \approx 1.202. \tag{3.2}$$

In this expression, we have introduced the geometrical mean of the harmonic trap frequencies $\omega_{ho} = (\omega_x\omega_y\omega_z)^{1/3}$, and the Riemann zeta function ζ. Physically, a BEC exists if $N > N_c(T)$ for a given temperature T. Equivalently, one can introduce a critical temperature $T_c(N)$ defined by $N_c(T = T_c) = N$. In such a case, a BEC exists if $T < T_c(N)$ for a given total number of particles. Experimentally, the temperature is lowered until condensation is reached. The condensed fraction is given by $f_c = N_0/N = 1 - (T/T_c)^3$ for a harmonic trap, and is also plotted in fig. 3.1.

The condensation threshold is often expressed in terms of phase space density $\mathcal{D}$,

$$\mathcal{D} = n\lambda_T^3 \qquad \text{with} \qquad \lambda_T = \sqrt{\frac{2\pi\hbar^2}{mk_B T}}, \tag{3.3}$$

which can be considered as the number of particles in a box, in phase space, of volume $\sim \hbar^3$ [Townsend et al. 1995]. The average phase space density of a thermal gas in a harmonic trap is

$$\mathcal{D} = N\left(\frac{\hbar\omega_{ho}}{k_B T}\right)^3, \tag{3.4}$$

and the condensation condition can be recast in $\mathcal{D} \geq \zeta(3)$. Note that in the case of a box trap (no harmonic confinement), the density is uniform and the condensation threshold is $\mathcal{D} \geq \zeta(3/2) \approx 2.612$. This threshold can be applied in the case of harmonic confinement when considering the peak density at the center of the trap.

Interactions

The results presented so far are derived for a non-interacting (ideal) Bose gas. The shape of the ground state wavefunction – the BEC – is however affected by the interactions in a non-trivial way. Indeed, in a harmonic trap, the size of the ground state is on the order of the harmonic length $a_{ho} = \sqrt{\hbar/(m\omega_{ho})}$, which itself is on the order of a micron. When condensed, the density becomes much higher than of a thermal cloud, and interactions must be taken into account.

At zero temperature, the equation that governs the density distribution in a mean-field

description is the stationary Gross-Pitaevskii equation

$$\left(-\frac{\hbar^2\nabla^2}{2m} + V_{\text{ext}}(\mathbf{r}) + gn(\mathbf{r}) - \mu_0\right)\sqrt{n(\mathbf{r})} = 0, \tag{3.5}$$

with V_{ext} being the external confining potential, and with the chemical potential given here by the thermodynamic relation $\mu_0 = \partial E/\partial N$. In this expression, $g = \int \mathrm{d}\mathbf{r}\, V_{\text{int}}(\mathbf{r})$ is given by the interaction energy $V_{\text{int}}(\mathbf{r})$ between particles. Short range interactions, *e.g.* van der Waals forces, can be approximated as contact interactions fully described by the scattering length, a_s, at low energy. Then,

$$g = \frac{4\pi\hbar^2 a_{\text{s}}}{m}, \tag{3.6}$$

with m the mass of a single particle.

If the interactions are repulsive ($a_{\text{s}} > 0$) and dominant compared to the kinetic energy term, we can apply the Thomas-Fermi approximation which directly relates the density profile $n(\mathbf{r})$ to the confining potential

$$n(\mathbf{r}) = \frac{1}{g}\left(\mu_0 - V_{\text{ext}}(\mathbf{r})\right). \tag{3.7}$$

For a harmonic trap, the density profile is an inverted parabola

$$n(\mathbf{r}) = \max\left\{n_0\left(1 - \frac{x^2}{R_x^2} - \frac{y^2}{R_y^2} - \frac{z^2}{R_z^2}\right), 0\right\} \quad \text{with} \quad R_i = \left(\frac{15N_0 g}{4\pi m\omega_i^2}\frac{\omega_{\text{ho}}^3}{\omega_i^3}\right)^{1/5}, \tag{3.8}$$

3.1.2 Stability of a dipolar BEC

With dyprosium, one also has to consider the effect of dipole-dipole interactions by adding the dipolar term to the mean field interaction, giving a non-local Gross-Pitevskii equation. The dipole-dipole potential between two particles can be recast as [Lahaye et al. 2009]

$$U_{\text{dd}}(\mathbf{r}) = \frac{\mu_0\mu^2}{4\pi}\frac{1 - 3\cos^2\theta}{r^3} = \frac{3\hbar^2 a_{\text{dd}}}{m}\frac{1 - 3\cos^2\theta}{r^3}, \tag{3.9}$$

where μ is the dipole moment, μ_0 is the vacuum permittivity and θ is the angle between the dipoles' orientations (assuming here to be the same, aligned with an external quantization field) and their relative position (see fig. 3.2). We also recall the expression of the dipolar length $a_{\text{dd}} = \mu^2\mu_0 m/12\pi\hbar^2$.

The stationary Gross-Pitaevskii equation becomes

$$\begin{aligned}&\left(-\frac{\hbar^2\nabla^2}{2m} + V_{\text{ext}}(\mathbf{r}) + gn(\mathbf{r}) + \Phi_{\text{dd}}(\mathbf{r}) - \mu_0\right)\sqrt{n(\mathbf{r})} = 0\\ &\text{with} \quad \Phi_{\text{dd}}(\mathbf{r}) = \int \mathrm{d}\mathbf{r}'\, U_{\text{dd}}(\mathbf{r} - \mathbf{r}')n(\mathbf{r}').\end{aligned} \tag{3.10}$$

The term $\Phi_{\text{dd}}(\mathbf{r})$ corresponds to a non-local mean-field interaction. The Thomas-Fermi approximation can still be applied and, in the case of a harmonic trap, the expressions

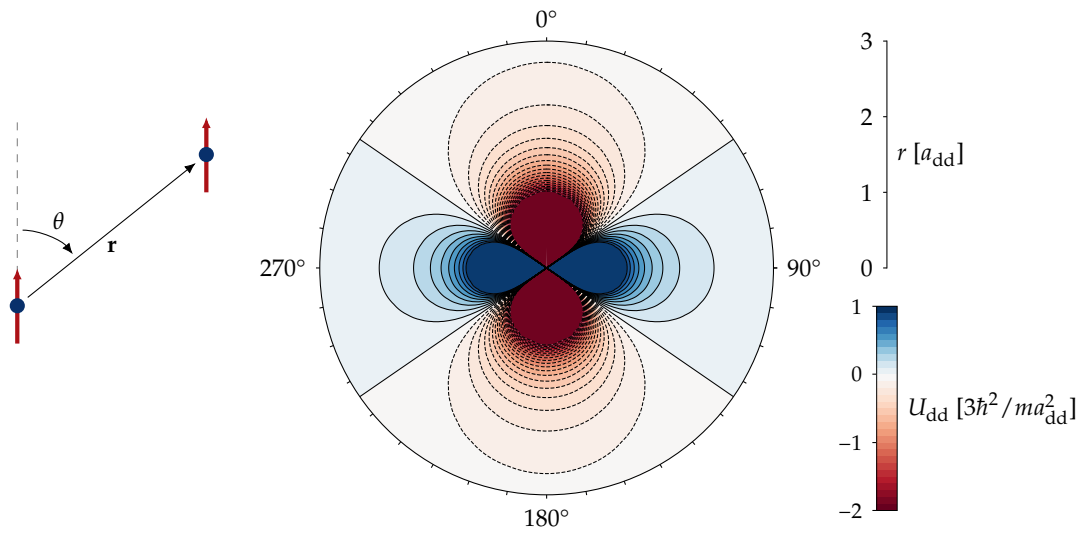

Figure 3.2 – Dipole interactions. The two red arrows (left) represent two dysprosium atoms, spin-polarized by an external magnetic field. The interaction energy between these dipoles is given by eq. (3.2), and is plotted in polar coordinates (right). We introduced the dipolar length $a_{\mathrm{dd}} = m\mu_0\mu^2/12\pi\hbar^2$. The interaction is attractive in the *heads to tails* configuration (red areas), and repulsive when the dipoles are aligned (blue areas). The interaction cancels at the angle $\theta_0 \approx 54.7°$.

for the radii are modified. Qualitatively, the effect of the dipole-dipole interactions, for a quantization field oriented along z, is to elongate the BEC along the z axis. Exact expressions have been calculated in [Eberlein et al. 2005] for a cylindrical trap $\omega_x = \omega_y = \omega_\rho$, and read

$$R_\rho = \left[\frac{15gN_0\kappa}{4\pi m\omega_\rho^2}\left(1+\epsilon_{\mathrm{dd}}\left(\frac{3}{2}\frac{\kappa^2 f(\kappa)}{1-\kappa^2}-1\right)\right)\right]^{1/5}. \tag{3.11}$$

In this expression, $\epsilon_{\mathrm{dd}} = a_{\mathrm{dd}}/a_{\mathrm{s}}$ is the dipolar parameter, $\kappa = R_\rho/R_z$ is the BEC aspect ratio, and is given by the solution of

$$3\kappa^2\epsilon_{\mathrm{dd}}\left[\left(\frac{\gamma^2}{2}+1\right)\frac{f(\kappa)}{1-\kappa^2}-1\right]+(\epsilon_{\mathrm{dd}}-1)(\kappa^2-\gamma^2)=0, \tag{3.12}$$

which depends on the trap aspect ratio $\gamma = \omega_z/\omega_\rho$. In the absence of dipolar interactions, $\kappa = \gamma$ and we recover the expressions given in eq. (3.8). The function $f(\kappa)$ is given by

$$f(\kappa) = \frac{1+2\kappa^2}{1-\kappa^2} - \frac{3\kappa^2 \operatorname{atanh}\sqrt{1-\kappa^2}}{(1-\kappa^2)^{3/2}}. \tag{3.13}$$

In fig. 3.3 we compute how the radii change as a function of the dipolar parameter ϵ_{dd}, and for different trap configurations.

As one can see, for $\epsilon_{\mathrm{dd}} \gtrsim 1$, the BEC shape becomes ambiguous: there are several possible values of the radii for a given trap configuration. As a matter of fact, when the dipolar interaction dominates, the BEC is most likely to be unstable. Indeed, the attractive part of U_{dd} (heads to tails configuration) can no longer be compensated by the repulsive

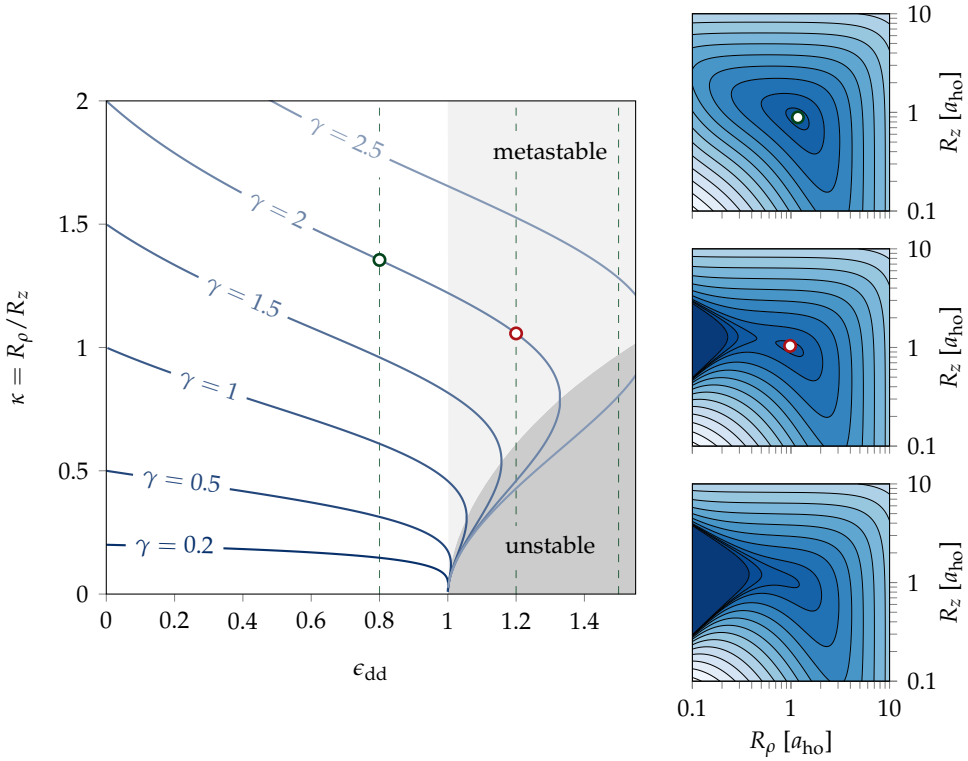

Figure 3.3 – Stability of a dipolar BEC. (Left) Cloud deformation $\kappa = R_\rho/R_z$ as a function of the dipolar parameter ϵ_{dd} for different trap geometries $\gamma = \omega_z/\omega_\rho$. For $\epsilon_{dd} \gtrsim 1$, one may find two possible solutions for κ. (Right) Energy landscapes for $\gamma = 2$ and $\epsilon_{dd} = 0.8,\ 1.2,\ 1.5$ (from top to bottom). Dark blue indicate lower energy. For $\epsilon_{dd} < 1$ (top), κ is uniquely defined and one has a stable minimum. For $\epsilon_{dd} > 1$, one either finds two solutions (middle) or none (bottom). When two solutions are found, only one of them corresponds to a metastable configuration (local minimum of the energy) and is physically acceptable (red circle), and the other one is unstable (saddle point). When ϵ_{dd} is too large, the energy landscape does not feature a minimum.

contact interaction (the scattering length is positive $a > 0$). The particles are accelerated towards each other, and the BEC collapses.

It is worth pointing out here that the collapse of a BEC with negative scattering length (attractive interactions) can be stabilized in the presence of a trap by the kinetic energy term (also called the *quantum pressure* term) that we have neglected in the Thomas-Fermi approximation. This stabilization can only occur at low enough atom number [Gammal et al. 2001].

For a dipolar BEC with a positive scattering length, the situation is qualitatively different than for a negative scattering length situation. The collapse of a dipolar BEC occurs by putting the particles in a very specific configuration – heads to tails – and can be prevented by geometrical considerations. Having a trapping potential more confining along the dipole alignment can stabilize the BEC even for $\epsilon_{dd} > 1$. This process can be quantitatively explored by considering the energy functional of a trapped BEC in a *pancake-like* configuration, for which $\gamma > 1$, or equivalently $\omega_z > \omega_\rho$.

Using a parabolic ansatz for the ground state wavefunction, and neglecting the kinetic energy term, one finds that the energy of the condensate is given by

$$E_{\text{tot}} = \frac{N_0}{14} m\omega_\rho^2 R_\rho^2 \left(2 + \frac{\gamma^2}{\kappa^2}\right) + \frac{15}{28\pi} \frac{N_0^2 g}{R_\rho^2 R_z} (1 - \epsilon_{\text{dd}} f(\kappa)), \tag{3.14}$$

with R_i the radii of the parabolic density profiles. The BEC is stable if the solutions given by eq. (3.11) correspond to a global minimum of the energy, and metastable if it corresponds to a local minimum. One finds that as long as $\epsilon_{\text{dd}} < 1$, the BEC is stable. For $\epsilon_{\text{dd}} > 1$, the BEC can be metastable if γ is large enough. This behavior, which is often referred as *geometrical stabilization*, is illustrated in fig. 3.3, in which we plot the energy landscape for a given $\epsilon_{\text{dd}} > 1$ in different cases.

Isotope

In the Thomas-Fermi regime discussed above, the value of ϵ_{dd} completely determines whether a dipolar BEC can be formed or not for a given trap geometry. In that prospect, we have chosen to work with ^{162}Dy, which background scattering length $a^{(162)} = 140(7)a_0$ [Böttcher et al. 2019a] is larger than the one of ^{164}Dy, $a^{(164)} = 69(4)a_0$ [Ferrier-Barbut et al. 2018], giving a smaller dipolar parameter: $\epsilon_{\text{dd}}^{(162)} = 0.92(5) < \epsilon_{\text{dd}}^{(164)} = 1.90(11)$. By choosing ^{162}Dy, we are in principle able to produce a stable BEC, because $\epsilon_{\text{dd}} < 1$[1]. A larger background scattering length is also beneficial in the evaporation process, as it increases the collision rate, giving a faster evaporation.

In any case, it is worth mentioning that the s-wave scattering length can always be tuned by the means of Feshbach resonances. The dependence of the scattering length on the magnetic field B is expressed as [Chin et al. 2010]

$$a(B) = a_{\text{bg}} \left(1 - \frac{\Delta}{B - B_0}\right), \tag{3.15}$$

where B_0 is the position of the resonance ($|a(B_0)| = \infty$), and Δ is the width of the resonance, associated to the zero-crossing of the scattering length: $a(B_0 + \Delta) = 0$.

In our experiment, we do not use any Feshbach resonance and work with the background scattering length of ^{162}Dy. Yet, we mention here that other dysprosium experiments use Feshbach resonances *e.g.* to study the crossover between condensation and supersolidity that can emerge in these kind of dipolar systems [Böttcher et al. 2019b; Chomaz et al. 2019]. The Feshbach spectrum of dysprosium is quite dense, and there are plenty of resonances even at relatively low field [Baumann et al. 2014; Maier et al. 2015].

3.2 Evaporation to degeneracy

In this section, we discuss the experimental realization of a ^{162}Dy BEC. We first describe the loading of the crossed dipole trap, which is facilitated by the ODT modulation and the Doppler cooling steps introduced in chapters 1 and 2 respectively. We then discuss the

[1] The scattering length for ^{162}Dy reported here is the latest available measurement. Yet, the value differs from previous measurements, and from measurements in other groups (by roughly 10 %). Either way, our trap aspect ratio is large enough to ensure metastability if ϵ_{dd} is slightly bigger than 1.

evaporation in the crossed trap. The experimental sequence corresponding to these steps is given in fig. 3.4

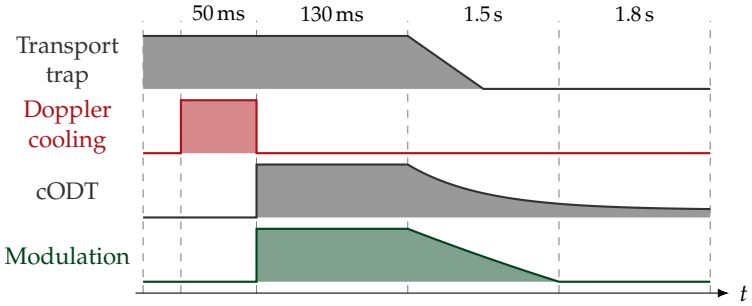

Figure 3.4 – Schematic view of the experimental sequence. After transport, the atoms are held in the transport ODT. The Doppler cooling stage is applied, before turning on the modulated cODT. A waiting time of 130 ms is applied with all the traps turned on, and the atoms fall in the crossed region. During the first evaporation ramp, the transport trap is rapidly turned off, while the modulation amplitude and the cODT power are slowly ramped down. After the modulation is turned off, a second evaporation ramp on the cODT allows to reach degeneracy.

3.2.1 Loading the crossed dipole trap

Once transported and Doppler-cooled, the atoms are loaded in the crossed optical dipole trap (cODT), which is described in chapter 1. Modulation of the ODTs is used to increase the effective volume of the cODT, and this helps to capture more atoms in the crossed region. We show in fig. 3.5 the size of the cloud, measured with the vertical imaging, as a function of the modulation amplitude. As expected, increased modulation is associated with larger clouds. Examples of pictures of the atomic cloud are also given for several modulation amplitudes.

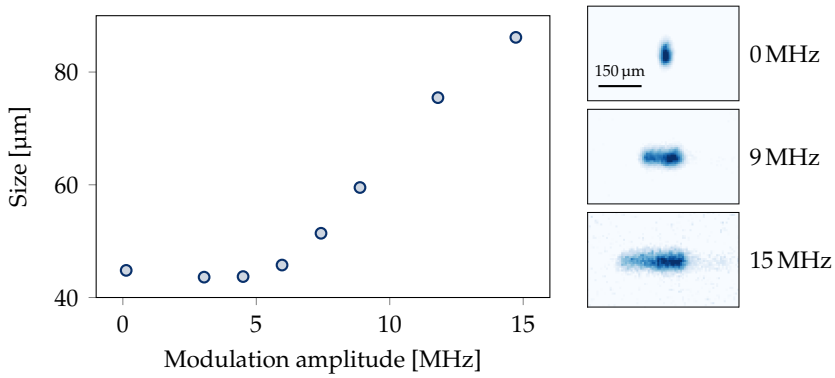

Figure 3.5 – Cloud size vs. modulation. Size of the cloud in the modulation direction, as a function of the modulation amplitude. These measurements were performed using a vertical imaging, after a free fall of 1 ms. Examples of cloud pictures are given in the right panels.

The effects of modulation for loading the cODT are evaluated by a direct measurement

of the atom number in the crossed region as a function of the modulation amplitude. This measurement is shown fig. 3.6, in which a single arm of the cODT is used, the crossed region being defined by the intersection of this arm and the transport trap. We can extract the fraction of atoms in the crossed region by fitting a two-gaussian model. In those measurements, the imaging axis is horizontal and orthogonal to the transport ODT.

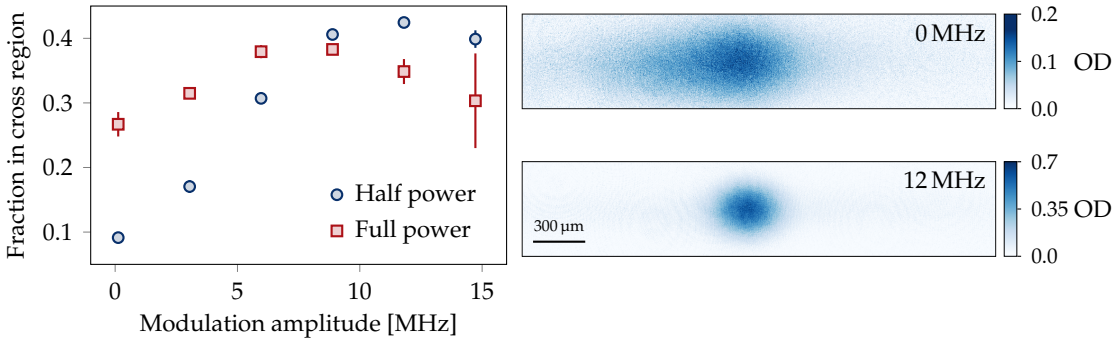

Figure 3.6 – Loading of the crossed region. The fraction of atoms in the crossed region is measured for several values of the modulation amplitude. During the loading, the transport trap power is also lowered ; we show here only two curves for comparison: lowering to half power (blue circles) and keeping it at full power (red squares). The modulation helps keeping the atoms in the cODT while the transport trap is turned off. The pictures of the right panel are examples of the atomic cloud without (top) and with (bottom) modulation.

The effect of modulation can be seen directly on the example pictures. In the absence of modulation (top picture), the cloud is relatively dilute, and expands a bit along the transport trap (horizontal axis in fig. 3.6). When the modulation is turned on for the loading, all the atoms concentrate in the crossed region, which is now much more dense. The pictures shown in fig. 3.6 correspond to measurements in which the power of the transport trap is reduced by half during the loading. In the end, the transport trap is completely turned off before the final evaporation stage is performed in the cODT, and modulation is thus quite helpful in keeping the atoms in the crossed region. Overall, we see that about 40 % of the Doppler-cooled atoms are loaded in the cODT, corresponding to a bit less than 20 % of the transported atoms.

The need for Doppler cooling is illustrated in fig. 3.7, in which we plot the gain in atom number $G = N_{\text{Dop}}/N_{\text{No Dop}}$ in the crossed region as a function of the Doppler beam frequency. The data taken sufficiently far from resonance corresponds to the absence of Doppler cooling and serves as a reference for $G = 1$. As we can see, the number of atoms in the crossed region is increased by about 75 % in the presence of the cooling beam. The data presented here corresponds to a Doppler beam turned on for 50 ms at an intensity $I/I_{\text{sat}} = 0.5$, and these values were obtained through an empirical optimization of the atom number after the cODT loading.

In conclusion, the efficiency of the cODT loading is greatly helped by both the modulation of the individual traps and the Doppler cooling stage. On the one hand, modulation increases the trap volume, allowing a higher number of atoms to be captured in the crossed region. On the other hand, the Doppler beam cools down the atoms, which compensates for the reduction of trap depth caused by the modulation. The combination of both

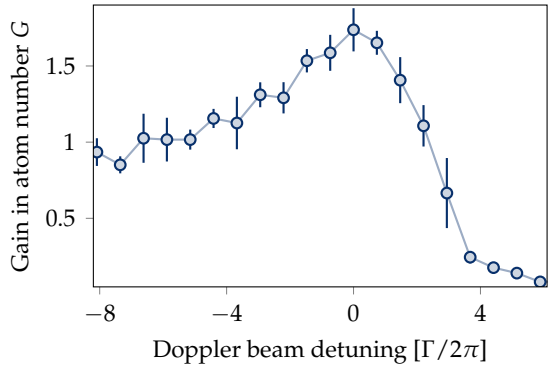

Figure 3.7 – Doppler cooling for loading the crossed region. The atom number in the crossed region is measured as a function of the Doppler cooling frequency. We give here the relative atom number, measured with respect to the atom number in the absence of Doppler cooling (corresponding to a far detuned beam). The zero of detuning is (arbitrarily) associated here to the position of the maximum atom number. In this data set, the Doppler cooling beam was turned on for 50 ms with $I/I_{\text{sat}} = 0.5$.

techniques allows us to trap about 5×10^5 atoms at a temperature $\sim 40\,\mu\text{K}$ in the crossed region prior to the forced evaporative cooling step. Considering the expected trapping frequency that we have with the modulation, the forced evaporative cooling is started with a phase space density of $\mathcal{D} \approx 10^{-3}$.

3.2.2 Forced evaporative cooling

Once the crossed dipole trap loaded, we proceed to the forced evaporative cooling. As shown in fig. 3.4, we have two steps for evaporation. The transport trap and the modulation are turned off in the first step, and the crossed dipole trap is slowly ramped down during the first and the second steps.

The idea of evaporative cooling is to let the particles with a high energy escape the trap in such a way that, after rethermalization, the temperature of the remaining particles is lowered. The usual description of evaporative cooling is given in a truncated harmonic trap, in which the trap depth is larger than the typical energy per particle. The trap depth is typically written as $U_0 = \eta k_\text{B} T$, with $\eta \approx 10$, while the energy per particle in a harmonic trap is $E/N = 3k_\text{B}T$. The principle of evaporative cooling is illustrated in fig. 3.8.

Ideally, η should be as big as possible: the escaping particles remove a large energy to the remaining cloud, and the evaporation process is more efficient (the decrease of temperature is large for every lost particle). The probability for a particle to be lost, however, decreases exponentially with η, and this process would be extremely long in the large η limit. In a real experiment, one needs to take into account loss and heating mechanisms in the trap, which limit the evaporation time (typically seconds). Quantitative kinetic studies have been realized in [Luiten et al. 1996; Cohen-Tannoudji 1996], which include the loss mechanisms. In particular, the efficiency of the evaporation can be quantified by

$$\chi = -\frac{\mathrm{d}\ln\mathcal{D}}{\mathrm{d}\ln N}, \tag{3.16}$$

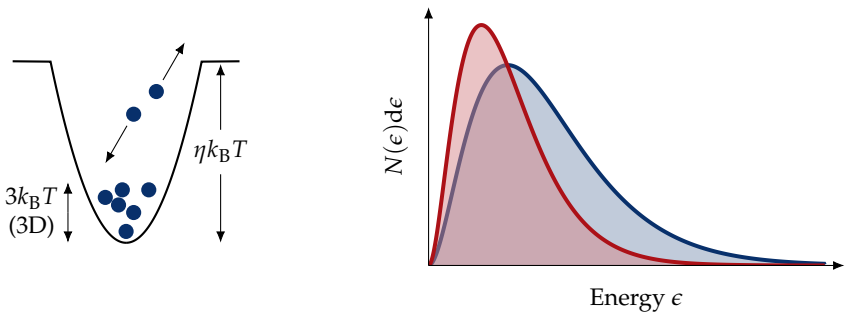

Figure 3.8 – Principle of evaporation. In the harmonic approximation, the trap (left) is a truncated parabola. The trap depth U_0 is characterized by the dimensionless parameter $\eta = U_0/k_B T$. At equilibrium, each particle has an energy $E/N = 3k_B T$. When two particles collide, energy is exchanged, and one particle can be ejected from the trap. The remaining particles rethermalize at a lower temperature. A high collision rate is thus beneficial for the evaporation process. This phenomenon can be seen on the energy distribution (right). The evaporation process basically cuts the tail of blue distribution, which then rethermalizes in the red one. The total atom number $N = \int d\epsilon N(\epsilon)$ decreases, as well as the mean energy.

which is a quantity that was already introduced at the end of chapter 2. The *runaway* regime, corresponding to an increasing collision rate with time, is given by $\chi \geq 2$ for a harmonic trap. Such a regime can only be accessed for an evaporation at fixed frequency [O'Hara et al. 2001], such as in magnetic traps. Yet, the evaporation efficiency χ remains a good figure of merit for characterizing the evaporation.

Experimentally, we optimize the evaporation ramps (including the ramping down of the modulation) by looking at the PSD $\mathcal{D}$. We choose to use exponential ramps, meaning that the typical parameters that we optimize are the total evaporation time, the final cODT power, and the 1/e time constant. Our evaporation ramps are given in fig. 3.9. We give the cODT total power, from which the mean trapping frequency ω_{ho} is computed (see chapter 1), as a function of time (we only show data after the transport trap is turned off).

In order to completely characterize the evaporation ramp, we measure the atom number and the temperature of the cloud throughout the ramp. Along with the trap frequency, we are then able to compute the phase space density (PSD), which expression for a harmonic trap is given in eq. (3.4). The results are shown in fig. 3.10.

As we can see, we are able to reach degeneracy after about 2.7 s of evaporation. The measured critical temperature is close to 100 nK.

The efficiency of the evaporation ramp is evaluated by looking at the evolution of the PSD as a function of the atom number, shown in fig. 3.11. From it, we can extract the value of χ as defined in eq. (3.16). Only the second evaporation ramp ($t \geq 1.5$ s) is fitted, and we obtain $\chi = 3.6(4)$, which would be above the runaway criterion, were we working at a fixed trap frequency. Yet, the collision rate as a function of the evaporation time, also given in fig. 3.11, shows that the collision rate decreases with time. This decrease slows down at the end of the evaporation, which yields an increase of the evaporation efficiency to $\chi = 5.3(5)$ right before the transition to degeneracy.

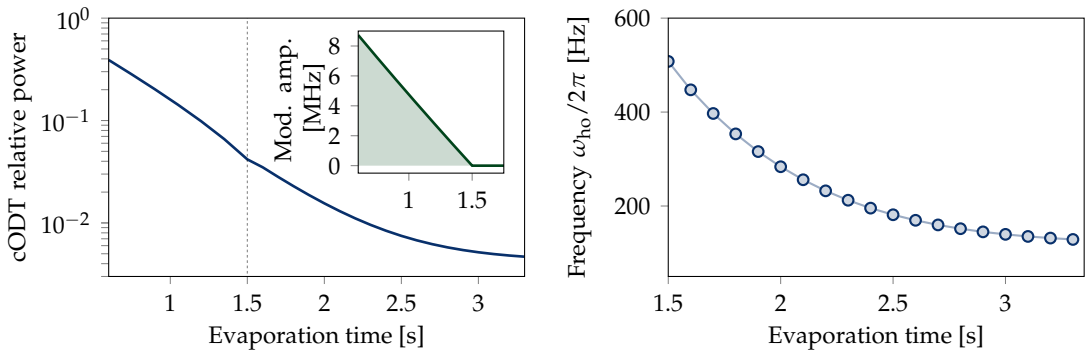

Figure 3.9 – Evaporation ramps. (Left) Relative cODT power as a function of time. Full power corresponds to $t = 0$ (not shown in the graph). At the end of the evaporation ramp, the total power is reduced by a factor ~ 200, which corresponds to about ~ 100 mW in each arm of the cODT. (Inset) modulation amplitude as a function of time. The modulation is completely turned off after 1.5 s of evaporation, which marks the end of the first ramp. (Right) Computed mean trap frequency ω_{ho}. We only show the second part of the evaporation, after the modulation is turned off. In this last part, the waists of the cODT are kept constant, and the frequency follows a $\sqrt{P}$ behavior.

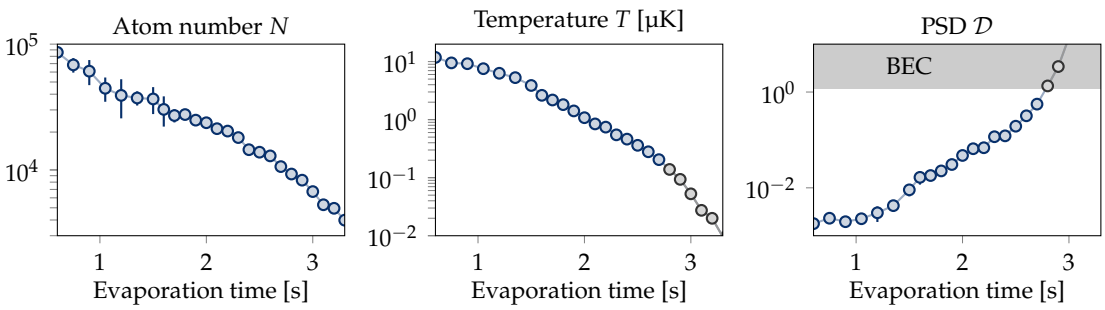

Figure 3.10 – Evaporation to degeneracy. Atom number (left), temperature (middle) and phase space density (right) of the atomic cloud as a function of the evaporation time. Degeneracy is reached after about 2.7 s of evaporation, when $\mathcal{D} \gtrsim 1.202$.

3.3 Degenerate Bose gases

The appearance of a condensed fraction is directly visible on the density profile of the atomic cloud. Indeed, before condensation, the density distribution in the trap is given by a gaussian, thermal distribution. In the condensate regime, the shape of the cloud is given by the Thomas-Fermi profile which, in the case of a harmonic trap, corresponds to an inverted parabola.

As such, the density distribution of the cloud becomes bimodal at the condensation threshold. This is illustrated in fig. 3.12, where we show pictures of the cloud in different regimes. The cloud pictures can then be fitted by a sum of a gaussian and an inverted parabola, corresponding to the thermal and condensed part. The thermal fraction can then be extracted from these fits.

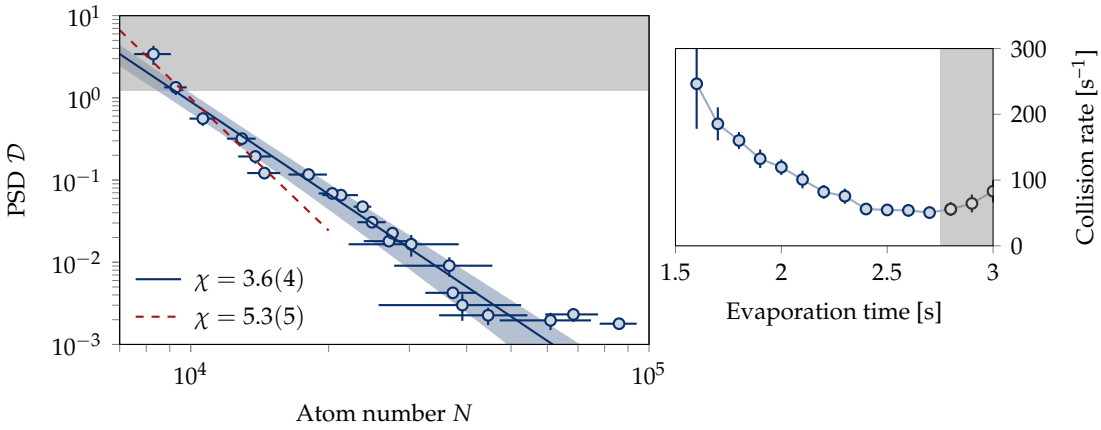

Figure 3.11 – Evaporation efficiency. (Left) The PSD $\mathcal{D}$ is plotted as a function of the atom number N in log scale. A linear fit allows us to extract the efficiency χ, as defined in eq. (3.16), for the second part of the evaporation (blue solid line) and for the very last part (red dashed line). (Right) Collision rate as a function of the evaporation time. As we can see, we are not in the runaway regime, even though the efficiency is relatively high.

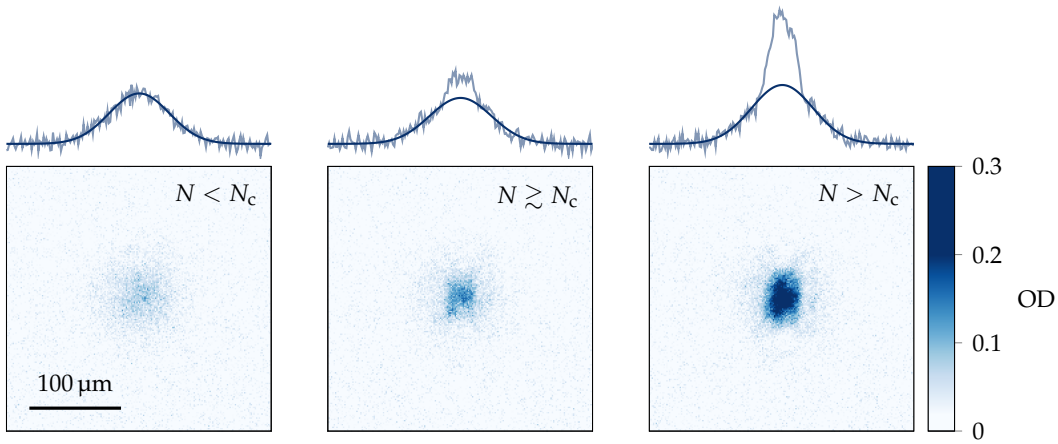

Figure 3.12 – Bose-Einstein condensation. The atomic clouds in these pictures, taken after 12 ms of time-of-flight, have the same temperature, but different atom numbers. The top graphs are integrated profiles. Below the condensation threshold ($N < N_c$), the density distribution after time-of-flight is gaussian, and corresponds to a thermal cloud. Above the condensation threshold ($N > N_c$), one can observe a clear bimodal distribution. The central peak corresponds to condensed atoms, with a density distribution well fitted by an inverted parabola, in agreement with the Thomas-Fermi approximation.

3.3.1 Expansion of a dipolar BEC

The density distribution that we show are taken after a given time-of-flight (ToF) duration. In principle, when the ToF duration is large compared to the timescale set by the trapping frequency (the so called *far-field* regime), and in the absence of interactions, the measured density distribution is equivalent to the in-situ momentum distribution. In the case of a thermal cloud, both the in-situ density and momentum distribution are

approximated to be gaussian[2].

It has been shown that, in the presence of interactions, the BEC density distribution remains parabolic during the free flight [Castin et al. 1996; Kagan et al. 1996]. The Thomas-Fermi radii merely follow a scaling law that only depends on the initial trap geometry. These scaling laws are usually written in the form

$$R_i(t) = \lambda_i(t) R_i(0), \tag{3.17}$$

with $R_i(0)$ the in-situ Thomas-Fermi radii, λ_i the scaling factors and $i = x, y, z$.

One of the consequences of these scaling laws, for the BEC, is the inversion of the ellipticity of the cloud shape. In the case of a trap with cylindrical symmetry, the initial cloud aspect ratio $R_z(0)/R_\perp(0)$ is solely given by the trap aspect ratio $\omega_z/\omega_\perp$, according to eq. (3.8). In the far-field regime, however, the cloud aspect ratio is inverted: a *pancake* cloud becomes *cigar*-like, while a *cigar* cloud becomes *pancake*-like. This effect can intuitively be interpreted by energy considerations[3]. In-situ, the cloud is quite dense, with a high interaction energy – it dominates over the kinetic energy in the Thomas-Fermi approximation. In the direction of strong confinement, the gradient of density is higher, resulting in stronger pressure. When the trap is released, the interaction energy is converted to kinetic energy, with an anisotropic distribution. The direction of strong confinement thus corresponds to large kinetic energy, and a larger spread of the wavefunction after ToF. The ellipticity inversion leads to a strong anisotropy of the distribution after time-of-flight, and was considered as a clear signature of degeneracy in the observation of the first BECs [Anderson et al. 1995; Davis et al. 1995].

In fig. 3.13, we show the time-of-flight expansion of our dipolar BEC. The aspect ratio inversion is quite clear: in our case, we go from a *pancake*-like configuration, which makes the condensate stable, to a *cigar* shape after ToF. The evolution of the Thomas-Fermi radii are consistent with the scaling law mentioned above, if we include the dipolar corrections calculated in [Giovanazzi et al. 2006]. For comparison, the expected time evolution of the radii in the absence of the dipolar term is also given in fig. 3.13. As one can see, the presence of dipole-dipole interactions increases the anisotropy of the expansion, with the occurrence of an ellipticity inversion earlier than with contact interactions only.

3.3.2 Calibration of the atom number

For most of the experiments performed in this work, the precise knowledge of the absolute atom number is not crucial, and relative variations are often enough to grasp the physical phenomena that we study. Yet, future projects involving the physics of many-body effects may require a precise calibration. We describe here how we use the condensation threshold to estimate our imaging efficiency.

The measured atom number, which essentially corresponds to the integrated measured optical density, can indeed be much smaller than the real atom number. The main reason for such a discrepancy is due to the unknown effective atom-light cross-section. During

[2]The corrections due to the Bose statistics occur right above the condensation threshold. They have no qualitative impact on the discussion here, and are not considered.

[3]Even in the absence of interactions, an ellipticity inversion is expected from Heisenberg's inequalities: the position distribution after a sufficiently long expansion corresponds to the in-situ momentum distribution, whose aspect ratio is inverted compared to the trap aspect ratio.

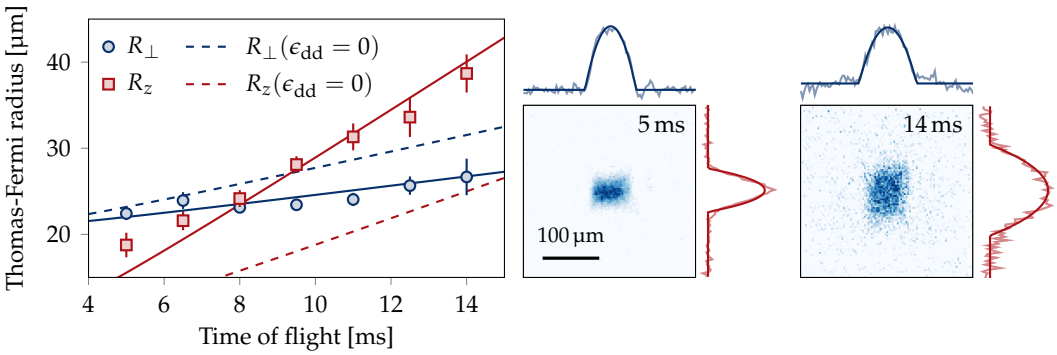

Figure 3.13 – Expansion of a dipolar BEC. The Thomas-Fermi radii in the vertical and transverse direction (R_z and $R_\perp$ respectively) of a pure BEC are measured for different time-of-flight durations. Examples of pictures are given in the right panels, along with the integrated profiles fitted by inverted parabolas, from which the radii are extracted. We observe an inversion of the ellipticity of the cloud, consistent with our models. The solid lines are fit the the expansion, taking into account the dipolar interactions. The dashed lines are the expected expansion in the absence of dipolar interaction, with the initial condition given by the fitted in-situ radii obtained with the solid lines.

the imaging pulse, optical pumping effects lead to complex spin dynamics, with different cross-sections for each of the spin components. We empirically determine the so called *fudge factor*, defined as $F = N_{\text{real}}/N_{\text{meas}}$.

In order to do so, we prepare a mixture of BEC and thermal cloud in a harmonic trap, at equilibrium. The temperature of the cloud is given by the trap frequencies, and is constant throughout the following measurement. The cloud is held for several seconds, leading to a decrease of atom number, and a picture of the cloud is taken after 15 ms of time-of-flight. A bimodal fit of the atomic density allows to extract the – *unfudged* – number of thermal atoms N_T and of condensed atoms N_0. By varying the hold duration, we have several values of N_T and N_0. The total number of atoms is denoted $N = N_0 + N_T$

The ideal Bose gas theory introduced in section 3.1 predicts a binary behavior: if $N < N_c$, with N_c the critical atom number, then $N_0 = 0$. Above the condensation threshold, one has a saturation of the thermal component, $N_T = N_c$, and all the additional particles enlarge the condensed component. Experimentally, however, we do not see such a behavior, and both the thermal and condensed components grow when increasing the total number of particle. This effect can be explained by the role of interactions, and was already explored in [Tammuz et al. 2011]. One has to take into account the repulsive interactions between the condensate and the thermal component. At first order in the interaction energy, one can write

$$N_T = N_c + \alpha \frac{\mu_0}{k_B T}, \tag{3.18}$$

with μ_0 the mean-field interaction energy (the chemical potential) which, in the Thomas-Fermi approximation, scales as $\mu_0 \propto N_0^{2/5}$.

Following these considerations, we plot in fig. 3.14 the number of thermal atoms as a

function of the number of condensed atoms $N_0^{2/5}$. We observe a linear behavior at low N_0, corresponding to a small value of the dimensionless parameter $\mu_0/k_\mathrm{B}T$. A linear fit allows us to extract the measured critical number $N_\mathrm{c}^{(\mathrm{meas})} = 2700(600)$. Only the data corresponding to a low interaction energy are fitted. We arbitrarily choose a threshold of $\mu_0/k_\mathrm{B}T < 0.15$, μ_0 being calculated with the unfudged atom number.

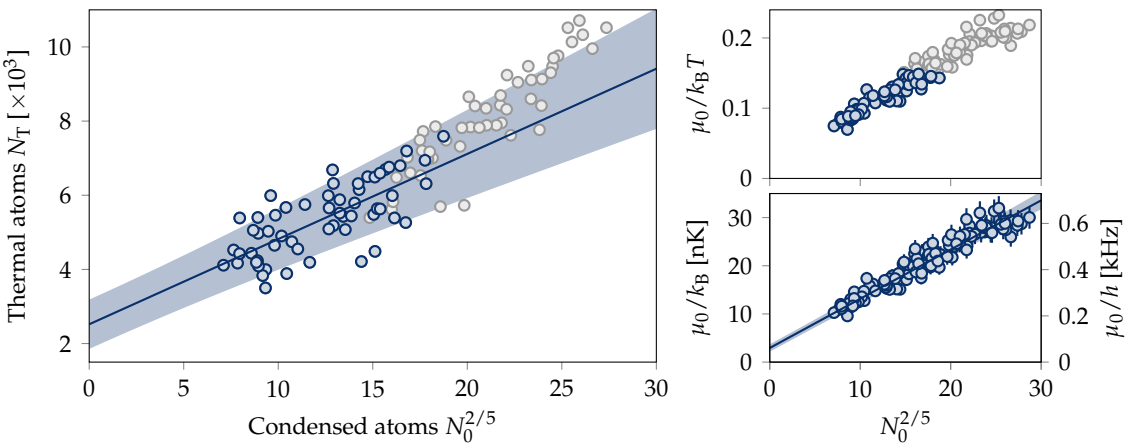

Figure 3.14 – Calibration of the atom number. (Left) The thermal and condensed components of a partially condensed cloud are measured for different total atom numbers. The critical atom number $N_\mathrm{c}^{(\mathrm{meas})}$ is extracted from a linear fit (solid line). (Right) Interaction parameter $\mu_0/k_\mathrm{B}T$ (top), calculated from the unfudged atom number N_0 in the condensate. The blue points are the ones used for the fit, and correspond to a low interaction energy. The threshold was arbitrarily chosen at $\mu_0/k_\mathrm{B}T < 0.15$. (Bottom) Interaction energy (given in nK and in kHz) as a function of the condensed atoms. The solid line is a linear fit.

On the other hand, the real critical atom number can be calculated using the measured temperature and trap frequencies. We observe a critical temperature $T_\mathrm{c} = 103(8)\,\mathrm{nK}$. Taking into account the expected shift of the critical temperature due to contact and dipolar interactions [Glaum et al. 2007], we derive an expected critical atom number $N_\mathrm{c}^{(\mathrm{real})} = 6800(1600)$, and a fudge $F = 2.7(9)$. This large errorbar is mainly due to the uncertainty we have on the determination of $N_\mathrm{c}^{(\mathrm{meas})}$ and T_c. We note that even considering this fudge factor, the corrected interaction parameter remains relatively small, precisely because it scales as $N_0^{2/5}$.

We also give in fig. 3.14 the interaction energy as a function of the number of condensed atoms, both in temperature and frequency units. We observe a linear behavior, consistent with the Thomas-Fermi approximation. The linear extrapolation gives an offset at $N_0 = 0$ on the order of a few nK, much smaller than the typical interaction energies on our system. The frequency unit is convenient for orders of magnitude: we have mentioned in the outlook of chapter 1 that probing interaction effects essentially requires that the magnetic noise be very small. We now have an order of magnitude: the noise should be well below $\sim 0.5\,\mathrm{kHz}$, corresponding to $\sim 300\,\mu\mathrm{G}$.

3.4 Conclusion

The experimental setup described in chapter 1 and the Doppler cooling apparatus described in chapter 2 provide all the tools to reach degeneracy. We are able to prepare a quasi-pure Bose-Einstein condensate of about 25×10^3 atoms[4], which will constitute the basis of most of the experiments we realize.

Dipolar interactions play a significant role in the stabilization and dynamics of the BEC. Globally, having dipolar interactions deforms the cloud, which becomes more elongated in the direction of the dipoles. We are able to observe these effects by looking, for example, at the cloud expansion during a time-of-flight experiment.

Interestingly, the BECs that we produce are in a metastable configuration. As explained in section 3.1.2, the trap geometry, which is more confining along the direction of the dipoles, allows us to stabilize the BEC against collapse. Increasing the dipolar parameter ϵ_{dd}, *e.g.* by decreasing the scattering length a_{s} using a Feshbach resonance or by using ^{164}Dy, would in principle prevent us from condensing with the trap geometry that we use at the moment.

It is worth pointing out here that beyond mean-field effects can also play a role in the stabilization of the condensate. Indeed, it has been observed [Kadau et al. 2016; Ferrier-Barbut et al. 2016] that stable condensates with small atom numbers but high densities, so-called *droplets*, may exist even when the dipolar interactions are stronger than what the trap geometry can sustain. Physically, in the unstable configuration, the cloud starts collapsing, greatly increasing its peak density. In the mean field regime, quantum fluctuations are neglected and the collapse destroys the system. For high density, however, an additional term in the interaction energy, called the Lee-Huang-Yang correction [Lee et al. 1957] and proportional to $\sqrt{na_{\mathrm{s}}^3}$, with n the atomic density, competes with the attractive mean-field term, and can stabilize the cloud.

[4] If we take into account the fudge factor

II

Quantum-enhanced sensing

4 Non-classical spin states: theoretical concepts

4.1 Large spin systems **60**
4.1.1 Collective spins and coherent spin states 61
4.1.2 Non-classical spin states 63
4.2 Quantum-enhanced sensing **66**
4.2.1 Standard quantum limit 68
4.2.2 Metrological gain 69
4.2.3 Heisenberg limit 70
4.2.4 Statistical distance 71
4.3 One-axis twisting **72**
4.3.1 Time-evolution 72
4.3.2 Metrological gain 74
4.3.3 Implementation with dysprosium 75
4.4 Conclusion **78**

THIS PART OF the manuscript is dedicated to the manipulation of the large spin of dysprosium with light. In this chapter, we introduce some of the physics of large spin systems. The experimental realization of what is discussed here will be detailed in chapter 5.

Quite generally, large spin systems are built from entities of smaller sizes. In section 4.1, we introduce the notion of collective spin states, obtained from an ensemble of elementary constituents, the *qubits*. In particular, we will see that the symmetric states of an ensemble of N qubits can be described by a collective spin of size $J = N/2$. In the case of dysprosium, the electronic spin is naturally relatively large, with $J = 8$. Strictly speaking, the spin of a single dysprosium atom, which originates with its unfilled $4f$ shell, cannot be partitioned in $2J = 16$ elementary qubits. Yet, the formalism that we introduce here will be useful to understand the intrinsic link between entanglement of the elementary qubits – valid in the case of a collective spin – and the notion of quantum enhanced sensing.

Entanglement between the qubits is what determines whether the collective state can be considered as *classical* or not. We introduce in this chapter witnesses of non-classicality, such as the Wigner function or the quantum Fisher information, which are precisely defined for a collective spin. In the case of a single dysprosium atom, even if the notion of

(internal) entanglement is unclear, non-classicality remains intuitive. We will introduce, for instance, the notion of Schrödinger cat states, which are quantum superpositions of a magnetic moment pointing *up* and *down* in the same time. Such a state does not exist classically.

In section 4.2, we review the notion of parameter estimation, using quantum states. We will see that non-classical states allow to be more sensitive, compared to classical states, to the parameter that needs to be estimated. The relation between entanglement and increase of sensitivity is discussed.

Finally, we give in 4.3 a brief study of the one-axis-twisting Hamiltonian, that allows to generate non-classical states. In particular, the last paragraph is dedicated to the implementation with dysprosium, using an off-resonant laser beam close to the intercombination line at 626 nm.

4.1 Large spin systems

In quantum mechanics, the simplest non-trivial system is constituted of two different states, and is often referred to as a *qubit*. Such a system can be mapped to a spin-1/2 system, and as such it is convenient to label the two states as $|\downarrow\rangle$ and $|\uparrow\rangle$, for *spin down* and *spin up* respectively. The spin operators, in that case, are given by the Pauli matrices, and can be constructed from the two states

$$\hat{j}_z = \frac{|\uparrow\rangle\langle\uparrow| - |\downarrow\rangle\langle\downarrow|}{2} \quad ; \quad \hat{j}_x = \frac{|\uparrow\rangle\langle\downarrow| + |\downarrow\rangle\langle\uparrow|}{2} \quad ; \quad \hat{j}_y = \frac{|\uparrow\rangle\langle\downarrow| - |\downarrow\rangle\langle\uparrow|}{2\mathrm{i}}. \tag{4.1}$$

Any pure state $|\psi\rangle$ that lives in the Hilbert space defined by the kets $|\uparrow\rangle, |\downarrow\rangle$ can be parametrized by two angles θ and φ, with

$$|\psi\rangle = \sin(\theta/2)\,|\downarrow\rangle + \cos(\theta/2)\mathrm{e}^{-\mathrm{i}\varphi}\,|\uparrow\rangle\,. \tag{4.2}$$

Such a state can be represented in the Bloch sphere, with θ the polar angle and φ the azimuthal angle (see fig. 4.1).

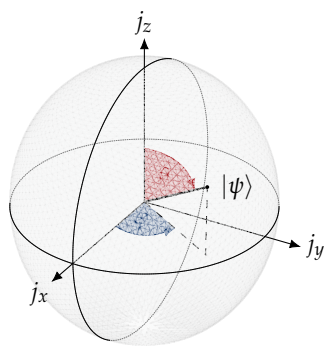

Figure 4.1 – Bloch Sphere. Any pure state $|\psi\rangle$ that lives in a Hilbert space of dimension 2 can be parametrized by two angles θ and φ, as given in eq. (4.2). These angles are respectively the polar and azimuthal angles of the Bloch sphere representation of the state $|\psi\rangle$.

This parametrization allows to conveniently define the classical direction of the state, as the average values of the spin operators – or equivalently the magnetizations – are simply given by (setting $\hbar = 1$)

$$\begin{aligned} m_x &= \langle\psi|\hat{j}_x|\psi\rangle = \frac{1}{2}\sin\theta\cos\varphi \\ m_y &= \langle\psi|\hat{j}_y|\psi\rangle = \frac{1}{2}\sin\theta\sin\varphi \\ m_z &= \langle\psi|\hat{j}_z|\psi\rangle = \frac{1}{2}\cos\theta \end{aligned} \tag{4.3}$$

In the following, we generalize this discussion to an ensemble of N identical qubits, which together form a collective spin.

4.1.1 Collective spins and coherent spin states

A collection of N qubits can be described by a set of operators simply obtained as the sum of individual spin operators

$$\hat{J}_i = \sum_{k=1}^{N} \hat{j}_i^{(k)} \qquad \text{with } i = x, y, z. \tag{4.4}$$

In this expression, k labels the individual particles and $\hat{j}_i^{(k)}$ refers to the single qubit operators given in eq. (4.1). These operators remain spin operators [Cohen-Tannoudji et al. 1973], meaning that they satisfy the commutation relations

$$[\hat{J}_\alpha, \hat{J}_\beta] = \mathrm{i}\sum_\gamma \epsilon_{\alpha\beta\gamma}\hat{J}_\gamma, \tag{4.5}$$

where $\epsilon_{\alpha\beta\gamma}$ is the Levi-Civita symbol.

The dimension of the Hilbert space spanned by this ensemble is 2^N. If we restrict ourselves to many-qubit states which are symmetric upon particle exchanges, or in other words to the eigenstates of $\hat{J}^2$, the Hilbert space dimension is drastically reduced to $N+1$, which is the dimension of the Hilbert space spanned by a total spin $J = N/2$ [Pezzè et al. 2018]. In the context of cold atoms experiments, such a system is naturally obtained *e.g.* with N bosons in a double well. In general, any system of N indistinguishable qubits and externally addressed collectively can be described in this reduced Hilbert space.

Formally, indistinguishable qubits can be described as *Schwinger Bosons* [Biedenharn et al. 1984]. In this formalism, the collective spin operators are expressed in terms of bosonic creation and annihilation operators in each of the qubit states. For instance, the ladder operators are given by

$$\hat{J}_+ = \hat{a}_\uparrow^\dagger \hat{a}_\downarrow \qquad \text{and} \qquad \hat{J}_- = \hat{a}_\downarrow^\dagger \hat{a}_\uparrow, \tag{4.6}$$

with $[a_\sigma, a_{\sigma'}^\dagger] = \delta_{\sigma,\sigma'}\hat{\mathbb{1}}$ and $\sigma = \uparrow, \downarrow$. Such expressions give an intuitive picture: for the collective spin, $\hat{J}_+$ increments the spin projection by one unit, and it corresponds microscopically to the creation of one qubit in $|\uparrow\rangle$ and the annihilation of a qubit in $|\downarrow\rangle$.

The other spin operators are then obtained as usual

$$\hat{J}_x = \frac{\hat{J}_+ + \hat{J}_-}{2} \quad ; \quad \hat{J}_y = \frac{\hat{J}_+ - \hat{J}_-}{2\mathrm{i}} \quad ; \quad \hat{J}_z = \frac{\hat{J}_+\hat{J}_- - \hat{J}_-\hat{J}_+}{2}. \tag{4.7}$$

Dicke states

In such a formalism, the eigenstates of $\hat{J}_z$, denoted $|J, m\rangle$ with $-N/2 \leq m \leq N/2$ the spin projection along z, are called *Dicke states* [Arecchi et al. 1972], and are obtained from the vacuum $|\mathrm{vac}\rangle$ with

$$|J, m\rangle = \frac{(a_\uparrow^\dagger)^{J+m}}{\sqrt{(J+m)!}} \frac{(a_\downarrow^\dagger)^{J-m}}{\sqrt{(J-m)!}} |\mathrm{vac}\rangle . \tag{4.8}$$

The Dicke states thus correspond to having $N/2 + m$ particles in $|\uparrow\rangle$ and $N/2 - m$ particles in $|\downarrow\rangle$, with the symmetry of the resulting states ensured by the bosonic operators. These states are the analogue of Fock states one may find in the context of quantum optics.

Coherent spin states

The analogy with quantum optics can be continued by introducing *coherent spin states* $|J; \theta, \varphi\rangle$ [Radcliffe 1971], which are constructed by putting all the elementary qubits in the same direction (or mode) (θ, φ). As such, we can define a *rotated* creation operator

$$a_{\theta,\varphi}^\dagger = \sin(\theta/2) a_\downarrow^\dagger + \cos(\theta/2) \mathrm{e}^{-\mathrm{i}\varphi} a_\uparrow^\dagger, \tag{4.9}$$

such that the single qubit introduced in eq. (4.2) will be written

$$|\psi\rangle = \sin(\theta/2) |\downarrow\rangle + \cos(\theta/2) \mathrm{e}^{-\mathrm{i}\varphi} |\uparrow\rangle = a_{\theta,\varphi}^\dagger |\mathrm{vac}\rangle . \tag{4.10}$$

The collective coherent spin state is then given by

$$|J; \theta, \varphi\rangle = \frac{(a_{\theta,\varphi}^\dagger)^{2J}}{\sqrt{(2J)!}} |\mathrm{vac}\rangle . \tag{4.11}$$

The coherent state $|J; \theta, \varphi\rangle$ is the eigenstate of the rotated spin operator $\hat{J}_{\theta,\varphi}$, with maximal eigenvalue J,

$$\hat{J}_{\theta,\varphi} |J; \theta, \varphi\rangle = J |J; \theta, \varphi\rangle , \quad \text{with } \hat{J}_{\theta,\varphi} = \sin\theta\cos\varphi \hat{J}_x + \sin\theta\sin\varphi \hat{J}_y + \cos\theta \hat{J}_z. \tag{4.12}$$

This can be understood intuitively by the fact that each component of the collective spin is oriented in the same direction θ, φ. In the Dicke state basis, the coherent spin states are decomposed along a binomial distribution

$$|J; \theta, \varphi\rangle = \sum_{m=-J}^{J} \sqrt{\binom{2J}{J-m}} \sin(\theta/2)^{J-m} \cos(\theta/2)^{J+m} \mathrm{e}^{-\mathrm{i}(J+m)\varphi} |J, m\rangle \tag{4.13}$$

There are no quantum correlations between the individual qubits that constitute the coherent spin state, and as such coherent states are often referred to as *classical states*[1]. The

[1] A classical magnet, in that sense, is a coherent state.

variance in any direction $(\mathbf{s})$ orthogonal to (θ, φ) is thus isotropic, and simply given by the sum of the variances of the individual components. Since the variance of a single qubit is always given by $\Delta\hat{j}_{\mathbf{s}}^2 = 1/4$, we deduce

$$\Delta\hat{J}_{\mathbf{s}}^2 = \frac{J}{2} \qquad \text{for any direction } (\mathbf{s}) \text{ orthogonal to } (\theta, \varphi). \tag{4.14}$$

As such, we realize that a coherent spin state corresponds to the state (with isotropic fluctuations) of minimal uncertainty. Indeed, the commutation relations given in eq. (4.5) lead to the Heisenberg uncertainty relations

$$\Delta\hat{J}_\alpha^2 \Delta\hat{J}_\beta^2 \geq \frac{\langle \hat{J}_\gamma \rangle^2}{4}, \tag{4.15}$$

with α, β, γ indexing the directions of an orthogonal basis. The coherent spin state thus *saturates* these inequalities.

Bloch sphere representation

The representation of a single qubit on the Bloch sphere, introduced with fig. 4.1, can be generalized for a collective spin. The generalized Bloch sphere is a sphere of radius J, on which we can define different types of distributions. We focus here on one of them, called the Wigner distribution.

The Wigner function of a collective spin is defined similarly to the one of a state of an electromagnetic field. The Wigner distribution has proven to be a useful tool to describe non-classical states, for instance in the context of quantum optics. For a collective spin, it is written as a sum over the spherical harmonics $Y_{kq}(\theta, \varphi)$, as [Dowling et al. 1994]

$$W(\theta, \varphi) = \sqrt{\frac{2J+1}{4\pi}} \sum_{k=0}^{2J} \sum_{q=-k}^{k} \rho_{kq} Y_{kq}(\theta, \varphi), \tag{4.16}$$

where ρ_{kq} are the density operator $(\hat{\rho})$ components of a multipole expansion[2]. The Wigner function is real, and its negative parts are often considered to be indicators of *non-classicality*, *i.e.* signs of entanglement or quantum correlations between elementary constituents of a larger system. For collective spin systems, coherent states also have negative regions, with an amplitude that decays exponentially with the number of particles [Pezzè et al. 2018]. Wigner distributions of coherent states and of a Dicke state are given in fig. 4.2.

4.1.2 Non-classical spin states

Dicke states, as we just saw with fig. 4.2, can be considered as examples of *non-classical states* in the sense that they have no classical counterpart. A more general definition can be given by considering the correlations between the individual qubits that form

[2] They are defined as

$$\rho_{kq} = \mathrm{Tr}[\hat{\rho}\hat{T}_{kq}^\dagger] \qquad \text{with} \qquad \hat{T}_{kq} = \sum_{\mu,\mu'=-J}^{J} (-1)^{J-\mu'} \langle J, \mu; J, -\mu' | k, q \rangle \, |J, \mu\rangle \langle J, \mu'| \,. \tag{4.17}$$

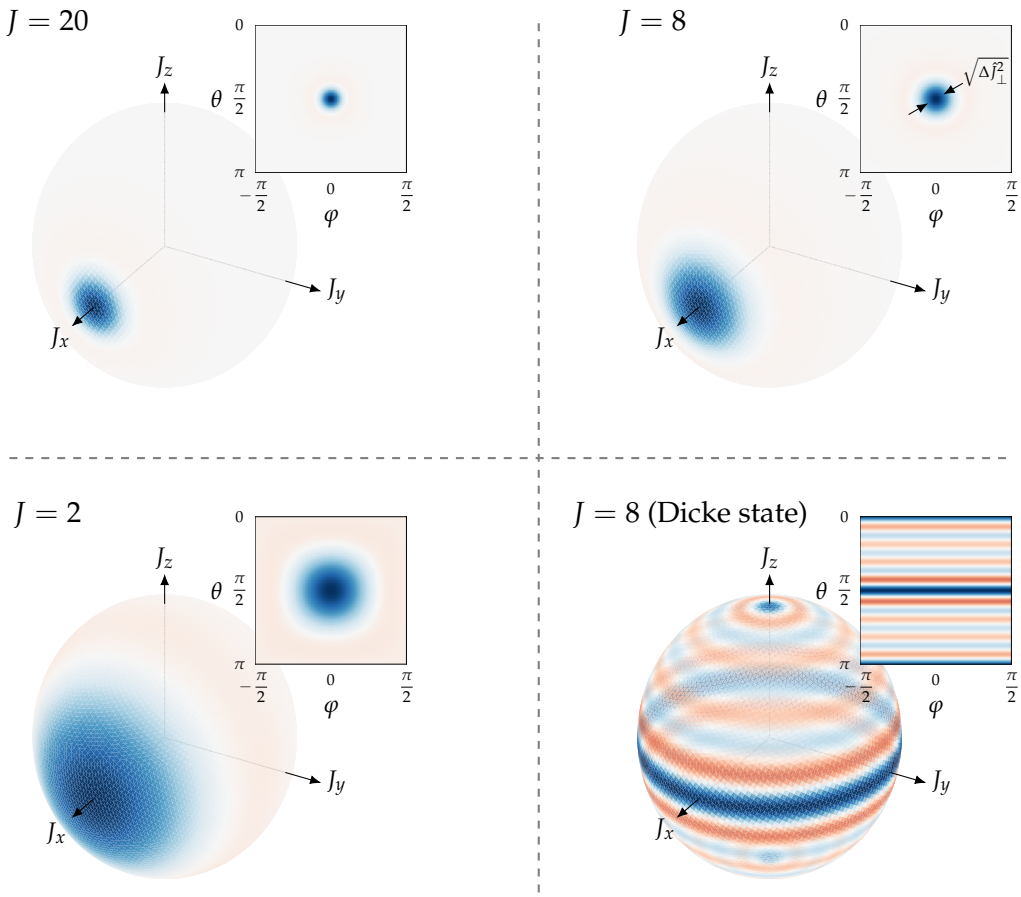

Figure 4.2 – Wigner distribution. We give here the Wigner distributions of coherent states pointing along x and for different collective spin length J (the radius of the sphere). Red regions indicate negative values. The Wigner distribution of a coherent state $|J;\theta,\varphi\rangle$ is essentially gaussian and centered around (θ,φ). The Wigner function is mostly positive for a coherent state, which can also be considered as a classical state. The amplitude of the negative regions decreases with increasing values of J. The relative width of the distribution $(\Delta J_{\mathbf{s}}^2)^{1/2}/J$ also decreases, with a $1/\sqrt{J}$ scaling. This can be seen on the planar representations of the distribution (insets). The relative size of a large coherent state ($J = 20$, top left) is much smaller than for a small spin (*e.g.* $J = 2$, bottom left). We also give the Wigner representation of the Dicke state $|J,m\rangle$ with $J = 8$ and $m = 0$. This state is analogous to *Fock states* in quantum optics, and its Wigner distribution has many regions with negative values, indicating non-classicality.

the collective spins. We will consider here that a spin-state is non-classical if some of its elementary constituents are entangled.

A many-body quantum state $|\psi_{\text{tot}}\rangle$ is said to be *separable* if it can be written in the form

$$|\psi_{\text{tot}}\rangle = |\psi_1\rangle \otimes |\psi_2\rangle \otimes \cdots \otimes |\psi_N\rangle\,, \tag{4.18}$$

where $|\psi_i\rangle$ are the single-particle states. In that sense, the coherent state constructed in eq. (4.11) is separable. Non-separable states – such as the Dicke state with $|m| \neq J$ – are called entangled states (see *e.g.* [Horodecki et al. 2009] for a review). We introduce below two

different kinds of non-classical spin-states: *spin-squeezed states* and *N00N* states.

Spin squeezed states

While a coherent state can be considered as an ensemble of uncorrelated qubits, spin squeezing emerges when some of the qubits are quantum-correlated. With well chosen correlations, the variance of the collective spin can be reduced in one direction, and increased in the other one, such that the Heisenberg inequality in eq. (4.15) remains saturated. Such a definition of a spin squeezed state was first proposed in [Kitagawa 1993]. We give in fig. 4.3 the Wigner distribution of a squeezed state with $J = 8$.

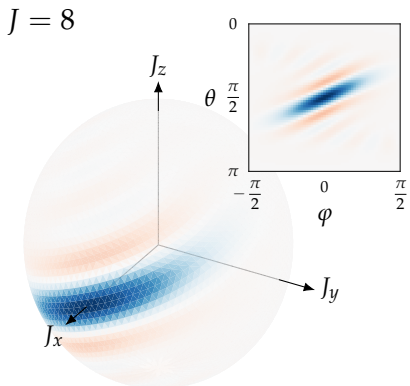

Figure 4.3 – Squeezed state. Wigner representation of a squeezed state. Squeezing is intuitively understood in the overall shape of the distribution, which is no longer rotationally invariant around its direction (θ, φ). In particular, the variance is reduced in one direction and increased in another one. The directions of minimal and maximal variance are often referred as *quadratures*. The non-classicality of the state is also visible in the negative regions of the distribution, depicted in red.

The amount of squeezing can be quantified using the squeezing parameter[3] [Wineland et al. 1992]

$$\xi_{\mathrm{R}}^2 = \frac{2J}{\langle \hat{J}_{\theta,\varphi} \rangle^2} \Delta \hat{J}^2_{\mathbf{s},\min}, \tag{4.19}$$

where $\langle \hat{J}_{\theta,\varphi} \rangle$ is the mean spin length in the direction in which the spin is oriented – defined by the direction that maximizes $\langle \hat{J}_{\theta,\varphi} \rangle$, and $\Delta \hat{J}^2_{\mathbf{s},\min}$ is the minimal variance in the orthogonal plane. A state is then squeezed if $\xi_{\mathrm{R}} < 1$. For a coherent state, we have $\xi_{\mathrm{R}} = 1$. The squeezing parameter was originally introduced to account for the gain in precision one could attain using a squeezed state in a Ramsey interferometer (which we will introduce in section 4.2), hence the index 'R'.

N00N states

A N00N state is a coherent superposition of coherent spin states with opposite directions on the Bloch sphere. Its name originates from the way the state vector is written: in

[3] This definition takes into account the *usefulness* of the squeezing. One may *e.g.* consider only the minimal variance, and say that the state is squeezed if it is smaller than the variance of a coherent state. However, if the other quadrature gets much bigger, the squeezed state might not be proven useful for metrology purposes (see section 4.2).

the case of a N00N state oriented along the z direction, we have

$$|\mathrm{N00N}\rangle = \frac{|N\rangle_\uparrow |0\rangle_\downarrow + \mathrm{e}^{\mathrm{i}\phi} |0\rangle_\uparrow |N\rangle_\downarrow}{\sqrt{2}} = \frac{|J,J\rangle + \mathrm{e}^{\mathrm{i}\phi} |J,-J\rangle}{\sqrt{2}}, \tag{4.20}$$

with $N = 2J$ the number of elementary constituents. It is a superposition of all qubits oriented *up* and all qubits oriented *down*. The N00N state is also called the GHZ state (for Greenbergen, Horne and Zeilinger, [Greenberger et al. 1990]) in the context of multipartite entanglement (see *e.g* [Monz et al. 2011]). It may also be referred to as a Schrödinger cat state, for it is a quantum superposition of classical states with opposite directions. The N00N states are said to be *maximally-entangled* states, and are highly sensitive to decoherence, making their experimental realization relatively challenging. Yet, they have been realized and studied with various many-body systems, *e.g.* with trapped ions [Leibfried et al. 2005] or with an array of Rydberg atoms [Omran et al. 2019].

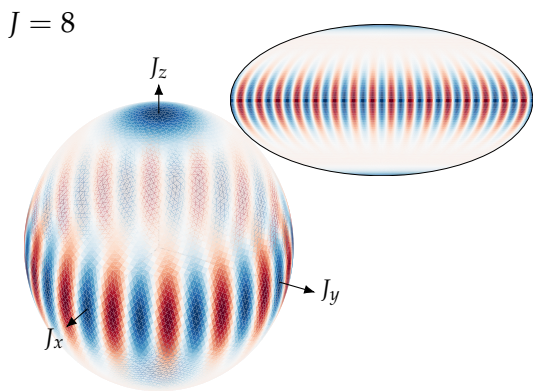

Figure 4.4 – N00N state. Wigner representation of a N00N state oriented along the z axis. The distribution clearly shows that the state is a superposition of two coherent states oriented along $+z$ and $-z$. The non-classicality of the state is also striking, with negative regions of amplitude equal to the positive ones along the equator.

We give in fig. 4.4 the Wigner distribution for a N00N state with $J = 8$. The Wigner function shows the coherence of the superposition on the equator of the Bloch sphere. We can see an oscillating behavior, of period π/J, and with a large amplitude. Such a pattern is highly sensitive to the phase ϕ of the superposition, making the N00N state more sensitive to rotations than coherent states.

4.2 Quantum-enhanced sensing

The notion of sensing, in the context of quantum mechanics, consists in giving an estimation of an external quantity *via* the measurement of an observable on the quantum sensor, represented by a state $\hat{\rho}$ (see fig. 4.5). In the scope of this thesis, the quantum sensor is the collective spin, of size J. The external quantity can be any quantity that causes a rotation of the collective spin, and for our experiment, it is an external magnetic field. In practice, this external field is aligned with the dominant field in the experiment, which determines the quantization axis. Upon a rotation, the collective spin accumulates a phase

Φ that can be measured with interferometry. The observables that we use depend on the quantum state of the sensor: the idea is to choose the observable that gives the best estimation of the phase Φ, or equivalently the smallest statistical variance $\Delta\Phi^2$. Yet, there are fundamental limits on the sensitivity of the probe state, and the best observables will be those allowing to reach these limits.

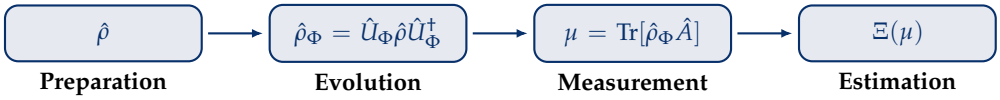

Figure 4.5 – Phase estimation: general process. A phase Φ, coming from an external evolution $\hat{U}_\Phi$, is encoded on the probe state $\hat{\rho}$. A measurement, represented by the operator $\hat{A}$, is then performed on $\hat{\rho}_\Phi$. The outcome of this measurement is μ. The phase Φ is then estimated by the estimator $\Xi(\mu)$, based on the measurement result μ.

Mathematically, these limits can be very well defined. We introduce in the following some relevant quantities for this manuscript, largely inspired by the discussion in [Pezzè et al. 2018]. One can introduce $P(\mu|\Phi)$ the probability to obtain the result μ knowing that the parameter to be estimated is Φ. We assume here that μ is part of a discrete set of real values, for examples the eigenvalues of an operator. We now introduce the estimator $\Xi(\mu)$, which associates an estimate of Φ to the measurement outcome μ. This estimator can give a statistical mean and variance

$$\bar{\Xi} = \sum_\mu P(\mu|\Phi)\Xi(\mu) \qquad \text{and} \qquad \Delta\Phi^2 = \sum_\mu P(\boldsymbol{\mu}|\Phi)[\Xi(\mu) - \bar{\Xi}]^2, \tag{4.21}$$

with the sum extending over all possible outcomes μ. In the following, we consider only *unbiased* estimators, for which $\bar{\Xi} = \Phi$, *i.e.* those that average directly to the true parameter value.

We now introduce the *Fisher information* $F(\Phi)$, which essentially measures the amount of information (a quantitative interpretation will be given in section 4.2.4), and can be extracted from the observables that allow to estimate Φ. It is defined as

$$F(\Phi) = \sum_\mu \frac{1}{P(\mu|\Phi)} \left(\frac{\partial P(\mu|\Phi)}{\partial \Phi} \right)^2, \tag{4.22}$$

and is used to define the *Cramér-Rao bound*, which sets a fundamental limit on the variance of the parameter to estimate

$$\Delta\Phi \geq \Delta\Phi_{\mathrm{CR}} = \frac{1}{\sqrt{\nu F(\Phi)}}, \tag{4.23}$$

where ν is the number of independent measurements.

With such definitions, the sensitivity of a probe state is formally limited by the Cramér-Rao bound. However, the probability distribution $P(\mu|\Phi)$ depends on the observable that is chosen for the measurement. We thus introduce the *quantum Fisher information*, $F_{\mathrm{Q}}(\hat{\rho}) = \max_{\{\hat{E}\}} F(\Phi)$, obtained from maximizing the Fisher information over all possible observables $\hat{E}$. The *quantum Cramér-Rao bound* is then defined as above,

$\Delta\Phi_{\mathrm{QCR}} = 1/\sqrt{\nu F_{\mathrm{Q}}(\hat{\rho})}$.

In the case of a pure state, which accumulates a phase due to the unitary evolution generated by the Hermitian operator $\hat{H}$, the quantum Fisher information takes the simple form [Pezzè et al. 2009]

$$F_{\mathrm{Q}}(\hat{\rho}) = 4\Delta\hat{H}^2, \tag{4.24}$$

with $\Delta\hat{H}^2$ the variance of $\hat{H}$, for the state $\hat{\rho}$. Yet, such a simple result should be taken with caution: *measuring* this Fisher information, *i.e.* measuring a phase sensitivity down to the Cramér-Rao bound in general requires a complicated protocol, because it is complicated to find and use the correct observable $\hat{E}$ that maximizes the Fisher information.

4.2.1 Standard quantum limit

The standard quantum limit is also called the *classical* limit, because it is a fundamental sensitivity limit for classical states, *i.e.* in the absence of quantum correlations. Such a limit applies to coherent states, and can be intuitively understood with the Wigner representation. We have seen that a coherent state has isotropic fluctuations in the plane orthogonal to its axis, of size $\Delta\hat{J}_{\mathbf{s}}^2 = J/2$. As such, two coherent states cannot be resolved from one-another if their centers are separated by less than $\Delta\hat{J}_{\mathbf{s}}$, which corresponds to an angle $\Delta\Phi_{\mathrm{min}} = 1/\sqrt{2J}$ on the Bloch sphere of radius J (see fig. 4.6). Such an intuitive approach, based on the overlap between different Wigner distributions, is actually quite general for evaluating the sensitivity of a given state [Zurek 2001].

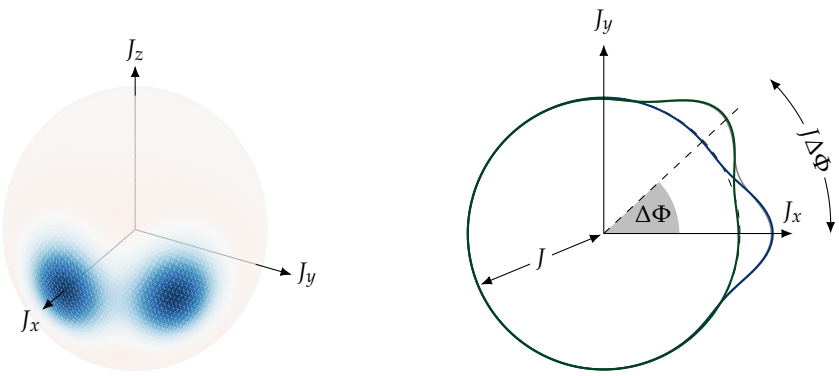

Figure 4.6 – Sensitivity of a coherent state. (Left) Wigner distribution of the sum of two coherent states separated by $\Delta\Phi$ (here we chose $J = 8$, and $\Delta\Phi = \pi/4$). (Right) Cut on the equator of the distribution given on the left panel. The two coherent states can be resolved from one another in a single measurement if their angular separation $J\Delta\Phi$ on the surface of the sphere is larger than their width $\Delta J_{\mathbf{s}}$.

This sensitivity can be recovered using the result in eq. (4.24). Let us consider for instance a coherent state oriented along x. The phase Φ is accumulated following a rotation about the z axis, governed by the operator $\hat{J}_z$. As such, one has $\Delta\hat{J}_z^2 = \langle\psi|\hat{J}_z^2|\psi\rangle = J/2$, with $|\psi\rangle = |J;\pi/2,0\rangle$, and consequently $F_{\mathrm{Q}} = 2J$ and $\Delta\Phi_{\mathrm{QCR}} = 1/\sqrt{2J}$. This quantum

Cramér-Rao bound, for the coherent state, defines the standard quantum limit (SQL)

$$\Delta\Phi_{\mathrm{SQL}} = \frac{1}{\sqrt{2J}}. \tag{4.25}$$

It is interesting to notice here that the sensitivity of a single measurement on a coherent state of the collective spin J is equivalent of having $2J$ independent measurements on a single qubit: the number of qubits and the number of measurements play the same role for the SQL. We recover the idea that a coherent state is simply a collection of uncorrelated qubits on which the same rotation is performed.

In practice, the sensitivity of a coherent state is measured using Ramsey interferometry, which is a general technique for phase measurements. In the context of an ensemble of qubits, Ramsey interferometry usually amounts to a transfer of the accumulated phase to a population difference between the two modes $\uparrow$ and $\downarrow$. Such a population measurement is equivalent to the measurement of the average value of $\hat{J}_z$, denoted m_z, provided that the rotation is about the z axis. A scheme for Ramsey interferometry is given in fig. 4.7.

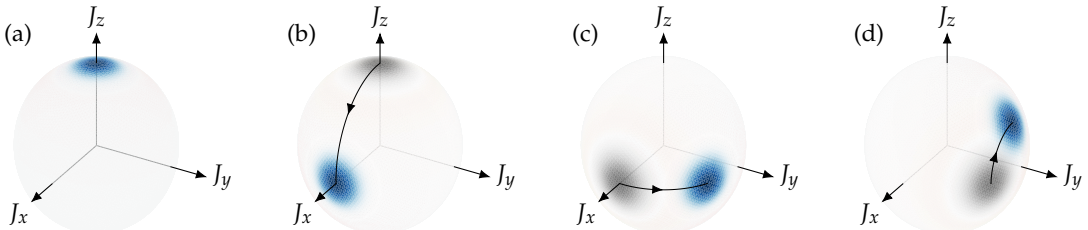

Figure 4.7 – Ramsey interferometry. (a) The initial state is prepared in the coherent state $|J;0,0\rangle$, *i.e.* all the qubits in $|\uparrow\rangle$. (b) This coherent state is brought on the equator to $|J;\pi/2,0\rangle$ with a rotation of $\pi/2$ about the y axis. (c) The phase Φ to be measured, resulting from a rotation around the z axis, is imprinted in the coherent state which becomes $|J;\pi/2,\Phi\rangle$. (d) A last rotation of $-\pi/2$ about the y axis gives the final state $|J;\Phi,\pi/2\rangle$. The phase Φ has thus been transfered to a population difference, read by the polar angle of the final state, or equivalently by $\langle\hat{J}_z\rangle$.

The phase sensitivity can then be measured using [Yurke et al. 1986]

$$\Delta\Phi = \left|\frac{\Delta m_z}{\partial_\Phi m_z}\right|. \tag{4.26}$$

The first two moments of the Ramsey fringe are given by $m_z(\Phi) = J\cos\Phi$ and $\Delta m_z(\Phi) = \sqrt{J/2}\sin\Phi$, yielding $\Delta\Phi = 1/\sqrt{2J}$, as expected. Such an estimation of the sensitivity, called the *method of moments*, is not optimal in general, and the Cramér-Rao bound is only reached in the case of gaussian states [Pezzè et al. 2018], whose quantum fluctuations are described by gaussian statistics and which saturate the Heisenberg inequalities.

4.2.2 Metrological gain

As we just saw, the sensitivity of a state is intrinsically related to the fluctuations of a well chosen observable. By reducing those fluctuations in one direction, it is thus possible

to increase the sensitivity of a state upon a rotation along this direction. In that sense, spin squeezed states can be more sensitive to rotations than coherent states (see fig. 4.8).

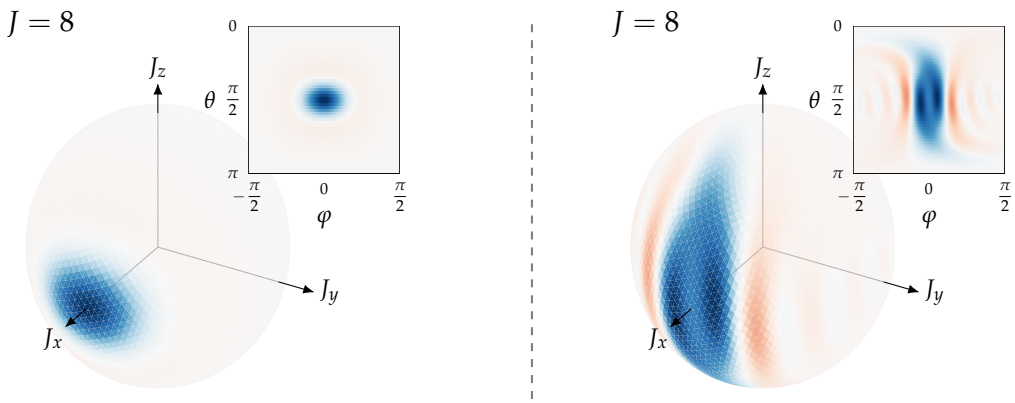

Figure 4.8 – Sensitivity of a squeezed state. (Left) Sum of the Wigner distributions of two coherent states pointing along the equator, separated by an azimuthal angle $\Delta\Phi = \pi/10$. Visually, one already sees that it is challenging to distinguish two different coherent state, even if $\Delta\Phi > \Delta\Phi_{\mathrm{SQL}}$ in this case. (Right) Sum of the Wigner distributions of two squeezed states, separated by the same angle $\Delta\Phi$. Here, we see that the reduction of the fluctuations allows to clearly distinguish the two states, provided they are well oriented.

Using the same arguments as for the coherent state, two squeezed states can be distinguished from one-another if they are separated by more than $\Delta\hat{J}_{\perp,\mathrm{min}}$ and if they are well oriented. As such, we write $\langle \hat{J}_{\theta,\varphi} \rangle \, \Delta\Phi_{\mathrm{min}} = \Delta\hat{J}_{\perp,\mathrm{min}}$, following the notation introduced in eq. (4.19). This allows to give a meaning to the squeezing parameter, as we can now write

$$\Delta\phi_{\mathrm{min}} = \frac{\xi_{\mathrm{R}}}{\sqrt{2J}} = \xi_{\mathrm{R}} \Delta\Phi_{\mathrm{SQL}}. \tag{4.27}$$

Such a comparison between the SQL and the sensitivity of a given state defines the metrological gain

$$G \equiv \left(\frac{\Delta\Phi_{\mathrm{SQL}}}{\Delta\Phi} \right)^2. \tag{4.28}$$

For spin squeezing, one simply has $G = \xi_{\mathrm{R}}^{-2}$.

Having a metrological gain $G > 1$ necessarily implies that $F_{\mathrm{Q}}(\hat{\rho}) > 2J$, which is a sufficient condition for entanglement between elementary constituents. In other words, only non-classical states can achieve a metrological gain above unity. As such, a measurement of squeezing can be used as a witness of entanglement (see *e.g.* [Gross et al. 2011]).

4.2.3 Heisenberg limit

Although non-classical states can be used to beat the SQL, the metrological gain remains bounded by the Heisenberg limit (HL). The non-classicality of a state can be quantified by the *entanglement depth* [Sørensen et al. 2001], which gives the size of the largest set of elementary constituents that cannot be factorized into a product state. If k is the entanglement depth, then it can be shown that the quantum Fisher information is bounded by $F_{\mathrm{Q}}(\hat{\rho}) \leq 2Jk$ [Pezzè et al. 2009]. The Heisenberg limit is then reached when

all the $N = 2J$ elementary constituents are entangled together, giving

$$F_{\mathrm{Q}}(\hat{\rho}) \leq 4J^2 \qquad \text{and} \qquad \Delta\Phi_{\mathrm{HL}} = \frac{1}{2J}. \tag{4.29}$$

The N00N state, which is maximally entangled, allows to reach the Heisenberg limit [Lee et al. 2002].

It is quite intuitive to understand why the N00N state is highly sensitive by looking at its Wigner distribution (see fig. 4.4). Upon a rotation about the z axis, which is the axis along which the state is oriented, the fringes on the equator will be shifted. The final state, after the rotation, becomes dinstinguishable from the initial state after a rotation $\Delta\Phi = 1/2J$, which constitutes the HL. This result can also be recovered using eq. (4.24) with $\hat{H} = \hat{J}_z$, encoding such a rotation, to get $F_{\mathrm{Q}}(\hat{\rho}_{\mathrm{N00N}}) = 4J^2$ and thus the Heisenberg limit. The difference between the initial and final states is encoded in the phase difference between the two *lobes* of the N00N states. The readout of this phase, however, requires non-linear observables.

The N00N state belongs to the set of *non-gaussian* states, which are characterized by the fact that a non-linear observable is needed to grasp their sensitivity [Gessner et al. 2019]. Coherent states and spin squeezed states, on the other hand, can be considered as gaussian states, because their sensitivity can be measured using rotations – and thus operators linear in $\hat{\mathbf{J}}$ – as shown in fig. 4.8. In the case of N00N states, one can use *e.g.* parity oscillations [Monz et al. 2011], which requires the ability to readout exactly the number of elementary constituents in each mode ($\uparrow$ or $\downarrow$), or transfer these high-order coherences to a collective quantity, easier to detect and less prone to experimental noise, using a non-linear evolution [Leibfried et al. 2004].

4.2.4 Statistical distance

Measuring the quantum Fisher information on the experiment, as we just saw, can be challenging, especially for non-gaussian states which require high order observables. In general, the best observable that allows to experimentally measure the quantum Fisher information is difficult to find and to implement.

Estimating the phase sensitivity is equivalent to quantifying how two quantum states are different from one-another. As such, one can use a statistical distance, defined in the Hilbert space, and which gives a quantitative meaning to the difference between two states [Wootters 1981]. We introduce the Hellinger distance, defined as

$$d_{\mathrm{H}}^2(0,\Phi) = 1 - \sum_{\mu} \sqrt{P(\mu|0)P(\mu|\Phi)} = \frac{1}{2}\sum_{\mu}\left[\sqrt{P(\mu|0)} - \sqrt{P(\mu|\Phi)}\right]^2, \tag{4.30}$$

which measures such a statistical distance between the two distributions $P(\mu|0)$ and $P(\mu|\Phi)$. Such a quantity can be computed when all the information about the probe state is available, *i.e.* when the distribution $P(\mu)$ is experimentally accessible. A Taylor expansion of d_{H}^2 shows that

$$d_{\mathrm{H}}^2(0,\Phi) = \Phi^2 \frac{F(0)}{8} + \mathcal{O}(\Phi^3), \tag{4.31}$$

which means that the Fisher information is intrinsically related to the rate of change of the distance with respect to the parameter Φ, or to the statistical velocity

$$F(0) = 8v_{\mathrm{H}}^2 \qquad \text{with} \quad v_{\mathrm{H}} = \left.\frac{\partial d_{\mathrm{H}}}{\partial \Phi}\right|_{\Phi=0}. \tag{4.32}$$

The quantum Fisher information is then obtained by maximizing the above result over all possible measurements, similarly as what was described at the beginning of section 4.2. The Hellinger distance was used *e.g.* in [Strobel et al. 2014] to quantify the entanglement in non-gaussian states. In principle, the Hellinger distance is the best way to exploit the results of a given experiment, because it uses all the available information. Yet, the specific protocol – the measurement process, or equivalently the observable that gives the distribution P – may be difficult to realize.

4.3 One-axis twisting

The generation of non-classical spin-states, by essence, requires to entangle the elementary constituents together. There are several ways of doing so ; see *e.g.* atom-atom collisions in BECs [Estève et al. 2008], quantum non-demolition light detection of ensembles of atoms [Schleier-Smith et al. 2010], or light-mediated interactions in ion chains [Sackett et al. 2000]. The key ingredient, in all these processes, is the implementation of a non-linear interaction between the single qubits. In this section, we describe in detail the simplest of non-linear spin Hamiltonians, called *one-axis twisting* (OAT), and given by

$$\hat{H} = \hbar\chi\hat{J}_{\mathbf{u}}^2. \tag{4.33}$$

Here, $\mathbf{u}$ denotes the orientation of the Hamiltonian, and can take any value on the sphere. The parameter χ encodes the coupling strength. This Hamiltonian was first introduced in [Kitagawa 1993], precisely in the context of spin squeezing.

4.3.1 Time-evolution

In the following, we focus on the OAT Hamiltonian with $\mathbf{u} = x$, applied to an initial state $|\psi_0\rangle = |J, -J\rangle$, *i.e.* a coherent state pointing on the south pole. All the results we present in this section are computed with $J = 8$. Such a situation, as we will see, corresponds to the experimental implementation that we realize with dysprosium atoms.

The Hamiltonian evolution governed by $\hat{H}$ is periodic, of period $T = 2\pi/\chi$. We show in fig. 4.9 the calculated evolution of the state, decomposed on the Dicke state basis $|J, m\rangle$, over one full period.

Starting from a well defined coherent state $|J; \pi, 0\rangle$ (which is also a Dicke state $|J, -J\rangle$), all the even-$|m\rangle$ states get gradually populated on relatively short timescales. The parity is conserved throughout the whole evolution ; this is a consequence of the $\hat{J}_x^2$ Hamiltonian, which only couples states with the same parity. On short timescales $\chi t \sim 1/\sqrt{2J}$, we observe a collapse of low order observables, such as the magnetization $\langle \hat{J}_z \rangle$, which quickly goes to 0, or the variance $\Delta\hat{J}_z^2$ which takes a finite value $\Delta\hat{J}_z^2 \approx 34$. This is a consequence of a dephasing effect, that can be understood by writing explicitly the evolution. We can

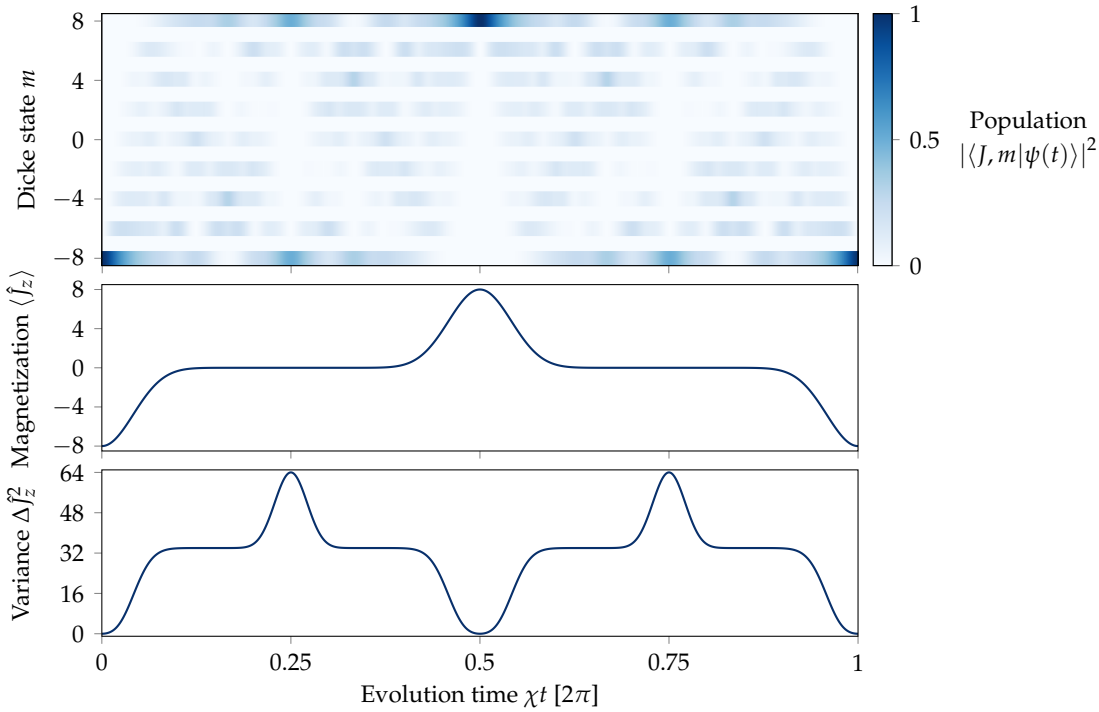

Figure 4.9 – One-axis twisting evolution. (Top) Decomposition of $|\psi(t)\rangle$ on the Dicke state basis $|J, m\rangle$ as a function of the evolution time, starting from $|J, -J\rangle$. (Middle) Average magnetization and (bottom) variance along the z direction as a function of the evolution time.

indeed make a basis change, such that, using eq. (4.13)

$$|\psi_0\rangle = |J, -J\rangle = \sum_{m=-J}^{J} c_m \mathrm{i}^m \, |J, m\rangle_x \qquad \text{with} \quad c_m = \frac{1}{2^J}\sqrt{\binom{2J}{J-m}}, \tag{4.34}$$

where we explicitly write $|J, m\rangle_x$ to designate the eigenstates of $\hat{J}_x$. The time evolution under this Hamiltonian is now quite explicit, as we have

$$|\psi(t)\rangle = \mathrm{e}^{-\mathrm{i}\chi t \hat{J}_x^2} |\psi_0\rangle = \sum_{m=-J}^{J} c_m \mathrm{i}^m \mathrm{e}^{-\mathrm{i}m^2\chi t} \, |J, m\rangle_x \,, \tag{4.35}$$

and the dephasing between the different Dicke states (in the x basis) causes the apparent collapse that we see in short timescales[4].

Yet, there are specific times of rephasing. At $\chi t = \pi$ for instance, the phase factors rephase to $\mathrm{e}^{-\mathrm{i}m^2\pi} = (-1)^m$, and the state $|\psi(t = \pi/\chi)\rangle = |J, J\rangle$ is in fact the coherent state oriented along the north pole. It is actually quite clear in fig. 4.9, where at $\chi t = \pi$ only the state $|J, J\rangle$ is populated, and the magnetization is equal to $\langle \hat{J}_z \rangle = J$. Another time of interest is at $\chi t = \pi/2$, where we recover, up to a global phase factor, a N00N state with

[4]The scaling of the apparent collapse time can be explained by considering *e.g.* the expression of the average magnetization $\langle \hat{J}_z(t) \rangle = -J\,[\cos(\chi t)]^{2J-1}$ [Kitagawa 1993]. By approximating the short time dynamics by a gaussian decay of the form $\langle \hat{J}_z(t) \rangle \approx -J \exp(-t^2/2t_c^2)$, one recovers a scaling of the form $\chi t_c \sim 1/\sqrt{2J}$ for the collapse time t_c.

$\phi = -\pi/2$,

$$|\psi(t = \pi/2\chi)\rangle = \frac{e^{i\pi/4}}{\sqrt{2}} \left(|J, J\rangle - i\,|J, -J\rangle\right). \tag{4.36}$$

This revival is also visible in fig. 4.9, where at $\chi t = \pi/2$ the states $|J, J\rangle$ and $|J, -J\rangle$ are equally populated, and the variance peaks at $\Delta\hat{J}_z = J^2$.

We show in fig. 4.10 the Wigner distribution along $0 \leq \chi t \leq \pi/2$ (the evolution at longer times can be deduced by symmetry). These distributions allow for a clear understanding of the dynamics. On very short time scales, the spin state gets squeezed. Such an effect can be understood qualitatively by the nature of the Hamiltonian: a $\hat{J}_x^2$ coupling can be interpreted as a rotation about the x axis, with a rotation strength that gets stronger further from the origin, and of opposite signs along $\pm x$. As such, we obtain a shearing effect that *twists* the distribution, and the distribution gets squeezed.

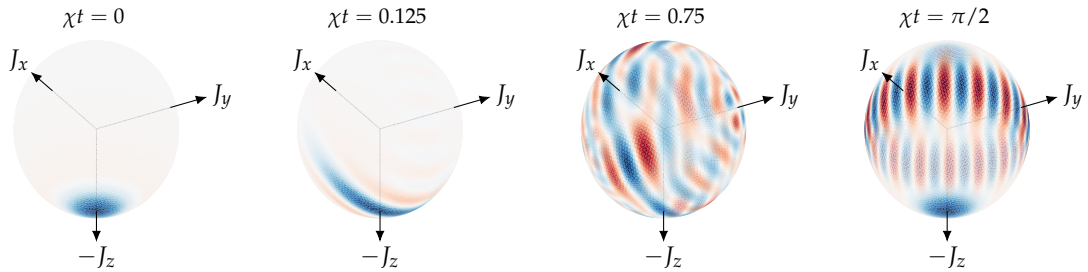

Figure 4.10 – One-axis twisting evolution: Wigner distributions. We show the Wigner distribution (bottom view) from the initial state ($\chi t = 0$) up to the N00N state at ($\chi t = \pi/2$), with intermediate times for a spin squeezed state ($\chi t = 0.125$) and a 'dephased' state ($\chi t = 0.75$).

When the squeezing becomes too important, the distribution wraps around the sphere, and the overall shape loses any identifiable structure. Such a state, represented for $\chi t = 0.75$, is referred as a 'dephased' state in fig. 4.10. At $\chi t = \pi/2$, as mentioned above, a rephasing occurs and we obtain the Wigner distribution of a N00N state.

4.3.2 Metrological gain

The one-axis twisting Hamiltonian allows, as we just saw, to bring a coherent state to a N00N state, *i.e.* to go from the standard quantum limit to the Heisenberg limit. We focus here on the evolution of the metrological gain.

Squeezing parameter

On short timescales, the state remains gaussian, but gets squeezed. We can extract the squeezing parameter as defined in eq. (4.19). Along the evolution, the state remains oriented along the south pole $\theta = \pi$, although the average spin length $\langle \hat{J}_{\pi,0} \rangle$ is reduced. The squeezing parameter is thus computed by finding the minimal variance in the (x, y) plane. Results are shown in fig. 4.11.

As we can see, starting from the polarized state $|J, -J\rangle$, the average spin goes quickly to 0. Squeezing is deduced from the drop of $\Delta J^2_{\mathrm{s,min}}$ at very short times. At longer times, the metrological gain defined from the squeezing parameter gets smaller than

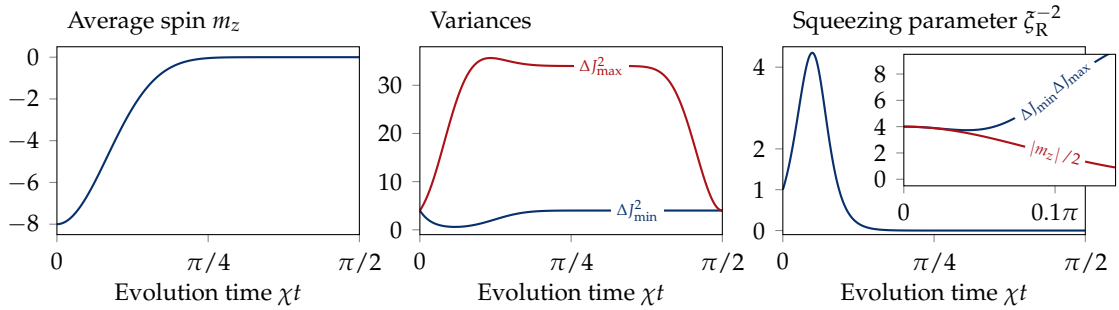

Figure 4.11 – Squeezing dynamics in the OAT. (Left) Average value of the spin m_z, which also gives the average spin length $\left|\langle \hat{J}_{\pi,0}\rangle\right| = |m_z|$. (Middle) Variance in the transverse plane $\Delta J^2_{\mathbf{s},\min}$ (in blue) and $\Delta J^2_{\mathbf{s},\max}$ (in red) as a function of time. (Right) Inverse squeezing parameter ξ_R^{-2} as a function of time, which also gives the metrological gain. (Inset) Comparison between the product of the quadrature sizes, $\Delta J_{\mathbf{s},\min}\Delta J_{\mathbf{s},\max}$ with the average spin length $|m_z|/2$ (see text).

1. In order to understand the transition from gaussian to non-gaussian, we also plot in the inset the product of the quadrature sizes and half the average spin length. These two quantities coincide only at very short times, corresponding to a nearly saturated Heisenberg inequalities and thus an approximately gaussian state. At longer time, the state is far from being gaussian, and the squeezing parameter is no longer able to account for the metrological gain.

Quantum Fisher information

The time for which the state remains approximately gaussian scales as $1/\sqrt{2J}$, and thus gets relatively shorter as J increases. At longer time, the metrological gain can be deduced from the quantum Fisher information, specifically using eq. (4.24). Indeed, the best sensitivity will be reached by rotating the state $|\psi(t)\rangle$ along the axis of largest variance. The value of the largest variance may differ form $\Delta J_{\mathbf{s},\max}$ given in fig. 4.11, which only considers the variances in the transverse plane. The quantum Fisher information is thus computed by maximizing $F_Q = 4\Delta\hat{J}^2_{\mathbf{u}}$ over all possible orientations $\mathbf{u}$ on the Bloch sphere. The metrological gain can then be deduced from the Cramér-Rao bound to obtain $G = F_Q/2J$. We insist once again on the fact that measuring such a bound is in general quite complicated. The result is plotted in fig. 4.12.

At short times, the metrological gain computed with the squeezing parameter and the one given by the Fisher information coincide, because the state remains approximately gaussian. At longer time, the quantum Fisher information gives a higher gain, which reaches a plateau at $G = J + 1/2$. When approaching $\chi t = \pi/2$, corresponding to the N00N state, the gain increases again to reach the Heisenberg limit $G_{\mathrm{HL}} = 2J$.

4.3.3 Implementation with dysprosium

As a conclusion to this chapter, we give a technical description of the implementation of the one-axis twisting Hamiltonian on dysprosium atoms. Here, the non-linear coupling is created with a tensor light-shift which acts on the internal state of dysprosium atoms.

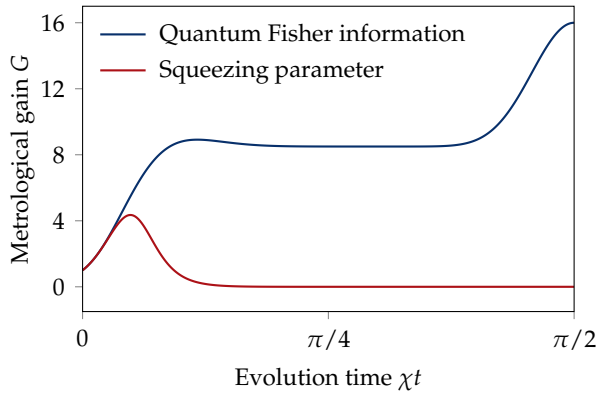

Figure 4.12 – Quantum Fisher information in the OAT. We represent here the metrological gain $G = F_Q/2J$ (blue curve), deduced from the quantum Fisher information (see text). It is compared to the gain obtained from the squeezing parameter (red curve), which only accounts for the metrological gain at very short times, when the state remains approximately gaussian.

As such, each dysprosium atom naturally carries a collective spin $J = 8$ – and each 'elementary qubit' of this collective spin cannot be addressed individually. Yet, all the descriptions given above remain valid, within the Hilbert space given by the ground state manifold of dysprosium atoms.

We consider the interaction of a dysprosium atom with a linearly polarized laser beam in the x direction (see fig. 4.13). An external magnetic field $\mathbf{B} = B\hat{\mathbf{z}}$ in the z direction defines the quantization axis. The total Hamiltonian of the dysprosium atom is

$$\hat{H} = \frac{\hat{\mathbf{p}}^2}{2m} + \hbar\omega_Z \hat{J}_z + \hat{V}_L, \tag{4.37}$$

where $\hat{\mathbf{p}}$ is the atom momentum, $\hbar\omega_Z = g_J \mu_B B$ is the Zeeman energy and $\hat{V}_L$ is the atom-light interaction.

The atom light interaction was already described in chapter 2, section 2.1. We recall here the expression of the light-shift operator in the case of a beam polarized in the x direction, given in eq. (2.3)

$$\hat{V}_L = V_0 \left[\alpha^s(\omega)\hat{\mathbb{1}} + \alpha^t(\omega) \frac{3\hat{J}_x^2 - \hat{\mathbf{J}}^2}{J(2J-1)} \right], \tag{4.38}$$

with $V_0 = I/2\epsilon_0 c$, and $\alpha^{s,t}$ the frequency-dependent polarizabilities of the ground state.

We now assume that the addressing laser beam is tuned close to the 626 nm transition, such that it dominates over all the other transitions in the computation of the polarizabilities, which now only depend on the detuning $\Delta = \omega - \omega_0$, with ω_0 the transition frequency. We also assume that $|\Delta| \gg \Gamma$, *i.e.* that we are sufficiently far away from the resonance to limit the effects of spontaneous emission. The polarizabilities can be

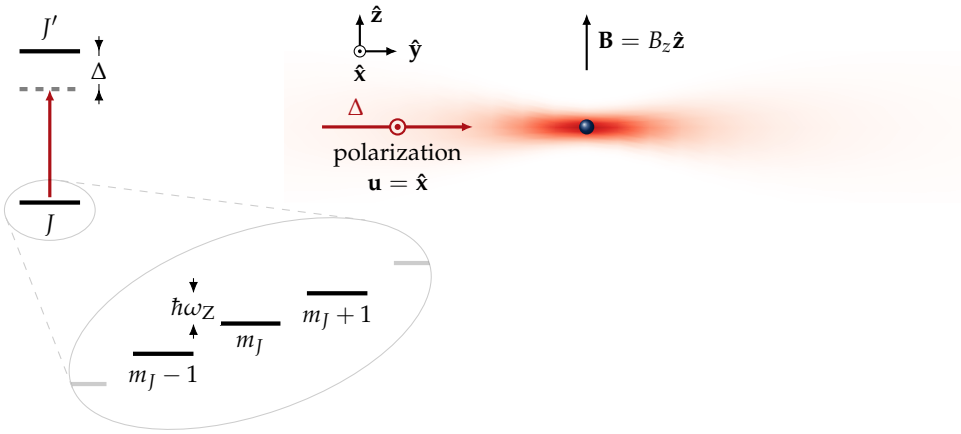

Figure 4.13 – Implementation of OAT with dysprosium. A laser beam, detuned by Δ from the 626 nm transition and linearly polarized along $\hat{\mathbf{x}}$ is set on the atoms. A quantization field $\hat{\mathbf{B}} = B\hat{\mathbf{z}}$ sets the quantization axis. The ellipse is a zoom into the ground state manifold, which degeneracy is lifted by the magnetic field.

expressed, in the case of the $J \to J' = J + 1$ transition that is used, as [Kien et al. 2013]

$$\begin{aligned}
\alpha^{\mathrm{s}} &= \frac{1}{\sqrt{3(2J+1)}}\alpha^{(0)} \\
\alpha^{\mathrm{v}} &= -\sqrt{\frac{2J}{(J+1)(2J+1)}}\alpha^{(1)} \\
\alpha^{\mathrm{t}} &= -\sqrt{\frac{2J(2J-1)}{3(J+1)(2J+1)(2J+3)}}\alpha^{(2)},
\end{aligned} \tag{4.39}$$

where we introduce

$$\alpha^{(K)} = (-1)^K\sqrt{2K+1}\begin{Bmatrix} 1 & K & 1 \\ J & J+1 & J \end{Bmatrix}(2J+3)\frac{3\pi\epsilon_0 c^3\Gamma}{\omega_0^3}\frac{1}{\Delta}. \tag{4.40}$$

Note that we have also written the vectorial component α^{v}, which is not used in this case but will be used in chapter 6. We get, for the atom-light interaction,

$$\hat{V}_{\mathrm{L}} = V_0\left[\alpha_0\hat{\mathbb{1}} + \alpha_2\frac{3\hat{J}_x^2 - \hat{\mathbf{J}}^2}{J(2J-1)}\right], \tag{4.41}$$

with

$$V_0 = \frac{3\pi c^2\Gamma}{2\omega_0^3}\frac{I}{\Delta} \quad ; \quad \alpha_0 = \frac{2J+3}{3(2J+1)} = \frac{19}{51} \quad ; \quad \alpha_2 = -\frac{J(2J-1)}{3(2J+1)(J+1)} = -\frac{40}{153}. \tag{4.42}$$

If we consider only the spin dynamics, *i.e.* we drop the scalar part and the kinetic energy term in the Hamiltonian, we obtain the one-axis twisting Hamiltonian, perturbed

by a longitudinal field

$$\hat{H} = \hbar\chi \hat{J}_x^2 + \hbar\omega_Z \hat{J}_z \qquad \text{with} \qquad \hbar\chi = -\frac{1}{153}\frac{3\pi c^2 \Gamma}{2\omega_0^3}\frac{I}{\Delta}. \tag{4.43}$$

The experimental implementation, and the effect of such a perturbation, will be discussed in the next chapter.

4.4 Conclusion

In this chapter, we introduced the concept of collective spins, formed by an ensemble of elementary qubits. We have seen that this collective spin can be used to measure *e.g.* external magnetic fields, by essentially measuring an accumulated phase in its state vector.

Entanglement between the elementary constituents leads to so-called *non-classical spin states*, which are states with improved phase sensitivity with respect to the standard quantum limit (SQL), obtained with classical – also called coherent – spin states. The non-classicality of a state can be depicted *e.g.* using its Wigner distribution, which is known to have negative parts in the presence of quantum correlations. We have seen as well that the presence of entanglement is revealed by the quantum Fisher information, which is a quantity that is also intrinsically related to the sensitivity improvement of the state.

The increase of sensitivity is measured by the metrological gain, which compares the sensitivity of a non-classical state to the SQL. The ultimate limit of sensitivity is reached when all elementary qubits are entangled together, and constitutes the Heisenberg limit (HL). Such a highly non-classical state is referred to as a N00N state here, but is sometimes also called a Schrödinger cat state, because it is a quantum superposition of maximally different classical states.

Being able to measure a metrological gain requires by essence to be able to measure the phase shift with the maximally allowed precision. We have seen that in general such a measurement requires non-linear observables. The HL, for instance, can be accessed by measuring the parity evolution of the N00N state. If all the information of the state is accessible, *i.e.* if one can measure the state of each elementary constituent individually, the measured gain can be optimized by computing the Hellinger distance, a statistical distance in the Hilbert space introduced in section 4.2.

Generating non-classical spin states requires non-linear interactions between the elementary qubits. In section 4.3, we have shown that the one-axis twisting Hamiltonian, although very simple, allows to prepare non-classical states, and especially the N00N state. We have also explained how it can be implemented with dysprosium, using the tensor light shift created by an off-resonant laser beam close to the 626 nm transition.

In the next chapter, we present the experimental realization of non-classical spin states *via* the implementation of the OAT Hamiltonian proposed here. In particular, we will see that we are able to prepare an almost perfect N00N state, measure its metrological gain, and reconstruct its Wigner distribution with a full state tomography.

5 Experimental realization of N00N states

5.1 Experimental implementation of one-axis twisting .. 80
5.1.1 Manipulation and detection of coherent states 80
5.1.2 Implementation of OAT 87
5.2 N00N state 89
5.2.1 Extraction of the gain: parity and non-linear interferometry 89
5.2.2 Gain from statistical distance 91
5.3 Tomography and decoherence 92
5.3.1 Reconstruction of the density matrix 93
5.3.2 Decoherence 94
5.4 Outlook 95
5.4.1 Squeezing and oversqueezing 96
5.4.2 Ground state of the OAT: exploring a quantum phase transition 96

THE THEORETICAL CONCEPTS introduced and discussed in the previous chapter are used here to realize a N00N state with the large spin of dysprosium atoms. We insist on the fact that the spin dynamics realized here take place in the internal state of each dysprosium atom, and do not stem from interactions between different particles.

The experimental implementation of the one-axis twisting (OAT) Hamiltonian, introduced in the previous chapter, is discussed in section 5.1. We first describe how we can manipulate the collective spins and perform arbitrary spin rotations using homogeneous fields, and how we detect the individual spin populations using a Stern-Gerlach measurement. As we will see, these manipulations allow for a precise calibration and tuning of the quantization axis. We then show that OAT is well implemented, by measuring the spin distribution's evolution as a function of the interaction time.

In section 5.2, we focus on the N00N state that we generate with OAT. We particularly focus on the enhanced sensitivity that such a state provides. We show two kinds of interferometric measurements, each of them allowing to extract a metrological gain significantly higher than the standard quantum limit (SQL). We furthermore show that we approach the quantum Cramér-Rao bound by extracting a metrological gain from the measurements of the Hellinger distance, which is computed thanks to our single-state resolution.

We complete the study of this N00N state with a full state tomography. We show in section 5.3 that the density matrix of the N00N state that we realize can be reconstructed from population measurements along different orientations on the Bloch sphere. The Wigner distribution, computed from this reconstruction, has all the characteristics of the N00N state already presented in the previous chapter (section 4.1.2). We also characterize the decoherence of such a highly non-classical state, and show that its reduced coherence time, with respect to classical states, is consistent with experimental shot-to-shot fluctuations of the magnetic field.

Most of the results presented in this chapter were published in [Chalopin et al. 2018b].

5.1 Experimental implementation of one-axis twisting

In all this chapter, we work with a sample of about 10^5 atoms at $T \approx 2\,\mu\text{K}$[1]. The study presented here was realized with ^{164}Dy, which is the most abundant isotope. This chapter is the only one, throughout this thesis, that uses this isotope. After transport and during the evaporation, the atoms remain spin-polarized in the lowest Zeeman state $|-J\rangle$, thanks to a vertical quantization field of about 0.5 G (the Zeeman splitting is $\hbar\omega_Z \approx 40\,\mu\text{K} \gg T$). The atoms are addressed collectively: we assume here that each individual atom follows the same evolution when interacting with laser light or with external magnetic fields.

5.1.1 Manipulation and detection of coherent states

The starting point of the experiment is thus the coherent state $|\theta = \pi\rangle$. We first discuss the measurement of the spin composition of the sample, as well as the implementation of rotations of coherent states.

Spin composition

Spin composition is measured using a Stern-Gerlach (SG) apparatus. The idea is to apply a m_J-dependent force during time-of-flight (ToF), where m_J designates the Zeeman sublevels. If the force is strong enough so that the separation between subsequent m_J-states is bigger than the thermal expansion of the cloud during ToF, we can physically separate and detect the atoms in the different Zeeman sublevels.

Experimentally, we apply a magnetic field gradient on top of a uniform field along the vertical direction (the z-axis), such that the force reads

$$\mathbf{F} = -g_J \mu_B m_J \boldsymbol{\nabla} |\mathbf{B}| \,. \tag{5.1}$$

The gradient is generated from a single magnetic coil placed below the glass cell (see fig. 1.10 in chapter 1 for a detailed view of the science cell and its surroundings). The electrical circuit to generate strong and fast pulses of current intensity is given in fig. 5.1.

We also show in fig. 5.1 the measured current as a function of time going through the coil. We are able to reach about 480 A at the peak value, in less than 1 ms. The total pulse duration is ~ 2 ms, and the gradient along z at the atoms' position is about $50\,\text{G}\,\text{cm}^{-1}$.

[1] We work here with an ultracold *thermal* gas, not a BEC. It is important to note that, in this study, we do not consider the effects of interactions between individual atoms, the temperature and density of the gas are thus of little importance.

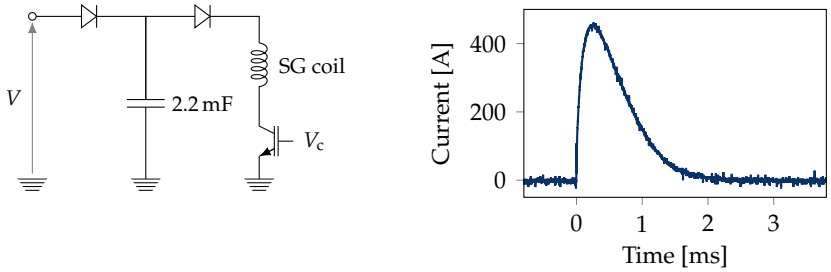

Figure 5.1 – Stern-Gerlach apparatus. (Left) Simplified electrical circuit for generating strong current pulses in the coil. A large capacitor is charged with a power supply, while the IGBT remains closed ($V_c = 0$). The capacitor is then discharged to the SG coil by opening the IGBT ($V_c > 0$). (Right) Measured current as a function of time. The IGBT is triggered at $t = 0$.

Such an apparatus allows to measure the spin composition along the z-axis, which is here defined by the direction of the force $\mathbf{F}$ in eq. (5.1), as long as the timescales associated to the gradient are much faster than the Zeeman splitting[2]. We stress here that in this measurement process, each individual atom is projected to a single Zeeman state $|m_J\rangle$. Having here N dysprosium atoms thus directly provides N independent projections. As such, from a single image we can retrieve the number of atoms in each of the sublevels m_J, which is interpreted as the probability, for a single atom, to be projected onto $|m_J\rangle$. We will give more details about the measurement of the populations later in this chapter. First, we focus on how we can use the SG apparatus for improved control of the direction of the quantization field.

Controlling the magnetic field applied on the atoms is crucial, because it sets the magnitude and direction of the additional $\hbar\omega_Z\hat{J}_z$ term that will perturb the one-axis twisting Hamiltonian (OAT) that we implement using tensor light-shifts. We use the SG apparatus, in a first experiment, to cancel the field component $B_\perp$ in the transverse (xy) horizontal plane[3].

The idea is to lower the magnetic field along z to a low value – typically 5 mG. If $B_\perp = 0$, then the atoms remain spin polarized in the lowest state $|-J\rangle$ (at such a field, the Zeeman splitting remains large enough to have negligible thermal population of the higher spin-states). If $B_\perp \neq 0$, the global direction of the magnetic field is no longer along the z-axis. The atoms remain spin polarized, but to the lowest Zeeman state given by the total field, which defines a new quantization axis. This state has a non-trivial decomposition in the $|m_J\rangle$-states basis along z, which are the one measured by the SG apparatus.

As such, we can measure the spin composition along z as a function of the transverse field $B_\perp$. Minimizing the transverse field is now equivalent to maximizing the population in the lowest state $|-J\rangle$ detected by the SG. An example of such a procedure is given in fig. 5.2.

[2]If the quantization field is not aligned in the z-direction and is too large, the current pulse in the gradient coil results in an adiabatic evolution of the individual spins, equivalent to a simple rotation. In order to have a projective measurement, the SG coil must be ramped up much faster than the Zeeman splitting. In the case where both the quantization axis and the SG axis (the z-axis) are the same, there are no possible rotations and the SG apparatus performs the desired measurement.

[3]For canceling the magnetic field, we use large compensation coils that surround the whole optical table.

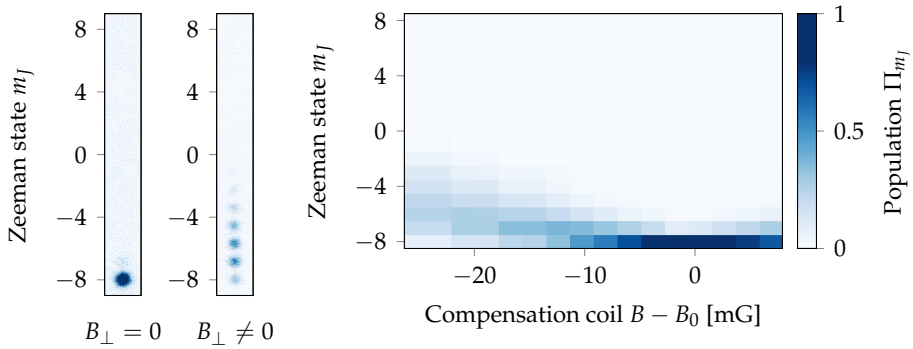

Figure 5.2 – Canceling the transverse field. (Left) Stern-Gerlach pictures, taken after 3.5 ms of ToF and for $B_z = 5\,\text{mG}$, with $B_\perp = 0$ and $B_\perp \neq 0$. In the former case, the lowest Zeeman state $m_J = -8$ is mostly populated, with negligible population in higher states. In the latter case, several other states are populated. (Right) Population in all 17 Zeeman states, extracted from SG pictures, as a function of the transverse field. The position of $B_\perp = 0$ is assigned to the point where the population in the lowest state is maximized.

This procedure allows to cancel the transverse field below the mG. The absolute value of the magnetic field, however, cannot be measured solely with this technique, but can be extracted using a Ramsey interferometry measurement, already introduced in the previous chapter (see section 4.1).

Ramsey interferometry

For a Ramsey sequence, one needs to put the coherent state originally at $\theta = \pi$ to the equator at $\theta = \pi/2$. This is implemented on the experiment by creating pulses of homogeneous fields along the transverse direction y. Those fields are generated by a pair of coils in a Helmholtz configuration, in which a pulse of current is sent.

These pulses, that we designate as $\pi/2$-pulses in the following, both need to be strong compared to the quantization field along z and fast with respect to the Larmor frequency. Within these considerations, we already see that having a low quantization field helps in the implementation of efficient $\pi/2$-pulses. The pulses we apply are typically $\sim 4\,\mu\text{s}$ long, and are generated with an arbitrary waveform generator (see fig. 5.3). The current going through the coil of inductance L reads

$$i(t) = \frac{1}{L}\int_0^t V(t')\mathrm{d}t', \tag{5.2}$$

where $V(\tau)$ is the voltage across the coil. As such, by outputting a single oscillation of a sine (angular frequency ω) on the waveform generator, we obtain a current pulse of the form $i(t) \propto \sin^2(\omega t/2)$.

The current going through the pair of coils is measured for a typical Ramsey sequence, and shown in figure 5.3. In practice, the amplitude of the pulse is chosen to be as large as possible, in order to reduce the time it takes to perform the $\pi/2$ rotation. The total time of the pulse is calibrated by looking at the spin composition after a single pulse and making sure the average magnetization $m_z = \langle \hat{J}_z \rangle$ vanishes. The Ramsey sequence consists in

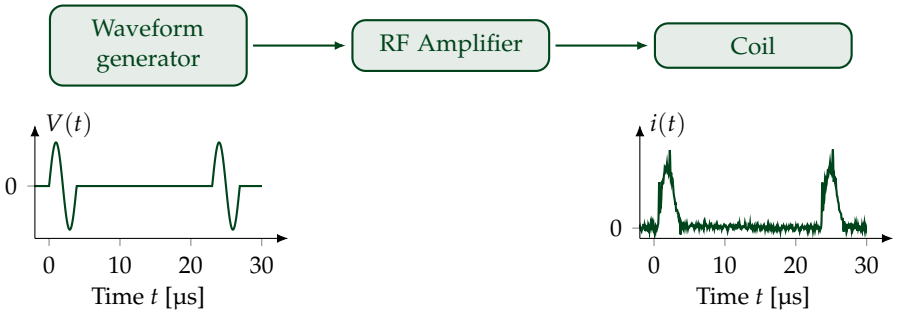

Figure 5.3 – Generating $\pi/2$-pulses. The current going through the pair of coils is induced by voltage pulses generated by an arbitrary waveform generator (see text). An RF amplifier is also used to increase the amplitude of the pulses (stronger pulses are associated to faster $\pi/2$ rotations). The left graph represents the voltage signal used to generate the current pulses. The right graph is the measured corresponding current trace $i(t)$ as a function of time.

generating two of these $\pi/2$-pulses separated by a precession time t. The phase acquired by the coherent state on the equator is then

$$\Phi(t) = \frac{g_J \mu_B}{\hbar} \int_0^t B_z(t')\mathrm{d}t', \tag{5.3}$$

where $B_z(t)$ is the amplitude of the quantization field. If constant in time, the phase Φ is simply proportional to both the time t and the magnetic field B_z. An example of Ramsey sequence is given in fig. 5.4, where we see a clear oscillation of the orientation of the state as a function of time.

These Ramsey sequences turn out to be a very convenient tool for several types of calibrations. The absolute value of the magnetic field is indeed directly given by the frequency of the oscillation, and we can use this to calibrate the magnetic coils. We have already mentioned in chapter 1, section 1.4, that we can calibrate the magnetic coils using losses induced by dipolar relaxation. Here, the Ramsey oscillation gives a much more precise calibration, but only works at relatively low fields (experimentally, having $\pi/2$-pulses above $\sim 180\,\mathrm{mG}$ is challenging). Yet it allows, in principle, to measure the magnetic field down to the standard quantum limit (SQL). We will see in section 5.2 that we do have such a precision with Ramsey interferometry.

These Ramsey sequences furthermore provide data sets in which every spin component is populated. These data are useful to calibrate relative imaging efficiency between different Zeeman sublevels. An example of a picture with several spin components populated is given in fig. 5.4. The population Π_{m_J} in each of these components is extracted from the number of atom in each of the clouds. With these populations, we have access to every moment of the spin distribution. The average magnetization, for instance, is given by

$$m_z = \langle \hat{J}_z \rangle = \sum_{m_J} m_J \Pi_{m_J}. \tag{5.4}$$

In order to calibrate the imaging efficiency, we study the total measured atom number as a function of the average magnetization. This quantity is given in fig. 5.4 (below left).

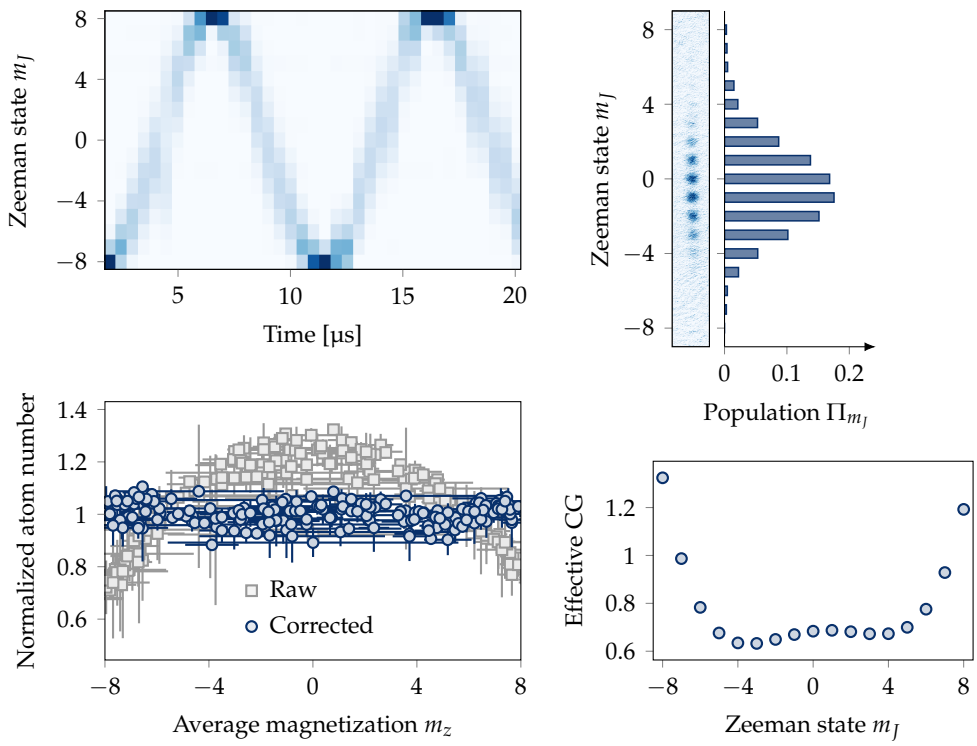

Figure 5.4 – Ramsey interferometry and imaging calibration. (Top left) Populations as a function of the precession time between the two $\pi/2$-pulses. (Top right) example of a SG picture. Each cloud is easily distinguishable, allowing to extract the population in each spin state. (Below left) Atom number as a function of the magnetization before (gray squares) and after (blue points) calibration of the effective Clebsch-Gordan (CG) coefficients. (Below right) Effective CG coefficients.

We assume here that the real total atom number, during the sequence, is conserved. We observe (see the gray data points) that the total measured atom number depends on the average magnetization, meaning that we do not detect all the spin states with the same efficiency. We use π-polarized light for the imaging, and the overall shape of the measured atom number is consistent with this choice ; we indeed see a symmetric shape, with roughly the same efficiency for $\pm m_J$, and lower efficiency on the large $|m_J|$ states, which is compatible with the fact that the Clebsch-Gordan coefficients (CG), for such a polarization, are higher for low $|m_J|$ than for large $|m_J|$. The presence of optical pumping during the imaging process[4], however, leads to complicated dynamics that prevents us from predicting a precise value of the effective CG coefficients.

The measured atom number in each m_J state is thus corrected by an effective coefficient $\mathrm{cg}(m_J)$, such that $N_{\mathrm{eff}}(m_J) = \mathrm{cg}(m_J) N_{\mathrm{meas}}(m_J)$. We obtain an effective total atom number and effective populations

$$N_{\mathrm{tot}} = \sum_{m_J} N_{\mathrm{eff}}(m_J) \qquad \text{and} \qquad \Pi_{m_J} = \frac{N_{\mathrm{eff}}(m_J)}{N_{\mathrm{tot}}}. \tag{5.5}$$

[4] A single imaging pulse typically lasts a few tens of µs, which roughly corresponds in total to about 50 absorption/emission cycles, in average, per atom.

The effective CG are obtained by minimizing the fluctuations of the total atom number, *i.e.* by minimizing the quantity $\Delta N_{\text{tot}}^2/\overline{N_{\text{tot}}}^2$, where here the mean value and the standard deviation is computed over the whole data set. The overall shape of $\text{cg}(m_J)$ is constrained to be symmetric. We empirically choose a polynomial shape of 4th degree, which reduces the number of free parameters and still gives acceptable results. We check that higher order polynomials do not significantly change the result of the minimization. The corrected number of atoms as a function of the magnetization is given by the blue points in fig. 5.4 (below left), and we see that the atom number is now independent of the magnetization, and the fluctuations are reduced. The value of the effective CG coefficients are given in fig. 5.4 as well (below right).

The Ramsey interferometry is also used to calibrate the coherence time of a classical state. Decoherence can have several sources. Inhomogeneous fields, for instance, would lead to a distribution of Larmor frequencies across the sample. Magnetic field fluctuations would lead to a broadening of the acquired phase. In our case, we find that we are limited by slow drifts of the magnetic field, causing shot-to-shot fluctuations.

The coherence of the classical state can be measured from the amplitude of the Ramsey oscillation as a function of time. We expect an oscillation signal of the form

$$m_z(t) = J_\perp(t)\cos(\Phi(t)), \tag{5.6}$$

where $J_\perp(t)$ decreases with time as a result of the decoherence. The amplitude of the oscillation is written as

$$J_\perp(t) = J\left\langle e^{i\delta\Phi(t)}\right\rangle, \tag{5.7}$$

with $\delta\Phi$ the phase fluctuations.

We assume here that the magnetic field does not fluctuate within a given experimental measurement – which typically lasts a few hundreds of µs – but rather changes from one run to the next (each run tyically lasts 20 s). As such, the phase fluctuation is proportional to the precession time, $\delta\Phi = g_J\mu_B\delta b t/\hbar$, where δb is the shot-to-shot field fluctuation. Using a gaussian ansatz for the noise, we obtain

$$J_\perp(t) = Je^{-t^2/2\sigma_t^2}, \tag{5.8}$$

where $\sigma_t = (g_J\mu_B\delta B_{\text{rms}}/\hbar)^{-1}$ accounts for the coherence time, and where δB_{rms} characterizes the magnetic field fluctuations[5].

We find experimentally that we can significantly increase the coherence time by taking into acount a measurement of the field fluctuations. A three-axis magnetic probe is installed on the experimental setup as close as possible to the atomic sample. For every run, we record the magnetic field measured by this probe. The Ramsey oscillation provides a calibration of the average magnetic field, or equivalently an average oscillation frequency. A correction proportional to the measured field fluctuation is furthermore applied on the phase acquired in each experimental run.

[5]These fluctuations were measured experimentally, and it was found that they are the strongest along the vertical direction, and substantially reduced overnight. We attribute them to metro lines passing below our building. We have thus installed an open-loop compensation which allows to roughly reduce the fluctuations by one order of magnitude, from several mG peak-peak to a few hundreds of µG. The fluctuations are furthermore reduced using a 50 Hz synchronization of the experimental sequence on the mains power line.

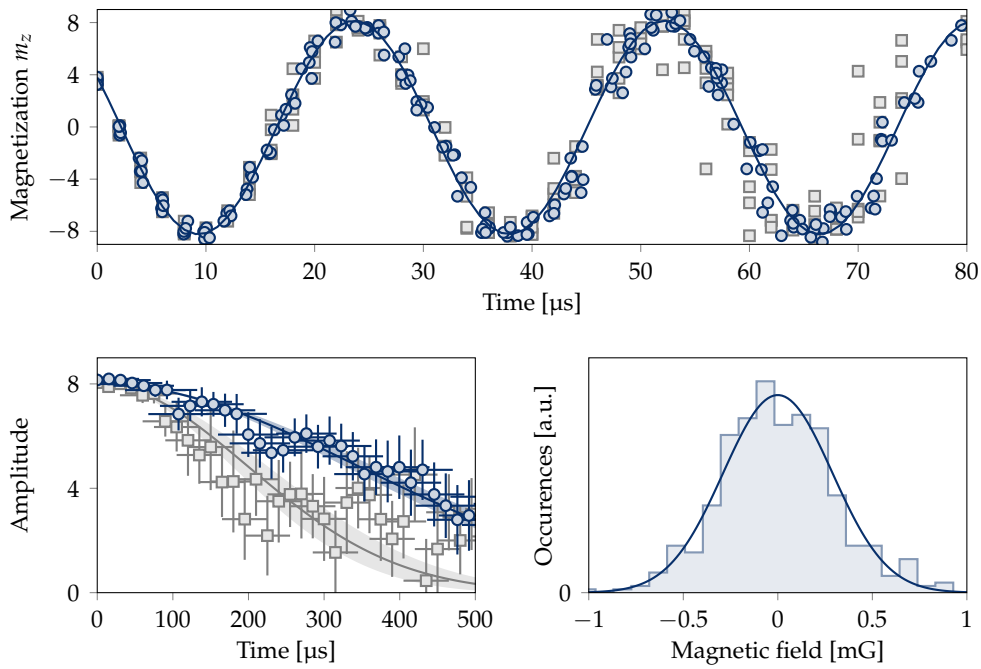

Figure 5.5 – Coherence of a classical state. (Top) Average magnetization oscillation obtained from a Ramsey sequence. The gray squares represent the raw data, while the blue points take into account the magnetic field fluctuations – equivalent to a shot-dependent rescaling of the time axis. (Below left) Coherence, measured from the mean amplitude of the Ramsey oscillation as a function of time. The blue data, which takes into account the correction, has an increased coherence time. (Below right) Measured field fluctuations along the z-axis from a magnetic probe. The distribution fits well a gaussian noise, with a standard deviation of $\delta B_{\text{rms}} = 0.29(3)$ mG.

Such a process is illustrated in fig. 5.5. The oscillation of the average magnetization is given in the top figure. The gray squares correspond to the measured magnetization prior to the correction. The blue points are obtained from the raw measurements by applying the correction mentioned above, and are much closer to the expected value, obtained from a sinusoidal fit over the first period.

As such, the effective coherence time is increased. In the bottom left panel of fig. 5.5, we show the coherence of the classical state as a function of time before (gray squares) and after (blue points) the correction. The coherence is obtained from the amplitude of the measured oscillation of magnetization. We are able to increase the coherence time from $\sigma_t = 200(20)$ µs to $\sigma_t = 340(20)$ µs.

It is worth noting here that we expect, according to the measurement of the field fluctuations, a coherence time of about 320 µs. The experimental value (before measurement) is lower than this expected value, and the discrepancy is attributed to the magnetic field fluctuations in the other directions, causing additional fluctuations of the orientation of the quantization field. After the correction, we manage to increase the coherence time above the expected value, but not by much. We believe we are limited by these orientation fluctuations, that we cannot correct on the data[6].

[6] A correction would be possible possible, in principle, if we had a good calibration of the amplitude of the

5.1.2 Implementation of OAT

The non-linear spin-dynamics are implemented using a laser beam tuned close to the intercombination line at 626 nm. The experimental setup that we use is illustrated in fig. 5.6.

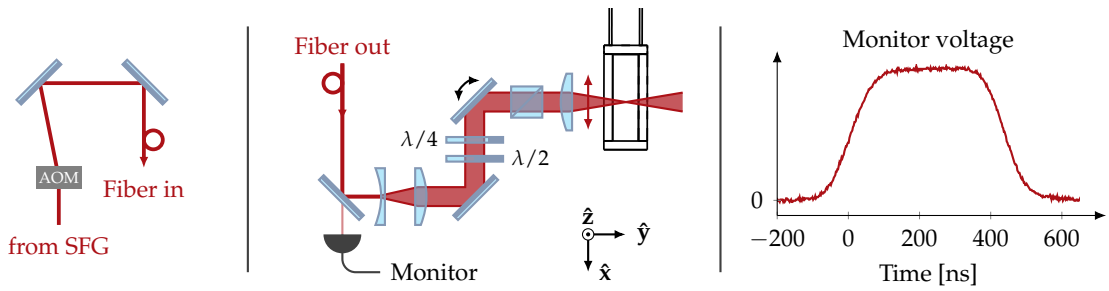

Figure 5.6 – One-axis twisting setup. (Left) The laser light, coming from the sum frequency generation setup (see appendix A), is coupled to a fiber after going through an AOM, which is used to control the intensity of light going through the fiber. (Middle) On the fiber output, the beam is shaped and sent to the atomic sample. A piezo mirror is used to finely tune the position of the beam. The last cube is placed to ensure linear and horizontal polarization on the atoms. The beam waist on the atoms is about 50 µm. The light intensity going through the fiber is monitored on a photodiode. (Right) Typical time trace of a light pulse.

We control both the interaction time and interaction intensity with an AOM, placed before a fiber in which the light is coupled. Such an AOM has a finite rising time (on the order of 100 ns). The beam is shaped to have an $1/e^2$ radius on the atoms of about 50 µm.

In these experiments, the detuning Δ to resonance is chosen to be negative. As such, the scalar part of the polarizability creates a trapping potential, that we use to align the laser beam on the atoms. Experimentally, it amounts to shining the laser beam on the atomic sample, holding it while releasing the dipole trap, and making sure the atoms that remain trapped in the 626 nm laser remain at their initial position. Note that the trapping dynamics, which occur on the ms scale, are irrelevant for the spin dynamics, which is several orders of magnitude faster, as explained below.

The detuning to resonance needs to be chosen carefully. In principle, we want the coupling to be as large as possible, in order to have a non-linear part of the Hamiltonian much larger than the Zeeman part. Large coupling strength are achieved by going closer to resonance. However, when tuning the laser close to resonance, the photon scattering rate becomes significant, and such an effect would greatly perturb the OAT dynamics. Experimentally, we choose the detuning to be $\Delta = -2\pi \times 1.5\,\text{GHz}$. Such a value is sufficiently close to achieve a coupling strength of about $\chi \approx 2\pi \times 3.5\,\text{MHz/W}$. Considering that we manage to send up to about 700 mW of laser light on the atoms, we expect that the OAT dynamics take place in a few hundreds of ns. Within these timescales, the probability to scatter a photon remains negligible[7].

field measured by the probe, as well as its fluctuations, with respect to the field at the position of the atoms. We then would be able to deduce both the orientation and the amplitude fluctuations, and apply further corrections. Such a calibration was not performed at that time.

[7] We roughly (over)-estimate the probability to have scattered a photon, after 100 ns, to be smaller than

The measured OAT dynamics is given in fig. 5.7. In these graphs, the x-axis scale is obtained from fitting the dynamics, from which we extract the coupling strength. Experimentally, we find that we are not limited by the finite rising time of the AOM, as long as we take it into account in the analysis[8].

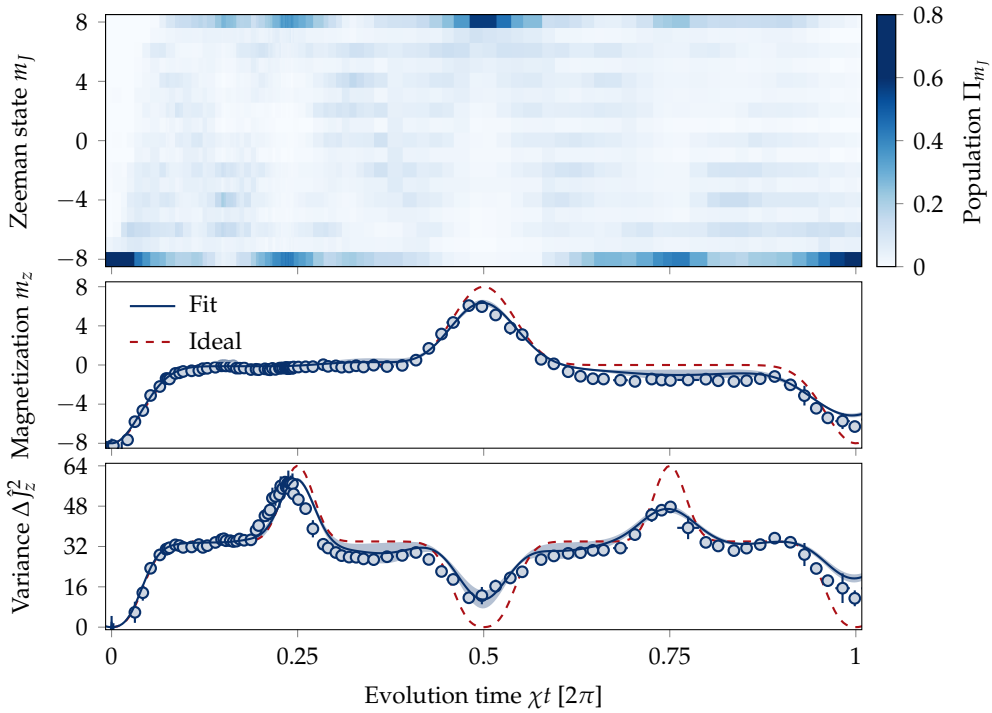

Figure 5.7 – Experimental realization of OAT. (Top) Populations in each Zeeman sublevel m_J as a function of the effective evolution time. We also give the first two moments of the distribution, namely the magnetization (middle) and the variance (bottom). In the bottom two panels, we also give the expected perfect evolution for the OAT Hamiltonian (dashed red), and the fitted evolution that takes into account experimental imperfections (solid blue).

The population dynamics in each of the Zeeman sublevels matches well the expected dynamics (see fig. 4.9 in the previous chapter). The apparent collapse that we already discussed theoretically is visible on the low order observables such as the magnetization and variance. We observe a relatively flat plateau of the magnetization before the first revival. A shorter plateau is also visible on the variance, before a N00N-state type revival.

In more detail, we observe that mostly the even m_J-states are populated, and we clearly see the expected N00N state at $\chi t = \pi/2$ and the spin inversion at $\chi t = \pi$. After one full period, we almost recover the initial state $|-J\rangle$. The spin inversion is most obvious on the average magnetization, which goes up to $m_z = 6.0(1)$, while the N00N state is indicated by the variance of the distribution, which peaks at $\Delta \hat{J}_z^2 = 57.1(2)$. Already with this measurement, we expect the metrological gain to be bounded by the Cramér-Rao bound. We recall that for a pure state, the quantum Fisher information is given by the

10^{-2} for each atom.

[8]What matters is the integrated interaction signal, which takes into account both the intensity and total time of the interaction. For each experimental run, we record the time trace as the one given in the right panel of fig. 5.6, and the integral of such a signal provides an effective time, which we use in the analysis.

variance of an operator – here $\hat{J}_z$ – which yields $G_{\max} = 14.3(1)$.

The fact that we do not measure exactly the expected evolution can be explained by some experimental imperfections. We have already mentioned, for instance, the presence of a small, yet non-negligible quantization field in the vertical direction. We thus fit the measured distribution with a model that takes into account this finite field, but also the presence of an angle mismatch between the light polarization and the quantization field, and the finite extent of the cloud, which leads to inhomogeneous broadening. The coupling strength χ is also a fit parameter. The resulting dynamics is given by the solid line in fig. 5.7, and matches relatively well the data. In particular, it explains the reduction in variance for the N00N state.

5.2 N00N state

From now on, we will focus solely on the N00N state that we produce. We just saw that the state we are able to prepare has a large variance $\Delta\hat{J}_z^2$, but not maximal, due to experimental imperfections. We explore in this section how this reduction of variance affects the metrological gain of the prepared state.

5.2.1 Extraction of the gain: parity and non-linear interferometry

As mentioned in the previous chapter, extracting a gain for the N00N state requires the measurement of non-linear observables, *e.g.* the parity of the state. Experimentally, we have access to such observables because we have single m_J-state detection. In other words, we are able to measure the average value of any of the projectors $\hat{\Pi}_{m_J} = |m_J\rangle\langle m_J|$ on the Zeeman states. Combined with the ability to perform arbitrary spin rotations, *i.e.* to measure these projectors along any axis, we have access to a large set of high order physical observables acting on the collective spin.

Parity oscillations

The N00N state that we prepare is oriented along the z-axis. We can measure its parity by measuring the population in all the m_J-states after a rotation of the state on the equator, with a $\pi/2$-pulse. The experimental procedure is illustrated in fig. 5.8.

Experimentally, we observe that the spin composition after the $\pi/2$-pulse strongly depends on the precession time, which corresponds to the delay between the state preparation and the measurement. More specifically, we see that the parity, defined as

$$p_z = \sum_{m_J} (-1)^{m_J} \Pi_{m_J}, \tag{5.9}$$

oscillates at $2J = 16$ times the Larmor frequency.

Such an increase of the frequency is expected from the non-classicality of the N00N state. The parity being an observable that allows, in principle, to measure phase shifts down to the Heisenberg limit, we do expect to see a $2J$-fold increase in sensitivity. This effect can also be intuitively appreciated by understanding the evolution undergone by the N00N state. After preparation, we have a state of the form (we discard the phase

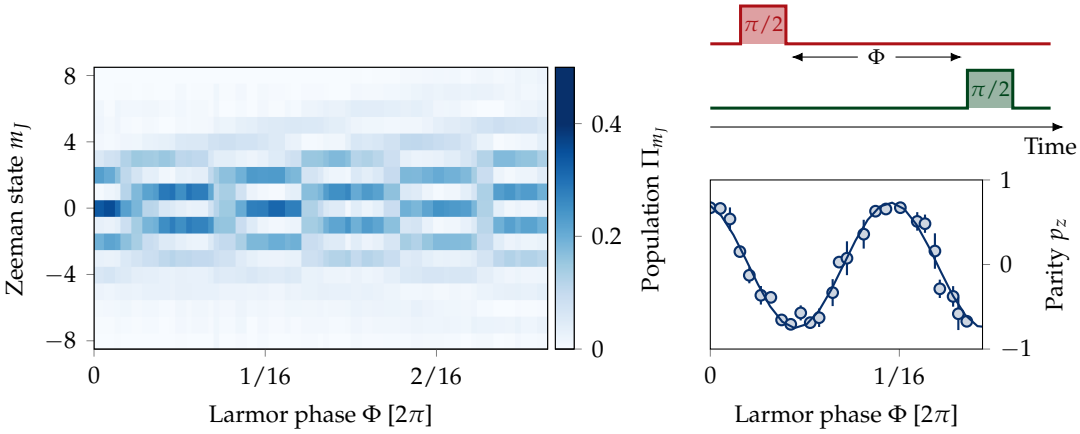

Figure 5.8 – Parity oscillation of a N00N state. (Left) evolution of the population as a function of the delay between the state preparation (red pulse) and the SG measurement along an arbitrary axis on the equator, performed using a $\pi/2$ rotation (green pulse). (Right) The parity is extracted from the populations, and oscillates at 16 times the Larmor frequency. The solid line is a sinusoidal fit.

factors here for simplicity)

$$|\mathrm{N00N}\rangle = \frac{|J\rangle + |-J\rangle}{\sqrt{2}}. \tag{5.10}$$

Once the non-linear interaction is off, the state still evolves in the external quantization field. In particular, after a precession time t, we have

$$|\mathrm{N00N}\rangle_\Phi = \frac{\mathrm{e}^{-\mathrm{i}J\Phi(t)}\,|J\rangle + \mathrm{e}^{\mathrm{i}J\Phi(t)}\,|-J\rangle}{\sqrt{2}}, \tag{5.11}$$

with $\Phi(t)$ the Larmor phase expressed by eq. (5.3). Each *lobe* of the N00N state thus acquires J times the Larmor phase, with opposite signs. Measuring the parity after the $\pi/2$-pulse amounts to a measurement of the phase difference between the two lobes, which oscillates $2J$ times faster than the classical Larmor nutation.

The imperfect preparation, however, leads to a reduction of the contrast C of the parity oscillation. When solely looking at such a quantity, we can define a metrological gain as $G \equiv 2JC^2$. The contrast is extracted from a sinusoidal fit, and the extracted gain reads $G = 8.8(4)$. Such a quantity remains far below the expected gain value $G_{\max} = 14.3(1)$, computed from the quantum Fisher information, and which also takes into account the preparation imperfection. Such a discrepancy suggests that the parity measurement itself is imperfect.

Non-linear Ramsey interferometry

Another possibility, for measuring a metrological gain, is to use a linear observable after a non-linear evolution. The idea, here, is to encode the phase acquired by the N00N state onto the magnetization, using a second $\pi/2$-pulse of non-linear coupling. This second pulse can be referred to as the *readout* pulse. The whole scheme will be called *non-linear Ramsey interferometry*, for it is similar to a Ramsey sequence such as the one

presented in fig. 5.4, replacing the linear $\pi/2$ rotations by non-linear pulses of light corresponding to $\chi t = \pi/2$ in the one-axis twisting evolution.

The sequence, illustrated in fig. 5.9, thus consists in two pulses of light separated by a precession time corresponding to a Larmor phase Φ. As we have just seen, the state after the precession time and before the second pulse is of the form given in eq. (5.11). The readout pulse then transfers the phases acquired by the N00N state to populations. Specifically, after the readout pulse, the final state takes the form

$$|\mathrm{N00N}\rangle_{\mathrm{f}} = \cos(J\Phi)\,|J\rangle + \sin(J\Phi)\,|-J\rangle\,, \tag{5.12}$$

which yields a magnetization $m_z(\Phi) = J\cos(2J\Phi)$. Results of such an experiment are given in fig. 5.9.

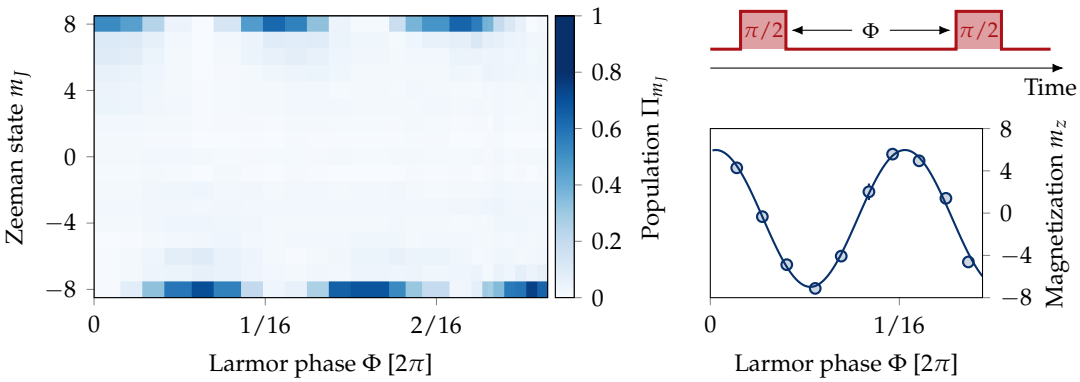

Figure 5.9 – Non linear Ramsey interferometry. (Left) Populations in the m_J states following a non-linear readout of the N00N state. The pulse sequence is indicated above the right panel. (Right) Measured magnetization as a function of the acquired Larmor phase Φ.

As expected from eq. (5.12), we observe that the atoms mostly populate the extremal states $|\pm J\rangle$, with small population of the intermediate Zeeman states. The average magnetization oscillates at 16 times the Larmor frequency. In a similar manner as what was done for the parity, we extract a metrological gain from the contrast of the oscillation. In this non-linear detection scheme, the contrast is a bit higher than for the parity oscillation, essentially because the information is localized on two states: their measurement is thus less sensitive to detection noise than for the parity, for which many states are populated. Yet, the metrological gain of such a measurement is $G = 2JC^2 = 11.2(13)$, which remains a bit below the expected value.

5.2.2 Gain from statistical distance

The gain we have extracted above comes from the measurement of average quantities. In the first case, we use the average parity, while the magnetization is used in the non-linear Ramsey scheme. Such measurements discard some of the information provided by the SG pictures, which give the evolution of all the populations in each of the Zeeman states.

In order to grasp all this information, we compute the Hellinger distance, which we

have already introduced in the previous chapter (see eq. (4.30)), and which basically quantifies how two probability distributions are different using all the available information. In our specific case, it is computed using the population distributions, as

$$d_{\mathrm{H}}^2(\Phi_0, \Phi) = \frac{1}{2} \sum_{m_J} \left[\sqrt{\Pi_{m_J}(\Phi_0)} - \sqrt{\Pi_{m_J}(\Phi)} \right]^2 . \tag{5.13}$$

Here $\Pi_{m_J}(\Phi)$ corresponds to the population in state m_J after a precession time corresponding to the Larmor phase Φ. We give the Hellinger distance for the two previous measurement schemes in fig. 5.10.

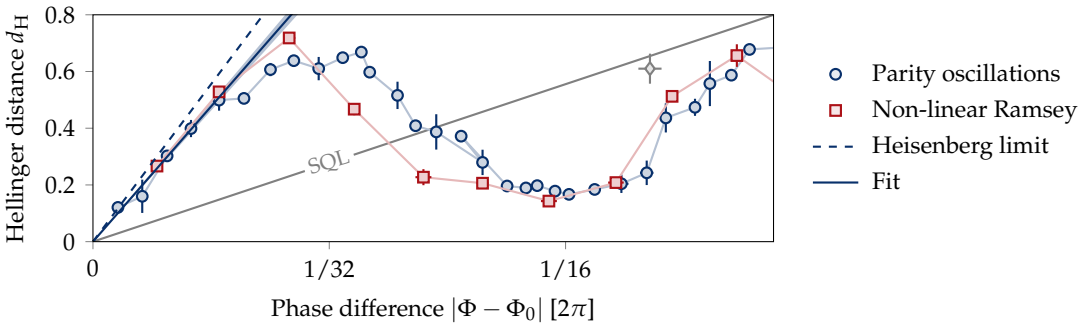

Figure 5.10 – Hellinger distance for metrological gain. Hellinger distance, computed using eq. (5.13) and for the two experiments described in section 5.2.1. The blue points correspond to the parity measurement, while the red squares correspond to the non-linear Ramsey scheme. The solid blue line is a linear fit for data at low $|\Phi - \Phi_0|$, while the dashed line corresponds to the HL. We also give, for comparison, the SQL. The single gray diamond corresponds to the Hellinger distance computed from the standard Ramsey scheme, corresponding to the data of fig. 5.4, and which is compatible with the SQL.

The metrological gain is extracted from the statistical velocity, corresponding to the change of the Hellinger distance upon a small variation of the phase. We perform a linear fit to the Hellinger distance for low values of $|\Phi - \Phi_0|$. Using the relation (see section 4.2.4 in chapter 4)

$$G \equiv \frac{8}{2J} v_{\mathrm{H}}^2 \qquad \text{with} \qquad v_{\mathrm{H}} = \left. \frac{\partial d_{\mathrm{H}}}{\partial \Phi} \right|_{\Phi=\Phi_0} , \tag{5.14}$$

we find a gain $G = 13.7(4)$. Such a value is notably larger than the gain extracted from the contrast of the oscillations, precisely because all the information we have is being used, and not solely the average value of a specific observable. This gain is furthermore much closer – compared to the contrast measurements – to the expected maximum gain $G_{\max} = 14.3(1)$, computed from the measured variance of the N00N state.

5.3 Tomography and decoherence

The non-classical nature of the generated state is revealed by the gain measurement in an unambiguous way. We can still take a step further and completely reconstruct the state's density matrix, and its Wigner distribution. In this section, we also discuss the

decoherence of the N00N state, and we will see that its enhanced sensitivity also leads to shorter coherence times.

5.3.1 Reconstruction of the density matrix

The full state density matrix, hereafter denoted $\hat{\rho}$, is reconstructed from a data set that consists in many measurements of the N00N state along the z-axis – which provides the populations on the diagonal of the density matrix – and on the (xy) plane – providing the off-diagonal coefficients. The measurement along an arbitrary axis on the equator is realized using same scheme as for measuring the parity (see fig. 5.8): the precise orientation (the phase φ) is reached by choosing the appropriate precession time between the preparation and the measurement.

The density matrix is constituted of $(2J+1)^2 - 1 = 288$ real coefficients. These coefficients are fitted to the whole data set, constituted of measurements along about 100 different axes, each of them giving 17 populations. The result of such a fit is given in fig. 5.11.

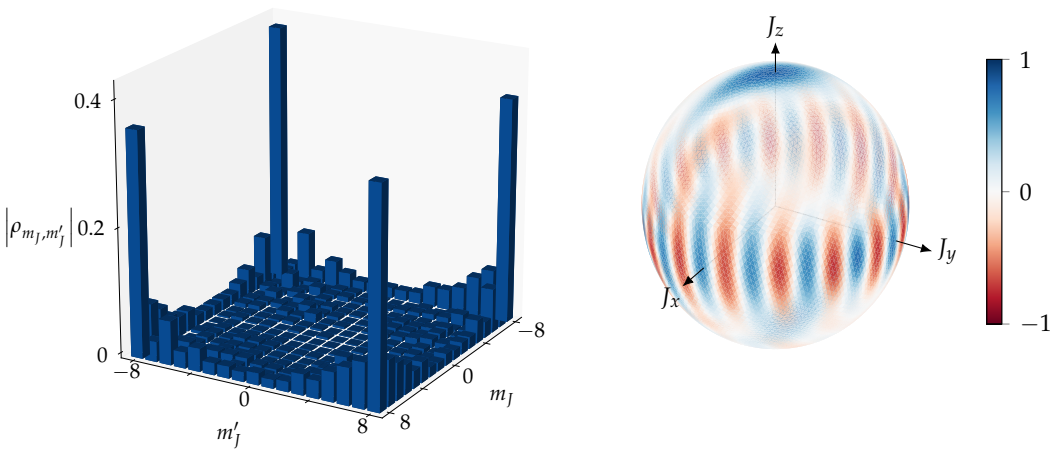

Figure 5.11 – Tomography of the N00N state. (Left) absolute value of the density matrix, reconstructed from a fit to the population measured along the z-axis and on the equatorial plane. (Right) Corresponding Wigner distribution. The colorscale is normalized to the maximum possible value of the Wigner function of a N00N state.

The reconstructed density matrix shows high non-classical coherences, expected from a N00N state. To be specific, we clearly see high populations $\rho_{J,J}$ and $\rho_{-J,-J}$, expected from the SG measurements along the z-axis, and we also see strong off-diagonal coherences $\rho_{J,-J}$ and $\rho_{-J,J}$. The ratio between the coherences and the populations, $2\,|\rho_{J,-J}|\,/\,(\rho_{J,J} + \rho_{-J,-J}) = 0.92(8)$, is close to unity, as expected from a N00N state. The value of this ratio is furthermore consistent with the metrological gain that we have measured from the Hellinger distance.

The Wigner distribution of the state is also computed from the density matrix reconstruction, and is given in fig. 5.11. The reconstructed distribution has all the features of

a N00N state: we see strong and positive regions on the poles $\theta = 0$ and $\theta = \pi$, and we clearly see the oscillatory behavior along the equator, with strong negative regions.

5.3.2 Decoherence

The reconstruction presented above is performed using data taken a few µs after the N00N state preparation, in order to map $0 \leq \varphi \leq \pi$. We find experimentally that the reconstructed density matrix depends on the waiting time between the preparation and the measurement. In particular, we observe a decrease of the coherences (the off-diagonal coefficients), while the populations (on the diagonal) remain approximately unchanged. Such a decrease is symptomatic of a decoherence process, that we characterize below.

We give in fig. 5.12 the reconstructed density matrix realized after about 70 µs of precession time. As we can see, the coherences are greatly reduced. The Wigner distribution reconstructed from this density matrix is also a witness of such a decoherence. While the two lobes at $\theta = 0, \pi$ are still present, reminiscent of the surviving populations on the diagonal, the oscillatory pattern on the equator has faded away, as a consequence of the vanishing coherences. As such, the reconstructed density matrix corresponds to an incoherent mixture of $|J\rangle$ and $|-J\rangle$.

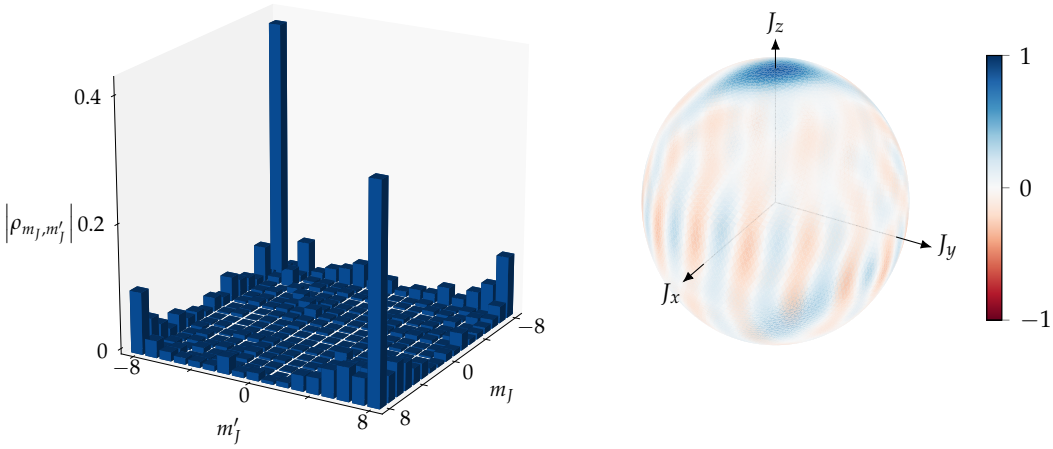

Figure 5.12 – Tomography of a dephased N00N state. Reconstruction of the density matrix identical to the one presented in fig. 5.11 but after a waiting time of 70 µs. The coherences are much lower, yielding to a vanishing pattern on the equatorial plane of the Wigner distribution.

In order to characterize such a decoherence, we record the evolution of magnetization resulting from a non-linear Ramsey interferometry, such as the one presented in fig. 5.9. The evolution of the contrast of the oscillation is extracted from a local sinusoidal fit, with a fixed frequency set to 16 times the Larmor frequency, and measured using the first few µs of evolution. The results are given in fig. 5.13.

The observed decoherence is consistent with the same ansatz we have used to characterize the decoherence of a classical state (see fig. 5.5). In the data we use here, the magnetic field fluctuations are also taken into account and corrected to increase the coherence time.

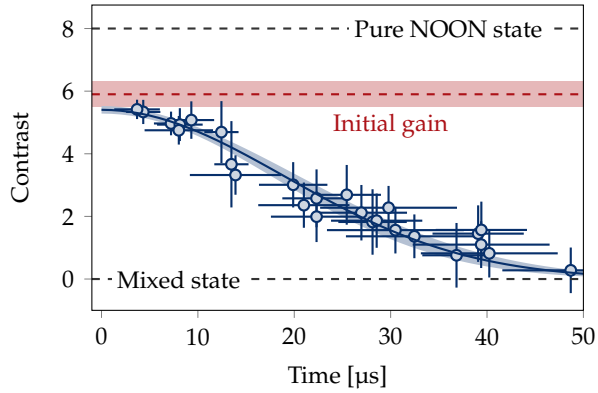

Figure 5.13 – Decoherence of the N00N state. The amplitude of a non-linear Ramsey interferometry (see fig. 5.9) is measured as a function of time. A pure N00N state would yield a constant amplitude of $J = 8$, while a mixed state corresponds to vanishing oscillations. A gaussian fit yields a coherence time $\sigma_t = 19(1)$ µs. The red dashed line indicate the measured contrast at very short times from fig. 5.9, and equivalent to a gain measurement.

We measure a coherence time, after correction, of $\sigma_t = 19(1)$ µs.

The measured ratio between the classical decoherence time and the N00N state decoherence time, $\sigma_t^{\text{cl.}}/\sigma_t^{\text{N00N}} = 18(2)$, is consistent with the underlying hypothesis on the nature of the decoherence. Indeed, by assuming an absence of fluctuations during the evolution, we directly have $\langle e^{i\delta\Phi(2Jt)}\rangle = \langle e^{i2J\delta\Phi(t)}\rangle$. In other words, the loss of coherence of a classical state at a time $2Jt$ is equivalent to the loss of coherence of a N00N state at a time t. It is thus expected to have a coherence time decreased by a factor $2J = 16$ in the case of a N00N state, because it is 16 times more sensitive to the magnetic field – and hence to its fluctuations.

5.4 Outlook

In this chapter, we have shown that our experimental setup allows for coherent manipulations of the large spin of dysprosium atoms. In particular, we have seen that we can use the tensor light-shift, created by an off-resonant laser beam, to implement the one-axis twisting (OAT) Hamiltonian. The chapter was entirely dedicated to the study of the N00N state that can be produced using OAT. Such a non-classical state allows to go beyond the SQL, reached for coherent states, and to have a quantum-enhanced sensitivity close to the Heisenberg limit. Such an enhancement has been measured on the N00N state that we prepare, thanks to the single Zeeman sublevel resolution granted by the Stern-Gerlach imaging.

The arbitrary rotations that we can apply on the spins furthermore permits the reconstruction of the density matrix of the prepared state, and its Wigner distribution. In particular, we have seen clear signatures of non-classicality, such as the presence of large off-diagonal coefficients in the density matrix, or strong negative regions of the Wigner distribution. Moreover, we have observed that the non-classicality is rapidly lost (compared to a coherent state), due to magnetic field fluctuations that induce decoherence. The

nature of the decoherence is relatively well understood, both for a classical state and for the N00N state.

As an outlook, we discuss other possibilities granted by the implemented OAT Hamiltonian. These possibilities have been studied in our group, but lie beyond the scope of this thesis. We only give here a quick glimpse of these studies.

5.4.1 Squeezing and oversqueezing

We introduced in chapter 4 the notion of spin squeezing, and we showed the OAT Hamiltonian does generate squeezing in a collective spin. Squeezing was explored experimentally, by studying the short time dynamics of the OAT. In particular, we were able to measure a metrological gain *via* Ramsey interferometry, using the usual definition of the gain, *i.e.* using linear observables: the average magnetization and variance of the distribution (see fig. 5.14).

Yet, as expected from the OAT dynamics described in chapter 4, we expect that such a metrological gain, equivalent to the squeezing parameter, vanishes after a typical timescale $\chi t = 1/\sqrt{2J}$. This decrease is due to the fact that the state becomes non-gaussian – or *oversqueezed*. Such states remain non-classical nonetheless, and in particular their quantum Fisher information should yield a higher metrological gain than the one given by the squeezing parameter. We were able to measure the optimal gain, *i.e.* reach the Cramér-Rao bound, by computing the Hellinger distance, in a similar manner than the gain we measured for the N00N state. Experimentally, we measured a gain $G = 8.6(6)$ after a time $\chi t \approx 1.2/\sqrt{2J}$, *i.e.* we can reach a relatively large gain (more than half of the N00N state) in a short time (less than one fifth of the time needed for the N00N state). It is important to point out here that the optimal gain was measured thanks to our single Zeeman sublevel resolution. We were furthermore able to reconstruct the Wigner distributions of a squeezed and oversqueezed state. These results were published in [Evrard et al. 2019].

5.4.2 Ground state of the OAT: exploring a quantum phase transition

As a closing paragraph, we briefly discuss the study of a quantum phase transition, occurring in the so-called Lipkin-Meshkov-Glick model (LMG). This model consists of N spin-1/2 with infinite range Ising interactions in a transverse field. In the collective spin representation with $J = N/2$, such a model is governed by a Hamiltonian

$$\hat{H} = -\frac{\hbar\lambda}{2J-1}\hat{J}_x^2 + \hbar\omega_z\hat{J}_z, \tag{5.15}$$

where λ gives the interaction strength between two spins. This Hamiltonian corresponds exactly to the OAT Hamiltonian, with the correspondence $\lambda = (2J-1)\chi$. Note that here, the sign of the interaction – tuned by the sign of the detuning to resonance – is important, and is set to be negative.

We studied the ground state of this Hamiltonian as a function of the interaction strength λ (see fig. 5.15). At $\lambda = 0$, the ground state is paramagnetic, with all the spins oriented along the transverse field in a coherent state. With increasing λ, pair correlations build up between individual constituents. When the interaction strength is comparable to the transverse field, a ferromagnetic phase transition occurs, and the ground state becomes

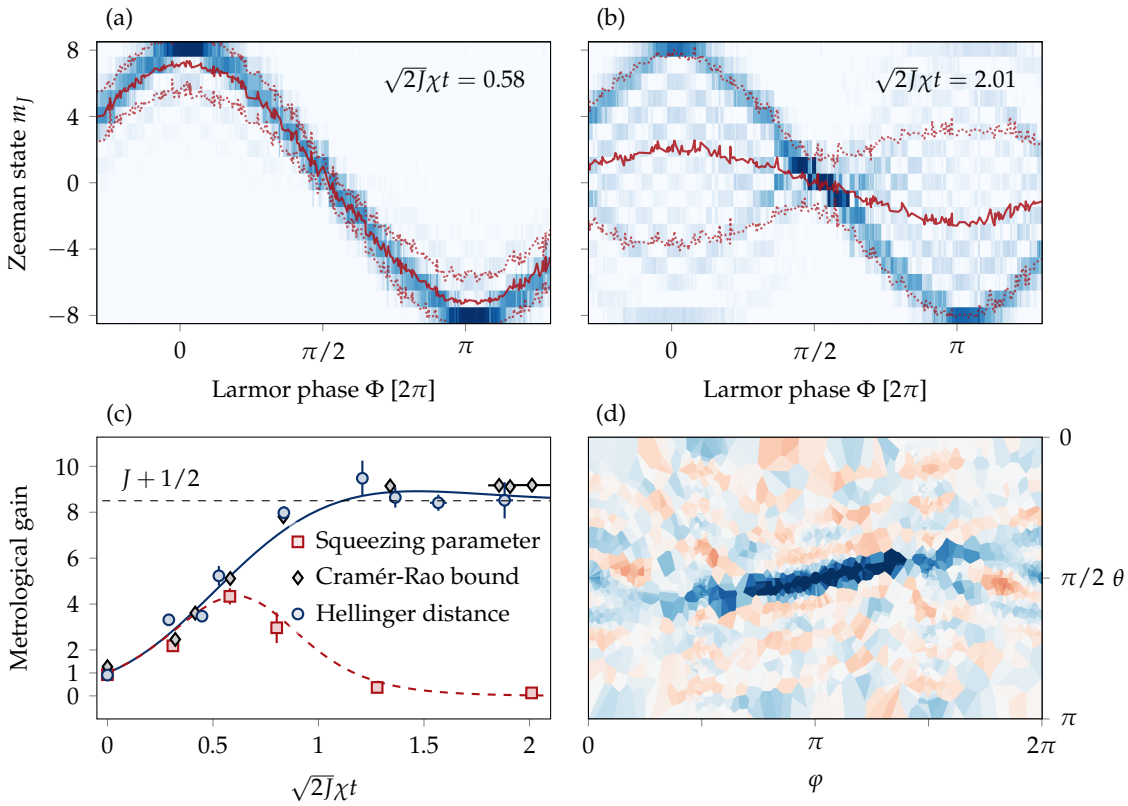

Figure 5.14 – Squeezing and oversqueezing. (a) Ramsey interferometry of a squeezed state and (b) of an oversqueezed state. In both cases, the solid red line is the average magnetization m_z, while the dotted lines give $m_z \pm \Delta\hat{J}_z$. In the squeezed case, the formula $\Delta\Phi = \Delta\hat{J}_z / |\partial_\Phi m_z|$ still provides a metrological gain above the SQL (if one measures at $\Phi = \pi/2$), because the variance is reduced and the slope remains high. In the oversqueezed case, the high variance and reduced slope yields a vanishing metrological gain. (c) Metrological gain extracted from the squeezing parameter (red squares), and the Hellinger distance (blue dots). The black diamonds represent the Cramér-Rao bound, calculated from the maximum variance of the prepared state. Solid lines are theoretical predictions. (d) Reconstructed Wigner distribution of the oversqueezed state (after rotation to the equator). The negative regions indicate non-classicality, while the fast-oscillating patterns between positive and negative values indicate quantum-enhanced sensitivity.

doubly degenerate. In principle, when $\lambda \to \infty$, the ground state is a N00N-like state. The phase transition was studied in this system, and particularly the link between the onset of an order parameter – the spin pair correlation – and the breaking of symmetry – here the parity.

The LMG Hamiltonian (5.15) conserves parity, associated to its $\mathbb{Z}_2$ symmetry. In the paramagnetic regime, symmetry is protected by the *parity gap*, which separates the even and odd sectors of the eigenstates. In the ferromagnetic regime and in the thermodynamic limit, the parity gap closes as the ground state becomes degenerate. As such, the underlying symmetry can be spontaneously broken, *e.g.* by external fluctuations.

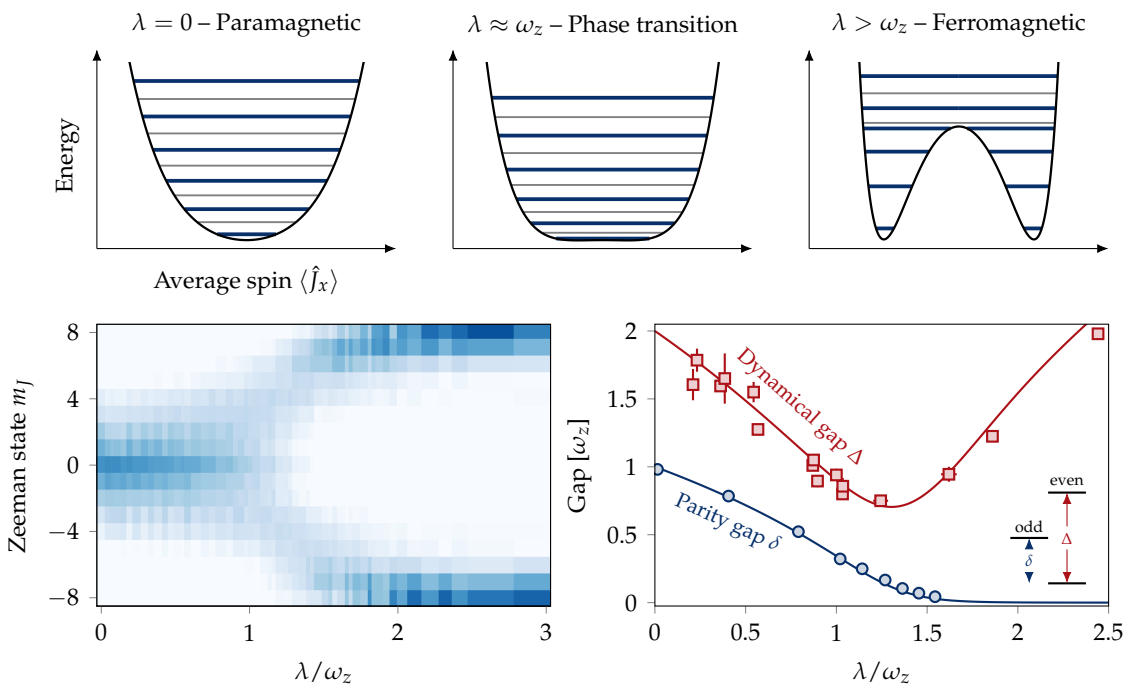

Figure 5.15 – Quantum phase transition in the LMG model. (Top) The LMG model can be understood by drawing effective potential landscapes for the average spin $\langle \hat{J}_x \rangle$. In the paramagnetic regime, the effective potential is quadratic around $\langle \hat{J}_x \rangle = 0$. At the phase transition $\lambda \approx \omega_z$, the potential becomes quartic, and in the ferromagnetic regime it becomes a double-well potential. (Bottom left) Measured spin composition in the x-direction as a function of the interaction strength. (Bottom right) Energy gap measurements across the transition. In the ferromagnetic regime, the parity gap closes as the ground state becomes degenerate (each well can be populated).

Experimentally, we measured the ground state spin composition as a function of the interaction λ (see fig. 5.15). Starting from the ground state $|-J\rangle$ along the z-axis, we observe a bifurcation towards a double-peak distribution, characteristic of a phase transition. We are thus able to adiabatically prepare non-classical states such as the N00N states described in this chapter. The energy gaps are also probed, and we check that the parity gap, which separates the odd and even sectors of the Hamiltonian, vanishes in the ferromagnetic regime. These results were published in [Makhalov et al. 2019].

III

Synthetic Landau levels

6 Quantum Hall effect in synthetic dimensions: elements of theory

6.1 Classical and quantum Hall effects 102
6.1.1 Classical Hall effect 102
6.1.2 Quantum Hall effect 103
6.1.3 The role of topology 108
6.2 SOC, artificial gauge fields and synthetic dimensions 111
6.2.1 Spin-orbit coupling in ultracold atoms 112
6.2.2 Synthetic dimensions 113
6.3 Implementation with dysprosium 114
6.3.1 Raman transitions 114
6.3.2 Quantum Hall effect with synthetic dimensions 117
6.4 Synthetic Landau levels 121
6.4.1 Energy spectrum 122
6.4.2 Lowest energy band 125
6.4.3 Conclusion 128

THE LAST PART of this thesis is dedicated to experiments that use the large spin of dysprosium as a *synthetic dimension*, together with a real dimension of space to form an effective two-dimensional system. In this chapter, we focus on the theoretical background that motivates such considerations, by introducing the relevant concepts, and by detailing the experimental implementation. We do not give any experimental result in this chapter, all of them being presented in the one that follows.

The experiment that we realize consists in implementing an analogue of the Landau Hamiltonian – which describes the two-dimensional dynamics of a charged particle in a constant external transverse magnetic field – encoding one of the two spatial dimensions in the spin of the atoms. We start with a discussion on the classical and quantum Hall effects, introducing concepts and properties that we will compare to our system and that will help us give meaning to the observables that we have. In particular, we discuss the notions of anomalous velocity, chiral edge modes, and topology, which are key features of Hall systems and that we also observe in our system.

We then quickly describe the concept of laser-induced spin-orbit coupling, and its realization in an ultracold atom experiment. This effect is the essential ingredient for our

physical implementation, that we describe in full detail. The implementation, and the analogy with *standard* quantum Hall systems, is made in section 6.3. In particular, we give a semi-classical description of our system, allowing to give more physical insight on the correspondence between real and synthetic dimensions.

Finally, section 6.4 is dedicated to the quantum study of the system we implement. The energy spectrum is presented, and we focus on the properties of the ground dispersion band, which we will also refer to as the lowest Landau level.

6.1 Classical and quantum Hall effects

Hall physics essentially covers the physics of 2D electrons in a perpendicular magnetic field. In this section, we give a quick review on the classical and quantum Hall effects. Special attention is given to the emergence of Landau levels and to the non-trivial topology of such systems, and their role in the quantization of the Hall conductance. We do not aim at giving a comprehensive description of the Hall physics, but rather a taste of the richness of the subject. More details can be found in review articles [Dalibard et al. 2011; Qi et al. 2011; Cooper et al. 2019; Ozawa et al. 2019] or lectures [Dalibard 2014; Tong 2016; Dalibard 2018], from which this section is greatly inspired.

6.1.1 Classical Hall effect

The system we consider here is an electron, of mass m and of charge $-e$ (where e is the elementary charge), constrained to move in the (x, y) plane, while a uniform and perpendicular magnetic field $\mathbf{B} = B\hat{\mathbf{z}}$ is applied. We also add a force $\mathbf{F} = F\hat{\mathbf{y}}$ in the y direction, *e.g.* by applying a uniform electric field $\mathbf{E}$. Its classical trajectory can be deduced from integrating the equations of motion, $m\dot{\mathbf{v}} = -e\mathbf{v} \times \mathbf{B} + \mathbf{F}$, yielding

$$\begin{cases} x(t) = x_0 - R\cos(\omega_c t + \phi) - Ft/eB \\ y(t) = y_0 - R\sin(\omega_c t + \phi), \end{cases} \tag{6.1}$$

where $\omega_c = eB/m$ is the cyclotron angular frequency. The center (x_0, y_0), the radius R and the phase ϕ can take any value. Examples of trajectories are illustrated in fig. 6.1.

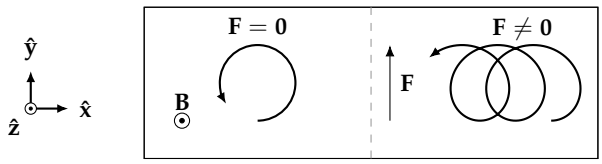

Figure 6.1 – Classical Hall effect. We illustrate here the classical trajectories of an electron (negatively charged) confined in the (x, y) plane, subjected to a magnetic field $\mathbf{B}$ in the transverse direction. In the absence of an additional force (left), the trajectories are cyclotron orbits. When applying a force $\mathbf{F} = F\hat{\mathbf{y}}$, with here $F > 0$, the trajectories drift in the x direction, orthogonal to the direction of the force.

One sees that, although the force $\mathbf{F}$ accelerates the particle in the y direction in the absence of a magnetic field, the presence of $\mathbf{B}$ yields a position drift in the transverse (x)

direction, with a drift velocity $\mathbf{v}_{\text{drift}} = (\mathbf{F} \times \mathbf{B})/(-eB^2)$. This phenomenon is what defines the classical Hall effect. The motion of the electrons in the transverse direction generates a current I_{H}, often referred as the *Hall current* when the force F comes from an electric field. The transverse response of the system, called the *Hall mobility*, characterizes the acquired transverse average velocity upon the application of the force. Here, it is expressed as

$$\mu_{xy} = \frac{\partial \langle \dot{x} \rangle}{\partial F_y} \quad ; \quad \mu_{xy}^{\text{Bulk}} = -\frac{1}{eB}. \tag{6.2}$$

The bulk value of the mobility is explicitly given in eq. (6.2), in the case of a uniform force F. In general though, the mobility depends on local properties of the system – such as disorder – and is thus perturbed in the presence of edges.

Edge effects

The edges of the sample can be modeled as a hard wall potential. Classically, when a cyclotron orbits gets close to the edge, the trajectory will *rebound* on it, resulting in so-called *skipping orbits*. We give in fig. 6.2 the computed trajectories, in the absence of a force, of electrons across a finite size sample.

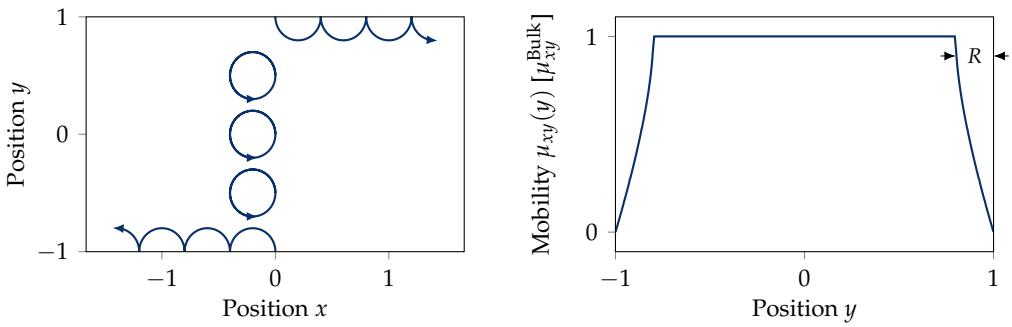

Figure 6.2 – Skipping orbits. (Left) Trajectories of electrons in the presence of edges, with $\mathbf{F} = \mathbf{0}$. Here, the initial velocity is chosen to be along $+y$, with a modulus such that the cyclotron radius is $R = 0.1L_y$, with L_y the size of the system in the y direction. The closed orbits of the bulk become skipping orbits on the edges. (Right) Local mobility as a function of the average position of the orbit. Close to the edge, *i.e.* within the orbit radius, the mobility is reduced.

As one can see, the presence of edges affects both the orbits and the local mobility, that we also give in fig. 6.2. The local mobility is computed with eq. (6.2) for different trajectories across the sample, and for a fixed radius $R = 0.1L_y$. As we can see, in the bulk, the mobility is flat and equal to $\mu_{xy}^{\text{Bulk}} = -1/eB$. Close to the edges, the mobility is reduced. When the average position of the orbit is precisely on the edge, *i.e.* for grazing orbits, the mobility vanishes. It is important to notice that for such orbits, an edge current is still present. The vanishing mobility reflects the fact that the orbit is not affected by the external force anymore.

6.1.2 Quantum Hall effect

Quantum effects arise when the typical trajectories of the electrons reach a scale at which Heisenberg's inequalities have a non-negligible role. Starting from $\Delta x \Delta p \approx \hbar$, and

using $\Delta x \approx R$ and $\Delta p \approx mR\omega_c$, one finds that a quantum description of the problem becomes necessary when the orbit size is of the order of the magnetic length

$$\ell = \sqrt{\frac{\hbar}{eB}}. \tag{6.3}$$

In conventional condensed matter samples, for magnetic fields on the order of teslas, one finds magnetic lengths of a few tens of nm and cyclotron frequencies of a few tens of GHz.

The quantization of the Hall effect is done by considering the Hamiltonian of an electron in an external magnetic field, obtained by substituting the momentum of the electron by its gauge-invariant form in the free-particle Hamiltonian,

$$\hat{H} = \frac{(\hat{\mathbf{p}} + e\mathbf{A}(\hat{\mathbf{r}}))^2}{2m}. \tag{6.4}$$

In this expression, $\mathbf{A}$ is the vector potential giving the magnetic field $\mathbf{B} = \boldsymbol{\nabla} \times \mathbf{A}(\hat{\mathbf{r}})$, such that the *kinetic momentum*, $m\hat{\mathbf{v}} = \hat{\boldsymbol{\pi}} = \hat{\mathbf{p}} + e\mathbf{A}(\hat{\mathbf{r}})$, where $\hat{\mathbf{v}}$ is the electron's velocity, is gauge invariant. There are several possible ways to diagonalize eq. (6.4), as many as there are gauge choices for the vector potential $\mathbf{A}$. In the end, all ways lead to the same spectrum, the so-called *Landau levels*.

Landau Levels

The spectrum of the Landau Hamiltonian can be computed without any gauge choice. For this, we compute the commutator between the kinetic momentum components to find[1] $[\hat{\pi}_x, \hat{\pi}_y] = -\mathrm{i}\hbar eB$. As such, we realize that the Hamiltonian (6.4) is essentially the same as the Hamiltonian of an harmonic oscillator. More specifically, it can be recast in

$$\hat{H} = \frac{\hat{\pi}_x^2 + \hat{\pi}_y^2}{2m} = \hbar\omega_c \left(\hat{a}^\dagger \hat{a} + \frac{1}{2}\right), \quad \text{with} \quad \hat{a}^\dagger = \frac{1}{\sqrt{2\hbar m\omega_c}}(\hat{\pi}_x + \mathrm{i}\hat{\pi}_y). \tag{6.5}$$

The energy levels are thus given by $E_n = \hbar\omega_c(n + 1/2)$, with n an integer. Those are the Landau levels: equally spaced energy levels, with a gap $E_{n+1} - E_n = \hbar\omega_c$ equal to the cyclotron frequency (see fig. 6.3(a)).

Landau gauge

The above description, while straight-forward, does not give any information on the structure of the particle wavefunction. However, one can still sense one of the key properties of the Landau levels: by reducing the two-dimensional Hamiltonian (6.4) to a one-dimensional harmonic oscillator, one degree of freedom is left aside, and we understand that each energy level must be macroscopically degenerate. This degeneracy can be understood classically by the fact that the center of the orbits can be chosen arbitrarily. As such, we expect the degeneracy to scale as the surface of the plane in which the electrons are moving.

In the following, we will work in the Landau gauge, which breaks translational invariance and favors one direction with respect to another. This choice, as we will see, is

[1] Using $[\hat{\mathbf{p}}, f(\hat{\mathbf{x}})] = -\mathrm{i}\hbar\boldsymbol{\nabla} f(\hat{\mathbf{x}})$.

convenient for a stripe geometry, which will be relevant when considering the physical implementation we realize with dysprosium atoms.

In the Landau gauge, the vector potential is written $\mathbf{A}(\hat{\mathbf{r}}) = -\hat{y}B\hat{\mathbf{x}}$, and the Hamiltonian (6.4) is recast in

$$\hat{H} = \frac{(\hat{p}_x - e\hat{y}B)^2}{2m} + \frac{\hat{p}_y^2}{2m}. \tag{6.6}$$

Translational invariance is still present in the x direction, which means that the eigenfunctions can be chosen in the form of a plane wave along x: $\psi_k(x,y) = \mathrm{e}^{\mathrm{i}kx}\varphi_k(y)$. Using this ansatz in eq. (6.6), one finds that the Hamiltonian acting on $\varphi_k(y)$ reduces to the one of a harmonic oscillator, centered around $y_k = k\ell^2$. In particular, the wavefunctions are given by the Hermite polynomials, and the ground state wavefunction, corresponding to the lowest Landau level (LLL), reads

$$\psi_{0,k}(x,y) \propto \mathrm{e}^{\mathrm{i}kx} \exp\left[-\frac{(y-y_k)^2}{2\ell^2}\right]. \tag{6.7}$$

Degeneracy

The degeneracy of each level is now more apparent. Indeed, while the energy levels only depend on a single quantum number n, which corresponds to the index of the Hermite polynomial, the wavefunctions have an additional degree of freedom granted by the wavenumber k. The degeneracy of each level then essentially corresponds to the number of values of k allowed in the system.

In order to compute this number, we consider a sample of size $L_x \times L_y$, with periodic boundary conditions in the x direction, giving a quantization of k in units of $2\pi/L_x$. In the y direction, the states are localized around $y_k = k\ell^2$, and the condition $0 \leq y \leq L_y$ becomes $k \leq L_y/\ell^2$. As such, the degeneracy of each level is given by

$$\mathcal{D} = \frac{L_y L_x}{2\pi\ell^2} = \frac{eBS}{2\pi\hbar} = \frac{SB}{\Phi_0}, \tag{6.8}$$

with S the surface of the sample, and $\Phi_0 = 2\pi\hbar/e$ the quantum of flux. The degeneracy of each Landau level can be very large: it corresponds to the ratio between the sample area and the area formed by an orbit of size given by the magnetic length, or in other words the number of flux quanta through the sample.

Hall conductance

The Hall conductivity quantifies the electron transport response to the application of an electric field. At the microscopic level, we can write $\mathbf{J} = \sigma\boldsymbol{\mathcal{E}}$, where $\mathbf{J}$ is the current density, σ is the conductivity tensor and $\boldsymbol{\mathcal{E}}$ is the electric field. In the following, we will consider that $\boldsymbol{\mathcal{E}} = -\mathcal{E}\hat{\mathbf{y}}$ (with $\mathcal{E} > 0$) is created by an electric potential V_y across the sample, and we will compute the Hall current I_x flowing in the transverse direction[2].

[2]Conductivity and conductance will be confused. The former is a microscopic quantity and is defined as the ratio between current density and electric field. The latter is a macroscopic quantity and is given by the ratio between electrical current and electrical potential. In a 2D uniform system, without any disorder, we can write $I_x = L_y J_x$ and $V_y = L_y\mathcal{E}$, making the conductivity and conductance equal. Note that in a real system, the conductivity depends on local disorder, while the conductance does not. As such, the conductance only is quantized and topologically protected, as we will see later in this section.

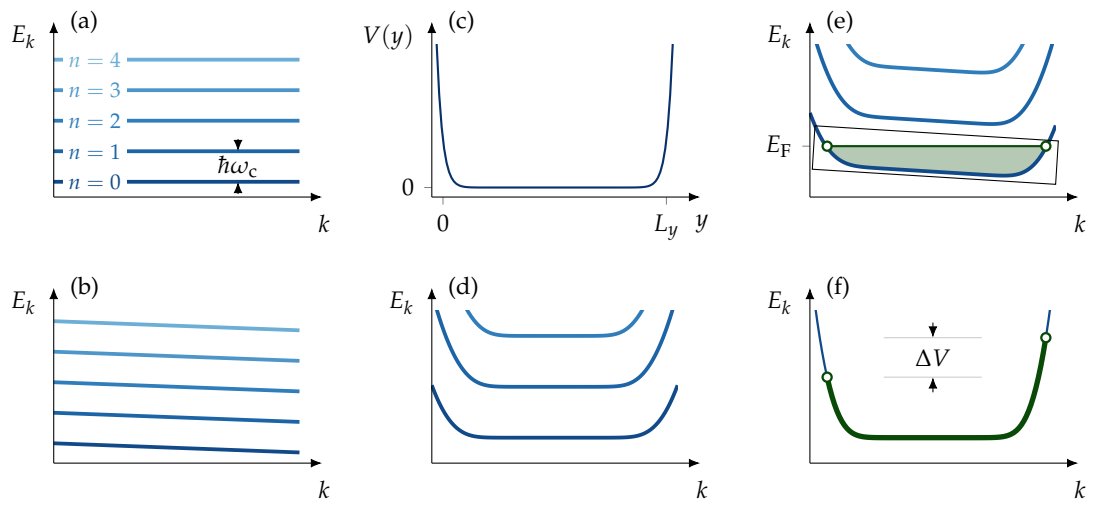

Figure 6.3 – Landau Levels. (a) The spectrum of a charged particle in a magnetic field is given by flat bands, equally spaced by $\hbar\omega_c$, and macroscopically degenerate. (b) In the presence of an electric field, the bands get tilted and the particles acquire a velocity proportional to $\partial_k E_k$. (c) Edges can be modeled by a smooth potential $V(y)$ which takes non-zero values for $y \notin [0, L_y]$. (d) The edges are also seen on the dispersion relation: the energy goes up for $k \leq 0$ and $k \geq L_y/\ell^2$, which yields non-zero chiral velocities on the boundaries only. (e) The conductance of the system is computed by considering both edges and a tilt created by an electric field. The electrons fill the bands, with the Fermi energy lying in the gap between bands. (f) Such situation is analogous to a non-tilted potential, but with a different chemical potetential on each side of the band. The energy difference corresponds to the voltage across the sample.

Such a uniform electric field along the y direction adds a term $-e\mathcal{E}\hat{y}$ in Hamiltonian (6.6), which effectively shifts the center of the harmonic oscillator in the y direction. The new wavefunctions can thus be recast in $\psi_{n,k}(x,y) = e^{ikx}\varphi_{nk}(y - mE/eB^2)$, where n here labels the order of the Hermite polynomial – or equivalently the Landau level. The energy is also changed, and acquires a linear dependence on the wavevector (see fig. 6.3(b))

$$E_{nk} = \hbar\omega_c\left(n + \frac{1}{2}\right) - e\mathcal{E}k\ell^2 - \frac{m}{2}\frac{\mathcal{E}^2}{B^2}, \tag{6.9}$$

which yields a non zero average velocity along x, $\langle\hat{v}_x\rangle = (\partial_k E_{nk})/\hbar = -\mathcal{E}/B$. We recover the classical bulk mobility already discussed in section 6.1.1, using $\mathbf{F} = e\mathcal{E}\hat{\mathbf{y}}$.

If we now consider a Fermi sea at zero temperature, such that the Fermi energy lies in the gap below the nth band (with $n = 0$ labeling the LLL), we find for the total current[3]

$$I_x = -\frac{en}{L_x}\sum_k \langle\hat{v}_x(k)\rangle = \frac{en}{L_x}\frac{\mathcal{E}}{B} \times \mathcal{D}. \tag{6.10}$$

The number of occupied states in each band is given by the degeneracy $\mathcal{D}$. Using $V_y = \mathcal{E}L_y$,

[3]Here, we sum the microscopic contributions to the current of each of the occupied states. Note that the length scales L_x, L_y are introduced here to give meaning to the degeneracy, but there are no edge effects taken into account in the calculation.

we end up with

$$\sigma_{xy} = \frac{I_x}{V_y} = n\frac{e^2}{h}. \tag{6.11}$$

We find that the conductance is quantized in units of e^2/h. Such a behavior precisely constitutes the integer quantum Hall effect, and was first observed experimentally in 1980 [Klitzing et al. 1980].

Edge effects

In the above calculation, we have seen that the current I_x is entirely related to the shape of the dispersion relation, and in particular to its derivative $\partial_k E_{nk}$. In the presence of a uniform electric field, the dispersion relation is tilted, which gives the same non-zero velocity to all states in the Landau levels. We describe below how the presence of edges in the system can also give a non-zero current.

Edges are introduced by adding a potential term $V(y)$ to the Hamiltonian (6.6). Quite generally, one can show that the velocity acquired by the state labeled k is given by[4] $\langle \hat{v}_x \rangle = (1/eB)(\partial_y V(y))|_{y=y_k}$, provided that the potential $V(y)$ changes smoothly with respect to ℓ. For sharp edges, the potential $V(y)$ takes non-zero values only for $y < 0$ and $y > L_y$; and vanishes otherwise. In fig. 6.3(c-f), and in the discussion below, we use the smooth potential approach, but the situation is not qualitatively changed in the case of sharp edges [Yoshioka 2002].

One sees that the velocity is non-zero only on the edges of the system, and that it furthermore exhibits a chiral behavior. The states on the edge $y = 0$ have a negative slope, which gives a negative velocity, while states at $y = L_y$ have a positive slope, giving a positive velocity. This chirality is also observed in the classical Hall effect, with the skipping orbits (see fig. 6.2). It is important to realize, however, that in the case of a sharp potential (typically varying on a much smaller length scale than the magnetic length), the conductance is not strictly equal to σ_{xy}. We will see that in our implementation, which uses a synthetic dimension (and thus infinitely sharp edges), the conductance is slightly reduced. Such a reduction may be explained by the fact that in the case of sharp edges, edge states within the gap are not always accessible upon a tilt of the potential.

The total current I_x can now be computed using formula (6.10), and we get for each Landau level

$$I_x^{(n)} = -\frac{e}{L_x}\frac{L_x}{2\pi}\int_0^{L_y} \mathrm{d}k\ \langle \hat{v}_x(k) \rangle = -\frac{1}{2\pi B}\frac{1}{\ell^2}\int_0^{L_y} \mathrm{d}y\ \frac{\partial V}{\partial y} = -\frac{e}{h}\Delta V, \tag{6.12}$$

with $\Delta V = V(L_y) - V(0)$ the energy difference between the two edges. In a symmetric situation, where $\Delta V = 0$, the local currents on the edges cancel each other and the total current vanishes. If now one applies an electrical potential such that $\Delta V = -eV_y$, we recover the result of eq. (6.11).

We can furthermore compute the local response of the system to an external force, which we have already introduced as the local mobility. From now on, the discussion is angled around numerical results with hard walls potentials. In order to keep it simple, we restrict the discussion to the LLL. We numerically compute the ground state wavefunction

[4] This result can be obtained by Taylor expanding $V(y)$ around y_k up to the first order.

$\psi_{0,k}(x,y)$, from which the average position and velocity are extracted as a function of the wavevector k. The local mobility is computed as a first order response of the average velocity to an external force F. Results are given in fig. 6.4.

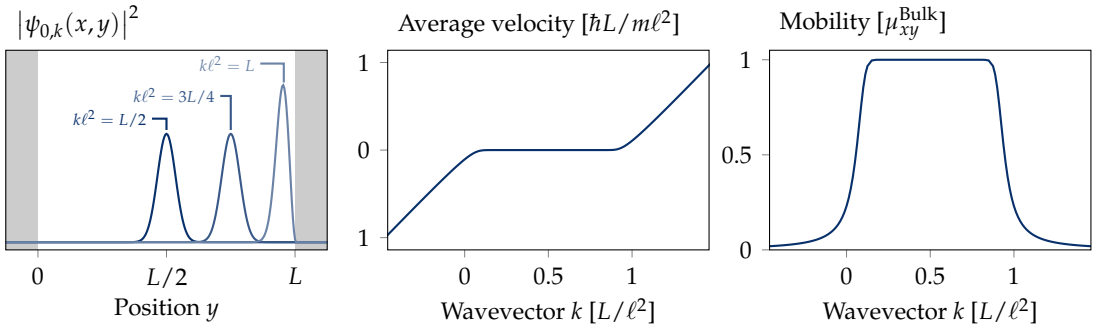

Figure 6.4 – Characteristics of the LLL. (Left) Wavefunction in the LLL as a function of the position y, for $L = 10\ell$. In the direction x, the wavefunction is a plane wave with wavevector k. In this graph, dark regions represent the edges. (Middle) average velocity $\langle \hat{v}_x \rangle$ in the LLL as a function of the wavevector k. (Right) Mobility $\mu_{xy}(y)$, in units of $\mu_{xy}^{\text{Bulk}} = -1/eB$, as a function of k.

Numerically, we recover that the wavefunction in the LLL is gaussian in the bulk. Close to the edges, the wavefunction is deformed, and gets narrower. We recover the expected behavior for the velocity, which vanishes in the bulk, and becomes non-zero and chiral on the edges, here corresponding to $k\ell^2 \approx 0$ or $k\ell^2 \approx L$. The mobility of a wavepacket is equal to μ_{xy}^{bulk}, while if gets reduced close to the edges. Such a behavior is similar to the one we had computed for classical orbits.

6.1.3 The role of topology

The above discussion leads us to the realization that Hall systems are very peculiar materials: they are insulators in the bulk, while modes with non-zero velocity can exist on the edges. Such properties are very generic properties of topological quantum systems [Hasan et al. 2010], and come from the non-trivial topology of their band structure.

In the discussion below, we adopt a slightly different geometry, which does not change the overall physics. Space is discretized to a lattice, with a spacing a, and we furthermore consider periodic boundary conditions, such that the system in invariant by translation of distance a in both directions. We furthermore point out that the following treatment is quite general, and does not necessarily apply to Hall Hamiltonians, but can be applied to any lattice-type non-interacting (single particle) Hamiltonian.

According to the Bloch theorem, we look for eigenfunctions of the problem in the form

$$\psi_{\mathbf{k}}^{(n)}(\mathbf{r}) = \mathrm{e}^{\mathrm{i}\mathbf{k}\cdot\mathbf{r}} u_{\mathbf{k}}^{(n)}(\mathbf{r}), \tag{6.13}$$

where n is the band index, $\mathbf{r} = x\hat{\mathbf{x}} + y\hat{\mathbf{y}}$ is the position and $\mathbf{k} = (k_x, k_y)$ is the (2D) lattice momentum. The functions $u_{\mathbf{k}}(x,y)$, called the Bloch functions, have the periodicity of the lattice: $u_{\mathbf{k}}(x+a,y) = u_{\mathbf{k}}(x,y)$ and $u_{\mathbf{k}}(x,y+a) = u_{\mathbf{k}}(x,y)$.

In order to understand some of the topological properties that will arise, we introduce

the Berry connection $\boldsymbol{\mathcal{A}}$ and the Berry curvature $\boldsymbol{\Omega}$ given by [Berry 1984]

$$\begin{aligned} \boldsymbol{\mathcal{A}}_{\mathbf{k}}^{(n)} &= \mathrm{i}\,\langle u_{\mathbf{k}}^{(n)} | \boldsymbol{\nabla}_{\mathbf{k}} u_{\mathbf{k}}^{(n)} \rangle \\ \boldsymbol{\Omega}_{\mathbf{k}}^{(n)} &= \boldsymbol{\nabla}_{\mathbf{k}} \times \boldsymbol{\mathcal{A}}_{\mathbf{k}}^{(n)}. \end{aligned} \tag{6.14}$$

The topology of a band n is then entirely defined by the integral of the Berry curvature over the first Brillouin zone (BZ). More precisely, we can define a quantity $\mathcal{C}^{(n)}$, called the Chern number, as

$$\begin{aligned} \mathcal{C}^{(n)} &= \frac{1}{2\pi} \int_{(\mathrm{BZ})} \mathrm{d}\mathbf{k}\, \boldsymbol{\nabla}_{\mathbf{k}} \times \boldsymbol{\mathcal{A}}_{\mathbf{k}}^{(n)} \\ &= \frac{\mathrm{i}}{2\pi} \int_{(\mathrm{BZ})} \mathrm{d}\mathbf{k}\, \left[\langle \partial_{k_y} u_{\mathbf{k}}^{(n)} | \partial_{k_x} u_{\mathbf{k}}^{(n)} \rangle - \langle \partial_{k_x} u_{\mathbf{k}}^{(n)} | \partial_{k_y} u_{\mathbf{k}}^{(n)} \rangle \right]. \end{aligned} \tag{6.15}$$

It can be shown that this number only takes integer values, $\mathcal{C}^{(n)} \in \mathbb{Z}$. Such a number, defined over the system as a whole, is a topological invariant: it does not change upon smooth changes of the system.

On the other hand, the conductivity σ_{xy} can be computed using linear response theory, as

$$\begin{aligned} \sigma_{xy} = \frac{\mathrm{i}e^2}{\hbar} \sum_{n,m} \int \frac{\mathrm{d}\mathbf{k}}{(2\pi)^2} \frac{1}{[E_{\mathbf{k}}^{(m)} - E_{\mathbf{k}}^{(n)}]^2} \Big[&\langle u_{\mathbf{k}}^{(n)} | \partial_{k_y} \tilde{H} | u_{\mathbf{k}}^{(m)} \rangle \langle u_{\mathbf{k}}^{(m)} | \partial_{k_x} \tilde{H} | u_{\mathbf{k}}^{(n)} \rangle \\ &- \langle u_{\mathbf{k}}^{(n)} | \partial_{k_x} \tilde{H} | u_{\mathbf{k}}^{(m)} \rangle \langle u_{\mathbf{k}}^{(m)} | \partial_{k_y} \tilde{H} | u_{\mathbf{k}}^{(n)} \rangle \Big]. \end{aligned} \tag{6.16}$$

In the above expression, the index n labels the filled bands, $E^{(n)} < E_{\mathrm{F}}$ with E_{F} the Fermi energy, and the index m labels the empty bands $E^{(m)} > E_{\mathrm{F}}$. The Hamiltonian $\tilde{H}$ is the reduced Hamiltonian that only acts on the Bloch functions

$$\tilde{H} \, |u_{\mathbf{k}}\rangle = E_{\mathbf{k}} \, |u_{\mathbf{k}}\rangle \,. \tag{6.17}$$

Formula (6.16) is known as the Kubo formula [Thouless et al. 1982]. After a bit of algebra, one finds

$$\begin{aligned} \sigma_{xy} &= \frac{\mathrm{i}e^2}{\hbar} \sum_{n} \int \frac{\mathrm{d}\mathbf{k}}{(2\pi)^2} \left[\langle \partial_{k_y} u_{\mathbf{k}}^{(n)} | \partial_{k_x} u_{\mathbf{k}}^{(n)} \rangle - \langle \partial_{k_x} u_{\mathbf{k}}^{(n)} | \partial_{k_y} u_{\mathbf{k}}^{(n)} \rangle \right] \\ &= \frac{e^2}{h} \sum_{n} \mathcal{C}^{(n)}. \end{aligned} \tag{6.18}$$

As we can see, the conductance is intrinsically related to the topology of the bands: the number n of eq. (6.11) corresponds to the sum of the Chern numbers over the filled bands. As such, we just showed here that each Landau Level has a Chern number $\mathcal{C}^{(n)} = 1$.

The intrinsic relation between the topology and the conductance was first put forth in a famous article by Thouless, Kohmoto, Nightingale and den Nijs [Thouless et al. 1982]. In the context of topological insulators, the Chern number is often referred as a *TKKN invariant* for this reason.

It is worth pointing out that the notion of topology here is quite general, and not limited to quantum systems. Topology is a property of dispersion bands, and topological *classical* systems can be engineered, *e.g.* with acoustic waves [Xiao et al. 2015] or even

mechanical resonators [Süsstrunk et al. 2015]. As we have already mentioned, a given topological phase of a system is robust against smooth changes, such as disorder. In that respect, topology in quantum systems is particularly interesting when one considers quantum statistics and many-body effects, in which case the many-body state would be robust thanks to the topological order.

On a last remark, we come back to the edges which were left aside by the choice of our geometry. An edge can be defined as the interface between distinct topologies. For example in a Hall system, it is the interface between the bulk ($\mathcal{C} = 1$) and the vacuum ($\mathcal{C} = 0$). A change in the topological invariant necessarily involves the gap to close at the boundary, which itself involves the existence of a gapless mode with a well-defined chirality [Cooper et al. 2019]. The relation between the topological invariant and the number of edge modes is given by the *bulk-edge correspondence* [Hasan et al. 2010], which essentially states that the number of edge modes is given by the difference in the Chern number between the two regions.

The Chern number of a system with open boundary conditions (such as in the presence of edges) is not well defined by eq. (6.15), because one cannot define a Brillouin zone. Yet, if the system is large enough, we still expect to see signatures of its topology deep in the bulk, where the edges should not have any effect. The link between conductance and Chern number, that we just derived, can be extended to the mobility, that we have discussed in section 6.1.2 (see fig. 6.4). In particular, we see that the mobility takes a non-zero and finite value in the bulk of the system ($k\ell^2 < L$), and decreases close to the edges. The local topology, on the other hand, can be expressed *via* a *local Chern marker* (LCM) $c(x, y)$, which probes the topology locally [Bianco et al. 2011]. It is important to realize here that the LCM, like the local mobility or the conductivity, depends on local properties of the system such as disorder, while the conductance, related to the Chern number, does not.

The local Chern marker is expressed as

$$c(x, y) = -2\mathrm{i}\pi \, \langle x, y | [\hat{P}\hat{x}\hat{P}, \hat{P}\hat{y}\hat{P}] | x, y \rangle \,, \tag{6.19}$$

where $\hat{P}$ is the projector onto the occupied states – we consider the ground band in the following. The operators $\hat{x}$ and $\hat{y}$ are the position operators. Even though $[\hat{x}, \hat{y}] = 0$, in general $\hat{x}\hat{P}\hat{y} \neq \hat{y}\hat{P}\hat{x}$. The local Chern marker is thus the average value, over the LLL, of the Hermitian operator $\mathrm{i}(\hat{x}\hat{P}\hat{y} - \hat{y}\hat{P}\hat{x})$.

We notice here that the LCM is the analogue of the Kubo formula, using local operators projected on the lowest band. The total Chern number is then given as the trace over all space of the LCMs ; it averages to zero in the case of a finite sample, for which the edges cancel the non-zero values of the bulk. In the geometry we consider here, *i.e.* infinite in the x direction and finite in the y direction with hard walls, the LCM only depends on the coordinate y and can be expressed as (see appendix B for a detailed calculation)

$$c(y) = \int \mathrm{d}k \, |\psi_{0,k}(x, y)|^2 \, \partial_k \langle \hat{y} \rangle_k \,, \tag{6.20}$$

where $\langle \hat{y} \rangle$ is the average position in state k, and where the integral runs over all the occupied states. The LCM, computed for hard walls, is given in fig. 6.5.

In this example, we chose for the occupied states all the states which lie within half

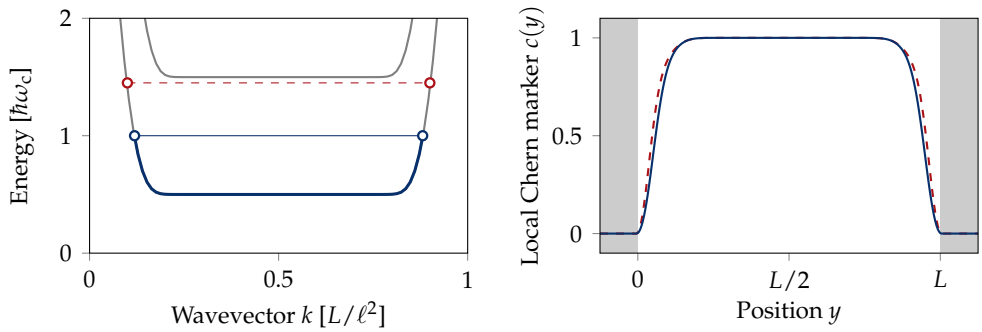

Figure 6.5 – Local Chern marker. (Left) The thick blue line represents the states taken into account for the computation. They correspond to a filled lowest band, up to half the gap. (Right) Local Chern marker, computed according to eq. (6.20) and using the occupied states given in the left plot. Dark areas mark the edges. The dashed red line correspond to the local Chern marker for a lowest band filled up close to the first excited band (red dashed on the left graph). As we can see, the local Chern marker is marginally changed, with differences on the edges only.

the bulk energy gap. As we can see, the LCM in such a case is equal to $c(y) = 1$ over a large region in the bulk. Close to the edges, the local Chern marker decreases to 0. In principle, in a finite system, the integrated Chern number vanishes and the LCMs are negative on the edges. In the semi-infinite geometry that we consider here, the integrated Chern number does not vanish. Such an effect indicate that the value of the LCM on the edges has a non-local character, as it strongly depends on the global geometry of the sample.

6.2 Spin-orbit coupling, artificial gauge fields and synthetic dimensions

In the previous section, we have given an overview of the peculiar phenomena arising with the quantum Hall effect. In particular, we have discussed the intrinsic link between the quantization of the Hall conductance and the topology of the Landau levels. Such correspondence, as we have mentioned, is very generic and is at the core of the study of topological insulators. In the field of ultracold atoms, and more precisely quantum simulation, tremendous efforts have been made to realize such systems (see *e.g.* [Cooper et al. 2019] for a recent review).

A fundamental distinction between ultracold atoms and electrons is of course that atoms are neutral, and not sensitive to external magnetic fields. A real challenge in the realization of quantum Hall systems with neutral particles thus lies in the implementation of an artificial gauge field $\hat{\boldsymbol{\mathcal{A}}}$, which would lead to Hamiltonians of the form

$$\hat{H} = \frac{(\hat{\mathbf{p}} - \hat{\boldsymbol{\mathcal{A}}})^2}{2m}. \tag{6.21}$$

As one can see, $\hat{\boldsymbol{\mathcal{A}}}$ is the analogue of the term $-e\mathbf{A}(\hat{\mathbf{r}})$ in the Landau Hamiltonian. This section is aimed at exposing the basic ideas behind spin-orbit coupling, which is one of the techniques used to implement artificial gauge fields. This method is specifically relevant

for us, our implementation will be described in section 6.3.

6.2.1 Spin-orbit coupling in ultracold atoms

Spin-orbit coupling consists in coupling the internal degree of freedom – the spin $\downarrow$ or $\uparrow$ – of an atom with its external state – its momentum π. In its minimal version, *i.e.* for a spin 1/2, it corresponds to the coupling of states $|\downarrow, \boldsymbol{\pi}\rangle$ and $|\uparrow, \boldsymbol{\pi}'\rangle$, with $\boldsymbol{\pi}' \neq \boldsymbol{\pi}$. It can be induced by laser light using Raman transitions (see fig. 6.6).

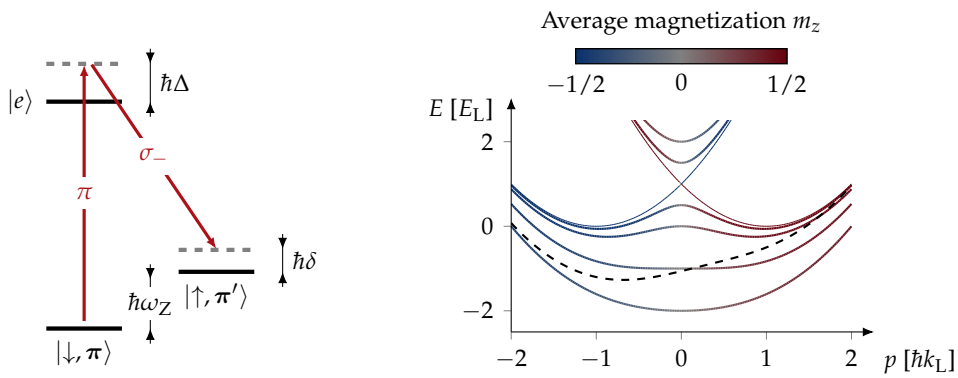

Figure 6.6 – Spin-orbit coupling. (Left) Raman transitions are two-photon transitions, and can be implemented with a $\pi - \sigma_-$ scheme. Here, the two laser beams involved have their frequency difference matching the Zeeman splitting ω_Z, such that states $|\downarrow, \boldsymbol{\pi}\rangle$ get coupled to $|\uparrow, \boldsymbol{\pi}'\rangle$ with $\boldsymbol{\pi}' = \boldsymbol{\pi} + 2\hbar\mathbf{k}_L$ (see text). (Right) Assuming Δ to be sufficiently large, the system can be reduced to a two-level system. We plot here the eigenenergies of the system for $\delta = 0$ and $\hbar\Omega/E_L = 0, 1, 2, 4$ and 6, with $E_L = \hbar^2\mathbf{k}_L^2/2m$ the natural energy scale. The upper bands for $\hbar\Omega/E_L = 4, 6$ lie above the graph. At $\Omega = 0$, the spectrum consists in two parabolas centered around $p = \pm\hbar k_L$, with p the component of $\mathbf{p}$ colinear with $\mathbf{k}_L$ (thin lines). Each parabola corresponds to a single spin state. By increasing Ω, a gap opens at $p = 0$, yielding to a mixing of the magnetization $m_z = \langle\hat{\sigma}_z\rangle/2$, and a shift of the minima towards small $|p|$. Above a critical value $\hbar\Omega_c = 4E_L$, the two minima merge into a single minimum at $p = 0$. The dashed line corresponds to the lower band at $\hbar\Omega = 4E_L$ and $\hbar\delta = E_L$. The additional detuning tilts the band and shifts the minimum ; for $\Omega < \Omega_c$, it favors one minimum with respect to the other.

In such a setup, spin-orbit coupling is induced by a two-photon optical transition between $|\downarrow\rangle$ and $|\uparrow\rangle$. The atom absorbs a photon at momentum $\hbar\mathbf{k}_L$ from one laser beam, and comes back to the ground state by stimulated emission of a photon in the counter-propagating beam. The total momentum acquired by the atom in such a process is thus $2\hbar\mathbf{k}_L$. Such an implementation requires the existence of an excited state $|e\rangle$, serving as an intermediate state for the two-photon transition. The lasers are detuned by Δ from the resonance, and in practice $\Delta \gg \Gamma$, where Γ is the natural linewidth, such that $|e\rangle$ can be adiabatically eliminated from the dynamics [Goldman et al. 2014]. An additional detuning δ from the two-resonance transition is chosen by setting the frequency difference between the two laser beams. Assuming $\delta \ll \omega_Z$, where $\hbar\omega_z$ is the Zeeman splitting between the two spin states, one can apply the rotating wave approximation (RWA) at the Zeeman

splitting, and the above process can be described by a two-level Hamiltonian

$$\hat{H}_{\mathrm{SOC}} = \frac{(\hat{\mathbf{p}} - \hbar \mathbf{k}_{\mathrm{L}} \hat{\sigma}_z)^2}{2m} + \frac{\hbar\Omega}{2}\hat{\sigma}_x + \frac{\hbar\delta}{2}\hat{\sigma}_z. \tag{6.22}$$

In this expression, $\hat{\sigma}_i$ are the Pauli matrices with $|\downarrow\rangle$ and $|\uparrow\rangle$ the eigenstates of $\hat{\sigma}_z$, and Ω is the two-photon Rabi frequency. The spectrum of $\hat{H}_{\mathrm{SOC}}$ is also given in fig. 6.6.

The spectrum of $\hat{H}_{\mathrm{SOC}}$ splits in two bands. We can denote $|-\rangle$ and $|+\rangle$ the dressed states which are eigenstates of $\hat{H}_{\mathrm{SOC}}$, and whose dispersion relations form the bands pictured in fig. 6.6. Assuming adiabatic evolution, one can then assume that the dynamics only take place in one of the bands, and derive an effective Hamiltonian for each band with a gauge field $\boldsymbol{\mathcal{A}}_{\pm}$. In our minimal example, this gauge field has no spatial dependence, meaning that the effective magnetic field is $\boldsymbol{\mathcal{B}} = \boldsymbol{\nabla} \times \boldsymbol{\mathcal{A}}_{\pm} = \mathbf{0}$. In order to actually have an effective field, one could for example have a space-dependent Raman coupling Ω or detuning δ (with their gradients not parallel to $\mathbf{k}_{\mathrm{L}}$), such that the dispersion relation would acquire a space-dependent term.

The first experimental realization of spin-orbit coupling in ultracold quantum gases was realized in the group of Prof. Spielman [Lin et al. 2011], following the realization of synthetic magnetic fields using space-dependent detunings [Lin et al. 2009].

More generally, it is worth noting that spin-orbit coupling is also intrinsically related to non-Abelian gauge fields. One sees indeed that in general, one could have a gauge field $\hat{\boldsymbol{\mathcal{A}}}$ which depends on operators (*e.g.* Pauli matrices), meaning that its cartesian components would not commute with each other. Such gauge fields are obtained when a subspace generated by the dressed states become degenerate or nearly degenerate [Dalibard et al. 2011]. Non-Abelian gauge fields are broadly related to more exotic physics, such as topological insulators or topological superluids. More information about the (theoretical) implementation of spin-orbit coupling and non-Abelian gauge fields with ultracold atoms can be found in [Zhou et al. 2013; Zhai 2015].

6.2.2 Synthetic dimensions

From now on, we will consider that the Raman process discussed above involves counter-propagating laser beams in the x direction, giving $\mathbf{k}_{\mathrm{L}} = k_{\mathrm{L}}\hat{\mathbf{x}}$, effectively yielding $\hat{\boldsymbol{\mathcal{A}}} = \hat{\mathcal{A}}_x\hat{\mathbf{x}}$ with $\hat{\mathcal{A}}_x = \hbar k_{\mathrm{L}}\hat{\sigma}_z$. As mentioned previously, this synthetic gauge field can be considered as a gauge field acting on a subspace of the Hilbert space defined by the two-level system, and can also be considered as a non-Abelian gauge field when the dressed states become nearly degenerate. Here, we adopt a different point of view, in which the internal states, $|\downarrow\rangle$ and $|\uparrow\rangle$, play the role of an effective position. Such a point of view, known as a *synthetic dimension*, was first introduced in the context of quantum simulation with ultracold atoms in [Celi et al. 2014], and experimentally realized with up to 3 internal states [Mancini et al. 2015; Stuhl et al. 2015]. As such, the 1D + internal state problem introduced by $\hat{H}_{\mathrm{SOC}}$ becomes 2D, and the gauge potential $\hat{\mathcal{A}}_x$ now acquires an effective position dependence, since it is different for $|\downarrow\rangle$ and $|\uparrow\rangle$.

The emergence of a non-trivial synthetic magnetic field becomes quite intuitive, even with the minimal two-level system we have considered so far. On the one hand, the spin states $|\downarrow\rangle$ and $|\uparrow\rangle$ correspond to opposite edges in the synthetic dimension. On the other hand, each of these spin states are associated to opposite velocities: $mv_{\downarrow} = -\hbar k_{\mathrm{L}}$ and

$mv_\uparrow = \hbar k_L$. In this two-level system, we thus have two chiral edge modes, without any bulk (see fig. 6.7).

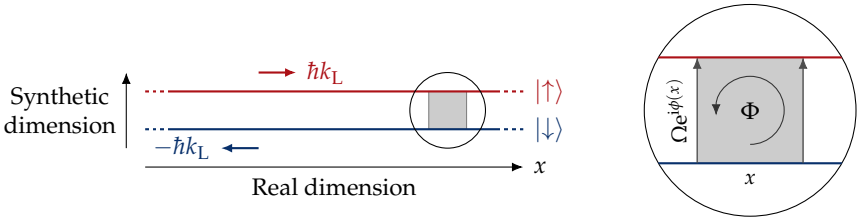

Figure 6.7 – Synthetic dimension. The internal states $|\downarrow\rangle$ and $|\uparrow\rangle$ can be considered as effective positions, making the system effectively two-dimensional, and only constituted of edges. The space is then continuous in the real dimension, and discretized in the synthetic dimension. In the presence of spin-orbit coupling, chiral edge modes emerge. Raman transitions can be interpreted as laser-induced hopping terms in the synthetic dimension, with the laser phase $\phi(x)$ imprinted in the tunneling element. Within this interpretation, a non-zero (synthetic) magnetic flux Φ emerges.

Topological properties of the system emerge by interpreting the Raman transitions as hopping in the synthetic dimension, with a phase coming from the phase difference of the lasers. The tunneling hopping term in the synthetic dimension is thus of the form $\Omega e^{i\phi(x)}$, where Ω is the coupling strength, and $\phi(x) = 2k_L x$ is the phase imprinted by the Raman lasers. In the context of ultracold atoms in optical lattices, the phase ϕ is often referred as the Peierls phase.

In this picture, a particle moving around a closed loop acquires a total phase $\Phi = \phi(x+a) - \phi(x) = 2k_L a \neq 0$, where a is the real space displacement. This phase is the equivalent of the Aharonov-Bohm phase $\Phi_{AB} = -eBA/\hbar$ acquired by an electron moving around a plaquette of area A, in the presence of a transverse magnetic field B [Aharonov et al. 1959], and is related to the emergence of bands with non-trivial topology [Cooper et al. 2019].

6.3 Implementation with dysprosium

We now move to the description of the experimental implementation. We only discuss here the experimental scheme, and detail the derivation of the Hamiltonian that governs the dynamics. A quantitative (theoretical) study of the system that we derive here will be given in section 6.4, and the experimental results are presented in the next chapter.

6.3.1 Raman transitions

We consider the experimental setup pictured in 6.8. Two counter propagating laser beams, close to the 626 nm transition, interact with the atomic cloud. We define as $\hat{\mathbf{x}}$ the propagation direction set by the beams. A quantization field $\mathbf{B} = B\hat{\mathbf{z}}$ splits the electronic ground states in 17 Zeeman sublevels, equally separated by $\hbar\omega_z$.

The polarizations $\mathbf{u}_1$ and $\mathbf{u}_2$ are chosen to be orthogonal with each other and at 45° with respect to the quantization field. This choice will be motivated in section 6.4. We

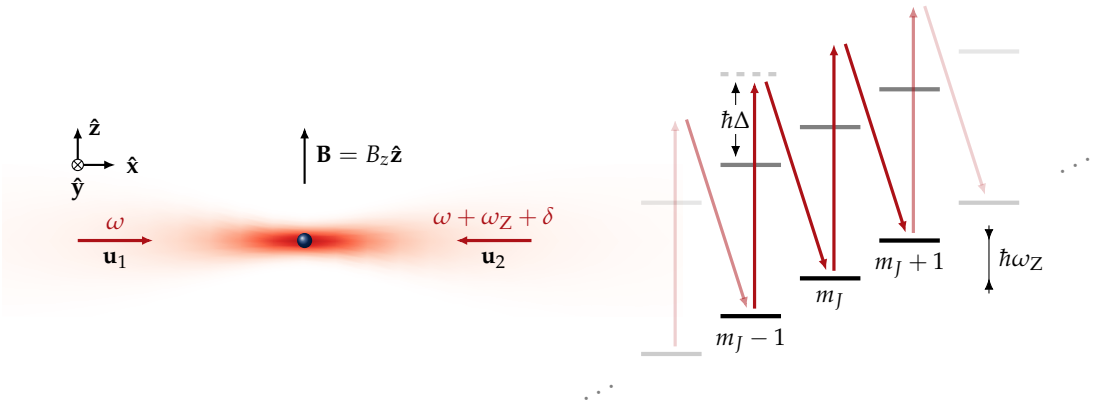

Figure 6.8 – Raman experimental setup. Two laser beams, counter propagating in the $\hat{\mathbf{x}}$ direction, interact with a dysprosium atom. An external field $\mathbf{B}$ oriented along $\hat{\mathbf{z}}$ lifts the degeneracy of the ground state and splits subsequent Zeeman states by $\hbar\omega_Z$. Each laser beam has a well-chosen polarization $\mathbf{u}$ (see text). The frequency difference between the two laser beams matches the Zeeman splitting, with an additional detuning δ. The laser frequency ω is detuned by Δ from the one-photon transition which involves the excited state manifold. In practice, we have $\Delta > 0$ and $\Delta \gg \omega_Z$ (the scheme is not to scale).

write

$$\mathbf{u}_1 = \frac{\hat{\mathbf{y}} + \hat{\mathbf{z}}}{\sqrt{2}} \quad \text{and} \quad \mathbf{u}_2 = \frac{\hat{\mathbf{y}} - \hat{\mathbf{z}}}{\sqrt{2}}. \tag{6.23}$$

The angular frequency difference between the two beams is written as $\omega_z + \delta$. The total Hamiltonian of a dysprosium atom then takes the form

$$\hat{H} = \hat{H}_0 + \hat{H}_\mathrm{L}, \tag{6.24}$$

where $\hat{H}_0$ contains the kinetic term and the Zeeman term, while $\hat{H}_\mathrm{L}$ describes the atom-light interaction. As such, we have

$$\begin{aligned} \hat{H}_0 &= \frac{\hat{\mathbf{p}}^2}{2m} + \hbar\omega_Z \hat{J}_z \\ \hat{H}_\mathrm{L} &= V_0 \left[\alpha_0 |\mathbf{u}|^2 \hat{\mathbb{1}} - \mathrm{i}\alpha_1 (\mathbf{u}^* \times \mathbf{u}) \frac{\hat{\mathbf{J}}}{2J} \right. \\ &\qquad \left. + \alpha_2 \frac{3[(\mathbf{u}^* \cdot \hat{\mathbf{J}})(\mathbf{u} \cdot \hat{\mathbf{J}}) + (\mathbf{u} \cdot \hat{\mathbf{J}})(\mathbf{u}^* \cdot \hat{\mathbf{J}})] - 2|\mathbf{u}|^2 \hat{\mathbf{J}}^2}{2J(2J-1)} \right]. \end{aligned} \tag{6.25}$$

In this expression, α_i, $i = 0, 1, 2$ are respectively the scalar, vectorial and tensorial coefficients of the considered transition (see chapter 5). The light coupling amplitude is given by

$$V_0 = \frac{3\pi c^2 \Gamma}{2\omega_0^3} \frac{I}{\Delta}, \tag{6.26}$$

with $\Gamma = 2\pi \times 135\,\mathrm{kHz}$ the natural transition linewidth, ω_0 the laser angular frequency, Δ the detuning to resonance and I the laser intensity. We also introduce the total position-

dependent polarization vector

$$\begin{aligned}\mathbf{u} &= \frac{1}{\sqrt{2}}\left[\mathrm{e}^{\mathrm{i}(kx-\omega_0 t)}\mathbf{u}_1 + \mathrm{e}^{\mathrm{i}(-kx-\omega_0 t-\omega_Z t-\delta t)}\mathbf{u}_2\right] \\ &= \frac{1}{2}\mathrm{e}^{-\mathrm{i}\omega_0 t}\left[\mathrm{e}^{\mathrm{i}kx}(\hat{\mathbf{y}}+\hat{\mathbf{z}}) + \mathrm{e}^{-\mathrm{i}(kx+(\omega_Z+\delta)t)}(\hat{\mathbf{y}}-\hat{\mathbf{z}})\right].\end{aligned} \tag{6.27}$$

Using eq. (6.27) in the expression of $\hat{H}_\mathrm{L}$ in eq. (6.25), one finds

$$\hat{H}_\mathrm{L} = V_0\left[\alpha_0\hat{\mathbb{1}} + \alpha_1\sin(\phi)\frac{\hat{J}_x}{2J} + \alpha_2\frac{\hat{\mathbf{J}}^2 - 3\hat{J}_x^2 + 3\cos(\phi)\left(\hat{J}_y^2 - \hat{J}_z^2\right)}{2J(2J-1)}\right], \tag{6.28}$$

where $\phi = 2kx + (\omega_\mathrm{z}+\delta)t$ is the phase difference between the two laser beams.

Rotating wave approximation

We now apply the rotating wave approximation (RWA). The RWA amounts to a unitary transformation, and the approximation lies in the fact that we neglect the fast oscillating terms that emerge. We write

$$|\psi\rangle \to |\tilde{\psi}\rangle = \hat{U}|\psi\rangle = \mathrm{e}^{\mathrm{i}(\omega_Z+\delta)t\hat{J}_z}|\psi\rangle. \tag{6.29}$$

In this rotating frame, the Schrödinger equation for $|\tilde{\psi}\rangle$ reads

$$\mathrm{i}\hbar\frac{\mathrm{d}|\tilde{\psi}\rangle}{\mathrm{d}t} = \tilde{H}|\tilde{\psi}\rangle, \qquad \text{with} \quad \tilde{H} = \mathrm{i}\hbar\frac{\mathrm{d}\hat{U}}{\mathrm{d}t}\hat{U}^\dagger + \hat{U}\hat{H}\hat{U}^\dagger. \tag{6.30}$$

We detail below the derivation of $\tilde{H}$.

The first term of $\tilde{H}$ is straightforward and simply gives $-\hbar(\omega_Z+\delta)\hat{J}_z$, which conveniently replaces the Zeeman term in $\hat{H}_0$ with $-\hbar\delta\hat{J}_z$. For the second term, we will use the Baker-Hausdorff formula,

$$\mathrm{e}^{\hat{A}}\hat{B}\mathrm{e}^{-\hat{A}} = \hat{B} + [\hat{A},\hat{B}] + \frac{1}{2!}[\hat{A},[\hat{A},\hat{B}]] + \dots. \tag{6.31}$$

We also introduce the angular momentum ladder operators $\hat{J}_+ = \hat{J}_x + \mathrm{i}\hat{J}_y$ and $\hat{J}_- = \hat{J}_x - \mathrm{i}\hat{J}_y$, which have convenient commutation relations[5], and using eq. (6.31) we have

$$\hat{U}\hat{J}_+\hat{U}^\dagger = \mathrm{e}^{\mathrm{i}(\omega_Z+\delta)t}\hat{J}_+ \qquad \text{and} \qquad \hat{U}\hat{J}_-\hat{U}^\dagger = \mathrm{e}^{-\mathrm{i}(\omega_Z+\delta)t}\hat{J}_-. \tag{6.32}$$

As such, in the new reference frame, one has

$$\begin{aligned}\frac{\tilde{H}_\mathrm{L}}{V_0} &= \alpha_0\hat{\mathbb{1}} + \alpha_1\sin\phi\left(\frac{\mathrm{e}^{\mathrm{i}(\omega_Z+\delta)t}\hat{J}_+ + \mathrm{e}^{-\mathrm{i}(\omega_Z+\delta)t}\hat{J}_-}{4J}\right) \\ &+ \frac{\alpha_2}{2J(2J-1)}\left[\hat{\mathbf{J}}^2 - \frac{3}{4}\left(\mathrm{e}^{2\mathrm{i}(\omega_Z+\delta)t}\hat{J}_+^2 + \mathrm{e}^{-2\mathrm{i}(\omega_Z+\delta)t}\hat{J}_-^2 + \hat{J}_+\hat{J}_- + \hat{J}_-\hat{J}_+\right)\right. \\ &\left. -\frac{3}{4}\cos\phi\left(\mathrm{e}^{2\mathrm{i}(\omega_Z+\delta)t}\hat{J}_+^2 + \mathrm{e}^{-2\mathrm{i}(\omega_Z+\delta)t}\hat{J}_-^2 - \hat{J}_+\hat{J}_- - \hat{J}_-\hat{J}_+ - \hat{J}_z^2\right)\right]\end{aligned} \tag{6.33}$$

[5] One has indeed $[\hat{J}_z,\hat{J}_+] = \hat{J}_+$ and $[\hat{J}_z,\hat{J}_-] = -\hat{J}_-$.

One now sees that fast oscillating terms have emerged. The approximation consists in keeping only terms without any oscillating contribution. Remembering that a time component $(\omega_Z + \delta)t$ is also present in the phase ϕ, one obtains after the RWA

$$\frac{\tilde{H}_L}{V_0} = \alpha_0 \hat{\mathbb{1}} + \frac{\alpha_1}{8iJ}\left[e^{2ikx}\hat{J}_- - e^{-2ikx}\hat{J}_+\right] + \frac{\alpha_2}{2J(2J-1)}\left[\hat{\mathbf{J}}^2 - \frac{3}{2}\left(\hat{J}_x^2 + \hat{J}_y^2\right)\right]. \tag{6.34}$$

We already see in the Hamiltonian that after the RWA, spin flip transitions, described by the terms $\hat{J}_\pm$, only occur with a change of momentum, given by the terms $e^{\mp 2ikx}$.

In order to make the spin-orbit terms more obvious, and recover $\hat{H}_{SOC}$ of eq. (6.22), we make a gauge transform, similar to the unitary transform we have just realized, but this time acting on the position

$$|\tilde{\psi}\rangle \to e^{2ik\hat{x}\hat{J}_z}|\tilde{\psi}\rangle. \tag{6.35}$$

Such a gauge transform allows to transfer the momentum kick associated to the spin-flip transition in the kinetic part of the Hamiltonian. Indeed, one has

$$e^{2ik\hat{x}\hat{J}_z}\frac{\hat{\mathbf{p}}^2}{2m}e^{-2ik\hat{x}\hat{J}_z} = \frac{1}{2m}\left[\hat{p}_y^2 + \hat{p}_z^2 + (\hat{p}_x - 2\hbar k\hat{J}_z)^2\right]. \tag{6.36}$$

From now on, we restrict our description to the $\hat{\mathbf{x}}$ axis, which is the only direction with non-trivial dynamics. We will thus drop the x-index and use the operator $\hat{p} \equiv \hat{p}_x$. After a bit of algebra, we obtain the final spin-orbit coupled Hamiltonian[6]

$$\hat{H} = \frac{(\hat{p} - \hbar K\hat{J}_z)^2}{2m} - \hbar\Omega\left[\hat{J}_y + \frac{\hat{J}_z^2}{2J+3}\right] - \hbar\delta\hat{J}_z, \tag{6.37}$$

where we introduced the two-photon recoil momentum $\hbar K = 2\hbar k$ and the two-photon Raman coupling $\hbar\Omega = 19V_0/612$ (using the polarizability coefficients α_1 and α_2 computed for a $J \to J' = J+1$ transition). We also omit the term proportional to the identity, which does not play any role in the dynamics[7].

6.3.2 Quantum Hall effect with synthetic dimensions

In the same spirit of section 6.2, the internal state encoded in the angular momentum operator $\hat{J}_z$ is interpreted as an effective position, and gives a synthetic dimension. We give an illustration of such a large synthetic system in fig. 6.9. The Hamiltonian given in eq. (6.37) is similar to the Hall Hamiltonian given in eq. (6.6), with the substitution $\hat{y} \leftrightarrow \hat{J}_z$. Yet, the correspondence $\hat{p}_y^2 \leftrightarrow \hat{J}_y$, which we detail below, is not straightforward.

In order to make a link between $\hat{H}$ and the Landau Hamiltonian, we first make a classical approximation, which consists in replacing the operators by real numbers. This approach is justified in the large spin limit $J \gg 1$. In the following, we set $\delta = 0$. As such,

[6] We come back to the notation with hats for operators, and drop the tilde.

[7] This term can in principle trap or anti-trap the atoms. However, the time scales involved in the experiment (on the order of a few hundreds of µs), and the fact that the strongest effects are in the yz plane, make it safe to neglect.

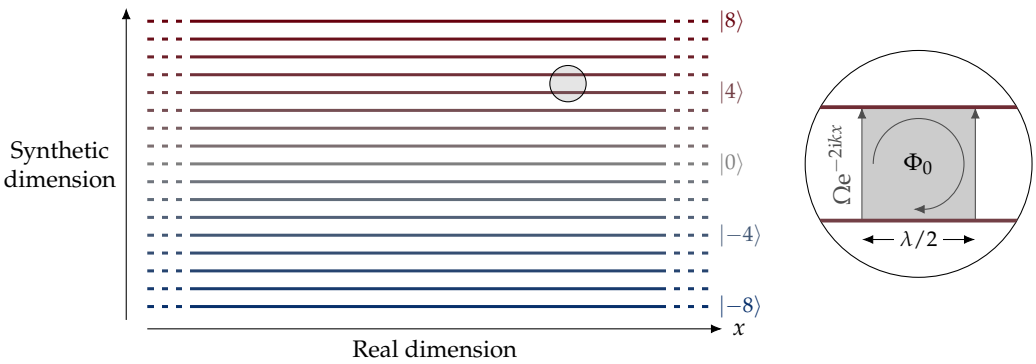

Figure 6.9 – Synthetic dimensions with dysprosium. A synthetic dimension is encoded in the internal state of dysprosium atoms, given $2J+1=17$ synthetic positions. The Raman transitions (see zoom) are spin-flip transitions with a momentum kick given by the laser recoil momentum $2\hbar k$. In the synthetic dimension picture, those transitions are equivalent to a tunneling term with a phase given by the laser phase. As such, one quantum of flux $\Phi_0 = 2\pi$ is realized in an elementary plaquette of size $1 \times \lambda/2$.

the spin operators $\hat{J}_i$, with $i = x, y, z$, are parametrized by two angles θ and φ, as

$$(\hat{J}_x, \hat{J}_y, \hat{J}_z) \leftrightarrow (J\sin\theta\cos\varphi, J\sin\theta\sin\varphi, J\cos\theta). \tag{6.38}$$

With such a parametrization, $m_z = J\cos\theta$ and φ are conjugate variables. The classical ground state of the system is thus given by $m_{z_0} = J\cos(\theta_0)$ and φ_0 which are solutions of $\partial_{m_z} H_c = 0$ and $\partial_\varphi H_c = 0$, where H_c is the classical Hamiltonian,

$$H_c = E_L\left[(\tilde{p} - m_z)^2 - \tilde{\Omega}\left((J^2 - m_z^2)^{1/2}\sin\varphi + q m_z^2\right)\right], \tag{6.39}$$

obtained from eq. (6.37) by the substitution of eq. (6.38). We have introduced the laser recoil energy $E_L = \hbar^2 K^2/2m$, and the reduced variables $\tilde{p} = p/\hbar K$, $\tilde{\Omega} = \hbar\Omega/E_L$ and $q = 1/(2J+3)$. The classical ground state is given by $\varphi_0 = \pi/2$ and θ_0 solution of

$$\frac{2\tilde{p}}{\tilde{\Omega}}\tan\theta_0 + 2J\sin\theta_0\left[q - \frac{1}{\tilde{\Omega}}\right] - 1 = 0. \tag{6.40}$$

The value of θ_0 as a function of $\tilde{p}$, for $J = 8$ and $\tilde{\Omega} = 1$, is given in fig. 6.10.

Note that a low order classical expansion of eq. (6.39) around φ_0 yields

$$H_c \approx E_L\left[(\tilde{p} - m_z)^2 + \frac{\tilde{\Omega}}{2}(J^2 - m_z^2)^{1/2}\Delta\varphi^2 - q\tilde{\Omega}m_z^2 - \tilde{\Omega}(J^2 - m_z^2)^{1/2}\right], \tag{6.41}$$

where $\Delta\varphi = \varphi - \varphi_0$. We recognize an expression similar to the Landau Hamiltonian, with the quadratic term $\Delta\varphi^2$ in the role of synthetic momentum. The additional term is interpreted as a m_z-dependent potential, *i.e.* an additional potential in the synthetic dimension. We thus recover the mapping $\hat{J}_y \leftrightarrow \hat{p}_y^2$, in such a classical, low-energy expansion.

In order to get a more precise description of the low-energy Hamiltonian, we proceed to a Holstein-Primakoff expansion of the spin operators [Holstein et al. 1940] around the

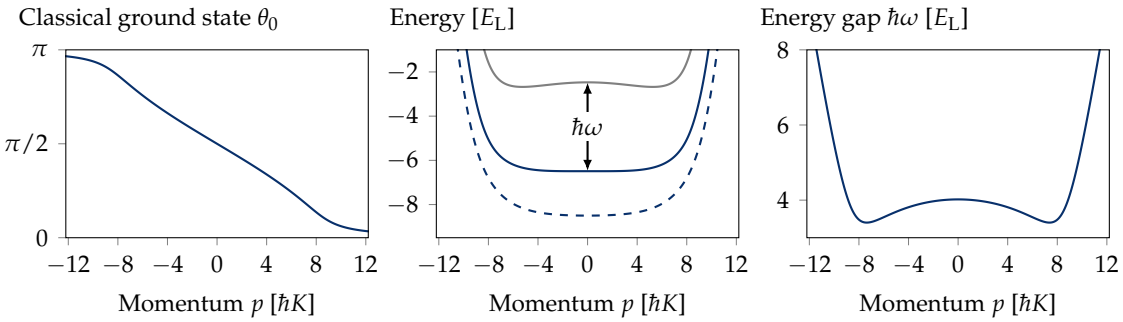

Figure 6.10 – Classical approximation. The classical ground state is obtained by minimizing the energy in eq. (6.39) for the two (classical) conjugate variables $m_z = J\cos\theta$ and φ. Here, we have $J = 8$ and $\hbar\Omega = E_L$. (Left) Angle θ_0 defining the classical ground state. As we can see, for $|p| > J$, the ground state lies close to the poles $\theta_0 \approx 0$ or π. (Middle) Classical energy dispersion (dashed line), along with first quantum corrections (solid lines). The quantum corrections are obtained from a lowest order Holstein-Primakoff expansion of the classical energy around the ground state, effectively giving quadratic terms that can be interpreted in terms of a harmonic oscillator with angular frequency ω. The ground state is then corrected by the zero-point energy $\hbar\omega/2$ (solid blue line), and the energy of the first excited state (solid gray line) is obtained from the gap $\hbar\omega$. The classical spectrum derived here resembles the one obtained in the context of the quantum Hall effect (see fig. 6.3). (Right) Energy gap as a function of the momentum p. The gap is not homogeneous, as one would expect from Landau levels, but the inhomogeneities remain relatively small compared to its value in the center of the band.

classical ground state. Such an approximation is quite standard to grasp the low energy physics of non-linear large spin models (see *e.g.* [Dusuel et al. 2004]). We first introduce the spin operators in a rotated basis, such that

$$\begin{cases} \hat{J}_z = \tilde{J}_z \cos\theta_0 - \tilde{J}_y \sin\theta_0 \\ \hat{J}_y = \tilde{J}_z \sin\theta_0 + \tilde{J}_y \cos\theta_0 \end{cases} \tag{6.42}$$

We then write the Holstein-Primakoff transformation

$$\begin{cases} \tilde{J}_z = J - a^\dagger a \\ \tilde{J}_+ = \sqrt{2J - a^\dagger a}\; a \\ \tilde{J}_- = a^\dagger \sqrt{2J - a^\dagger a}\,, \end{cases} \tag{6.43}$$

with $a^\dagger$ and a bosonic ladder operators. The expansion is then realized up to quadratic order in $a, a^\dagger$, to obtain

$$\begin{aligned} H_c &= E_L(H_0 + H_2), \qquad \text{with} \\ H_0 &= (\tilde{p} - J\cos\theta_0)^2 - \tilde{\Omega}\left[J\sin\theta_0 + qJ^2\cos^2\theta_0\right] \\ H_2 &= \left[\tilde{p}\cos\theta_0 - J\cos^2\theta_0(1-\tilde{\Omega}q) + \frac{\tilde{\Omega}}{2}\sin\theta_0\right](X^2 + P^2 - 1) + \\ &\qquad\qquad J\sin^2\theta_0(1-\tilde{\Omega}q)P^2, \end{aligned} \tag{6.44}$$

where $X = (a^\dagger + a)/\sqrt{2}$ and $P = \mathrm{i}(a^\dagger - a)/\sqrt{2}$. We check that there are no terms in first order in a or $a^\dagger$ – as expected from the fact that θ_0 minimizes the energy.

We see that the semi-classical Hamiltonian is then written as the sum of a classical ground state energy H_0, which is nothing less but the expression of H_c in eq. (6.39) for $(\theta, \varphi) = (\theta_0, \varphi_0)$, and a first quantum correction, written in terms of the 'synthetic' position and momentum operators X and P. The first quantum correction can be put in a more convenient way – an explicit harmonic oscillator – as

$$H_2 = \frac{P^2}{2m} + \frac{1}{2} m\omega^2 X^2 + \Delta E \tag{6.45}$$

where m is an effective mass and ω gives frequency of the harmonic oscillator. The additional term ΔE accounts for the additional zero-point energy corrections. Note that all the quantities in eq. (6.45), including the operators X and P, are momentum-dependent. These terms are given by

$$\begin{aligned} \Delta E &= -\left(\tilde{p}\cos\theta_0 - J\cos^2\theta_0(1-\tilde{\Omega}q) + \frac{\tilde{\Omega}}{2}\sin\theta_0\right) \\ \frac{1}{m} &= 2\tilde{p}\cos\theta_0 + \tilde{\Omega}\sin\theta_0 + 2J(\tilde{\Omega}q - 1)\cos 2\theta_0 \\ \omega^2 &= -\frac{2\Delta E}{m} \end{aligned} \tag{6.46}$$

The above derivation thus allows to give a physical insight on the nature of $\hat{H}$, through the calculation of the low-energy quantum corrections to the classical ground state. There are precisely two types of corrections that appear in the expansion. First, there are zero-point energy offsets, in the form of the additional term ΔE, and from the harmonic oscillator energy $\omega/2$. These terms add a non-negligible shift to the classical energy H_0. Then, the harmonic oscillator frequency directly gives the gap between the energy bands. These corrections are plotted in fig. 6.10.

It is important to notice that the energy gap is not constant with respect to p, even in the bulk region. Although this effect is relatively small, it illustrates the limits of the analogy, even at low energy. The inhomogeneity of the gap is even more pronounced for higher energy states, as we will show in the next section.

To conclude this section, we compare the classical ground state – hereafter denoted $|\psi_\mathrm{c}\rangle$ – with the exact ground state $|\psi_0\rangle$ computed from a diagonalization of eq. (6.37). At 0th order, the classical ground state can be approximated by a coherent state $|\psi_\mathrm{c}\rangle \approx |\theta_0, \varphi_0\rangle$ which points in the direction (θ_0, φ_0) that minimizes the classical energy. The first order quantum fluctuations described by eq. (6.45) are taken into account in order to refine the comparison. These fluctuations take the form of a harmonic oscillator, meaning that we can extract a variance $\Delta m_z^2 = J\sin^2\theta_0 m(p)\omega(p)\hbar/2$ along the synthetic dimension (taking into account the rotated basis). This classical variance is compared to the exact variance $\langle \Delta \hat{J}_z^2 \rangle$ (computed from the exact ground state) in fig. 6.11. The correspondence, which is relatively good, suggests that the classical ground state has the shape of a gaussian squeezed state, such as the ones we have introduced in chapter 4. For comparison, we also give in fig. 6.11 the Wigner distribution of the exact ground state for several values of Ω and for $p = 0$. For very low values of Ω, this approximation breaks down.

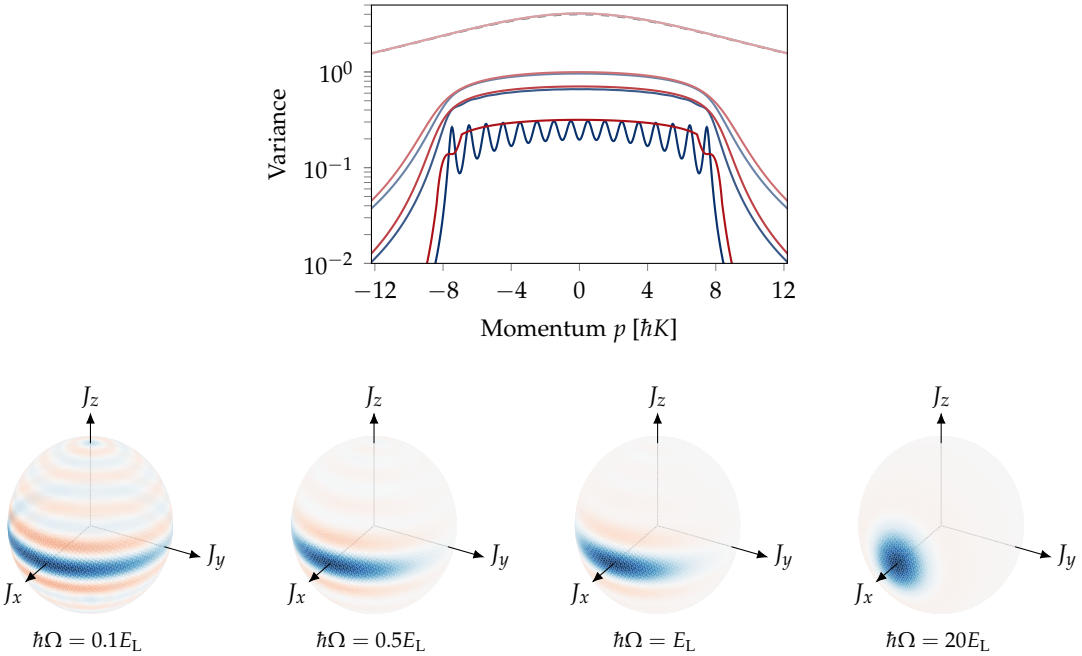

Figure 6.11 – Comparison with the exact ground state. (Top) Variance of the states in the exact ground band as a function of p (blue curves) and variance computed from the classical ground state (red curves) using the lowest order quantum fluctuations. The curves correspond to $\hbar\Omega/E_L = 0.1, 0.5, 1.0$ and 20, from the darkest curve to the lightest. The dashed line (hidden behind the lightest red curve) corresponds to the variance of the coherent state $|\theta_0, \varphi_0\rangle$. (Bottom) Wigner distribution of the exact ground state at $p = 0$. At low values of Ω, the ground state resembles a Dicke state. With increasing Ω, the ground state becomes more gaussian (squeezed states) until it becomes classical (coherent state at $\hbar\Omega = 20E_L$). Note that in the experimental realization presented in next chapter, we work at $\hbar\Omega = E_L$.

We can conclude *in fine* that the exact ground state, for intermediate values of Ω, is well described by a squeezed gaussian state, with the quadrature along the synthetic dimension m_z given by the harmonic oscillator fluctuations Δm_z^2. The squeezing effect gets reduced for larger values of Ω, for which a coherent state approximates well the exact ground state. For very low values of Ω, the squeezing description does not hold anymore, which is intuitively understood by the fact that the exact ground state overlaps with a single $|m_J\rangle$ state, and is thus described by a Dicke state. We can see such an effect in the discretization pattern that emerges at low values of Ω. As such, the *continuum* description of the synthetic dimension is no longer valid, and a full quantum description is necessary.

6.4 Synthetic Landau levels

The classical approximation detailed in the previous section allows to understand the analogy between Hamiltonian (6.37) and the quantum Hall Hamiltonian (6.6). In particular, we have seen that the classical analogy is enough, in a given parameter range, to appreciate the nature of the ground state of the system. The dispersion relation that we computed agrees qualitatively with the one of a Hall system, in the Landau gauge.

In this section, we study the properties of $\hat{H}$ without any classical approximation, and specifically the lowest energy band. The energy dispersion relation is computed, as well as the ground state properties.

6.4.1 Energy spectrum

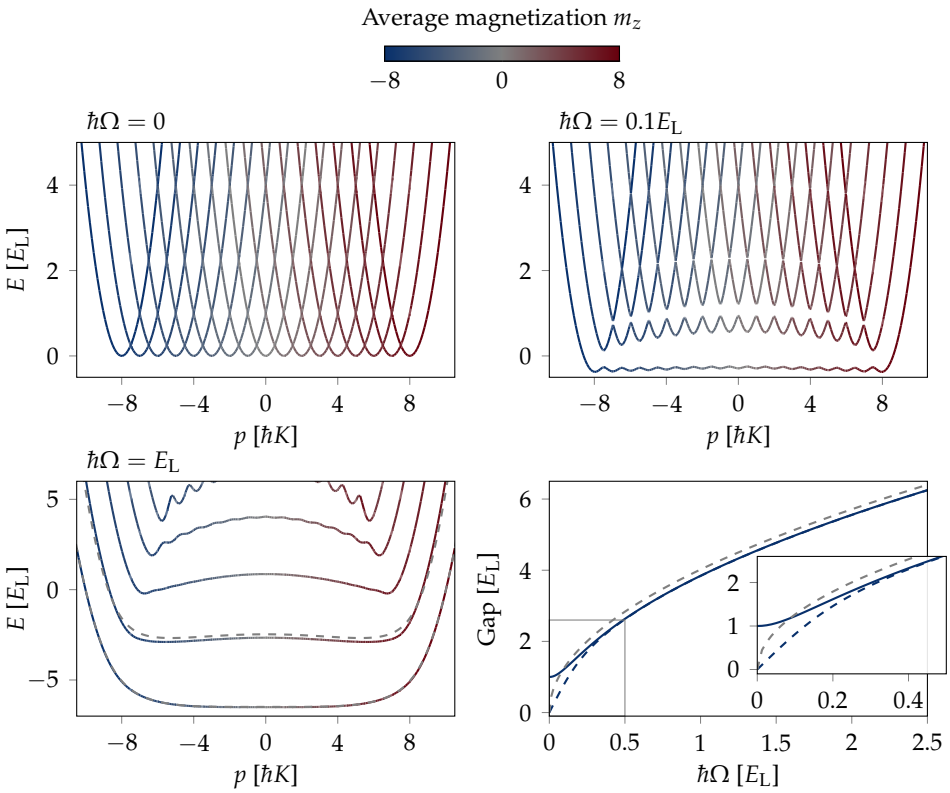

Figure 6.12 – Energy spectrum. Eigenenergies of $\hat{H}$ for $\hbar\Omega/E_L = 0, 0.1$ and 1.0 as a function of the momentum p. The color of the line encodes for the average magnetization m_z (see text). For $\hbar\Omega = E_L$, we also show the semi-classical energy of the ground state and the first excited state (dashed gray lines), computed in the previous section (see fig. 6.10). The agreement is nearly perfect for the lowest band. (Bottom right) Energy gap at $p = 0$ (solid blue line) and at $p = \hbar K/2$ (dashed blue line). Both curves become equal when ω is sufficiently large ($\hbar\Omega \gtrsim 0.5E_L$). The dashed gray line is the classical approximation, given in eq. (6.46). A zoom on the region $\hbar\Omega \leq 0.5E_L$ (rectangle) is given in the inset.

The energy spectrum of $\hat{H}$ for $\delta = 0$ is given in fig. 6.12 for several values of Ω. At $\Omega = 0$, the spectrum consists in 17 uncoupled parabolas, each of them corresponding to a shifted free-particle spectrum. Each of the spin states is thus independent. As soon as Ω is non-zero, a coupling between neighboring spin-states is raised. In the dispersion relation, gaps are opened where crossings become avoided crossings, and the spectrum, at low energy, is separated in independent bands. When $\hbar\Omega$ is raised to the order of the laser recoil energy E_L, the discretization reminiscent of the free-particle parabolas disappear, and the low energy spectrum is constituted of smooth, flat bands. These bands are similar to the ones computed by the classical approximation.

In fig. 6.12, we have also indicated the magnetization corresponding to each state. For

a given p, the diagonalization of $\hat{H}$ gives the eigenenergies and the eigenstates $|\psi_n(p)\rangle$, where n here labels the band. The average magnetization $m_z = \langle\psi_n(p)|\hat{J}_z|\psi_n(p)\rangle$ of each eigenstate is computed for every p, and is encoded in the colorscale of the graphs. We can thus clearly distinguish the effects of spin-orbit coupling: negative (positive) momenta are associated to negative (positive) magnetizations in the low energy bands. In terms of synthetic dimensions, one recovers the association between the momentum p_x and the position $y \equiv m_z$ that was discussed in section 6.1. A more quantitative analysis of the magnetization of the lowest band will be given below.

The energy gap between the lowest band and the first excited band also grows with Ω, and sets the global energy scale of the spectrum. We give in fig. 6.12 the energy gap at the center of the band as a function of Ω. For large values of Ω, the gap at $p = 0$ and $p = \hbar K/2$ coincide, which indicates that the discretization effects that we see at low values of Ω have disappeared. We also see that the classical approximation detailed in the previous section matches relatively well the exact diagonalization.

Overall, the low energy spectrum of our system is very similar to the one of a Hall system with boundaries (see fig. 6.3). In particular, the lowest band reproduces quite well the lowest Landau level (LLL), and we explore below some of the fundamental properties that we can find in our system.

Polarization and detuning to resonance

Before studying in detail the properties of the lowest band, we discuss the choice of polarizations $\mathbf{u}_1$, $\mathbf{u}_2$ that was made at the beginning of section 6.3, as well as the role of the detuning to resonance Δ.

As illustrated in fig. 6.8, the Raman transitions emerge from two-photon transitions, consisting of the absorption of a photon from one laser beam, and of the stimulated emission in the second laser beam. There are two distinct ways of realizing such a scheme: either a $\pi - \sigma_-$ scheme, or a $\sigma_+ - \pi$ scheme. The circular polarization can be obtained *via* the polarization component orthogonal to the B field, $\hat{\mathbf{y}}$ in our case. Indeed, one can write

$$\hat{\mathbf{y}} = \frac{\hat{\boldsymbol{\sigma}}_+ - \hat{\boldsymbol{\sigma}}_-}{\sqrt{2}\mathrm{i}}. \tag{6.47}$$

We can thus consider two extremal cases. In the first one, $\mathbf{u}_1 = \hat{\mathbf{z}}$ carries the π transition while $\mathbf{u}_2 = \hat{\mathbf{y}}$ carries the σ transition, while the roles are inverted in the second case. These situations are illustrated in fig. 6.13.

We can see that the energy spectrum strongly depends on the choice of polarizations. This can be explained by the asymmetry in the coupling coefficients between subsequent Zeeman states, that is also given in fig. 6.13. We specifically plot the coupling strengths

$$\Omega_{m_J,m_J+1} = \left|\langle m_J|\hat{H}|m_J+1\rangle\right|, \tag{6.48}$$

for both cases and in the *symmetric* case, which is the case we implement experimentally by choosing polarizations aligned along $\hat{\mathbf{y}} \pm \hat{\mathbf{z}}$. As we can see, these polarizations essentially allow to have both processes $\pi - \sigma_-$ and $\sigma_+ - \pi$ with equal weights, giving symmetric couplings between the different Zeeman states, and flat bands in the low energy limit[8].

[8] It is also worth pointing out that the symmetric case is achieved whenever $\mathbf{u}_1$ and $\mathbf{u}_2$ have the same

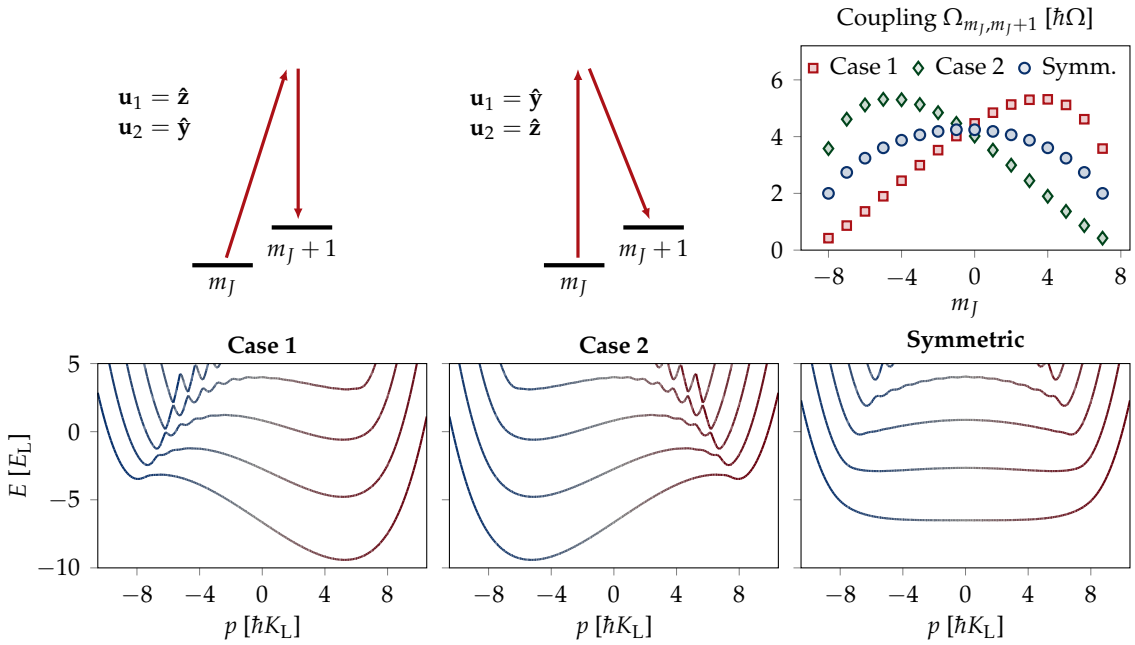

Figure 6.13 – Polarization of the Raman beams. In the first case, the first Raman beam caries the π transition, while the second one carries the σ transition. The roles are inverted in the second case. The bottom plots give the eigenenergies of the resulting Hamiltonians, in the RWA, and for $\hbar\Omega = E_L$. As one can see, both cases are highly asymmetric. The top right plot give the couplings between subsequent Zeeman states – or equivalently the hopping coefficients between different synthetic lattice sites – for both cases. The symmetric case (blue dots) is the one introduced in the previous section, and puts equal weights on both Raman contributions. In the symmetric case, the couplings are more uniform in the synthetic dimension, and are symmetric around $m = 0$. As a consequence, the energy bands are also symmetric – and flatter.

The detuning Δ to resonance is also important, as it sets the sign of the Raman coupling Ω. So far, all the calculations that we have performed assumed a positive detuning $\Delta > 0$, yielding $\Omega > 0$. Although the sign of Ω does not matter for the $\hat{J}_y$ term in $\hat{H}$, it sets the sign of the additional $\hat{J}_z^2$ coupling, which can be seen as a quadratic potential in the synthetic dimension. For positive Ω, this additional term is *anti-trapping*, as it favors extremal states $m_J = \pm J$. In the opposite case, the central state $m_J = 0$ is more energetically favorable.

In order to quantify this effect, we give in fig. 6.14 the energy bands for $\hbar\Omega = \pm E_L$. As we can see, the case of positive Ω gives a flatter band than the other opposite case, which itself motivates our choice of a positive detuning.

A more thorough analysis can be performed by considering the effects of the $\hat{J}_z^2$ term independently, which would be equivalent of being able to tune the parameter q in $\hat{H}$ at will. In practice, it can be done by applying another laser beam on the atoms, with vertical

projection on the z-axis. Here, we consider the case where the angle $(\mathbf{u}_1, \hat{\mathbf{z}}) = -(\mathbf{u}_2, \hat{\mathbf{z}}) = \theta = 45°$. For $\theta = 0°$, *i.e.* when both polarizations are vertical, we only have a $\hat{J}_z^2$ coupling (π-polarization). For $\theta = 90°$, *i.e.* when both polarizations are horizontal, there is only a $\hat{J}_y^2$ term which is off-resonant (it only couples Zeeman substates of the same parity). In the intermediate cases, θ sets the balance between the quadratic terms and the linear $\hat{J}_y$ term.

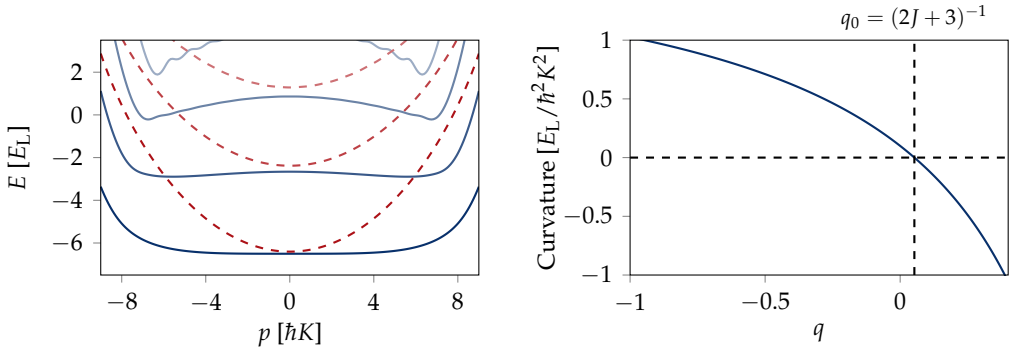

Figure 6.14 – Sign of the detuning. (Left) Low energy spectrum of $\hat{H}$ for $\hbar\Omega = E_L$ (blue solid lines) and $\hbar\Omega = -E_L$ (red dashed lines). The sign of Ω is set by the sign of the one-photon transition detuning Δ of the Raman beams. Positive detunings add an anti-trapping term in the synthetic dimension, and flattens the band. (Right) Curvature at $p = 0$ as a function of the strength q of the $\hat{J}_z^2$ term in $\hat{H}$. The natural value $q_0 = (2J+3)^{-1}$ already gives a curvature very close to 0.

polarization, effectively creating a tensor light shift proportional to $\hat{J}_z^2$. We give in fig. 6.14 the curvature (the second derivative with respect to p) at the center of the lowest band as a function of the parameter q, and for positive Ω. The 'natural' value $q_0 = (2J+1)^{-1}$ allows to almost cancel the curvature, for $\hbar\Omega = E_L$.

6.4.2 Lowest energy band

We now focus on states of the lowest energy band, and explore their properties such as the position in the synthetic dimension (the magnetization), the velocity in the real dimension, and the response to an external force.

Magnetization

The average magnetization was already introduced in fig. 6.12 to qualitatively illustrate the effects of spin-orbit coupling. We go a bit more in details here as we compute the probability distribution over all the m_J states. Results are given in fig. 6.15.

We have seen in section 6.1 that in the Landau gauge, the average transverse position of an electron is proportional to the momentum (we had derived $y_0 = k\ell^2$, with ℓ the magnetic length). We recover this effect in our system, in the bulk, where now the transverse direction is given by the magnetization. In other terms, we can identify the bulk as being the region in momentum space for which $\hbar K m_z \approx Jp$. For large values of $|p|$, we reach the edges of the system, defined by $m_J = \pm J$.

Velocity

The (real dimension) velocity of the ground state can be computed *via* the velocity operator, given in our case by

$$\hat{v} = \dot{\hat{x}} = \frac{1}{i\hbar}\left[\hat{x}, \hat{H}\right] = \frac{1}{m}(\hat{p} - \hbar K \hat{J}_z). \tag{6.49}$$

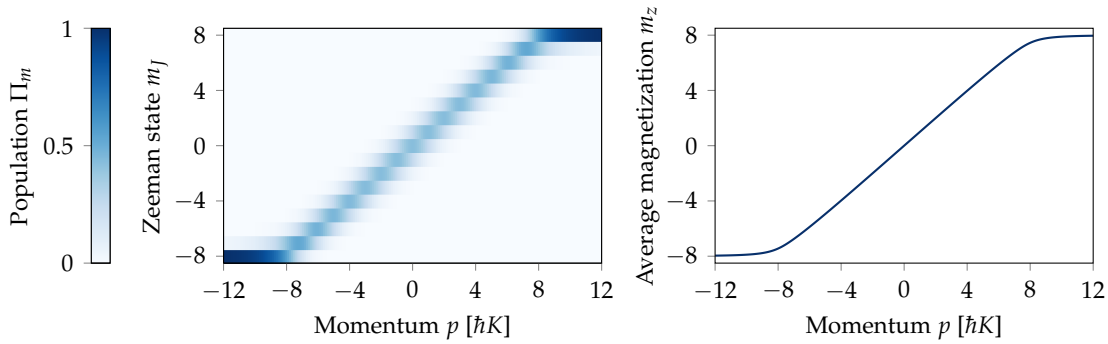

Figure 6.15 – Magnetization of the ground state. (Left) Probability distribution over the m_J states in the LLL, for $\hbar\Omega = E_\mathrm{L}$ and $\delta = 0$. (Right) Corresponding average magnetization.

As such, we recover the kinetic momentum $m\hat{v} = \hat{p} - eB\hat{y}$ introduced in the context of an electron in an external field in section 6.1. The velocity distribution computed for $\hbar\Omega = E_\mathrm{L}$ and $\delta = 0$ is given in fig. 6.16.

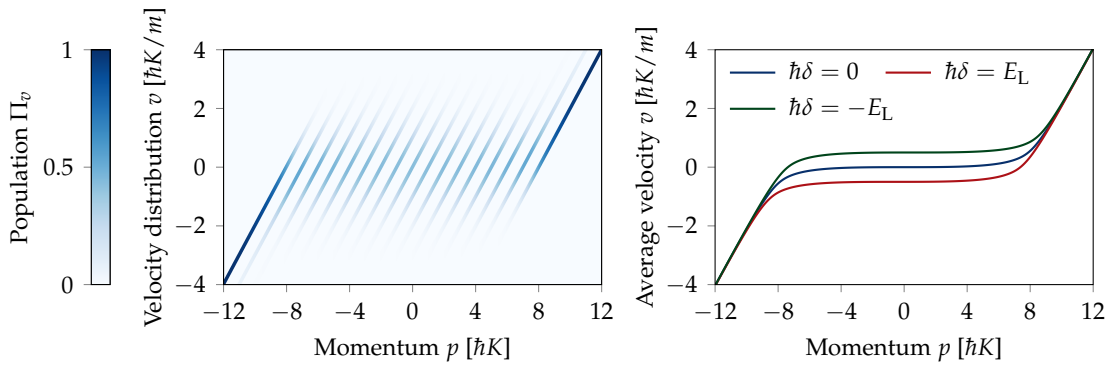

Figure 6.16 – Velocity of the ground state. (Left) Velocity probability distribution in the LLL, for $\hbar\Omega = E_\mathrm{L}$ and $\delta = 0$. (Right) Corresponding average velocity (blue), and average velocities computed for $\hbar\delta = \pm E_\mathrm{L}$ (red and green lines, resp.).

The velocity distribution allows to fully appreciate the specificities of the LLL. On the edges, *i.e.* for $|p| \geq J$, the velocity is non-zero and is chiral, as expected from the discussion of section 6.1. In the bulk, the average velocity goes to 0, which is characteristic of the flat energy dispersion relation.

We furthermore explore the velocity of the ground state in the presence of an additional detuning δ. Such a detuning is associated to the additional $-\hbar\delta\hat{J}_z$ term in $\hat{H}$, which can be interpreted here, in the language of Hall physics, as a voltage across the two edges $m_z = \pm J$ of the sample. Indeed, such a term creates a linear energy shift along the synthetic dimension, effectively creating an energy offset $\Delta V = -2J\hbar\delta$ between the two edges. In fig. 6.16, we see that a non-zero velocity emerges in the bulk when the detuning is non-zero. We thus recover the anomalous velocity we expect in Hall physics: a uniform force in the synthetic dimension gives a non-zero velocity in the real dimension. Numerically, we

estimate the conductance by the ratio

$$\sigma = \frac{I}{\Delta V} = -\frac{1}{2J\hbar\delta}\int \frac{\mathrm{d}p}{h} v(p), \tag{6.50}$$

where the current I is given by the integral over the whole band of the velocity, and we find $\sigma = 1/h$ up to numerical precision, which is consistent with the quantization of the Hall conductance defined by eq. (6.11).

Local density of state

Both the magnetization and velocity, that we just discussed, are gauge dependent quantity: they are expressed as a function of the momentum p, which is a good quantum number in the Landau gauge only. In order to get rid of the gauge dependence, we compute the combined probability distribution $P(v, m_J)$, which can be considered here as a local density of states. Results are given in fig. 6.17. As we can see, there is a clear correlation between the synthetic position m_J and the velocity v. In particular, we recover the chiral edge modes in $m_J = \pm J$, and a vanishing velocity in the bulk.

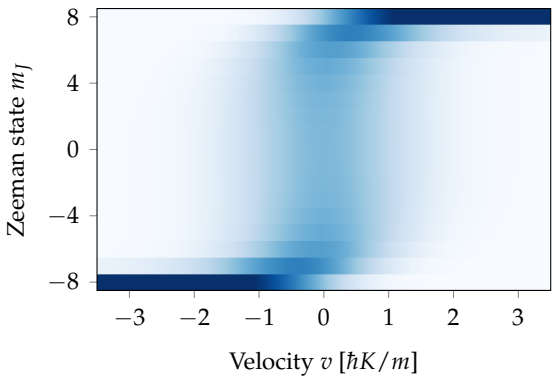

Figure 6.17 – Local density of states. Joint probability distribution $P(v, m_z)$, as a representation of the local density of states, for $\hbar\Omega = E_\mathrm{L}$ and $\delta = 0$.

Local markers of topology

The topology of the system can be exhibited using the local Chern marker (LCM) that we have already introduced in section 6.1. Its expression is adapted from eq. (6.19) to synthetic dimensions by the substitution $\hat{y} \leftrightarrow \hat{J}_z$, and we simply write

$$c(x, m_J) = -2\mathrm{i}\pi \langle x, m_J | [\hat{P}\hat{x}\hat{P}, \hat{P}\hat{J}_z\hat{P}] | x, m_J \rangle . \tag{6.51}$$

Its expression can be simplified to (see appendix B for a detailed calculation)

$$c(m_J) = \frac{1}{\hbar K}\int \mathrm{d}p \Pi_{m_J}(p) \partial_p [p - mv(p)]. \tag{6.52}$$

For the integration, we take the values of p such that the maximum energy lies at half the gap at $p = 0$. The LCMs are given in fig. 6.18. We recover a similar behavior than for the standard quantum Hall effect (see fig. 6.5), namely a Chern marker equal to 1 in the bulk, and a sharp decrease on the edges.

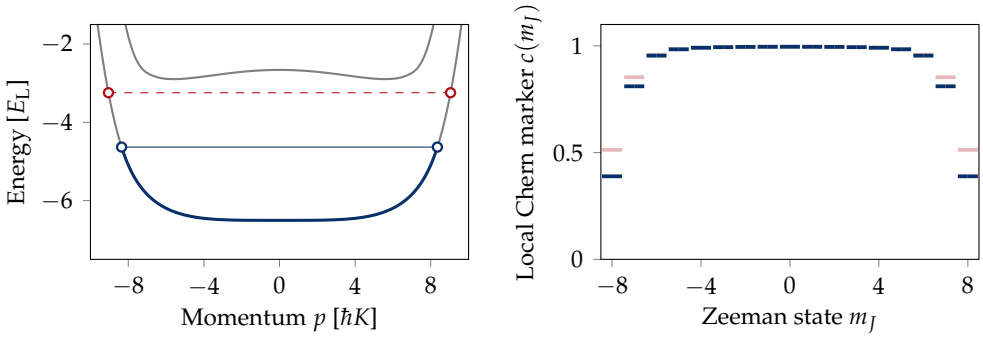

Figure 6.18 – Local Chern marker in synthetic dimension. (Left) The states used for computation of the LCM are indicated in blue, and correspond to all the momenta p such that the ground band energy lies below half the gap at $p = 0$. (Right) Local Chern marker as a function of the synthetic position. In red we give the local Chern markers corresponding to a lowest band filled almost up to the first excited band (red dashed line on the left graph). As we can see, the LCMs stay the same deep in the bulk, and are changed only close to the edges.

We furthermore point out here that the integration domain chosen here, if used on eq. (6.50), yields a reduction of the conductance of about 5 %. Such a reduction is precisely a consequence of the sharp edge effects mentioned in section 6.1.

6.4.3 Conclusion

In this chapter, we have detailed how we can realize a Hall Hamiltonian in the Landau gauge, by implementing spin-orbit coupling on dysprosium atoms and by considering the internal state as a synthetic dimension. In particular, we have extensively described the energy spectrum of the realized Hamiltonian, and shown that its structure is very similar to the one a the *standard* quantum Hall effect, using charged particles and real magnetic fields.

In this last section, we have focused on the ground state, which mimics the lowest Landau level (LLL). We were able to give meaning to the characteristics of the LLL in terms of synthetic dimension. As such, we expect to see a *locking* between the momentum p and the synthetic position m_z, as well as a suppression of the kinetic energy in the bulk and the appearance of chiral edge modes. With such a description, we can already define bulk and edge regions in our system, and appreciate their relative sizes. In fig. 6.16 for instance, we see that the average velocity is close to zero over a large region in p-space. To be more quantitative, we have $|v| \leq 0.1\hbar K/m$ for $|p| \lesssim 5.5\hbar K$. As such, we expect to be able, experimentally, to probe both the bulk and the edges of the system.

A key advantage of using synthetic dimensions lies in the detection scheme. Our Stern-Gerlach apparatus indeed gives us access to the populations in each of the m_J states. In other term, we have a *single site resolution* in the synthetic dimension. We will see in the next chapter see that this feature allows us, in combination with the usual time-of-flight detection, to probe *locally* the elementary excitations of the system, known as cyclotron and skipping orbits.

Finally, we have briefly mentioned the anomalous transport properties that we expect as well. We have discussed at the beginning of the chapter how these transport properties are intrinsically linked to the topology of the energy bands. These properties will also be explored in the next chapter, dedicated to the experimental implementation that we have discussed here.

7 Experimental realization of synthetic Landau levels

7.1 Experimental implementation **132**
7.1.1 Alignment and intensity calibration 133
7.1.2 Conservation of canonical momentum 134
7.2 State preparation in the ground band **134**
7.2.1 Velocity and magnetization distributions 137
7.2.2 Local density of states 138
7.3 Cyclotron orbits **139**
7.3.1 Experimental protocol 139
7.3.2 Cyclotron orbits and gap measurement 140
7.4 Hall conductance and topological markers **142**
7.4.1 Hall mobility 142
7.4.2 Hall conductance 143
7.4.3 Local Chern marker 144
7.5 Conclusion **145**

In the previous chapter, we extensively described how we can realize Landau levels by implementing spin-orbit coupling on dysprosium atoms, and by considering the internal angular momentum state as a *synthetic dimension*. This chapter is dedicated to the experimental realization of such a scheme. In this study, we use a BEC of dysprosium, of typically 20×10^3 atoms at roughly 100 nK[1]. For the sake of simplicity, we write again the Hamiltonian that we implement,

$$\hat{H} = \frac{(\hat{p} - \hbar K \hat{J}_z)^2}{2m} - \hbar\Omega \left(\hat{J}_y + \frac{\hat{J}_z^2}{2J+3} \right) - \hbar\delta \hat{J}_z, \tag{7.1}$$

and that was derived in section 6.3.

Here, we start with a description of the technical implementation of $\hat{H}$, *i.e.* the optical setup and the beam intensity calibration. We then move to the preparation of the ground

[1] Here again, we stress that we do not probe interaction effects between individual atoms. As for the study of chapter 5, the temperature and density of the cloud are of little importance.

state. The protocol is described in details, and we give the measured magnetization and velocity distributions, already introduced at the end of the previous chapter.

We are furthermore able to probe the elementary excitations of the system, called *magnetoplasmons*, and which are the quantum analogue of classical cyclotron and skipping orbits. These measurements allow to give a complete and intuitive analogy between our system and a quantum Hall system, with a clear distinction of behavior between the edges and the bulk.

We finally probe the transport properties that arise in quantum Hall systems, namely the emergence of a quantized transverse conductance. In particular, we make the link between the measured conductance with the emergence of a non-trivial topology in the bulk of the system, that we can probe locally by measuring local Chern markers.

Most of the results presented in this chapter were published in [Chalopin et al. 2020].

7.1 Experimental implementation

The experimental setup used to realize $\hat{H}$ is given in fig. 7.1. It essentially consists in installing a second laser beam, identical to the one used to realize the non-classical spin states discussed in chapter 5. This second laser beam is counter-propagating to the first one, in order to realize Raman transitions discussed in section 6.3. A constant magnetic field is applied, such that the splitting between two subsequent Zeeman levels is about 300 kHz. This splitting is enough to ensure negligible contribution of the non-resonant terms in the Raman processes, and thus apply the rotating-wave approximation (RWA).

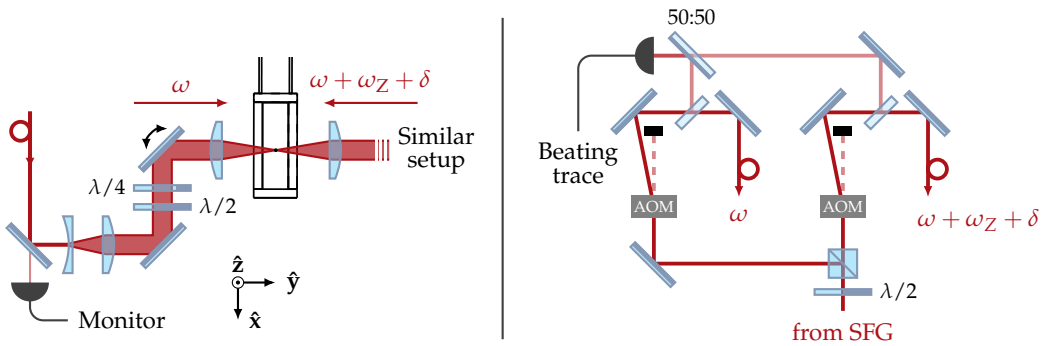

Figure 7.1 – Raman setup. (Left) Simplified optical setup around the glass cell. Each beam comes from a fiber, and its shape is adjusted to have a waist of $\sim$ 50 µm on the atoms. The intensity of each beam is monitored on a photodiode. The polarization can be arbitrarily chosen using the waveplates, and the position of the beams can be finely tuned using piezo-mirrors. (Right) Simplified optical setup before the fibers. A 626 nm laser beam, coming from the sum frequency generation setup (SFG, see appendix A), is split in two beams. The frequency and intensity of each beam can be independently tuned with the AOMs. A small fraction of each beam is also collected, and sent to a photodiode in order to record a beating trace and access the frequency difference.

7.1.1 Alignment and intensity calibration

As discussed in chapter 6, we choose a positive detuning $\Delta > 0$ with respect to the excited state. To give orders of magnitude, we have $\Delta \approx 2\pi \times 21\,\text{GHz}$ and waists on the atoms of $w_0 \approx 50\,\mu\text{m}$. A coupling $\hbar\Omega = E_\text{L}$ is then reached for an optical power $P \approx 10\,\text{mW}$ in each beam. Here, we describe the alignment and calibration protocol of the individual laser beams.

Each blue-detuned beam produces a repulsive light-shift on the atoms, that we can use for alignment. One of the laser beams is shone on the atoms, while the dipole traps are turned off and gravity is compensated by a magnetic field gradient along the vertical direction. The intensity of the beam and duration of the pulse are empirically chosen to see a displacement of the atoms without completely losing them. We typically use 100 mW and a few ms. The cloud shape is then recorded, and the beam is moved until the density distribution after application of the pulse is radially symmetric. The atoms are indeed expelled in every direction away from the laser beam, and we see a ring of atoms. Examples of images are given in fig. 7.2.

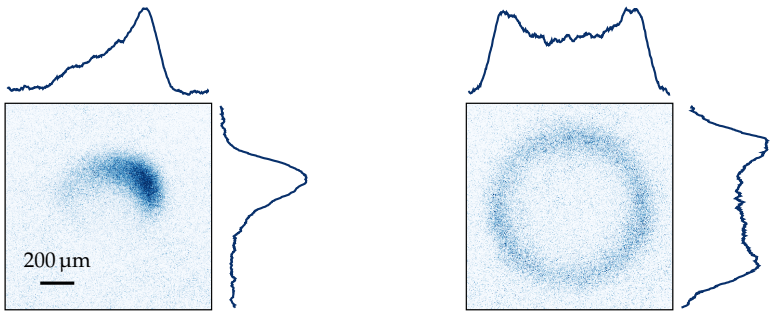

Figure 7.2 – Alignment procedure. Each beam, being blue-detuned, creates a repulsive potential on the atoms. We record the density distribution after pulsing the beam on the atoms. Before alignment (left picture), the density distribution is anisotropic. After alignment (right picture), the density distribution is radially symmetric and the cloud forms a ring. Solid lines are integrated profiles.

Once aligned on the atomic cloud, the light intensity can also be calibrated by looking at the size of the formed ring. Indeed, the expelled velocity v_e of an atom is directly related to the applied repulsive potential U, by energy conservation

$$\frac{1}{2}mv_\text{e}^2 = U. \tag{7.2}$$

Using the expression for the atom-light interaction, given by the term $\hat{H}_\text{L}$ in eq. (6.25) in the previous chapter, for a linearly polarized beam and considering that the atoms are each spin polarized in the $|-J\rangle$ state, one can write

$$U = \frac{3\pi c^2\Gamma}{2\omega_0^3}\frac{I}{\Delta}\left[\alpha_0 + \frac{\alpha_2}{J(2J-1)}\left[3\left\langle -J\right|\left|\mathbf{u}\cdot\hat{\mathbf{J}}\right|^2\left|-J\right\rangle - J(J+1)\right]\right], \tag{7.3}$$

with $\mathbf{u}$ the beam polarization. The expelled velocity thus directly gives the intensity I on the atoms, all the other parameters being known.

The velocity is given by $v_e = \dot{r}(t)$, where $r(t)$ is the ring radius after a time t. An example of such a measurement is given in fig. 7.3.

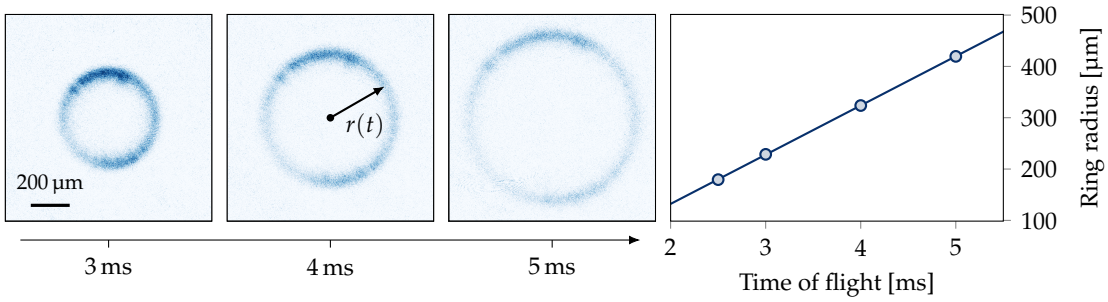

Figure 7.3 – Intensity calibration. We calibrate the beam intensity by measuring the velocity of the expelled atoms. On the left, we show pictures of the ring for different times. The radii are extracted from a ring-shape fit, and plotted against time in the right graph. The velocity is extracted from a linear fit.

7.1.2 Conservation of canonical momentum

One of the key features of the Hamiltonian (7.1) is the conservation of the *canonical momentum* $p = \langle \hat{p} \rangle$, as one has $[\hat{p}, \hat{H}] = 0$. In our case, the canonical momentum is given by

$$\hat{p} = m\hat{v} + \hbar K \hat{J}_z, \tag{7.4}$$

where $m\hat{v}$ is the kinetic momentum. This conservation law can directly be observed experimentally. Indeed, the velocity distribution in the cloud can be accessed by time-of-flight measurements, while the spin distribution is measured by the Stern-Gerlach apparatus.

We give in fig. 7.4 examples of images that show that the momentum is indeed conserved. Starting with a BEC at rest in the lowest Zeeman sublevel $|m_J = -J\rangle$, we quench the Raman coupling on resonance ($\delta = 0$). Each spin flip induced by the Raman transition is also accompanied by a velocity kick in the real dimension, hence the conservation of p.

7.2 State preparation in the ground band

The ground band is probed by measuring both the velocity and magnetization distributions for several values of the momentum p. Experimentally, a given p-state is prepared by a sweep of the additional detuning δ, as follows.

The counter-propagating Raman beams create a running wave on the atomic cloud. In the RWA, and for $\delta = 0$, this running wave becomes a standing wave for the atoms. As such, $\delta \neq 0$ is associated to a moving lattice[2].

We can now consider the dynamics in the lattice reference frame, moving at a velocity δ/K with respect to the lab frame. A detuning that changes with respect to time is then

[2]The beam polarizations being orthogonal, the Raman beams do not create an optical lattice in the usual way (an intensity interference pattern). In our case, the lattice we consider is associated to the periodic modulation of the light field polarization.

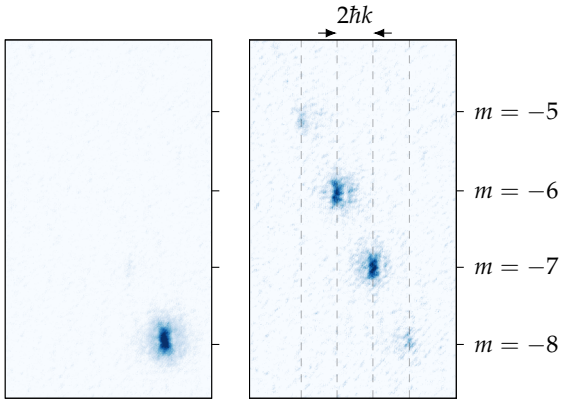

Figure 7.4 – Conservation of canonical momentum. Each picture is an average of about 10 experimental realizations. (Left) Initial state, without the Raman coupling. The atoms are at rest, in the lowest Zeeman sublevel $|-J\rangle$. (Right) After quenching the Raman coupling, higher Zeeman states get populated, and the atoms acquire a non-zero velocity. Overall, the quantity $\langle\hat{p}\rangle = mv + \hbar K m_z$ is conserved.

associated to an accelerated reference frame. An inertial force $F = m\dot{\delta}/K$ emerges from such a moving frame, and the Newton equation $\dot{p} = F$ yields

$$p = p_0 + m\frac{\delta}{K}, \tag{7.5}$$

with p_0 the initial momentum. In our case, we always start with a spin-polarized BEC at rest, such that $p_0 = -J\hbar K$. The momentum p can thus be arbitrarily chosen, simply by changing the detuning δ. The state preparation protocol is illustrated in fig. 7.5.

Experimentally, the detuning is set by means of a voltage controlled-oscillator, which controls the frequency of one of the Raman beams. We typically use detuning ramps of about 2 kHz/µs. In order to check whether the ramp is actually the one we aim for, we record, for each experimental run, a beating trace between the two beams. This technique allows to precisely measure the final detuning, and consequently the p-state that is prepared. A typical beating trace is also given in fig. 7.5.

The ramp speed is chosen according to simulations of the ground state preparation protocol. Numerically, the time-dependent Schrödinger equation resulting from the time-dependent value of δ is integrated, giving a final state $|\psi_f(t)\rangle$. In the simulation, the momentum p is not changed and is equal to $p_0 = -J\hbar K$. The resulting state is then compared to the expected ground state $|\psi_0(p)\rangle$ at $\delta = 0$ and with the substitution $p = p_0 + m\delta/K$, *via* the overlap $|\langle\psi_f(t)|\psi_0(p)\rangle|^2$. Results are given in fig. 7.6.

In the simulation, we apply linear ramps, with $\hbar\delta$ going from $-10E_L$ to $42E_L$. These values correspond to $p = -13\hbar K$ and $p = 13\hbar K$ respectively. As expected, we see that adiabaticity is lost for large ramp speeds. We point out here that for intermediate ramp speeds, the final state (large p) is reached with a better overlap than all the intermediate states[3]. In order to get a quantitative estimation of the ramp speed that we need, we

[3]This effect can be understood by writing the time evolution of the state. A precise calculation shows indeed that the state is the time-dependent ground state dressed by an additional term essentially proportional

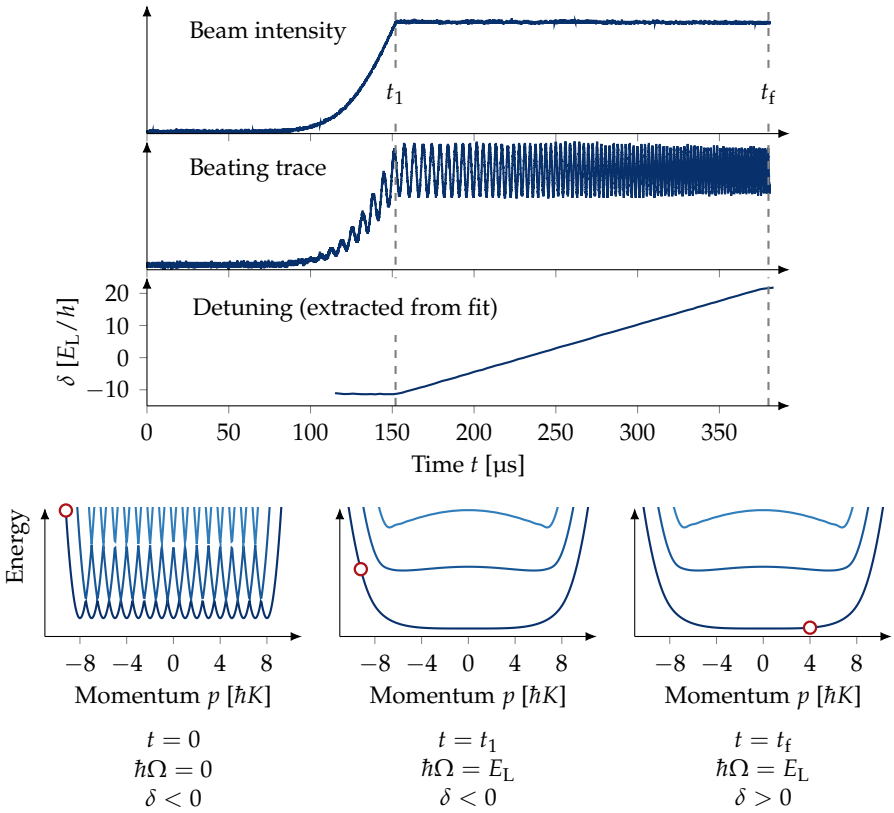

Figure 7.5 – State preparation protocol. The time traces of the beam intensity, of the beating signal, and of the detuning are given in the top graphs. We start with a detuning δ_i large and negative, and ramp up the beam intensity for $0 \leq t \leq t_1$, to a value that corresponds to $\hbar\Omega = E_L$. The detuning, at time t, is extracted from a local fit of the beating trace around time t. For $t \leq t_1 \leq t_f$, the detuning is linearly ramped to its final value δ_f. In the lattice frame, our initial state corresponds to $p_i = p_0 + m\delta_i/K < -J$. The state is marked by the red circle on the dispersion relation. At $t = t_1$, we are still at $p = p_i$, but the gap is now opened. At $t = t_f$, we are at $p = p_f = p_0 + m\delta_f/K$

compute the final magnetization of the state, after a ramp to $p = 18\hbar K$, as a function of the ramp speed, and we compare it to the experiment. Results are given in fig. 7.6. We see that the simulations agree relatively well with the data, and that we reach the expected final states for ramp speeds up to $\sim 4\,\text{kHz}/\mu\text{s}$. This experimental check furthermore supports our choice of $2\,\text{kHz}/\mu\text{s}$. We also check numerically that the overlap with all intermediate states, throughout the whole ramp, remains above 95 %. In fact, such a ramp speed value is a good trade-off between perfect state preparation and experimental difficulties arising from long experimental protocol. Indeed, longer ramps are associated to an increasing probability to scatter photons, leading to heating of the cloud and decoherence. To give orders of magnitude, we have $E_L/\hbar = 2\pi \times 12.58\,\text{kHz}$, which means that a typical ramp $p = -13\hbar K \to p = 13\hbar K$ already takes $\sim 330\,\mu\text{s}$ in the case of a ramp speed of $2\,\text{kHz}/\mu\text{s}$. Given the experimental parameters that we use (namely detuning and intensity), we estimate the probability to have scattered a photon to be on the order of 0.5 % after the

to the rate of change of the Hamiltonian and inversely proportional to the energy gap. At the end of the ramp, this additional term has a smaller effect than at the center of the band, where the gap is a lot smaller.

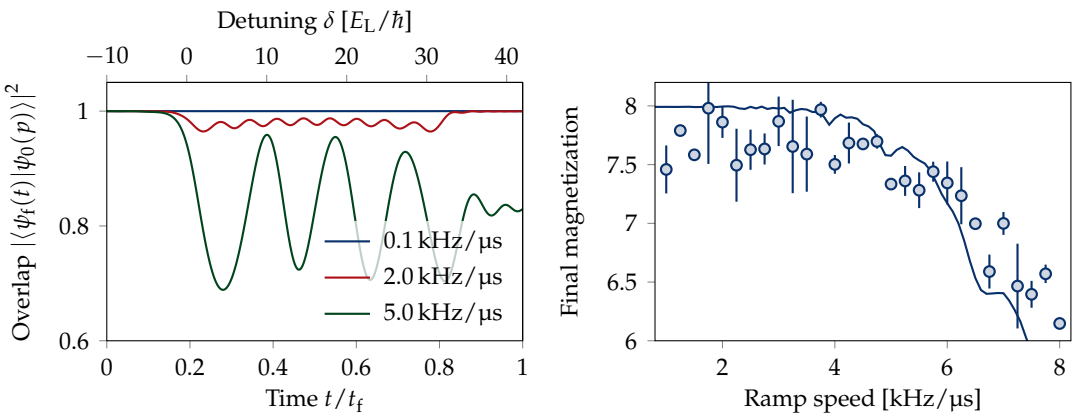

Figure 7.6 – Adiabaticity of the ground state preparation. (Left) Overlap between the prepared state (obtained from numerical integration) and the target state (obtained from diagonalization). The detuning ramp is linear and goes from $-10E_L/\hbar$ to $42E_L/\hbar$. Three different ramp speeds are shown. (Right) Experimentally, adiabaticity is checked by measuring the final magnetization as a function of the ramp speed, for a final detuning corresponding to $p = 18\hbar K$. The solid line is obtained from numerical simulations.

preparation, which is considered negligible here. For slower ramps, this probability is increased, and the preparation protocol breaks down[4].

7.2.1 Velocity and magnetization distributions

Both the spin and velocity distribution are measured as a function of the canonical momentum p. The spin composition is given in fig. 7.7.

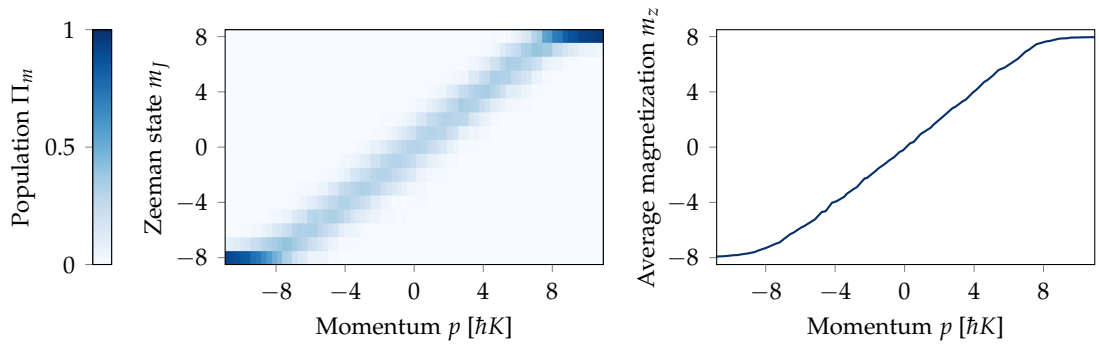

Figure 7.7 – Spin distribution of the ground band. (Left) Measured population in each of the Zeeman sublevels and (right) computed averaged magnetization $m_z = \langle \hat{J}_z \rangle$.

We recover the expected behavior, derived in section 6.4 of the previous chapter. For $|p| \leq J$, we observe a *spin-momentum locking* mechanism, for which the average magnetization is well defined by $m_z = p/\hbar K$. This region of p-state will often be referred

[4]Experimentally (not shown here), we indeed observe that the state prepared for slow ramps does not match the target state.

as the bulk region of the band. In terms of quantum Hall physics, we recover the relation between momentum in one direction and position in the transverse (synthetic) direction, which is characteristic of the Landau gauge.

For $|p| > J$, the magnetization is solely given by $m_z = J\,\mathrm{sign}(p)$. Physically, such a behavior is associated to the boundaries of the system. Indeed, in the synthetic dimension, the highest and lowest states, $|m_J = J\rangle$ and $|m_J = -J\rangle$, correspond to the edges. These edges get populated when the momentum p corresponds to the regions of the energy band in which we have the parabola branches reminiscent of the free-particle dispersion relation.

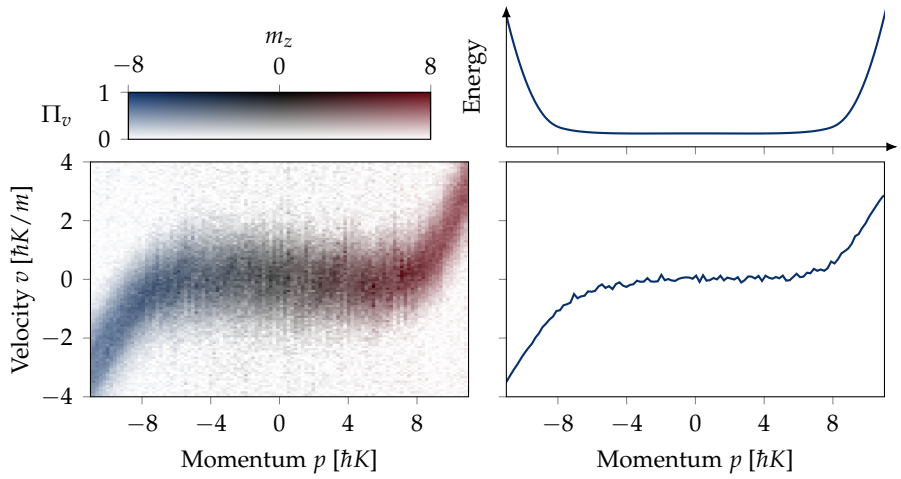

Figure 7.8 – Velocity distribution of the ground band. (Left) Measured velocity distribution as a function of the momentum. Colored regions indicate high population. The color encodes the average magnetization, given in fig. 7.7. (Right) Average value of the velocity (bottom). The dispersion relation of the ground band is also given (top) for reference (see text for details).

The measured velocity distribution is given in fig. 7.8. Again, we have two distinct behaviors, associated to the bulk and edge regions. In the bulk, the velocity distribution is centered around 0, while it becomes non-zero on the edges. The edge velocity furthermore exhibit a striking chiral behavior: the velocity is on average negative on the $|-J\rangle$ edge, while it is positive on the other one.

We also give in fig. 7.8 the average value of the velocity as a function of p, along with the dispersion relation. One can see that the overall behavior of the velocity is qualitatively consistent with the result $v = \partial_p E(p)$, and that was already mentioned in chapter 6. Indeed, in the bulk, a flat band yields a vanishing velocity, while the non-zero chiral behavior comes from the parabola branches on each edge.

7.2.2 Local density of states

A more intuitive representation of the physics of the ground band is obtained from the combined probability distribution $P(m_J, v)$, which we introduced as a gauge-independent quantity that represents the local density of states (see section 6.4.2 in the previous chapter). We can compute it by combining the measured data of fig. 7.7 and fig. 7.8. The resulting distribution is given in fig. 7.9.

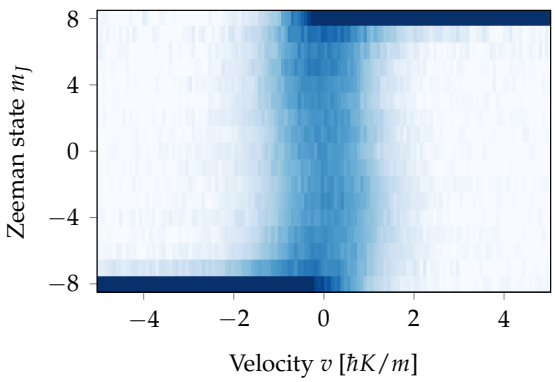

Figure 7.9 – Local density of states. Probability distribution in magnetization and velocity space, giving an intuitive picture of the distinction between the edge and the bulk physics.

The chiral behavior, and its correlation with the (effective) position in synthetic space, is here again unambiguous. Over a wide region $|m_J| \lesssim 5$, considered as the bulk region, the velocity distribution is centered around 0. Only on the edges does one find non-zero velocities. More specifically, states with negative average velocities are associated to one edge ($m_J = -J$), while positive velocities are found on states in the other edge ($m_J = J$).

Overall, the representation given in fig. 7.9 matches well the expected results one may find in the quantum Hall effect. Indeed, as we have seen in chapter 6, a quantum Hall system exhibits distinct behaviors on the edges and in the bulk. The boundaries of the system are the support of chiral edge states, corresponding in our case to the non-zero velocities acquired by particles in $|m_J = \pm J\rangle$. In the bulk of a quantum Hall system, the average velocity also vanishes, and we measure it for $|m_J| \lesssim 5$ in our case.

7.3 Cyclotron orbits

In the previous section, we have seen how the magnetization and velocity of the ground states behave. In particular, we have directly observed a bulk/edge distinction, with the emergence of chiral edge modes. This section is dedicated to elementary excitations that we can measure in the ground band. The semi-classical analogue of these excitations are the famous cyclotron orbits (bulk) and skipping orbits (edges), that one may derive by considering the classical motion of a charged particle in a magnetic field.

7.3.1 Experimental protocol

The elementary excitations above the ground band are induced by pertubative quenches of the system. Experimentally, we prepare a given p-state using the protocol described in fig. 7.5. We then quench the detuning δ by $\delta_0 = 2E_L/\hbar$, such that the prepared state is no longer an eigenstate of the system, but rather a quantum superposition of the first excited bands. These excitations are often referred to as *magnetoplasmons* [Cooper et al. 2019]. This experimental scheme is illustrated in fig. 7.10.

The magnetization and velocity distributions are then recorded as a function of time. We clearly observe an oscillation of both distributions, as a consequence of the quench.

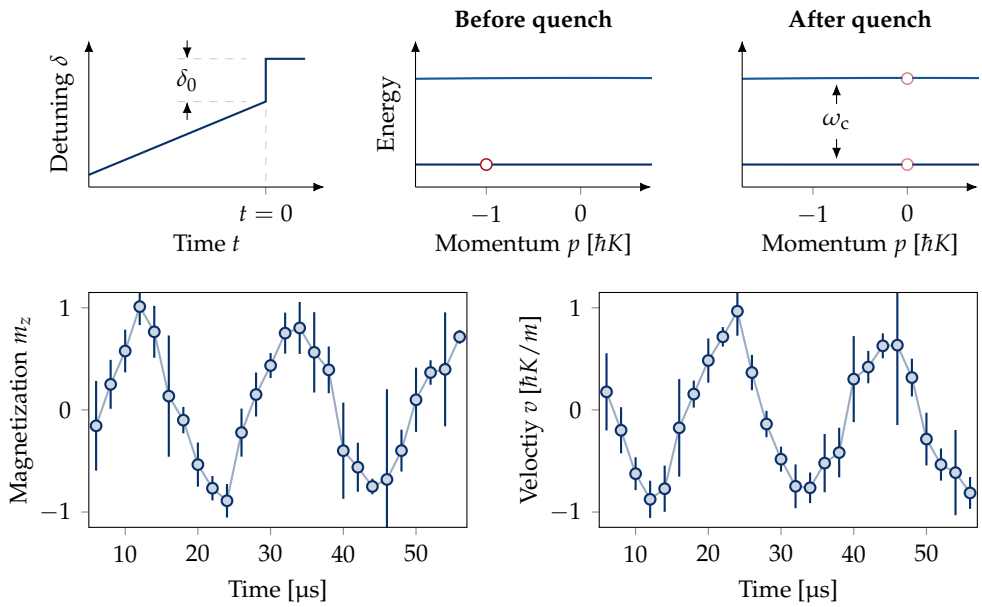

Figure 7.10 – Probing elementary excitations. The initial state is prepared using the protocol described in fig. 7.5. The detuning is then quenched by $\delta_0 = 2E_L/\hbar$, and we define $t = 0$ the time of this quench (top left plot). The prepared state, after the quench, becomes a superposition of the first two bands. We then measure the average magnetization (bottom left) and average velocity (bottom right) as a function of time. These observables oscillate at the gap frequency ω_c. For these traces, the prepared state, preceding the quench, corresponds to $m_z \approx -1$.

Examples of oscillations are given in fig. 7.10. In order to actually represent the trajectory of the state, the position x is computed from the measured average velocity, as $x = \int \mathrm{d}t\, v(t)$. The resulting trajectory is given in fig. 7.11.

The trajectory that is reconstructed is approximately a closed, cyclotron orbit. We measure here almost two full circles, with a negligible global drift.

7.3.2 Cyclotron orbits and gap measurement

The above measurement is repeated for several initial states in the bulk region and on the edges. We give a global picture of the trajectories in fig. 7.12. All the orbits in this figure are obtained using the same experimental protocol described above, except for the edge trajectory starting in $|m_J = J\rangle$ (represented in red), for which we rather quench the amplitude of the Raman coupling, with the detuning on resonance. We find it experimentally easier to do this, because such an initial state is naturally obtained after evaporation. It does not fundamentally change the results: by quenching the coupling, several bands are populated and we measure the subsequent time evolution of the system.

Again, the bulk/edge difference is striking. We measure closed cyclotron orbits in the bulk, for $|m_z| \lesssim 5$. As in the example of fig. 7.11, the position drift of these orbits is negligible. Close to the edges, we can still distinguish orbits, but we can now see a global drift of the position.

This drift is a signature of the edge effects, and is most visible when the initial state

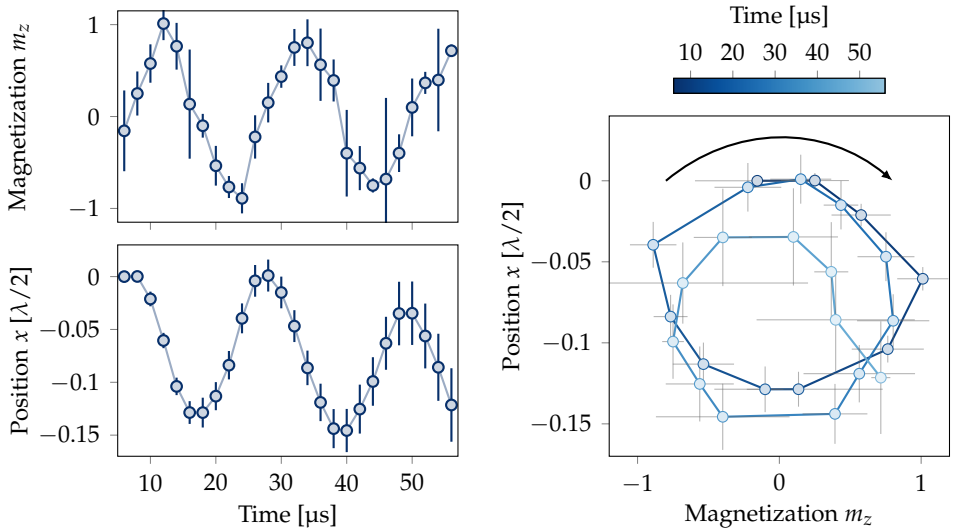

Figure 7.11 – Bulk cyclotron orbit. (Left) Magnetization (top, same as in fig. 7.10) and position (bottom, computed from the integration of the velocity) as a function of time. (Right) Resulting orbit in (m_z, x) coordinate system. The color encodes for time, and the arrow indicates the direction of movement.

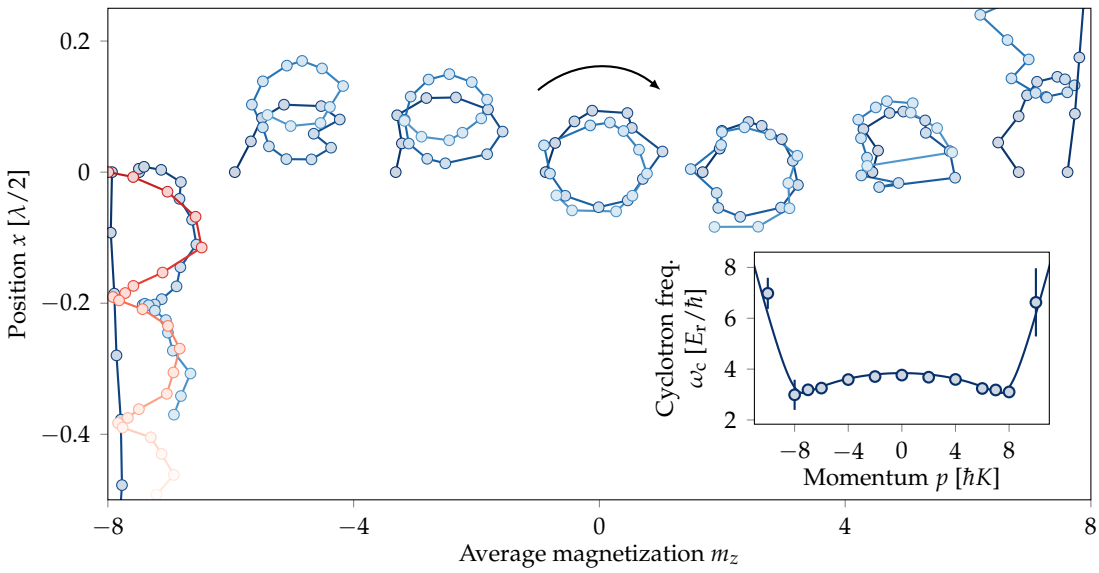

Figure 7.12 – Cyclotron orbits. Trajectories measured for several initial states. The red trajectory, which starts at $m_z = -J$, is obtained from a quench of the Raman beam intensity rather than detuning. (Inset) Measured cyclotron frequencies, given, by definition, by the oscillations frequencies. The solid line is the expected behavior for $\hbar\Omega = E_L$.

precisely sits on the boundary. In that case, we observe skipping orbits, which are an expected feature of a Hall system with sharp boundaries. For an intuitive picture, one may interpret these trajectories by semi-classical cyclotron trajectories which are truncated by the sharp boundaries, and *rebound* on the edge. As a result, a non-zero chiral drift emerges on the edges.

As for the physics of a charged particle in a magnetic field, the frequency associated to these orbits corresponds the gap frequency, given by the energy difference between the lowest and the first excited Landau levels. This is quite clear, considering our quench protocol. Indeed, by preparing a superposition of the lowest and first excited bands, the gap frequency becomes the only possible energy scale that is found in the dynamics. We can thus extract the gap over the whole band, simply by measuring the frequency of each orbit. The results are given in the right graph of fig. 7.12, and match well the theoretical prediction indicated by the solid line.

7.4 Hall conductance and topological markers

In this last section, we focus on the Hall effect that emerges in our system, namely the occurrence of an anomalous drift upon the application of a force, and the existence of a non-trivial topology.

7.4.1 Hall mobility

As we have seen in the previous chapter, the classical Hall effect consists in the emergence of a transverse velocity when a force is applied on the charge carriers. Such a transport property is often referred to as the *Hall current*.

In our system, we can measure the real space velocity resulting from the application of a force in the synthetic dimension. The *synthetic* force comes from the detuning δ which, in the laboratory reference frame, causes an additional term $-\hbar\delta\hat{J}_z$ in the Hamiltonian. Such a term results in an energy difference between the two edges of the system, similarly to the application of an electrical potential on the edges of a standard Hall system. Here specifically, the energy difference is $\Delta V = -2J\hbar\delta$, which causes an effective force in the synthetic direction $F = -\Delta V/2J = \hbar\delta$ (see fig. 7.13).

In order to compute the mobility, we consider the perturbative action of the force on the Hamiltonian. In particular, we can write

$$\hat{H}_{\hat{p}} - \hbar\delta\hat{J}_z = \hat{H}_{\hat{p}+m\delta/K} - \frac{\delta}{K}\hat{p} + \mathcal{O}[(\hbar\delta)^2], \tag{7.6}$$

where $\hat{H}_{\hat{p}}$ is the unperturbed Hamiltonian, given by eq. (7.1) in the case $\delta = 0$, and whose eigenstates are denoted $|\psi_p\rangle$. The eigenstates of the perturbed Hamiltonian are then obtained from $|\psi_{p+m\delta/K}\rangle$, but with an additional velocity $-\delta/K$. Overall, one finds, up to leading order in $\hbar\delta$,

$$\langle\hat{v}\rangle = \langle\hat{v}\rangle_0 + \mu\hbar\delta \qquad \text{with} \qquad \mu = \frac{1}{\hbar K}\frac{\partial}{\partial p}\left(m\langle\hat{v}\rangle - p\right), \tag{7.7}$$

where $\langle\hat{v}\rangle_0$ is the velocity of the unperturbed state. The Hall mobility μ characterizes the linear response of the system to the application of the force $F = \hbar\delta$.

In the bulk, since $\langle\hat{v}\rangle$ vanishes, we expect to have a non-zero mobility $\mu = \mu_0 = -1/\hbar K$. Considering the analogy $\hbar K\hat{J}_z \leftrightarrow eB\hat{y}$, such a mobility is easily understood, as it is the analogue of the standard mobility $\mu = -1/eB$ that we had derived in the previous chapter (section 6.1) for a classical system.

We extract the Hall mobility from the measured velocity distribution already presented in fig. 7.8. Results are given in fig. 7.13.

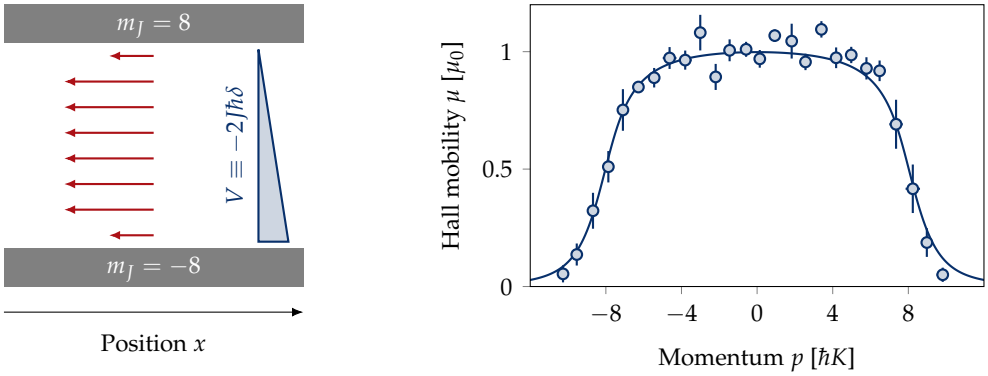

Figure 7.13 – Hall mobility. (Left) The detuning δ amounts to an energy difference between the two synthetic edges of the system. The mobility measures the transverse particle drift that arises (red arrows). (Right) The data of fig. 7.8 is used to compute the mobility μ according to eq. (7.7). The solid line is the expected behavior for $\hbar\Omega = E_{\mathrm{L}}$. The mobility is given in units of $\mu_0 = -1/\hbar K$.

As expected, the measured velocity takes a non-zero value in the bulk equal to $\mu_0 = -1/\hbar K$. Closer to the edges, *i.e.* for momenta $|p| \gtrsim 5\hbar K$, the mobility starts to decrease. For large momenta, the mobility vanishes. The overall behavior is very similar to the one we had derived in the standard quantum Hall effect in the Landau gauge.

7.4.2 Hall conductance

The Hall mobility, as already mentioned, remains a classical quantity. The specificities of the *quantum* Hall effect lie in the quantization of the conductance, which arises from the fermionic statistics of the charge carriers filling the bands. In our case, we do not measure the conductance *per se*, because we use bosonic particles which collectively occupy single p-states (up to a thermal width). Yet, were we using fermions, the conductance of the lowest band would be defined as the sum of the individual contributions of each occupied state. Experimentally, we do measure the velocity of each occupied state, even though we cannot measure a global fermionic behavior.

The conductance of the lowest band was already introduced in section 6.4.2 in the previous chapter. It was defined as the ratio between the particle drift (the Hall current) and the energy difference (the electrical potential), as

$$\sigma = \frac{\dot{N}}{\Delta V} = -\frac{1}{2J\hbar\delta}\int \frac{\mathrm{d}p}{h} v(p), \tag{7.8}$$

where $v(p)$ is the velocity of the state at momentum p, resulting from the energy difference ΔV. As such, the above expression can be recast in

$$\sigma = -\frac{1}{2Jh}\int \mathrm{d}p\mu(p), \tag{7.9}$$

where we have dropped the 0th order term of the velocity, whose contribution vanishes

after integration[5]. One needs to pay attention to the integration domain. Putting aside technical difficulties, the fact that we use bosons allow to virtually probe every momentum from $p = -\infty$ to $p = +\infty$. With fermions, such a situation is unphysical: one cannot occupy an arbitrary number of p-states without filling upper bands as well.

As such we use the same prescription introduced in section 6.4.2, in which we chose to fill the band up to half of the energy gap at $p = 0$, thus defining the integration domain. Doing so, we extract a conductance $\sigma_{\text{exp}} = 0.94(1) \times 1/h$, close to the expected value $\sigma_{\text{th.}} \approx 0.95 \times 1/h$, which itself remains close to the value we expect in the case of an infinite size system, $\sigma_{J=\infty} = 1/h$.

7.4.3 Local Chern marker

We conclude this section with the measurement of local topological markers in our system. In the previous chapter, we introduced the notion of *local Chern marker* (LCM), which characterizes the topological properties of the system locally. In particular, we have seen that the correspondence between the Chern number and the conductance, which are global quantities, is also found between the LCM and the conductivity, which are local quantities. Moreover, the LCM is a gauge-invariant quantity, while the mobility we have extracted depends on the momentum p, and thus only makes physical sense in the Landau gauge. We insist here once again that their local character makes them sensitive to local perturbations, such as disorder, while the Chern number – or the conductance – are by definition topologically protected.

We remind here the expression of the LCM for our system, taking into account the translational invariance in the real dimension

$$c(m_J) = -2\mathrm{i}\pi \langle x, m_J | [\hat{P}\hat{x}\hat{P}, \hat{P}\hat{J}_z\hat{P}] | x, m_J \rangle = \frac{1}{\hbar K} \int \mathrm{d}p \Pi_{m_J}(p) \partial_p [p - mv(p)]. \tag{7.10}$$

We can thus compute the LCMs from the data of fig. 7.7. The results are given in fig. 7.14.

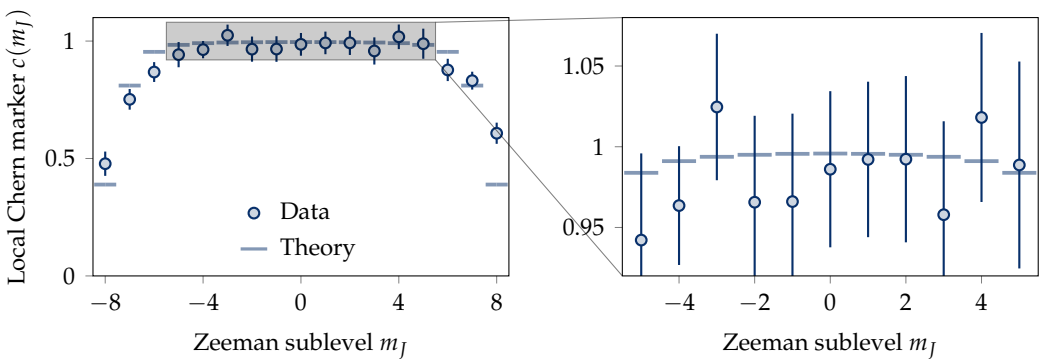

Figure 7.14 – Local Chern marker. The topology of the band is probed by computing the local Chern marker (see text). We give a zoom of the bulk region in the right plot. The theory is indicated by the solid lines.

The experimentally measured LCMs follow the expected behavior. In the bulk, the

[5]The term $\langle \hat{v} \rangle_0$ is an odd function of the momentum p, and we assume here that the integration domain is centered around $p = 0$.

LCMs take the finite value $c(m_J) \approx 1$ over a relatively large region, while it gets smaller on the edges. A zoom in the bulk $|m_J| \lesssim 5$ shows that the measured value and the theoretical prediction agree within errorbars. In fact, this allows to define the bulk unambiguously in terms of position in synthetic dimension, and thus in a gauge-independent way. The total range over which the LCM is close to unity furthermore confirms that our system has a large bulk compared to the edge sizes. By definition of the local Chern marker, we can thus assert that our system realizes, on a mesoscopic scale, the peculiar physics of the quantum Hall effect.

7.5 Conclusion

In this chapter, we have described the experimental realization of the Hamiltonian $\hat{H}$ given in eq. (7.1). In chapter 6, we had seen that the low energy spectrum of $\hat{H}$ is very similar to the Landau levels, which constitute the energy spectrum of a charged particle in an external magnetic field. We had furthermore introduced the specificities of such systems, in particular of the ground state, known as the lowest Landau level (LLL). In this chapter, we have shown that we are able to prepare the LLL and probe its main properties, with a fairly good agreement with the expected ones.

As such, we have measured a clear distinction between the bulk and the edges, both in terms of synthetic position (the magnetization is proportional to the momentum in the bulk, and saturates to $m_z = \pm J$ on the edges) and velocity (the kinetic energy vanishes in the bulk, while non-zero chiral edge modes arise on the boundaries). We are furthermore able to measure the cyclotron and skipping orbits, which result from a perturbative excitation, and are key features of the classical Hall effect.

Quantum effects are revealed by considering the transverse conductance of the system. We first showed that the application of a force in one of the two directions results in a non-zero velocity in the other direction, which is a very well known results for classical Hall systems. The quantization of the conductance, in principle, can be measured by considering a uniformly filled band of spin-less fermions. Thanks to the intrinsic relation between conductance and topology, we can reveal the quantization of the conductance *via* the measurement of a local topological quantity introduced as the local Chern marker. This quantity is equal to 1 in the bulk, indicating a non-trivial topological order, and is reduced close to the boundaries, because of edge effects.

Such a marker, however, remains a local quantity, and is thus subjected to local perturbations. In that regard, the fact that we measure the expected value of the mobility or the local Chern marker intrinsically means that the system we realize is *clean*, in the sense that there is no measurable local perturbations. Although we did not discuss it in detail here, we have furthermore checked numerically that in the presence of disorder (a random potential in both the real and synthetic dimensions), even though the Chern markers are affected locally, the integrated value $C_{\text{tot}} = \sum_{m_J} c(m_J)/2J$ remains robust, *i.e.* it is not significantly changed up to disorder depths on the order of E_{L}. Such a result is in agreement with the fact that the quantization of the Hall conductance is very robust to experimental imperfections.

Yet, all the results presented here remain single-particle physics. The next chapter, as an outlook for this thesis, is dedicated to the exploration of many-body effects in our

system, expected to give rise to new phases of matter with exotic properties as well.

8 Summary and outlook

8.1 Summary **147**

8.2 Outlook: towards topological many-body states . . . **148**

8.2.1 Measuring the interactions 149

8.2.2 Many-body ground state of synthetic Landau levels 150

As a concluding chapter, we give a short summary of the work that was presented throughout this thesis. We then continue with perspectives naturally following the last part of this manuscript, concerning the realization of synthetic Landau levels, by considering the role of interactions in such systems.

8.1 Summary

This thesis is oriented into three relatively independent parts. In part I, we described the experimental setup, which allows to bring a bosonic gas of dysprosium down to degeneracy. A key step of our cooling process was described in chapter 2, where we show that we can use the relatively narrow intercombination line at 626 nm transition to implement in-trap Doppler cooling. In particular, we have highlighted the fact that, at our dipole trap's wavelength, the differential polarizability between the ground state and the excited state (corresponding to the considered transition) can be finely tuned by the trap's polarization. Such an effect is exploited to implement efficient cooling, and to reach Bose-Einstein condensation. We have furthermore been able to observe that the peculiar properties of dysprosium, such as its high dipole moment, qualitatively change the properties of the BEC.

The second part was dedicated to the realization of non-classical spin states in the internal degree of freedom of individual dysprosium atoms. After a theoretical introduction of the concepts of collective spin states, we have described in chapter 5 the implementation of one-axis twisting, and the realization of N00N states, which are highly non-classical states. We have demonstrated a metrological gain close to the Heisenberg limit, that we were able to measure thanks to our single-state resolution provided by our Stern-Gerlach apparatus. Moreover, we have been able to completely characterize such a non-classical state through its full state tomography, and through the measurement of decoherence. In particular, we have observed clear signatures of non-classicality (*e.g.* from the negative parts of the

Wigner distribution), and we have observed an increased sensitivity to magnetic field noise.

Finally, we have shown in part III that we can interpret the large spin of dysprosium as an effective position, realizing a so-called synthetic dimension. By extending the techniques developed in the first two parts, namely the coherent manipulation of internal degrees of freedom using laser light, we are able to implement spin-orbit coupling on the atoms, effectively realizing the Landau Hamiltonian with a synthetic dimension. Throughout chapter 6, we extensively compared our synthetic system to a standard quantum Hall system, and we show that we expect to see all the characteristic properties of such a system. In chapter 7, which describes the experimental implementation, we show observation of those properties. In particular, we observe a clear distinction between the bulk and the edge of the system, in terms of kinetic energy, cyclotron excitations, and topology.

8.2 Outlook: towards topological many-body states

As it was already mentioned in this manuscript, the achievement of topologically-protected many-body states is a very active area of research. The last part of this manuscript was dedicated to experiments that allow us to realize single-particle topological models. The natural extension to this work is thus to add an ingredient – the interactions between particles – and look for many-body quantum states of interest.

In our system, consisting of a real dimension and of a synthetic dimension, the interactions can be quite peculiar. In the real dimension, we already know that we have anisotropic dipole-dipole interactions (DDI). If restricted to a one-dimensional system, the DDI remain short-range [Lahaye et al. 2009], and can be taken into account in the contact interactions – which now depend on the orientation of the individual dipoles. In the synthetic dimension, however, the interactions are non-local: any Zeeman substate can in principle interact with any other substate. As such, interactions in the synthetic dimension are described by a set of interaction parameters $g_{m_1,m_2;m_3,m_4}$, and most of them are unknown.

It is important to point out that having such a strong anisotropy in the interactions – contact in one dimension, infinite range in the other one – can lead to specific and exotic many-body phases [Barbarino et al. 2015; Bilitewski et al. 2016]. In the approach that we will detail in section 8.2.2, we propose a simpler system, in which the interactions are rendered short-range, by physically separating the different Zeeman states. We will see that with such a simpler approach, we recover similar results as what is usually obtained with two-dimensional rotating BECs (see *e.g.* [Chevy et al. 2000; Abo-Shaeer et al. 2001; Engels et al. 2003]). Yet, our system presents some non-negligible advantages. The presence of hard walls in the synthetic dimension, for instance, have a qualitative impact on the shape of the ground state wavefunction, similarly to what is expected from a confined rotating gas [Fetter et al. 2005]. Another aspect to consider is the energy gap between the lowest band and the excited state, which is of several µK for the Raman coupling that we used throughout chapter 7. Such a gap value is several orders of magnitude larger than what is usually expected in rotating gases, for which the energy gap is of the same order of magnitude as the rotation frequency, and thus considerably facilitating the loading and study of the ground band only.

8.2.1 Measuring the interactions

In the low magnetic field and low temperature regime, interactions between two particles, labeled 1 and 2, are described by rotationally symmetric s-wave collisions, where the total angular momentum $\hat{\mathbf{J}}_{\text{tot}} = \hat{\mathbf{J}}_1 + \hat{\mathbf{J}}_2$ is a conserved quantity. We consider bosonic particles here, meaning that the total wavefunction – including both the spatial and the spin part – must be symmetric upon particle exchange, and thus enforcing the total spin of the pair to be even [Stamper-Kurn et al. 2013]. As such, the scattering properties of a pair of bosonic dysprosium atoms can be reduced to a set of $J+1$ scattering lengths a_{2j}, where $0 \leq j \leq J$ is an integer. The scattering amplitude of any collisional process $m_1 + m_2 \to m_3 + m_4$ can be computed using these $J+1$ coefficients. To our knowledge, the only known scattering parameter is the one that we have already mentioned in this thesis, namely a_{2J}, corresponding to the scattering process between two atoms polarized in stretched states $m_J = \pm J$.

The interaction parameters can be measured using a degenerate gas. We have seen indeed in chapter 3 that the expansion dynamics of a BEC depends on the interactions between the individual bosons. As such, if we can prepare a BEC in a given Zeeman state $|m_J\rangle$, we could in principle be able to extract the corresponding interaction parameter g.

Preparation of a single-component BEC

The preparation of a single component BEC can be realized using well chosen light potentials acting on the spin of the atoms. We have seen in parts II and III that we can use vector and tensor light-shifts, corresponding to linear and quadratic spin operators. Let us consider for instance a spin Hamiltonian of the form

$$\hat{H}_{\text{spin}}(\alpha) = \hat{J}_z + \alpha \hat{J}_z^2, \tag{8.1}$$

which can be simply realized using the quantization field for the linear part, and the tensor light-shift resulting from a π-polarized beam close to the 626 nm transition for the quadratic part.

For $\alpha = 0$, the ground state of $\hat{H}_{\text{spin}}$ is the spin-polarized state $|m_J = -J\rangle$, which is the one we use as a starting point throughout all the coherent spin manipulation that we have presented throughout this thesis. For $\alpha > 1$, the quadratic part dominates, and the ground state becomes the Dicke state $|m_J = 0\rangle$. Any intermediate Dicke state between $|m_J = -8\rangle$ and $|m_J = 0\rangle$ can be the ground state of $\hat{H}_{\text{spin}}(\alpha)$, provided that α is well chosen between 0 and 1.

One thus sees that all these Dicke states can be prepared, if for example the evaporation takes place in the corresponding light potential. If the scattering properties are not beneficial for the evaporation, we could also imagine preparing these Dicke states through adiabatic ramps, similarly to the adiabatic preparation of a given p-state that we realize in chapter 7. Here, we could for example start with a spin-polarized state $|m_J = -J\rangle$, open a gap with a transverse spin component $\hat{J}_x$ (created using a vector light-shift or with a transverse magnetic field), and adiabatically ramp α to the target value. The target Dicke state would then be obtained by slowly ramping down the transverse component.

All these protocols can be readily implemented and tested on the experiment, using the intercombination line that we have used in this thesis. We could also use other transitions

lying in the near infrared spectrum, and that we have mentioned in the outlook of chapter 1. Using a $J = 8 \to J' = 8$ transition, for instance, provides a stronger tensor light-shift – compared to the scalar term – than the $J = 8 \to J' = 9$ transition than we have used so far.

Mixtures

Before continuing to the exploration of many-body topological phases, it is worth mentioning that our system should be prone to the study of spin-mixture BECs. We can employ the techniques briefly mentioned in the outlook of chapter 5 (see also [Makhalov et al. 2019]) to adiabatically prepare a two-component BEC with large and opposite magnetization, and study its dynamics. It is predicted, for instance, that the DDI should enrich the phase diagram that characterizes the miscible to immiscible transition, with the formation of rotons [Wilson et al. 2012]. It has also been shown that such systems, in the immiscible regime, have several types of metastable configurations in their interface patterns, including the so-called *labyrinth pattern*, or an hexagonal Rosensweig pattern with supersolid behavior [Saito et al. 2009].

8.2.2 Many-body ground state of synthetic Landau levels

We now focus on the ground state of the system that was studied in chapters 6 and 7, in the presence of interactions between the particles, and for a large filling factor, *i.e.* when the number of atoms per quantum of flux is very large. As already mentioned, we restrict the discussion to the case of contact interactions both in the real and in the synthetic dimension. Such a situation can be obtained *e.g.* by adding a magnetic field gradient along the quantization axis, spatially separating the different spin components. We furthermore consider the situation where all the interaction strengths are equal and given by a single parameter

$$g = \frac{4\pi\hbar^2 a}{m}, \tag{8.2}$$

where a is the (state-independent) scattering length. Even though we consider an ideal situation here, we do not except the real situation to be significantly different, as long as all the scattering lengths are positive and of the same order of magnitude.

Gross-Pitaevskii equation in synthetic dimension

As we introduced in chapter 3, the dynamics of the BEC in the presence of interactions is described by the Gross-Pitaevskii equation. The quantum state of our system is here described by a spinor classical field $\psi_{m_J}(x)$, with $-J \leq m_J \leq J$. In the presence of the Raman coupling, and using the consideration mentioned above, the ground state will be given by the stationary solutions of

$$\begin{aligned} \mathrm{i}\hbar\partial_t\psi_{m_J}(x) = \frac{\hbar^2}{2m}\left(\mathrm{i}\partial_x + \hbar K m_J\right)^2\psi_{m_J}(x) \\ - \frac{\hbar\Omega}{2\mathrm{i}}\left[\sqrt{J(J+1) - m_J(m_J+1)}\psi_{m_J-1}(x) - \sqrt{J(J+1) - m_J(m_J-1)}\psi_{m_J+1}(x)\right] \\ - \hbar\Omega\frac{m_J^2}{2J+3}\psi_{m_J}(x) + gN\left|\psi_{m_J}(x)\right|^2\psi_{m_J}(x), \end{aligned} \tag{8.3}$$

with N the total number of atoms.

The stationary ground state solutions are obtained using evolution in imaginary time [Fetter et al. 2005]. In our case, we expect a ground state similar to a triangular array of vortices – the Abrikosov lattice [Abrikosov 1957] – that emerge for a rotated BEC. Some questions, however, remain: how are vortices defined for the discrete, synthetic dimension? what are the effects of the edges on the vortex arrangement? In a 'real' material (a type II supraconductor), the vortex density and their size depends on the strength of the applied magnetic field (which directly gives the magnetic length $\ell = \sqrt{\hbar/eB}$). In our system, the equivalent quantities are defined by the Raman coupling strength Ω – how does the many-body ground state depend on such an external parameter?

For the simulation, we choose a cylindrical geometry (see fig. 8.1) to account for the infinite length in the real dimension. Such a choice assumes that the ground state is periodic in space, which we verify numerically. The initial wavefunction is chosen to be random, and we find the ground state configuration for several values of Ω. Examples of the calculated ground states are given in fig. 8.1.

The ground state configuration is determined by finding the cylinder circumference L_0 that minimizes the ground state energy. We give in fig. 8.1 the energy as a function of the cylinder circumference in two cases, for which the interaction energy E_{int} is different. For $E_{\text{int}} = E_{\text{L}}$, one sees that the energy is minimized at $L_0 \approx 0.33 \times \lambda/2$, and we recover an energy minimum at $2L_0$. These minima correspond to a configuration with 4 lines of vortices. For $E_{\text{int}} = 2E_{\text{L}}$, the energy minimum is found at $L_0 \approx 0.75 \times \lambda/2$, and corresponds to 5 lines of vortices[1]. The other local minima of energy can be interpreted as frustrated configurations, with different number of vortices.

Vortices

The vortices in the wavefunction can be identified as being the local minima of the density [Castin et al. 2006], and thus counted. They can also be identified using the information of the phase of the wavefunction. In a continuous two-dimensional system, such as a rotating BEC, each vortex carries a quantized charge, which is determined as the circulation of the velocity field around the vortex

$$\oint \mathbf{v}(\mathbf{r}) \cdot \mathrm{d}\mathbf{r} = \pm \frac{2\pi\hbar}{m}. \tag{8.4}$$

Such a relation originates from the relation between the velocity and the phase of the wavefunction, $\mathbf{v}(\mathbf{r}) = (\hbar/m)\boldsymbol{\nabla}\phi(\mathbf{r})$, where $\psi(\mathbf{r}) = |\psi(\mathbf{r})|\,\mathrm{e}^{\mathrm{i}\phi(\mathbf{r})}$. In other words, to each vortex is associated a phase winding of the wavefunction, and the total number of vortices in a closed area can be found by calculating the circulation of the velocity field along the path enclosing the area.

In our semi-continuous system with a stripe geometry, one cannot define a circulation of the phase along the synthetic dimension, because of the discretization of space. In the limit of infinite system size in the real dimension, however, the circulation of the phase along the real dimension will dominate over the synthetic contribution. The total number

[1] Strictly speaking, this minimum is $2L_0$, as it corresponds to a configuration of 10 vortices in total. However, the symmetries of the eq. (8.3) prevent odd configurations to be found. As such, every configuration with an odd number of vortex lines will be found at even multiples of the fundamental circumference.

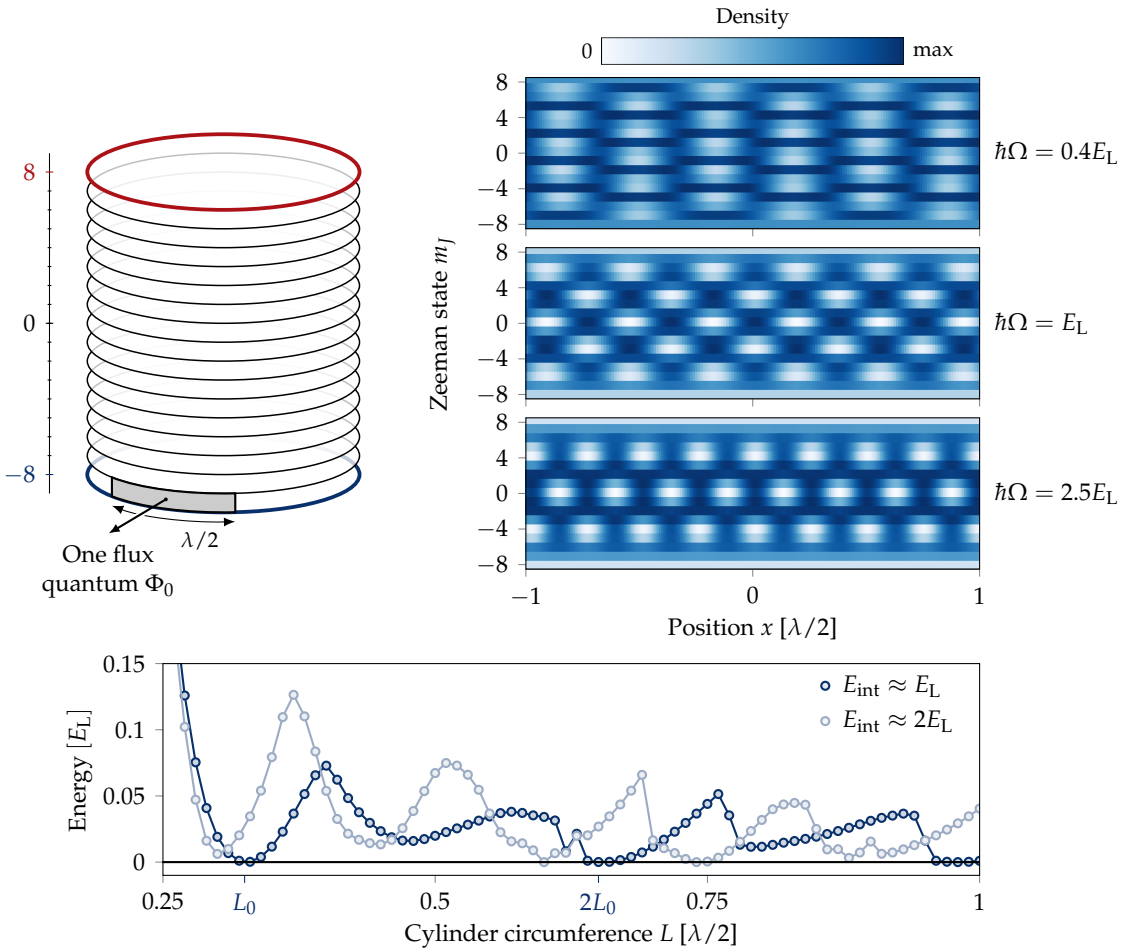

Figure 8.1 – Many-body ground state. (Left) Geometry of our simulation. We consider periodic boundary conditions, with a total circumference found to minimize the ground state energy. (Right) Examples of calculated ground states for several values of $\hbar\Omega$. The 'holes' in the wavefunction – the local minima – are considered to be vortices. (Bottom) The fundamental circumference L_0 of the cylinder is defined as to be the the one that minimizes the ground state energy (here the minimum of energy is arbitrarily set to 0). We check that the same configuration is found at integer multiples of L_0. The examples given here correspond to two different minimizations at different interaction energies (both at $\hbar\Omega = E_L$). See text for additional details.

of vortices N_v can thus be computed as

$$N_v = \frac{1}{2\pi} \lim_{L\to\infty} \left[\int_{-L/2}^{L/2} \nabla\phi_{-J}(x)\mathrm{d}x + \int_{L/2}^{-L/2} \nabla\phi_J(x)\mathrm{d}x \right], \tag{8.5}$$

where $\phi_{\pm J}(x)$ is the phase of the wavefunction associated to the Zeeman state $|\pm J\rangle$: $\langle \pm J|\psi(x)\rangle = |\psi_{\pm J}(x)|\,\mathrm{e}^{\mathrm{i}\phi_{\pm J}(x)}$.

Now that we can give a meaning to vortices in synthetic dimensions, we can study their number in the many-body ground state as a function of the external parameters, such

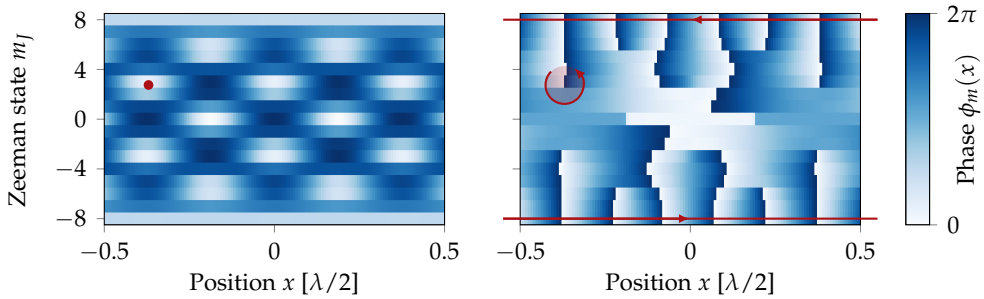

Figure 8.2 – Vortex identification. (Left) Density profile and (right) corresponding phase profile. Local minima of the density profile are identified as being vortices. The minima correspond to a phase winding of the wavefunction, represented by the circular arrow on the phase profile. In the infinite ribbon geometry, the total number of vortices is given by the sum of the integral of the gradient of the phase of both edges (straight red lines).

as the Raman coupling or the interaction energy[2]. We give in fig. 8.3 the vortex density n_v, defined as the average number of vortices per unit of length $\lambda/2$, as a function of the interaction energy and for $\hbar\Omega = E_L$.

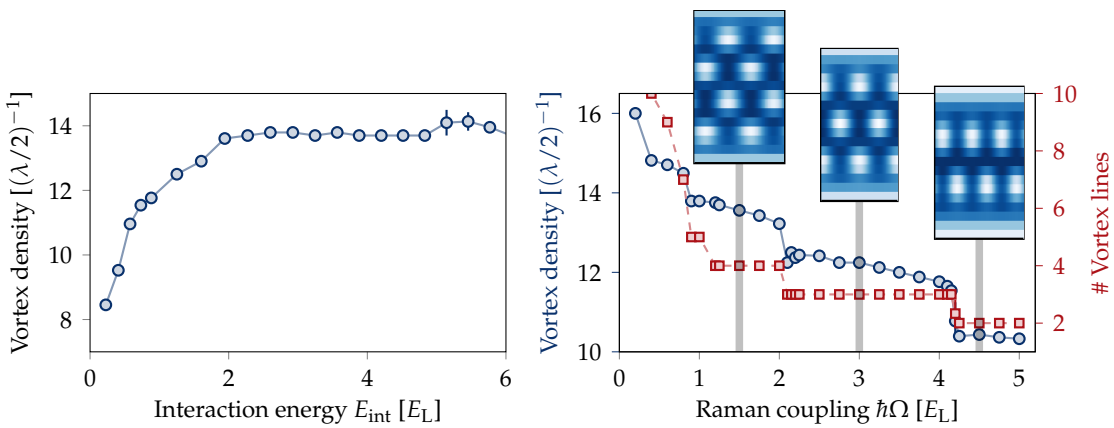

Figure 8.3 – Ground state configuration. (Left) Vortex density as a function of the interaction energy at $\hbar\Omega = E_L$. As we can see, we reach a universal behavior, indicated by the plateau of the vortex density close to $n_v \approx 13.7(\lambda/2)^{-1}$, when the interaction energy lies in the gap, sufficiently higher than the bandwidth of the LLL. (Right) Vortex density of the many-body ground state as a function of the Raman coupling $\hbar\Omega$. Here, the interaction energy is chosen to be in the universal behavior defined by the left graph. The simulation predicts sudden changes of configurations, indicated by jumps of the vortex density. These sudden changes originate from the fact that the number of vortex lines suddenly change from one value of the coupling to the other.

We see that at low energy, the vortex density increases with the interaction strength, before it saturates at a plateau around $n_v \approx 13.7(\lambda/2)^{-1}$. We interpret such behavior as follows: when the interactions are week, the lowest band is not filled ; only a few

[2]The interaction energy can be changed by tuning the total number of atoms in the system, as long as we remain in the large filling situation.

momentum states p are populated. With increasing interactions, more states in the LLL are populated, until the whole band is approximately filled. At this point, *i.e.* when the interaction energy is much bigger than the bandwidth, the plateau is reached. We note that for large interaction energy, even when the higher bands get populated, we observe that the vortex density stays the same. Such a regime is referred to as *universal*: it is a regime for which the ground state configuration does not depend much on the interaction parameters. Note that the interaction parameter at which this regime is observed depends on the Raman coupling Ω, on which the bandwidth and the band gap depend.

We then study the influence of the Raman coupling on the ground state configuration. We run the simulation for several values of $\hbar\Omega$ ranging from $0.2E_{\mathrm{L}}$ to $5E_{\mathrm{L}}$, adjusting the interaction parameter in order to be in the universal regime we just described[3]. We show in the right graph of fig. 8.3 the vortex density and the corresponding number of vortex lines as a function of Ω.

We see that with increasing value of Ω, the vortex density decreases. Such a behavior can be qualitatively understood in term of the vortex size, given by the synthetic magnetic length $\ell_{\mathrm{s}} \propto \Omega^{1/4}$. With increasing Ω, the vortices get bigger and interact more with each other and with the edges of the ribbon. The vortex spacing along the synthetic dimension is thus increased, allowing fewer lines of vortices. It is also important to note that with increasing Ω, the lowest band's curvature is more pronounced, preventing higher momentum states from being populated. Such an effect may also reduce the total number of vortices.

Experimental detection of vortices

As we just saw, the vortex density is relatively high, and a direct detection is thus challenging, as it requires an optical resolution well below $\lambda/2 = 323\,\mathrm{nm}$. One possibility for detection is to realize a telescope that magnifies the in-situ density profile for imaging after time-of flight. As we know, the density profile after time-of-flight reflects the in-situ momentum distribution, provided that the duration of free-flight is sufficiently large. As such, if the in-situ density distribution is converted into a momentum distribution, *e.g.* by putting the state in a harmonic trap and letting it evolve for a quarter of its period, then the distribution after time-of-flight is a magnification of the in-situ density profile. The magnification factor depends on the harmonic trap frequency and the duration of the free-flight. Such a technique, called *refocusing*, is commonly used for ultracold atoms (see *e.g.* [Shvarchuck et al. 2002]).

Another possibility is an indirect detection of the vortices by looking only at the momentum distribution, *i.e.* directly after time-of-flight. Indeed, the presence of an ordered vortex lattice breaks the translational symmetry of the system in the real dimension, and thus should correspond to a detectable population of momentum states corresponding to the vortex lattice spacing, and different from the trivial recoil momentum $p_{\mathrm{L}} = \hbar K$ imposed by the Raman lasers. Such a signature has been used *e.g.* in [Atala et al. 2014], where the transition from a vortex-phase to a Meissner-like phase (screening of the applied artificial magnetic field) is detected through the momentum peaks of the system.

[3] In practice, we set $g \propto \sqrt{\Omega}$ in the simulation, because we know the gap is roughly $\propto \sqrt{\Omega}$.

Fractional quantum Hall states

As a concluding paragraph, we mention that our system should be the host of fractional quantum Hall (FQH) states in the limit where the filling fraction is on the order of unity. The FQH effect was experimentally discovered in the 1980s, through the measurements of plateaux of conductance at fractional values of the von Klitzing constant (see *e.g.* [Tsui et al. 1982; Willett et al. 1987]). In condensed matter systems, the FQH effect arises at fractional filling of the Landau levels, and is intrinsically related to the Coulomb interactions between the electrons. As such, for filling fractions smaller than unity, one expects the ground state of the system to be a FQH state if the interaction energy is bigger than the bandwidth – essentially set by disorder in the system – and smaller than the band gap.

Numerically, finding the ground state of such a problem is challenging, for the Hilbert space dimension grows exponentially with the number of particles and perturbative approaches are inadequate. The shape of the ground state wavefunction was guessed by Laughlin [Laughlin 1983] using a trial wavefunction, which, in the symmetric gauge (for which the states can be labeled by their angular momentum projection), and for fractional filling factors $\nu = 1/m$, reads

$$\psi(\{z_i\}) \propto \left[\prod_{i<j}(z_i - z_j)^m\right] \exp\left[-\sum_{i=1}^{N} \frac{|z_i|^2}{4\ell^2}\right]. \tag{8.6}$$

Here, $z_i = x_i + \mathrm{i}y_i$ encodes the position of particle labeled i, and ℓ is the magnetic length. Although such a wavefunction has uniform density, it still carries vortices within bounds between particles: a phase winding appears when one particle encircles another particle [Cooper 2008]. The Laughlin state has gapped excitations, which is a signature of an incompressible fluid (there is no phononic branch in the spectrum). One furthermore sees that the Laughlin wavefunction vanishes whenever two particles have the same position, yielding a strong anti-bunching between the particles, and indicating a vanishing interaction energy of the ground state.

In our system, there are $2J = 16$ flux quanta per $\lambda/2$, and we thus expect to reach the quantum Hall regime when the density becomes such that we have a few atoms in this typical lengthscale. Numerical calculations at filling factors $\nu = 1/2$ show that indeed we expect a ground state with vanishing interaction energy and gapped excitations, indicating the presence of a FQH state.

IV

Appendices

A Laser system

A.1 Laser at 626 nm 159

A.2 Laser at 421 nm 161

We give in this appendix a description of our laser system for the two cooling transitions: the narrow intercombination line (626 nm) and the broader blue transition (421 nm).

A.1 Laser at 626 nm

Laser light at 626 nm is generated using a sum-frequency generation (SFG) setup. We give in fig. A.1 a global scheme of our system.

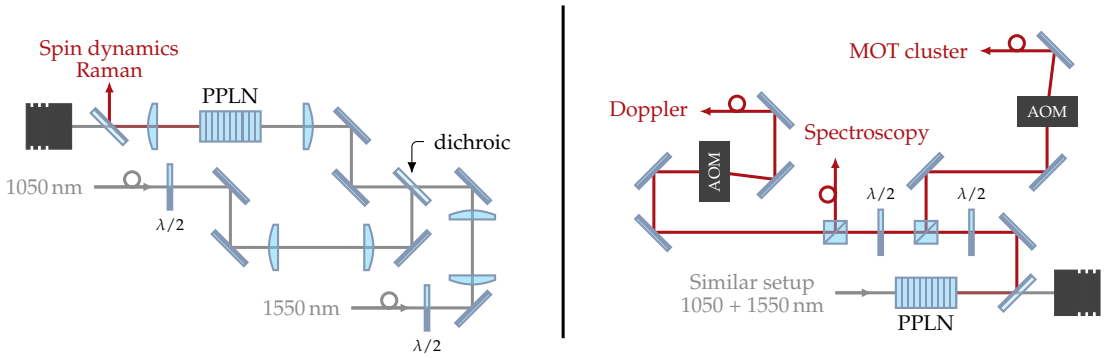

Figure A.1 – Red laser setup. (Left) Detail of one the sum frequency generation (SFG), whose output goes to the spin dynamics setup (see schemes in figs. 5.6 and 7.1). (Right) A second setup is used for spectroscopy, for the MOT, and for the Doppler cooling. See text for additional details.

We have two independent systems that produce light at 626 nm. Both of them have the same scheme: two pumps at 1050 nm and 1550 nm are focused inside a non-linear crystal, which produces the sum frequency at 626 nm.

Sum frequency generation

Sum frequency generation (SFG) originates from the non-zero second order susceptibility $\chi^{(2)}$ of the crystal, which can convert two photons of frequency ω_1 and ω_2 to the sum frequency at $\omega_3 = \omega_1 + \omega_2$. In order for the conversion to be efficient, the phase matching condition $\Delta k = k_3 - k_1 - k_2$ must be met. This condition cannot be fulfilled throughout the whole crystal, because of its frequency-dependent diffraction index.

The idea of the PPLN crystal – for *Periodically Poled Lithium Niobate* – is to periodically invert the orientation of the second-order susceptibility. If the period Λ of the crystal matches the phase difference, *i.e.* if one has $\Delta k = 2\pi/\Lambda$, the *quasi phase matching* condition is met, and the conversion can take place. The geometry of the PPLN crystal is given in fig. A.2.

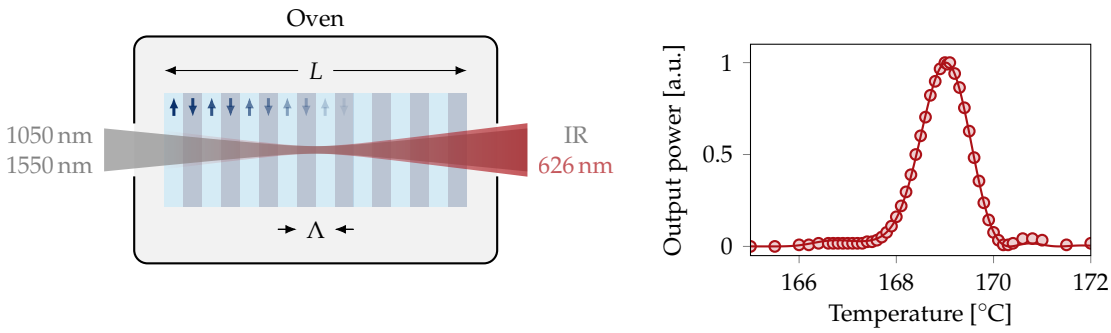

Figure A.2 – Sum frequency generation in a PPLN crystal. (Left) Scheme of the PPLN crystal. The orientation of the non-linear susceptibility is indicated by the arrows. It is inverted periodically, the period being Λ. For our crystal, $\Lambda \approx 10.9\,\mu\text{m}$. The infrared (IR) pumps are focused at the center of the crystal, which produces 626 nm on the output. The crystal is placed in an oven for temperature control. (Right) Output power as a function of the oven temperature. As one can see, the conversion efficiency strongly depends on the temperature, which is precisely controlled. The solid line is a fit of the Boyd-Kleinman theory in eq. (A.2).

The phase difference is temperature-dependent and is written as

$$\Delta k = 2\pi \left(\frac{n_3(T)}{\lambda_3} - \frac{n_1(T)}{\lambda_1} - \frac{n_2(T)}{\lambda_2} \right), \tag{A.1}$$

where λ_i is the wavelength and n_i is the diffraction index. Its temperature dependence can be computed using the Sellmeier equation [Jundt 1997]. In the Boyd-Kleinman theory [Boyd et al. 1968], the output power of light at 626 nm is expressed as

$$P_3^{(\text{out})} = \frac{32\pi^2 d_{\text{eff}}^2 L h(a,b)}{\epsilon_0 c \lambda_1 \lambda_2 \lambda_3^3 \left(n_1/\lambda_1 + n_2/\lambda_2 + n_3/\lambda_3\right)^2} \times P_1 P_2, \tag{A.2}$$

where P_i is the pump power, d_{eff} is the second order susceptibility coefficient, L is the total length of the crystal and $h(a,b)$ is the Boyd-Kleinman coefficient

$$h(a,b) = \frac{1}{4a} \left| \int_{-a}^{a} \frac{\mathrm{d}\tau \mathrm{e}^{-\mathrm{i}b\tau}}{1 + \mathrm{i}\tau} \right|^2, \tag{A.3}$$

using the reduced variables $a = L/2z_R$ and $b = (\Delta k - 2\pi/\Lambda)z_R$, where z_R is the Rayleigh range of the beams.

The shape of the pumps is thus found by maximizing the Boyd-Kleinman factor. In particular, we find $a_{max} \approx 2.84$, and considering that our crystals are $L = 4$ cm long, it fixes the Rayleigh range to $z_R \approx 7$ mm, and thus the waists of the incoming beams to roughly 40 µm. The quasi-phase matching condition is then tuned by changing the temperature of the crystal, which is placed in an oven (see fig. A.2). We expect a maximum efficiency $\eta = P_3/(P_1P_2)$ of about 75.5 mW/W^2.

Spin dynamics setup

For the spin dynamics setup, the two pumps come from fiber amplifiers, seeded by narrow line diodes. We have 10 W of 1050 nm light, and 5 W of 1550 nm light. The output frequency is chosen by tuning the seed diode of the 1550 nm laser. In fig. A.1, we have represented the two seeds in gray. A half-wave plate is used to set the polarization of the pumps, which should match the axis of the crystal. Both pumps are shaped with telescopes, and combined on a dichroic mirror. A lens then focuses the pumps at the center of the crystal. The produced red light is then sent to the experiment (see figs. 5.6 and 7.1), while the remaining infrared light is dumped. On the best days, we can output up to 3 W of light at 626 nm, close to the maximum expected efficiency. Note that this beam is used off-resonant, and we do not lock its frequency on an atomic reference.

MOT setup

The MOT setup is very similar: the two pumps are fiber amplifiers seeded by diodes, and we use the 1050 nm diode to adjust the output frequency. Here, the two pumps are 5 W lasers, and the output power goes up to about 1.3 W on the best days. Most of the power is dedicated to the MOT beams itself. A single beam goes through an AOM, that we use to control the total MOT power, and then coupled to a fiber. The output of this fiber is then split in 6 beams which go on the atoms. The rest of the power is used for the spectroscopy, and for the Doppler beam.

A.2 Laser at 421 nm

Our Blue laser system is a commercial system from Toptica[1]. We give in fig. A.3 a global scheme of the setup.

Laser light at 421 nm is generated from a second-harmonic generation (SHG), using a non-linear doubling crystal in a bow-tie cavity. The seed laser, at 842 nm, comes from an external-cavity diode laser (ECDL), amplified using a tapered amplifier (TA). The whole system outputs typically 450 mW.

The blue laser beams is then split in different paths.

1. A few mW is taken right at the output of the laser and coupled to a fiber. This part is used for the 2D molasses.

[1] TA-SHG Pro, Toptica.

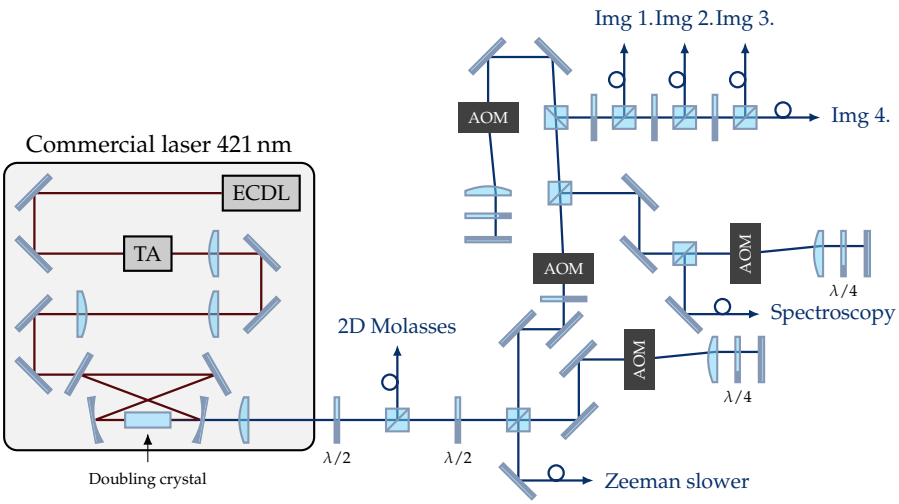

Figure A.3 – Blue laser setup. For clarity, we have indicated only a few half-wave plates (designated $\lambda/2$) and quarter-wave plates ($\lambda/4$). All the cubes are polarizing beam splitters (PBS). See text for additional details.

2. About 200 mW is dedicated to the Zeeman slower. The beam goes through a double-pass AOM, before it is coupled to a fiber.

3. Among the remaining power, about 20 mW is dedicated to the spectroscopy. Again, the light goes through a double-pass AOM, before it is coupled to a fiber. The output is used to lock the frequency of the laser, by acting on the ECDL current.

4. The rest of the power is dedicated to imaging. A double-pass AOM is used again, allowing to freely tune the imaging frequency. We then have one fiber for each imaging path.

B Local Chern marker

B.1 Stripe geometry in real dimensions 163
B.2 Synthetic quantum Hall system 166

B.1 Stripe geometry in real dimensions

We compute here the local Chern marker (LCM) in a stripe geometry in a *standard* quantum Hall system. We recall the expression of the LCM $c(x,y)$ [Bianco et al. 2011]:

$$c(x,y) = -2\mathrm{i}\pi \langle x,y|[\hat{P}\hat{x}\hat{P}, \hat{P}\hat{y}\hat{P}]|x,y\rangle \,, \tag{B.1}$$

where $\hat{P}$ is the projector on the ground band. We write the eigenfunctions of the LLL in the form (throughout this chapter, we set $\hbar = 1$)

$$\psi_k(x,y) = \frac{1}{\sqrt{2\pi}} \mathrm{e}^{\mathrm{i}kx} \phi_k(y), \tag{B.2}$$

Where $\phi_k(y)$ is the shape of the wavefunction across the ribbon. We take here the normalization condition $\int \mathrm{d}y\, |\phi_k(y)|^2 = 1$. The ground band projector is written as

$$\begin{aligned} \hat{P} &= \int \mathrm{d}k\, |\psi_k\rangle \langle \psi_k| \\ \text{with} \quad |\psi_k\rangle &= \int \mathrm{d}x\mathrm{d}y\, \psi_k(x,y)\, |x,y\rangle = \frac{1}{\sqrt{2\pi}} \int \mathrm{d}x\mathrm{d}y\, \mathrm{e}^{\mathrm{i}kx} \phi_k(y)\, |x,y\rangle \,. \end{aligned} \tag{B.3}$$

One can check that $\langle \psi_k|\psi_q\rangle = \delta(k-q)$ and thus $\hat{P}^2 = \hat{P}$. One notices that the LCM can be written as

$$c(x,y) = -2\mathrm{i}\pi \langle x,y|\hat{P}(\hat{x}\hat{P}\hat{y} - \hat{y}\hat{P}\hat{x})\hat{P}|x,y\rangle \,. \tag{B.4}$$

It is thus the expectation value of the hermitian operator $\mathrm{i}(\hat{x}\hat{P}\hat{y} - \hat{y}\hat{P}\hat{x})$ in the LLL. Using such properties, it is recast in the form

$$c(x,y) = 4\pi\, \mathrm{Im} \langle x,y|\hat{P}\hat{x}\hat{P}\hat{y}\hat{P}|x,y\rangle \,. \tag{B.5}$$

In the computation of $c(x,y)$, we shall compute terms of the form $\langle\psi_q|\hat{x}|\psi_k\rangle$ and $\langle\psi_k|\hat{y}|\psi_p\rangle$, which we detail below. We have

$$\begin{aligned}\langle\psi_q|\hat{x}|\psi_k\rangle &= \frac{1}{2\pi}\int \mathrm{d}x\mathrm{d}y\mathrm{d}u\mathrm{d}v\,\mathrm{e}^{-\mathrm{i}qx}\mathrm{e}^{\mathrm{i}ku}\phi_q^*(y)\phi_k(v)\,\langle x,y|\hat{x}|u,v\rangle \\ &= \frac{1}{2\pi}\int \mathrm{d}x\mathrm{d}y\,x\mathrm{e}^{\mathrm{i}x(k-q)}\phi_q^*(y)\phi_k(y) \\ &= -\mathrm{i}\int \mathrm{d}y\,\phi_q^*(y)\phi_k(y)\delta'(k-q).\end{aligned} \tag{B.6}$$

In the last line, we have used

$$\int \mathrm{d}x\,x\mathrm{e}^{\mathrm{i}kx} = -2\mathrm{i}\pi\partial_k\delta(k) = -2\mathrm{i}\pi\delta'(k), \tag{B.7}$$

where $\delta'(k)$ is the derivative of the δ distribution[1]. For the second term, we write

$$\begin{aligned}\langle\psi_k|\hat{y}|\psi_p\rangle &= \frac{1}{2\pi}\int \mathrm{d}x\mathrm{d}y\mathrm{d}u\mathrm{d}v\,\mathrm{e}^{-\mathrm{i}kx}\mathrm{e}^{\mathrm{i}pu}\phi_k^*(y)\phi_p(v)\,\langle x,y|\hat{y}|u,v\rangle \\ &= \frac{1}{2\pi}\int \mathrm{d}x\mathrm{d}y\,\mathrm{e}^{\mathrm{i}x(p-k)}y\phi_k^*(y)\phi_p(y) \\ &= \int \mathrm{d}y\,y\phi_k^*(y)\phi_p(y)\delta(p-k).\end{aligned} \tag{B.9}$$

The LCM can now be written as

$$c(x,y) = 4\pi\,\mathrm{Im}\,\langle x,y|\left[\int \mathrm{d}q\mathrm{d}k\mathrm{d}p\,|\psi_q\rangle\,\langle\psi_q|\hat{x}|\psi_k\rangle\,\langle\psi_k|\hat{y}|\psi_p\rangle\,\langle\psi_p|\right]|x,y\rangle\,. \tag{B.10}$$

The last two terms can be readily calculated by integrating over p,

$$\begin{aligned}\int \mathrm{d}p\,\langle\psi_k|\hat{y}|\psi_p\rangle\,\langle\psi_p| &= \int \mathrm{d}p\int \mathrm{d}y_1\,y_1\phi_k^*(y_1)\phi_p(y_1)\delta(p-k)\,\langle\psi_p| \\ &= \int \mathrm{d}y_1\,y_1\phi_k^*(y_1)\phi_k(y_1)\,\langle\psi_k| \\ &= \langle\hat{y}\rangle_k\,\langle\psi_k|\,.\end{aligned} \tag{B.11}$$

In the last line, we introduced the average position for the momentum k, namely $\langle\hat{y}\rangle_k = \int \mathrm{d}y\,|\phi_k(y)|^2\,y$. The LCM now reads

$$c(x,y) = 4\pi\,\mathrm{Im}\,\langle x,y|\left[\int \mathrm{d}q\mathrm{d}k\,|\psi_q\rangle\,\langle\psi_q|\hat{x}|\psi_k\rangle\,\langle\hat{y}\rangle_k\,\langle\psi_k|\right]|x,y\rangle\,. \tag{B.12}$$

[1] It can be defined by its action on a test function as

$$\int \mathrm{d}k f(k)\delta'(k-k_0) = -f'(k_0). \tag{B.8}$$

We now focus on the integration over k, which is performed using the result of eq. (B.6)

$$\begin{aligned}\int \mathrm{d}k \, \langle \psi_q | \hat{x} | \psi_k \rangle \, \langle \hat{y} \rangle_k \, \langle \psi_k | &= -\mathrm{i} \int \mathrm{d}k \mathrm{d}y_1 \, \phi_q^*(y_1) \phi_k(y_1) \delta'(k-q) \, \langle \hat{y} \rangle_k \, \langle \psi_k | \\ &= \mathrm{i} \int \mathrm{d}y_1 \, \phi_q^*(y_1) \partial_q \left[\phi_q(y_1) \, \langle \hat{y} \rangle_q \, \langle \psi_q | \right] \\ &= \mathrm{i} \int \mathrm{d}y_1 \, \phi_q^*(y_1) \partial_q \phi_q(y_1) \, \langle \hat{y} \rangle_q \, \langle \psi_q | + \mathrm{i} \partial_q \left[\langle \hat{y} \rangle_q \, \langle \psi_q | \right] .\end{aligned} \tag{B.13}$$

In this last lines, the derivative of the bra $\langle \psi_q |$ implicitly means that we will differentiate the term $\langle \psi_q | x, y \rangle$. We have also used the normalization condition of $|\phi_q(y)|^2$. The LCM now writes

$$\begin{aligned}c(x,y) = 4\pi \, \mathrm{Im} \Big\{ \mathrm{i} \int \mathrm{d}q \, \mathrm{d}y_1 \; \langle x, y | \psi_q \rangle \, \phi_q^*(y_1) \partial_q \phi_q(y_1) \, \langle \hat{y} \rangle_q \, \langle \psi_q | x, y \rangle \\ + \mathrm{i} \int \mathrm{d}q \; \langle x, y | \psi_q \rangle \, \partial_q \left(\langle \hat{y} \rangle_q \, \langle \psi_q | x, y \rangle \right) \Big\} .\end{aligned} \tag{B.14}$$

Using the decomposition of $|\psi_q\rangle$ on the $|x, y\rangle$ basis, and dropping the i factor by switching to the real part, we find

$$\begin{aligned}c(x,y) &= 2 \, \mathrm{Re} \Big\{ \int \mathrm{d}q \, \mathrm{d}y_1 \, \mathrm{e}^{\mathrm{i}qx} \phi_q(y) \phi_q^*(y_1) \partial_q \phi_q(y_1) \, \langle \hat{y} \rangle_q \, \mathrm{e}^{-\mathrm{i}qx} \phi_q^*(y) \\ &\qquad + \int \mathrm{d}q \, \mathrm{e}^{\mathrm{i}qx} \phi_q(y) \partial_q \left(\langle \hat{y} \rangle_q \, \mathrm{e}^{-\mathrm{i}qx} \phi_q^*(y) \right) \Big\} \\ &= 2 \, \mathrm{Re} \Big\{ \int \mathrm{d}q \; |\phi_q(y)|^2 \, \langle \hat{y} \rangle_q \int \mathrm{d}y_1 \, \phi_q^*(y_1) \partial_q \phi_q(y_1) \\ &\quad + \int \mathrm{d}q \, \phi_q(y) \left[\partial_q \, \langle \hat{y} \rangle_q \, \phi_q^*(y) + \langle \hat{y} \rangle_q \, \partial_q \phi_q^*(y) - \mathrm{i}x \, \langle \hat{y} \rangle_q \, \phi_q^*(y) \right] \Big\} .\end{aligned} \tag{B.15}$$

We make use of the identity $\partial_q |\phi_q(y)|^2 = 2 \, \mathrm{Re}(\phi_q(y) \partial_q \phi_q^*(y))$, to simplify the above expression in

$$\begin{aligned}c(x,y) = \int \mathrm{d}q \; |\phi_q(y)|^2 \, \langle \hat{y} \rangle_q \int \mathrm{d}y_1 \, \partial_q |\phi_q(y_1)|^2 + 2 \int \mathrm{d}q \; |\phi_q(y)|^2 \, \partial_q \, \langle \hat{y} \rangle_q \\ + \int \mathrm{d}q \, \langle \hat{y} \rangle_q \, \partial_q |\phi_q(y)|^2 .\end{aligned} \tag{B.16}$$

Note that we dropped the explicit real part notation on the second term, because it is already real. The first term vanishes, as

$$\int \mathrm{d}y_1 \, \partial_q |\phi_q(y_1)|^2 = \partial_q \int \mathrm{d}y_1 \; |\phi_q(y_1)|^2 = \partial_q(1) = 0, \tag{B.17}$$

We now perform an integration by parts on the last term, to get

$$\int \mathrm{d}q \, \langle \hat{y} \rangle_q \, \partial_q |\phi_q(y)|^2 = \left[\langle \hat{y} \rangle_q \, |\phi_q(y)|^2 \right] - \int \mathrm{d}q \, |\phi_q(y)|^2 \, \partial_q \, \langle \hat{y} \rangle_y , \tag{B.18}$$

The first term of (B.18) vanishes when the integration bounds are taken to ∞. We finally

obtain the expression for the local Chern marker that we have given in chapter 6

$$\boxed{c(x,y) = \int \mathrm{d}q \left|\phi_q(y)\right|^2 \partial_q \left\langle \hat{y} \right\rangle_q .} \tag{B.19}$$

We notice that the LCM does not depend on x, as expected from translational invariance along the x direction.

B.2 Synthetic quantum Hall system

We now simply adapt the results we have derived above for our synthetic system, *i.e.* with the position y encoded in the Zeeman substate $|m_J\rangle$. The formula is almost unchanged, as we write for the LCM

$$c(x, m_J) = 4\pi \,\mathrm{Im}\, \langle x, m_J | \hat{P}\hat{x}\hat{P}\hat{J}_z\hat{P} | x, m_J \rangle \,, \tag{B.20}$$

where now the wavefunctions reads

$$\psi_k(x, m_J) = \frac{1}{\sqrt{2\pi}} \mathrm{e}^{\mathrm{i}kx} \phi_k(m_J). \tag{B.21}$$

The synthetic part of the wavefunction directly gives the population distribution associated to the state k: $\Pi_{m_J}(k) = |\phi_k(m_J)|^2$. The final result can be found by adapting the average position $\langle \hat{y} \rangle_k$ of the real dimension to synthetic dimensions. In our case, it is simply given by $\langle \hat{y} \rangle_k \leftrightarrow m_z(k)$, *i.e.* the average magnetization of the state. The final formula thus reads

$$c(x, m_J) = \int \mathrm{d}q \Pi_{m_J}(q) \partial_q m_z(q). \tag{B.22}$$

In order to link it to what we have presented in chapter 6, we remind that the average magnetization and the average velocity are related by

$$p - \hbar K m_z(p) = m v(p). \tag{B.23}$$

We then recover the formula used in the main text,

$$\boxed{c(m_J) = \frac{1}{\hbar K} \int \mathrm{d}p \Pi_{m_J}(p) \partial_p \left[p - m v(p)\right].} \tag{B.24}$$

Rapid Communications

Anisotropic light shift and magic polarization of the intercombination line of dysprosium atoms in a far-detuned dipole trap

Thomas Chalopin,[1] Vasiliy Makhalov,[1] Chayma Bouazza,[1] Alexandre Evrard,[1] Adam Barker,[2] Maxence Lepers,[3,4] Jean-François Wyart,[3,5] Olivier Dulieu,[3] Jean Dalibard,[1] Raphael Lopes,[1,*] and Sylvain Nascimbene[1]

[1]*Laboratoire Kastler Brossel, Collège de France, CNRS, ENS-PSL Research University, UPMC-Sorbonne Universités, 11 place Marcelin Berthelot, F-75005 Paris, France*

[2]*Clarendon Laboratory, University of Oxford, Oxford OX1 3PU, United Kingdom*

[3]*Laboratoire Aimé Cotton, CNRS, Université Paris-Sud, ENS Paris-Saclay, Université Paris-Saclay, 91405 Orsay, France*

[4]*Laboratoire Interdisciplinaire Carnot de Bourgogne, CNRS, Université de Bourgogne Franche-Comté, 21078 Dijon, France*

[5]*LERMA, Observatoire de Paris-Meudon, PSL Research University, Sorbonne Universités, UPMC Univ. Paris 6, CNRS UMR8112, 92195 Meudon, France*

(Received 23 May 2018; published 22 October 2018)

We characterize the anisotropic differential ac-Stark shift for the Dy 626 nm intercombination transition, induced in a far-detuned 1070 nm optical dipole trap, and observe the existence of a "magic polarization" for which the polarizabilities of the ground and excited states are equal. From our measurements we extract both the scalar and tensorial components of the dynamic dipole polarizability for the excited state, $\alpha_E^s = 188(12)\alpha_0$ and $\alpha_E^t = 34(12)\alpha_0$, respectively, where α_0 is the atomic unit for the electric polarizability. We also provide a theoretical model allowing us to predict the excited state polarizability and find qualitative agreement with our observations. Furthermore, we utilize our findings to optimize the efficiency of Doppler cooling of a trapped gas, by controlling the sign and magnitude of the inhomogeneous broadening of the optical transition. The resulting initial gain of the collisional rate allows us, after forced evaporation cooling, to produce a quasipure Bose-Einstein condensate of ^{162}Dy with 3×10^4 atoms.

DOI: 10.1103/PhysRevA.98.040502

Lanthanide atoms offer a new and exciting test bed on which to explore long-awaited physical phenomena such as the appearance of the roton excitation in dipolar Bose-Einstein condensates, due to their large magnetic moments [1–4], or the occurrence of exotic superfluid phases based on narrow transition lines and a dense Feshbach resonance spectrum [5–9].

These unique properties arise thanks to the partially filled, submerged $4f$ shell but, due to the large number of unpaired electrons, come with a drawback in terms of complexity. For instance, the dynamic (dipole) polarizability, which is of fundamental importance as it sets the strength of light-matter interactions, is theoretically challenging to estimate [10,11]. Several experimental efforts have been made to benchmark these theoretical models but have, so far, mainly addressed the polarizability of the ground state [12–14].

In the case of the 626 nm intercombination transition used in several dysprosium (Dy) cold atom experiments, little is known about the excited state polarizability [15–17]. Besides its fundamental interest, its characterization plays an important role when considering the action of near-resonant light on a gas confined in the high-intensity field of an optical dipole trap [18]. In particular, when the ground and excited states have different polarizabilities, one expects a differential light shift in the resonance line proportional to the trapping light intensity.

If the differential light shift is close to or larger than the linewidth of the transition, the light-matter interaction becomes strongly affected by the trapping optical beam. In particular, due to the spatial variation of the light intensity, the coupling becomes spatially dependent. This effect received much attention in the case of atomic clocks since it couples the external and internal degrees of freedom, degrading the coherence of spectroscopic measurements. For alkali [18] and alkaline-earth atoms, the existence of "magic wavelengths" helped to suppress this nuisance [19–24]. Furthermore, the line shift induced by the presence of off-resonant optical traps also affects the laser cooling efficiency [25,26] and can be used to spatially tailor light-matter interactions [27].

For lanthanide atoms, due to the significant tensorial contribution to the total atomic polarizability, the differential light shift strongly depends on the trapping light polarization [12,14]. This offers the possibility to locally vary the transition resonance frequency by fine-tuning the trapping beam polarization; this feature has also been applied in a similar manner to alkali-metal atoms, using the differential vectorial polarizability [28]. The magic-wavelength behavior is then replaced by a "magic polarization."

In this Rapid Communication we characterize the anisotropic differential light shift in the case of the Dy 626 nm transition ($|g\rangle = |J = 8, m_J = -8\rangle \rightarrow |e\rangle = |J' = 9, m_{J'} = -9\rangle$) for a cold gas trapped in a far-detuned 1070 nm optical trap (see Fig. 1) [29]. Using theoretical predictions for the polarizability of the ground state [10,30] (see also measurements of Ref. [13]), we extract the excited

*raphael.lopes@lkb.ens.fr

 ©2018 American Physical Society

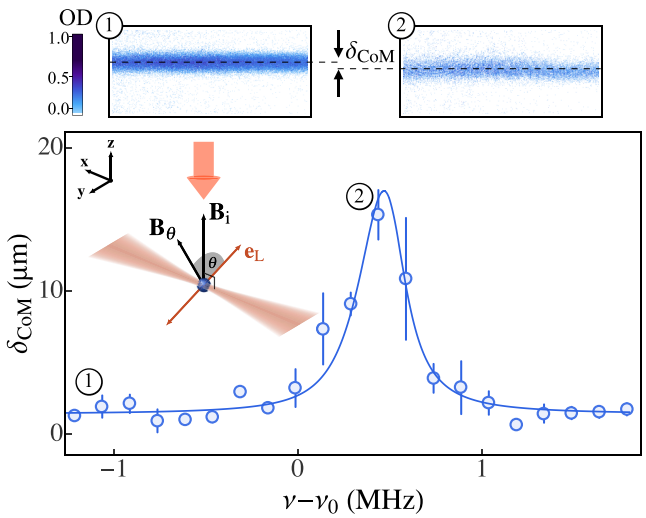

FIG. 1. Center-of-mass displacement resonance. Schematic drawing: a near-resonant (626 nm) beam is applied to a cold atomic sample optically trapped around the focal point of a 1070 nm laser beam propagating along the x axis. The magnetic field bias is orientated in a plane perpendicular to the optical beam propagation axis, forming an angle θ with the polarization vector $\mathbf{e}_\mathrm{L}$. Two orientations of $\mathbf{B}$ are represented: the initial vertical orientation ($\mathbf{B}_\mathrm{i}$) and the value corresponding to the resonance curve shown in the main panel ($\mathbf{B}_\theta$). The beam is applied for a short duration and accelerates the atoms, leading to a displacement of the cloud center-of-mass (CoM), measured after time of flight (ToF) represented by the dashed lines (see top panels). The center-of-mass displacement (δ_{CoM}) is plotted as a function of the laser frequency ν for $\theta = 80^\circ$ and fitted using Eq. (7) with the free parameter $\Delta\alpha(\theta)$. The error bars denote the rms. deviation of three independent measurements.

state polarizability, and identify a tensorial component of much larger amplitude than for the ground state. By tuning the relative angle between the laser polarization and an external magnetic field, we find a magic polarization for which the differential light shift between $|g\rangle$ and $|e\rangle$ is canceled. We compare our results to a theoretical model described in Se. II and find qualitative agreement. As a concrete example of the relevance of this magic-polarization behavior, we implement a one-dimensional Doppler cooling experiment which we optimize by adjusting the spatially dependent differential light shift. We observe a significant gain in the collisional rate for the case of a small, positive differential light shift which leads to an enhanced (red) detuning of the cooling light at the trap center. We interpret this result as a suppression of light-assisted collisions at the bottom of the potential where the atomic density is higher, while cooling remains efficient in the wings. This cooling stage allows us to significantly boost the cloud initial phase-space density, and, after a 4 s forced evaporation procedure, to reach quantum degeneracy for a cloud of ^{162}Dy at a critical temperature $T_c \approx 120(20)$ nK and atom number $N \approx 7 \times 10^4$.

I. DIFFERENTIAL LIGHT SHIFT: MAGIC POLARIZATION

The interaction between an atom and a monochromatic laser field of frequency ω gives rise to two types of effects. First, the atom can scatter photons into empty modes of the electromagnetic field via spontaneous emission processes. Second, each atomic level may be shifted by the light field (ac-Stark shift). Here we restrict ourselves to the case of a nonresonant light field, which in our case corresponds to the laser beam used for trapping the atoms, so that the first type of effect is negligible and we focus on the latter.

Let us consider, for instance, the atomic ground level G, with angular momentum J. At lowest order in laser intensity, the atom-light interaction leads to stimulated Raman processes in which the atom passes from the Zeeman state $|G, J, m\rangle$ to another state $|G, J, m'\rangle$ with $|m' - m| \leqslant 2$. The light-shift operator is then a rank-2 tensor acting on the manifold G. It can be expressed in terms of the dynamic polarizability, $\underline{\underline{\alpha}}_G(\omega)$, with scalar ($\alpha_G^\mathrm{s}$), vectorial ($\alpha_G^\mathrm{v}$), and tensorial ($\alpha_G^\mathrm{t}$) contributions.

For a laser beam with linear polarization $\mathbf{e}_\mathrm{L}$, the vectorial contribution is suppressed by symmetry and the restriction of the atom-light interaction to G can be written

$$\hat{H}_{\text{a-l,G}} = \tilde{V}(\mathbf{r})\left\{\alpha_G^\mathrm{s}\hat{\mathbb{1}} + \alpha_G^\mathrm{t}\frac{3(\hat{\mathbf{J}}\cdot\mathbf{e}_\mathrm{L})^2 - \hat{\mathbf{J}}^2}{J(2J-1)}\right\}, \tag{1}$$

where $\hat{\mathbf{J}}$ is the angular momentum operator. Here $\tilde{V}(\mathbf{r}) = -\frac{1}{2\epsilon_0 c}I(\mathbf{r})$ where $I(\mathbf{r})$ is the laser beam intensity, ϵ_0 the vacuum permittivity, and c the speed of light.

In the presence of a static magnetic field $\mathbf{B}$, the Hamiltonian describing the dynamics within G is thus

$$\hat{H}_G = \hat{H}_{0,\mathrm{G}} + \hat{H}_{\text{a-l,G}}, \tag{2}$$

with $\hat{H}_{0,\mathrm{G}} = g_J\mu_\mathrm{B}\,\mathbf{J}\cdot\mathbf{B}$, g_J the Landé g factor, and μ_B the Bohr magneton. Let us assume for now that the tensorial contribution to $\hat{H}_{\text{a-l,G}}$ can be treated at first order in perturbation theory with respect to $\hat{H}_0$ (this assumption will be released later). The energy shift for the state of lowest energy $|g\rangle$ in the manifold G is then given by

$$E_g = E_{g,0} + \tilde{V}(\mathbf{r})\left\{\alpha_G^\mathrm{s} + \frac{\alpha_G^\mathrm{t}}{2}(3\cos^2\theta - 1)\right\}, \tag{3}$$

where θ is the angle between the static magnetic field and the beam polarization (see Fig. 1).

A similar analysis can be performed for any relevant excited electronic level E, in particular the one used here for Doppler cooling. The energy difference between the states of lowest energy in each manifold, $|g\rangle$ and $|e\rangle$, is equal to

$$h\nu_0'(\mathbf{r}) = h[\nu_0 + \Delta\nu_\alpha(\mathbf{r})], \tag{4}$$

where $h\nu_0 = \Delta E_0 = E_{e,0} - E_{g,0}$, and

$$h\Delta\nu_\alpha(\mathbf{r}) = \tilde{V}(\mathbf{r})\Delta\alpha, \tag{5}$$

with $\Delta\alpha = \Delta\alpha^\mathrm{s} + \frac{1}{2}\Delta\alpha^\mathrm{t}(3\cos^2\theta - 1)$ and $\Delta\alpha^{(\mathrm{s,\,t})} = \alpha_E^{(\mathrm{s,\,t})} - \alpha_G^{(\mathrm{s,\,t})}$. Importantly, for $|\Delta\alpha^\mathrm{t}/\Delta\alpha^\mathrm{s} - 1/2| \geqslant 3/2$, the differential light shift cancels for a specific polarization angle $\theta_\mathrm{magic} = \arccos[\sqrt{\frac{1}{3}(1 - 2\frac{\Delta\alpha^\mathrm{s}}{\Delta\alpha^\mathrm{t}})}]$, that we will refer to as a magic-polarization angle in the following text.

We begin by producing a cold sample of 10^7 ^{164}Dy atoms in the state $|g\rangle$, held in a 1070 nm dipole trap beam. The beam polarization is linear and oriented at approximately 60°

relative to the magnetic field ($\mathbf{B}_i$) initially aligned with the vertical $\hat{\mathbf{z}}$ axis (see Fig. 1); as shown hereafter, this seemingly arbitrary angle corresponds to θ_{magic}. The magnetic field is then reorientated to probe different values of θ. The duration of the reorientation is chosen long enough for the atoms to follow adiabatically the state $|g\rangle$ [31].

In order to probe the resonance frequency for the $|g\rangle \rightarrow |e\rangle$ transition, we apply for $\tau = 30$ μs a near-resonant beam, circularly polarized (σ^-) and propagating along $\hat{\mathbf{z}}$ [32]. In the limit of a short pulse, the momentum kick experienced by the atoms reaches its maximum value when the laser frequency equals the transition frequency. This leads to a maximum displacement of the cloud center of mass (CoM) after time of flight (ToF), allowing us to extract, as a function of the dipole trap intensity, the transition resonance frequency and the differential light shift.

In more detail, the mean radiative force exerted on an atom at a position $\mathbf{r}$ is given by [33]

$$\mathbf{F}(\Delta\omega(\mathbf{r}), v_z) = -\hbar k \frac{\Gamma}{2} \frac{s_0}{1 + s_0 + 4\left(\frac{\Delta\omega(\mathbf{r}) - k v_z}{\Gamma}\right)^2} \hat{\mathbf{z}}, \quad (6)$$

where $k = 2\pi/\lambda$ is the recoil momentum, with $\lambda = 626$ nm, $s_0 = I_0/I_{\text{sat}}$ the saturation parameter with $I_{\text{sat}} = 72\ \mu W/\text{cm}^2$, $\Delta\omega(\mathbf{r}) = 2\pi \times [\nu - \nu_0'(\mathbf{r})]$, v_z the atomic velocity along $\hat{\mathbf{z}}$, and $\Gamma = 2\pi \times 136$ kHz the transition linewidth. During the application of this pulse the cloud displacement is negligible (on the order of 1–2 μm) and the only sizable effect of the pulse is a sudden change of the atomic velocity. Furthermore, the acquired Doppler shift during the pulse is negligible compared to Γ. The optical dipole trap is then switched off and an absorption image is taken after a ballistic expansion of duration $t_{\text{ToF}} = 1.5$ ms. The momentum kick as a result of the pulse translates into a CoM position shift, δ_{CoM}, given by

$$\delta_{\text{CoM}} = \frac{t_{\text{ToF}}}{m} \tau \int d\mathbf{v}\, d\mathbf{r}\, n(\mathbf{r}, \mathbf{v}) F(\Delta\omega(\mathbf{r}, \mathbf{v})), \quad (7)$$

where m is the atom mass and $n(\mathbf{r}, \mathbf{v})$ is the normalized spatial and velocity distribution of the cloud, computed for an initial cloud temperature $T \approx 100$ μK and a harmonic trapping potential with frequencies $\{\omega_x, \omega_{y,z}\} = 2\pi \times \{9(1)\text{ Hz}, 1.9(1)\text{ kHz}\}$.

In Fig. 1 we show a typical CoM-displacement resonance as a function of the laser frequency, ν. The origin of the frequency axis is set by the bare resonance frequency, ν_0, that we extract from a similar resonance measurement performed in the absence of the trapping beam [34]. Using Eq. (7) we record, for different values of $\tilde{V}(\mathbf{0})$ the resonance position ν_0' (see Fig. 2, top panels). We verify that ν_0' varies linearly with $\tilde{V}(\mathbf{0})$ and extract $\Delta\alpha(\theta)$ from the slope. The same procedure is then repeated for several orientations of the magnetic field $\mathbf{B}_\theta$ thus probing different relative angles θ (see Fig. 1).

We recover the expected dependence of the total polarizability difference, $\Delta\alpha$, as a function of θ, as shown in Fig. 2 (main panel). We observe that $\Delta\alpha = 0$ for $\theta_{\text{magic}} = 57(2)^\circ$, corresponding to a cancellation of the differential light shift, and characteristic of magic-polarization behavior. The fitting function shown in Fig. 2 (main panel) corresponds to the differential light shift computed numerically from the energy difference between the state of lowest energy ($|g\rangle$)

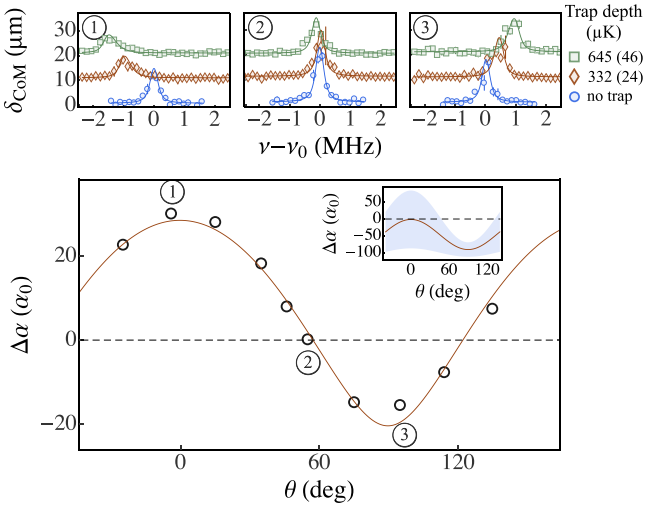

FIG. 2. Differential light shift as a function of the relative angle θ. Top panels: CoM resonances as a function of the trap depth experienced in $|g\rangle$ (see legend) for three different angles: 0°, 55°, and 100°. The CoM values have been shifted with respect to each other for clarity. The error bars denote the rms deviation of three independent measurements. Main panel: $\Delta\alpha$ as a function of θ. The solid line corresponds to a fit based on the energy difference between excited and ground states following the diagonalization of $\hat{H}$ given in Eq. (2) with $\Delta\alpha^{\text{s}}$ and $\Delta\alpha^{\text{t}}$ as free parameters. Inset: Differential polarizability as a function of θ using Eq. (5) and the theoretical values given in Sec. II. The shaded region represents the differential polarizability uncertainty.

of Eq. (2) and its equivalent solution for the excited state manifold ($|e\rangle$), with free parameters $\Delta\alpha^{\text{s}}$ and $\Delta\alpha^{\text{t}}$. We find $\Delta\alpha^{\text{s}} = -5(2)\alpha_0$ and $\Delta\alpha^{\text{t}} = 33(2)\alpha_0$, where $\alpha_0 = 4\pi\epsilon_0 a_0^3$ and a_0 is the Bohr radius. Using the theoretical values of $\alpha_G^{(\text{s, t})}$ (see Sec. II) we determine the excited state scalar and tensorial polarizabilities $\alpha_E^{\text{s}} = 188(12)\alpha_0$ and $\alpha_E^{\text{t}} = 34(12)\alpha_0$, respectively. The small error bars reported here are purely statistical but systematic effects can play an important role in the quantitative determination of $\alpha_E^{(\text{s, t})}$. For instance, deviations from the theoretical values of $\alpha_G^{(\text{s, t})}$, such as the ones reported for 1064 nm (see Ref. [13]), would automatically shift the reported absolute values of $\alpha_E^{(\text{s, t})}$. However, the existence of the magic polarization angle (θ_{magic}) is robust with respect to these systematic effects.

Our observations imply that, although the scalar components of the dynamic polarizability are similar for both states, the tensorial contribution of the excited state is much larger than for the ground state. Note, however, that the tensorial component of the excited state does not alone fulfill the condition $\alpha_E^{\text{t}} > 2\alpha_E^{\text{s}}$ needed to cancel the light shift of that state.

II. THEORETICAL ESTIMATION OF THE EXCITED STATE POLARIZABILITY

The scalar α^{s} and tensor polarizabilities α^{t} are calculated using the sum-over-state formula (see, e.g., [30]). For the ground state, the data of Ref. [30] give $\alpha_G^{\text{s}} = 193(10)\alpha_0$ and $\alpha_G^{\text{t}} = 1.3(10)\alpha_0$ at 1070 nm [35].

For the excited state $|e\rangle$ considered above, the energies and transition dipole moments (TDMs) toward even-parity levels are required to estimate the polarizability. For levels belonging to configurations that were observed experimentally, energies and TDMs were explicitly calculated with the semiempirical method implemented in Ref. [36], which has been extended by some of us [11,30,37]. Those levels are split into three groups of configurations: (i) $4f^{10}6s^2 + 4f^{10}5d6s + 4f^96s^26p$; (ii) $4f^{10}6s7s + 4f^{10}6s6d$, and (iii) $4f^95d6s6p$ [38]. Following Ref. [37], we multiply the relevant monoelectronic TDMs by a scaling factor (0.794 for $\langle ns|\hat{r}|n'p\rangle$, 0.923 for $\langle nf|\hat{r}|n'd\rangle$, and 0.80 for $\langle nd|\hat{r}|n'p\rangle$), in order to improve the least-square fit of the measured TDMs by the calculated ones. Some unobserved levels are likely to significantly contribute to the polarizability; for instance, those belonging to the $4f^{10}6p^2$ configuration. We account for those levels using the effective model of Ref. [11], with configurations $4f^{10}6p^2$, $4f^{10}6sns$ ($n = 8$–10) and $4f^{10}6snd$ ($n = 7$–9). Transition energies are calculated using the corresponding observed energy levels in ytterbium, while monoelectronic TDMs are the *ab initio* values multiplied by the scaling factors given above. Overall, we find $\alpha_E^{\mathrm{s}} = 132(33)\alpha_0$ and $\alpha_E^{\mathrm{t}} = 61(33)\alpha_0$.

As shown in Fig. 2 (inset) our model is consistent, within error bars, with the experimental observation of a magic polarization. Such agreement relies on a large difference between the tensorial contributions of the excited and ground states. The predicted magic polarization angle ($-60^\circ < \theta < 60^\circ$) although in qualitative agreement with our observations, does not allow one to quantitatively account for our results. This is due to the aforementioned difficulty to accurately resolve the excited state polarizability which leads to a large differential polarizability uncertainty.

III. APPLICATION TO DOPPLER COOLING

We demonstrate the relevance of a magic polarization by considering Doppler cooling in an optical dipole trap [26,39–42]. This process is implemented in order to significantly reduce the cloud temperature over a short timescale, typically set by the weakest trapping frequency. For this purpose, we use the 626 nm transition considered above where $\Gamma = 2\pi \times 136$ kHz. Since Γ is small compared to the typical differential light shifts reported in Fig. 2, one expects the cooling efficiency to be strongly dependent on the optical beam polarization.

In order to optimize the cooling efficiency we vary slightly the value of θ around the magic polarization angle θ_{magic} (see Fig. 3) [43]. We observe two regimes with distinct behavior. In the case of a negative differential light shift [$\Delta\nu_\alpha(\mathbf{r}) < 0$], the cooling is inefficient. On the other hand, for small, positive values of the differential light shift, the cooling stage is efficient and leads to an increased collisional rate ($\Gamma_{\mathrm{col.}}$). The qualitative explanation for that behavior is summarized schematically in Fig. 3 (top panels). In the first case, the denser, central region of the atomic cloud is, due to the strong negative differential light shift, closer to resonance and therefore interacts strongly with the cooling beam. However, the local density is large and light-assisted collisions are predominant; this results in a very poor cooling efficiency as shown in Fig. 3(a). For the case of a positive differential light shift the situation is reversed. The central region is strongly detuned, and light-assisted collisions are reduced while cooling taking place in the wings, where the density is lower, is very efficient [see Fig. 3(b)].

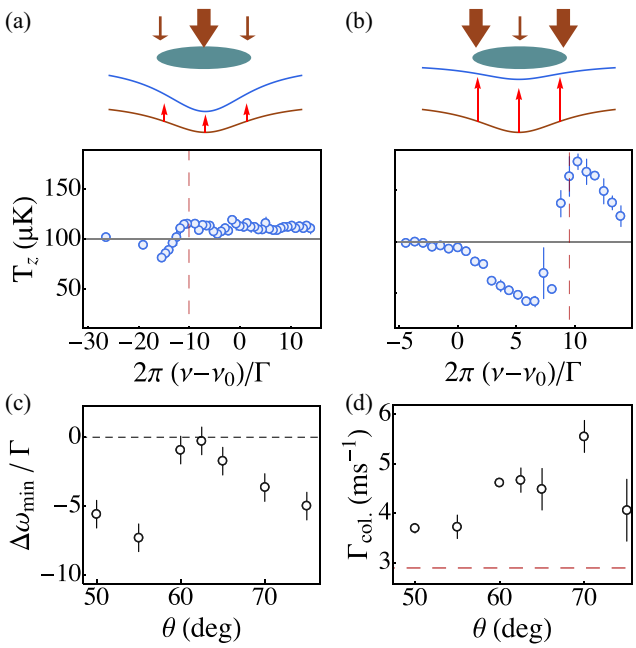

FIG. 3. Doppler cooling efficiency as a function of θ and gain in phase-space density: Cooling efficiency for (a) $\theta = 50^\circ$ and (b) $\theta = 75^\circ$ as a function of the cooling beam frequency ν, for $s_0 = 0.5$ and a pulse time $\tau = 20$ ms. The vertical red dashed line indicates the transition resonance at the trap center. (c) Detuning from the trap center for which the minimal temperature is recorded ($\Delta\omega_{\mathrm{min}}$) as a function of θ. The black dashed line indicates the zero-detuning limit. (d) Collisional rate, $\Gamma_{\mathrm{col.}}$, as a function of θ. An optimum is visible for $\theta = 70^\circ$ corresponding to a small, positive differential light shift. The horizontal dashed red line corresponds to the value of $\Gamma_{\mathrm{col.}}$ prior to the Doppler cooling stage. The error bars denote the rms deviation of three independent measurements.

To better understand the above empirical description of the cooling and heating mechanisms at work, we also report the detuning frequency at which the minimal temperature is recorded for several different values of θ [see Fig. 3(c)]. The detuning is expressed with respect to the resonance frequency at the trap center, such that $\Delta\omega_{\mathrm{min}} = 2\pi \times [\nu_{\mathrm{min}} - \nu_0'(\mathbf{0})]$. In the case of a negative differential light shift we observe an optimum cooling efficiency for large negative detuning values. This behavior suggests that the cooling beam is also responsible for local heating and losses at the trap center; processes which are minimized by increasing the absolute frequency detuning. In the case of a differential light-shift cancellation, the detuning is compatible with the textbook $-\Gamma/2$ result. For positive differential light shifts we also observe an optimum at an enhanced negative detuning. This is expected since the cooling mechanism mainly occurs in the outer regions of the cloud, where the differential light shift is smaller and therefore the frequency detuning from the trap center is larger (see Fig. 3, top panels).

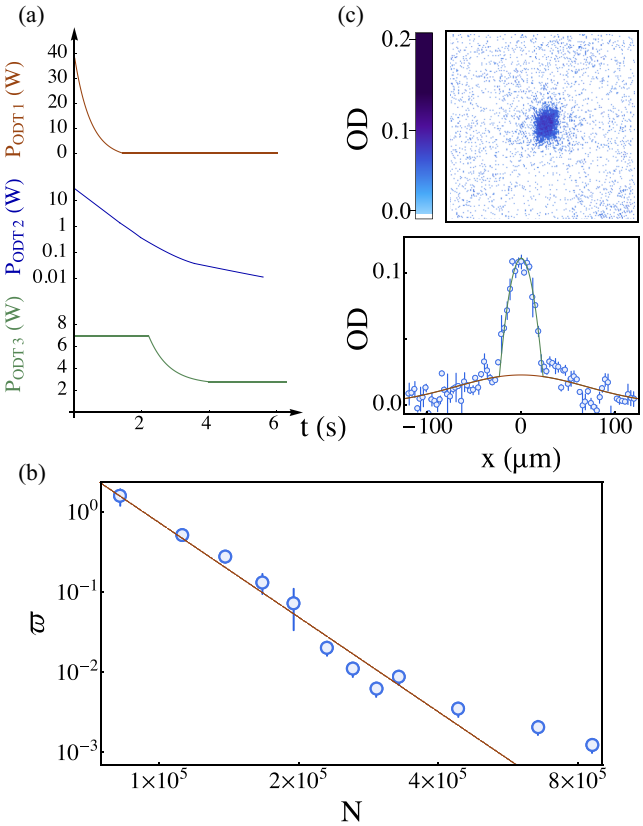

FIG. 4. Condensation of ^{162}Dy: (a) Schematic representation of the evaporation procedure in the optical dipole trap. (b) Phase-space density, ϖ, as a function of the atom number N in logarithmic scale. (c) Two-dimensional picture and integrated profile of a dipolar Bose-Einstein condensate with a condensed fraction of 50%. The solid line corresponds to a Gaussian plus parabolic fit.

We optimize the cooling efficiency by maximizing the collisional rate $\Gamma_{\text{col.}}$, which is a natural figure of merit toward achieving Bose-Einstein condensation. For each value of θ we maximize $\Gamma_{\text{col.}}$ by adjusting the frequency and τ for a fixed $s_0 = 0.5$. As shown in Fig. 3(d), we observe that for small positive differential light shifts ($\theta \approx 70^\circ$) a maximum is reached. A similar method has also been applied to reach the quantum limit of Doppler cooling in the case of strontium atoms [26].

Production of a ^{162} Dy BEC

We now discuss the production of a Bose-Einstein condensate after evaporative cooling in a crossed dipole trap (see Fig. 4). We used the ^{162}Dy isotope as it exhibits a larger background scattering length, which enhances the elastic collision rate compared to the ^{164}Dy isotope. We checked that the electric polarizability and the Doppler cooling work equivalently for the two isotopes, as expected since the nuclear spin is zero in both cases.

The optimization of the Doppler cooling stage allows us to reach a phase-space density of $\varpi = 5.7(10) \times 10^{-4}$, and to load approximately 9×10^5 atoms in a crossed dipole trap formed of the laser discussed in previous sections (ODT 1), a circular Gaussian beam with waist of 25 μm operating at 1064 nm with a maximum output power of 45 W (ODT 2) and an elliptical Gaussian beam with waists of 63 μm and 41 μm operating at 1064 nm and with 9 W maximum output power (ODT 3). The circular Gaussian beam (ODT 2) is spatially modulated (at a frequency of 50 kHz) through the use of a deflector which makes it effectively elliptic. The modulation is reduced through the evaporation in order to increase the collisional rate and maximize the evaporation efficiency. All three optical beams lie on the horizontal plane and form angles with respect to ODT 1 of -56° (ODT 2) and 30.6° (ODT 3). The magnetic field is kept at a fixed value of 1.45 G, away from any Feshbach resonance.

A schematic representation of the evaporation procedure is shown in Fig. 4(a). The evaporation efficiency given by $\gamma = -d \log \varpi / d \log N$ is, for most of the evaporation protocol, close to 4 [see Fig. 4(b)]. Bose-Einstein condensation is then reached at a critical temperature of 120(20) nK. After further evaporative cooling, we obtain a quasipure BEC with $\sim 3 \times 10^4$ atoms in an harmonic trap with aspect ratio $\omega_z / \sqrt{\omega_x \omega_y} = 1.7$.

In conclusion, we have observed the tunability of the differential light shift for the 626 nm transition in the case of a thermal Dy cloud confined in a far-detuned, 1070 nm, optical dipole trap. We observe that, for a given trapping beam polarization angle, a total cancellation of the differential light shift can be achieved. This observation is in qualitative agreement with the most recent theoretical models as discussed in Sec. II and provides valuable information on the excited state polarizability. We demonstrate the relevance of the magic-polarization behavior by optimizing a Doppler cooling stage which led us to reach a degenerate dipolar gas. Furthermore, the magic-polarization behavior opens the prospect of sideband cooling in optical lattices for the purpose of single site imaging [44].

ACKNOWLEDGMENTS

This work is supported by PSL University (MAFAG project), European Union (ERC UQUAM and TOPODY), and DIM Nano-K under the project InterDy. We thank Davide Dreon and Leonid Sidorenkov for contributions in earlier stages of the experiment.

[1] L. Santos, G. V. Shlyapnikov, and M. Lewenstein, Phys. Rev. Lett. **90**, 250403 (2003).
[2] R. M. Wilson, S. Ronen, J. L. Bohn, and H. Pu, Phys. Rev. Lett. **100**, 245302 (2008).
[3] A. Boudjemâa and G. V. Shlyapnikov, Phys. Rev. A **87**, 025601 (2013).
[4] L. Chomaz, R. M. W. van Bijnen, D. Petter, G. Faraoni, S. Baier, J. H. Becher, M. J. Mark, F. Wächtler, L. Santos, and F. Ferlaino, Nat. Phys. **14**, 442 (2018).
[5] S. Nascimbène, J. Phys. B: At., Mol. Opt. Phys. **46**, 134005 (2013).

[6] X. Cui, B. Lian, T.-L. Ho, B. L. Lev, and H. Zhai, Phys. Rev. A **88**, 011601 (R) (2013).
[7] N. Q. Burdick, Y. Tang, and B. L. Lev, Phys. Rev. X **6**, 031022 (2016).
[8] I. Ferrier-Barbut, H. Kadau, M. Schmitt, M. Wenzel, and T. Pfau, Phys. Rev. Lett. **116**, 215301 (2016).
[9] H. Kadau, M. Schmitt, M. Wenzel, C. Wink, T. Maier, I. Ferrier-Barbut, and T. Pfau, Nature (London) **530**, 194 (2016).
[10] V. A. Dzuba, V. V. Flambaum, and B. L. Lev, Phys. Rev. A **83**, 032502 (2011).
[11] H. Li, J.-F. Wyart, O. Dulieu, and M. Lepers, Phys. Rev. A **95**, 062508 (2017).
[12] W. Kao, Y. Tang, N. Q. Burdick, and B. L. Lev, Opt. Express **25**, 3411 (2017).
[13] C. Ravensbergen, V. Corre, E. Soave, M. Kreyer, S. Tzanova, E. Kirilov, and R. Grimm, Phys. Rev. Lett. **120**, 223001 (2018).
[14] J. H. Becher, S. Baier, K. Aikawa, M. Lepers, J.-F. Wyart, O. Dulieu, and F. Ferlaino, Phys. Rev. A **97**, 012509 (2018).
[15] T. Maier, H. Kadau, M. Schmitt, A. Griesmaier, and T. Pfau, Opt. Lett. **39**, 3138 (2014).
[16] E. Lucioni, G. Masella, A. Fregosi, C. Gabbanini, S. Gozzini, A. Fioretti, L. Del Bino, J. Catani, G. Modugno, and M. Inguscio, Eur. Phys. J.: Spec. Top. **226**, 2775 (2017).
[17] E. Lucioni, L. Tanzi, A. Fregosi, J. Catani, S. Gozzini, M. Inguscio, A. Fioretti, C. Gabbanini, and G. Modugno, Phys. Rev. A **97**, 060701(R) (2018).
[18] N. Lundblad, M. Schlosser, and J. V. Porto, Phys. Rev. A **81**, 031611 (R) (2010).
[19] T. Ido, Y. Isoya, and H. Katori, Phys. Rev. A **61**, 061403(R) (2000).
[20] H. Katori, M. Takamoto, V. G. Pal'chikov, and V. D. Ovsiannikov, Phys. Rev. Lett. **91**, 173005 (2003).
[21] M. Takamoto, F.-L. Hong, R. Higashi, and H. Katori, Nature (London) **435**, 321 (2005).
[22] J. Ye, H. J. Kimble, and H. Katori, Science **320**, 1734 (2008).
[23] H. Katori, K. Hashiguchi, E. Y. Il'inova, and V. D. Ovsiannikov, Phys. Rev. Lett. **103**, 153004 (2009).
[24] A. D. Ludlow, M. M. Boyd, J. Ye, E. Peik, and P. O. Schmidt, Rev. Mod. Phys. **87**, 637 (2015).
[25] T. Ido and H. Katori, Phys. Rev. Lett. **91**, 053001 (2003).
[26] M. Chalony, A. Kastberg, B. Klappauf, and D. Wilkowski, Phys. Rev. Lett. **107**, 243002 (2011).
[27] S. Stellmer, B. Pasquiou, R. Grimm, and F. Schreck, Phys. Rev. Lett. **110**, 263003 (2013).
[28] H. Kim, H. S. Han, and D. Cho, Phys. Rev. Lett. **111**, 243004 (2013).
[29] The 1070 nm laser light is provided by a commercial multimode IPG (50 W) laser. A similar magic-polarization behavior was observed using a 1064 nm single-mode Azur Light (45 W) laser.
[30] H. Li, J.-F. Wyart, O. Dulieu, S. Nascimbène, and M. Lepers, J. Phys. B: At., Mol. Opt. Phys. **50**, 014005 (2017).
[31] As discussed in Sec. II, for the ground-level polarizability the scalar component is much larger than the tensorial one. Consequently, the rotation of the magnetic field does not modify the trapping potential experienced by the atoms in $|g\rangle$.
[32] We use a collimated beam with a waist of 5.5 mm, much wider than the cloud spatial extension and therefore uniform for the sample. We have also performed several experiments with different pulse durations but did not observe significant changes of the differential light shift for pulse lengths varying between 10 and 100 μs. The 30 μs pulse length thus corresponds to the shortest pulse guaranteeing a good signal-to-noise ratio.
[33] C. Foot, *Atomic Physics*, Oxford Master Series in Physics (Oxford University Press, New York, 2005).
[34] We checked that neither the red-pulse duration length ($10 < \tau < 100\,\mu$s) nor the cloud temperature affected substantially the value of ν_0.
[35] To be noted that the data of Ref. [30] slightly differs from the recent calibration of the ground-state polarizability in the presence of a 1064 nm optical beam reported in Ref. [13] in which $\alpha_G^{\rm s} = 184.4(2.4)\alpha_0$ and $\alpha_G^{\rm t} = 1.7(6)\alpha_0$ were found.
[36] R. Cowan, *The Theory of Atomic Structure and Spectra* (University of California Press, Berkeley, 1981) .
[37] M. Lepers, H. Li, J.-F. Wyart, G. Quéméner, and O. Dulieu, Phys. Rev. Lett. **121**, 063201 (2018).
[38] The xenon-core configuration [Xe] preceding the configurations has been omitted for clarity.
[39] P. D. Lett, W. D. Phillips, S. L. Rolston, C. E. Tanner, R. N. Watts, and C. I. Westbrook, J. Opt. Soc. Am. B **6**, 2084 (1989).
[40] J. Dalibard and C. Cohen-Tannoudji, J. Opt. Soc. Am. B **6**, 2023 (1989).
[41] P. O. Schmidt, S. Hensler, J. Werner, T. Binhammer, A. Görlitz, and T. Pfau, J. Opt. Soc. Am. B **20**, 960 (2003).
[42] T. Maier, Interactions in a Quantum Gas of Dysprosium Atoms, Ph.D. thesis, Universität Stuttgart, 2015.
[43] A 2G bias field ensures that the Zeeman splitting is much larger than the transition linewidth. Therefore, small imperfections of the laser beam polarization are not particularly relevant. Furthermore, the weak Clebsch-Gordan coefficients for π and σ^+ transitions compared to the σ^- transition render these imperfections even less relevant.
[44] H. Ott, Rep. Prog. Phys. **79**, 054401 (2016).

nature COMMUNICATIONS

ARTICLE

DOI: 10.1038/s41467-018-07433-1 OPEN

Quantum-enhanced sensing using non-classical spin states of a highly magnetic atom

Thomas Chalopin[1], Chayma Bouazza[1], Alexandre Evrard[1], Vasiliy Makhalov[1], Davide Dreon[1,2], Jean Dalibard[1], Leonid A. Sidorenkov[1,3] & Sylvain Nascimbene[1]

Coherent superposition states of a mesoscopic quantum object play a major role in our understanding of the quantum to classical boundary, as well as in quantum-enhanced metrology and computing. However, their practical realization and manipulation remains challenging, requiring a high degree of control of the system and its coupling to the environment. Here, we use dysprosium atoms—the most magnetic element in its ground state—to realize coherent superpositions between electronic spin states of opposite orientation, with a mesoscopic spin size $J = 8$. We drive coherent spin states to quantum superpositions using non-linear light-spin interactions, observing a series of collapses and revivals of quantum coherence. These states feature highly non-classical behavior, with a sensitivity to magnetic fields enhanced by a factor 13.9(1.1) compared to coherent spin states—close to the Heisenberg limit $2J = 16$—and an intrinsic fragility to environmental noise.

[1] Laboratoire Kastler Brossel, Collège de France, CNRS, ENS-PSL University, Sorbonne Université, 11 Place Marcelin Berthelot, 75005 Paris, France. [2] Present address: Department of Physics, ETH Zurich, 8093 Zurich, Switzerland. [3] Present address: SYRTE, Observatoire de Paris, PSL University, CNRS, Sorbonne Université, LNE, 61 avenue de l'Observatoire, 75014 Paris, France. Correspondence and requests for materials should be addressed to L.A.S. (email: leonid.sidorenkov@obspm.fr)

Future progress in quantum technologies is based on the engineering and manipulation of physical systems with highly non-classical behavior[1], such as quantum coherence[2], entanglement[3], and quantum-enhanced metrological sensitivity[4,5]. These properties generally come together with an inherent fragility due to decoherence via the coupling to the environment, which makes the generation of highly non-classical states challenging[6]. An archetype of such systems consists in an object prepared in a coherent superposition of two distinct quasi-classical states, realizing a conceptual instance of Schrödinger cat[7]. Such states have been realized in systems of moderate size—referred to as 'mesoscopic' hereafter—with trapped ions[8,9], cavity quantum electrodynamics (QED) systems[10–12], superconducting quantum interference devices[13], optical photons[14–17], and circuit QED systems[18,19]. Non-classical behavior can also be achieved with other types of quantum systems, including squeezed states[20–31].

Inspired by the hypothetical cat state $|\text{dead}\rangle+|\text{alive}\rangle$ introduced by Schrödinger in his famous Gedanken experiment, one usually refers to a cat state in quantum optics as a superposition of quasi-classical states consisting in coherent states of the electromagnetic field, well separated in phase space and playing the role of the $|\text{dead}\rangle$ and $|\text{alive}\rangle$ states[7]. Such cat states can be dynamically generated in photonic systems, e.g. using a Kerr non-linearity[18,32]. For a spin J, a quasi-classical coherent state is represented as a state $|\pm J\rangle_{\hat{\mathbf{u}}}$ of maximal spin projection $m=\pm J$ along an arbitrary direction $\hat{\mathbf{u}}$. It constitutes the best possible realization of a classical state of well-defined polarization, as it features isotropic fluctuations of the perpendicular spin components, of minimal variance $\Delta J_{\hat{\mathbf{v}}}=\sqrt{J/2}$ for $\hat{\mathbf{v}}\perp\hat{\mathbf{u}}$[33]. A cat state can then be achieved for large J values, and it consists in the coherent superposition of two coherent spin states of opposite magnetization, which are well separated in phase space. We mention that the Hilbert space dimension of $2J+1$ scales linearly with the separation between the two coherent states of the superposition. Such cat states can be created under the action of non-linear spin couplings[34–37]. These techniques have been implemented with individual alkali atoms, using laser fields to provide almost full control over the quantum state of their hyperfine spin[38–42]. However, the small spin size involved in these systems intrinsically limits the achievable degree of non-classical behavior.

Non-classical spin states have also been created in ensembles of one-electron and two-electron atoms[5]. When each atom carries a spin-1/2 degree of freedom, a set of N atoms evolving identically can collectively behave as an effective spin $J=N/2$, that can be driven into non-classical states via the interactions between atoms[34–37,43]. In such systems, spin-squeezed states have been realized experimentally[20–22,25,26,28–31], as well as non-gaussian entangled states[44]. Yet, cat states remain out of reach due to their extreme sensitivity to perturbations in such systems. This behavior results from the large size 2^N of the Hilbert space (when taking into account non-symmetric quantum states), which scales exponentially with the system size N, resulting in a large number of decoherence channels (e.g. losing a single particle fully destroys their quantum coherence).

In this work, we use samples of dysprosium atoms, each of them carrying an electronic spin of mesoscopic size $J=8$. We exploit the AC Stark shift produced by off-resonant light[38] to drive non-linear spin dynamics. Each atomic spin independently evolves in a Hilbert space of dimension $2J+1=17$, much smaller than the dimension $2^N\sim10^5$ of an equivalent system of $N=16$ spins 1/2. We achieve the production of quantum superpositions of effective size 13.9(1.1) (as defined hereafter), close to the maximum allowed value $2J=16$ for a spin J. As this size can be considered large, but not macroscopic according to the original Schrödinger idea, we will hereafter refer to such quantum superpositions as Schrödinger kitten states[45]. We provide a tomographic reconstruction of the full density matrix of these states and monitor their decoherence due to the dephasing induced by magnetic field noise.

Results

Experimental protocol. Our experimental scheme is sketched in Fig. 1a. We use an ultracold sample of about 10^5 ^{164}Dy atoms, initially spin-polarized in the absolute ground state $|-J\rangle_z$, under a quantization magnetic field $\mathbf{B}=B\hat{\mathbf{z}}$, with $B=18.5(3)$ mG (see Methods). The non-linear spin dynamics results from spin-dependent energy shifts induced by a laser beam focused on the atomic sample. The laser wavelength is chosen close to the 626-nm resonance line, such that the light shifts are proportional to the polarizability tensor of a $J=8$ to $J'=9$ optical transition. For a linear light polarization along x, the light shift operator reduces to a coupling $\propto J_x^2$ (up to a constant), and we expect the spin dynamics to be described by the Hamiltonian[38]

$$\hat{H}=\hbar\omega_{\mathrm{L}}\hat{J}_z+\hbar\omega\hat{J}_x^2, \tag{1}$$

where the first term corresponds to the Larmor precession induced by the magnetic field, and the second term is the light-induced spin coupling. The light beam intensity and detuning from resonance are set such that the light-induced coupling frequency $\omega=2\pi\times1.98(1)$ MHz largely exceeds the Larmor precession frequency $\omega_{\mathrm{L}}=2\pi\times31.7(5)$ kHz. In such a regime the Hamiltonian of Eq. (1) takes the form of the so-called one-axis twisting Hamiltonian, originally introduced for generating spin squeezing[21,22,43]. We drive the spin dynamics using light pulses of duration $t\sim10$ ns to 1. Once all laser fields are switched off, we perform a projective measurement of the spin along the z-axis in a Stern–Gerlach experiment (see Fig. 1c). Measuring the atom number corresponding to each projection value m allows to infer the projection probabilities Π_m, $-J\le m\le J$.

Quantum state collapses and revivals. We first investigated the evolution of the spin projection probabilities Π_m as a function of the light pulse duration t. As shown in Fig. 2, we find the spin dynamics to involve mostly the even $|m\rangle_z$ states. This behavior is expected from the structure of the $\hat{J}_x^2$ coupling, which does not mix the even-$|m\rangle_z$ and odd-$|m\rangle_z$ sectors.

Starting in $|-J\rangle_z$, we observe for short times that all even-$|m\rangle_z$ states get gradually populated. The magnetization $m_z\equiv\langle\hat{J}_z\rangle$ and spin projection variance ΔJ_z^2 relax to almost constant values $m_z=-0.3(2)$ and $\Delta J_z^2=33(1)$ in the whole range $0.2\pi<\omega t<0.36\pi$. This behavior agrees with the expected collapse of coherence induced by a non-linear coupling. To understand its mechanism in our system, we write the initial state in the x basis, as

$$|-J\rangle_z=\sum_m(-1)^m c_m|m\rangle_x,\quad c_m=2^{-J}\sqrt{\binom{2J}{J+m}}. \tag{2}$$

In this basis, the non-linear coupling $\hat{J}_x^2$ induces m-dependent phase factors, leading to the state

$$|\psi(t)\rangle=\sum_m(-1)^m\mathrm{e}^{-\mathrm{i}m^2\omega t}c_m|m\rangle_x. \tag{3}$$

The variations between the accumulated phase factors lead to an apparent collapse of the state coherence[46]. The collapse timescale t_{c} can be estimated by calculating the typical relaxation time of the magnetization, yielding $t_{\mathrm{c}}=1/(\sqrt{2J}\omega)$,

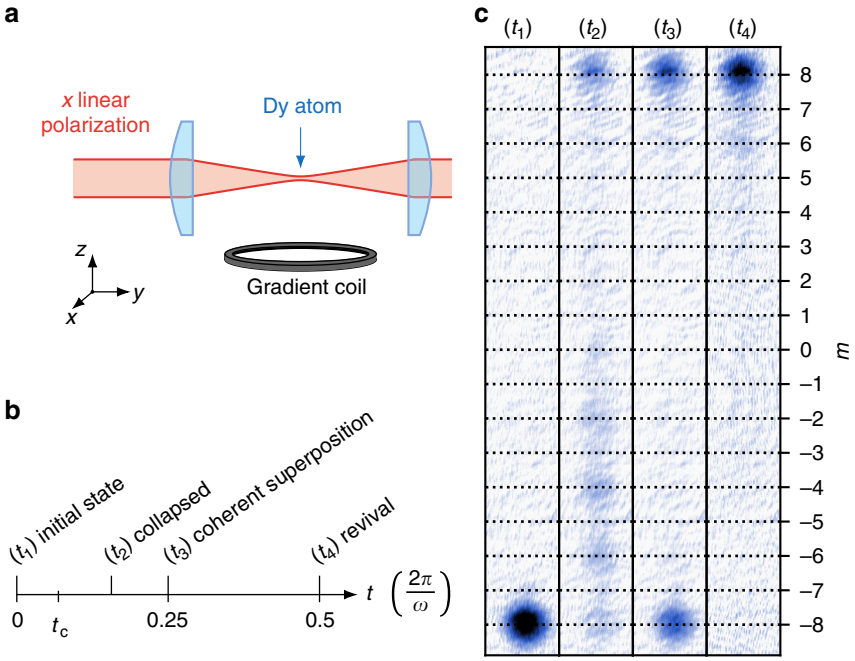

Fig. 1 Experimental scheme and expected spin dynamics. **a** Experimental scheme. The spin $J = 8$ of Dy atoms is manipulated using an off-resonant laser field linearly polarized along x, leading to a non-linear coupling $\hbar\omega\hat{J}_x^2$. The spin state is subsequently probed by imaging the atoms after a Stern–Gerlach separation of magnetic sublevels $|m\rangle_z$, allowing to determine their individual populations. **b** Expected spin dynamics. The spin, initially prepared in $|-J\rangle_z$ (corresponding atom image in panel **c** for time t_1), first collapses to a featureless state (time t_2) on a fast timescale $t_c \ll 1/\omega$. We subsequently observe the formation of a superposition between states $|-J\rangle_z$ and $|J\rangle_z$ (time t_3) and later of the polarized state $|J\rangle_z$ (time t_4). Each image is the average of typically 10 resonant absorption images

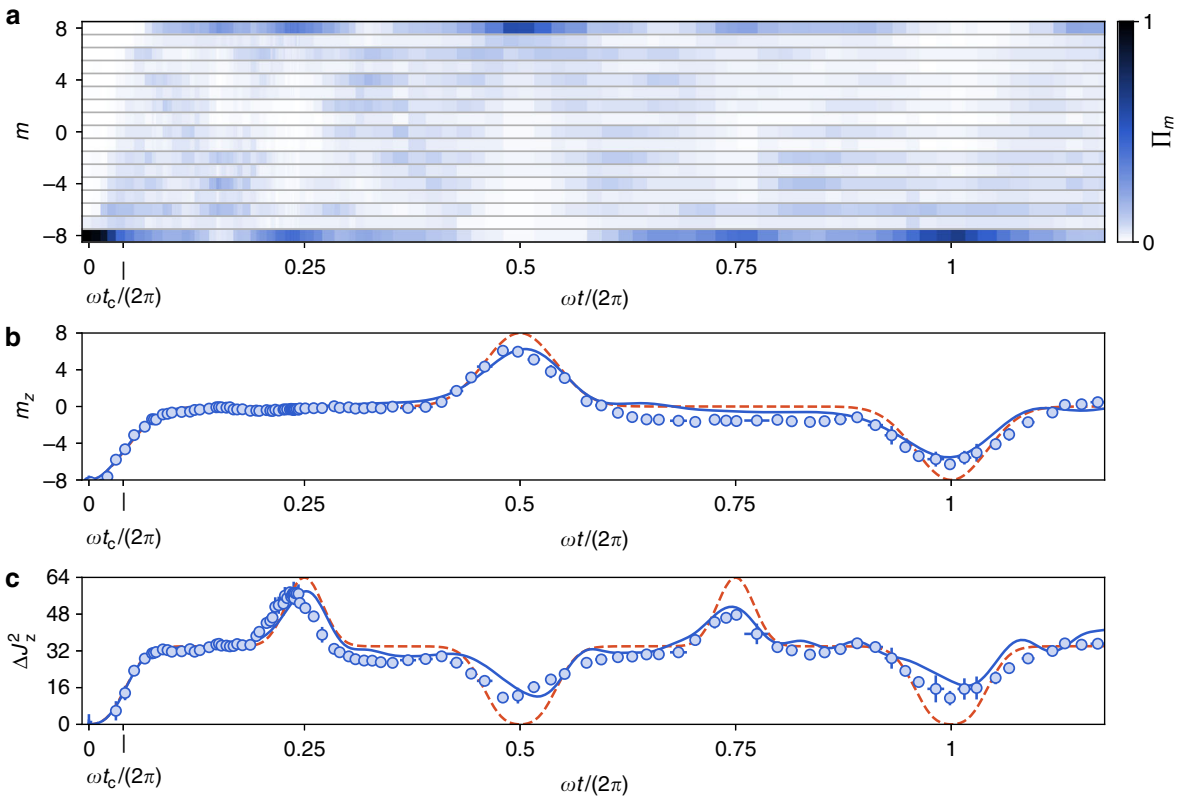

Fig. 2 Collapses and revivals in the non-linear spin dynamics. **a** Evolution of the spin projection probabilities Π_m along z as a function of the light pulse area ωt. **b**, **c** Evolution of the magnetization m_z and of the variance in the spin projection ΔJ_z^2 calculated from the Π_m distributions. The dashed red lines represent the ideal evolution for a $\hat{J}_x^2$ coupling[43], and the blue solid lines correspond to a fit taking into account experimental imperfections (see Methods). Each point is the average of five measurements, and the error bars represent the 1σ statistical uncertainty

i.e. $\omega t_c = 0.08\pi$[37,43] (see the Supplementary Note 1 and Supplementary Fig. 1).

For longer evolution times, we observe the occurence of peaks in $m_z(t)$ or ΔJ_z^2, that we interpret as the formation of states with significant quantum coherence[18,47,48]. After a quarter of the period, i.e. $\omega t = \pi/2$, all odd-m (and all even-m) phase factors in Eq. (3) get in phase again, leading to the superposition

$$|\psi_{\text{kitten}}\rangle = \mathrm{e}^{\mathrm{i}\pi/4}(|-J\rangle_z - \mathrm{i}|J\rangle_z)/\sqrt{2}, \tag{4}$$

between maximally polarized states of opposite orientation[35,37], that we refer to as a 'kitten' state[14]. We observe that, for durations $0.45\pi < \omega t < 0.49\pi$, the magnetization remains close to zero while the variance in the spin projection features a peak of maximal value $\Delta J_z^2 = 57.1(2)$ (see Fig. 2).

For pure quantum states, such a large variance is characteristic of coherent superpositions between states of very different magnetization. However, from this sole measurement we cannot exclude the creation of an incoherent mixture of $|\pm J\rangle_z$ states. We observe at later times revivals of magnetization that provide a first evidence that the state discussed above indeed corresponds to a coherent quantum superposition. The first revival occurs around $\omega t = \pi$, and corresponds to a re-polarization of the spin up to $m_z = 6.0(1)$, with most of the atoms occupying the state $|J\rangle_z$. We detect another revival of magnetization around $\omega t = 2\pi$, corresponding to a magnetized state close to the initial state ($m_z = -6.0(2)$). Between these two revivals, we observe another superposition state (large spin projection variance $\Delta J_z^2 = 47.0(6)$) around $\omega t = 3\pi/2$.

The observed spin dynamics qualitatively agrees with the one expected for a pure $\hat{J}_x^2$ coupling[43] (dashed red line in Fig. 2), while a more precise modeling of the data—taking into account the linear Zeeman coupling produced by the applied magnetic field, as well as a fit of experimental imperfections (see Methods)—matches well our data (blue line in Fig. 2).

Probing the coherence of the superposition. In order to directly probe the coherences we follow another experimental protocol allowing us to retrieve the spin projection along directions lying in the xy equatorial plane, corresponding to observables $\hat{J}_\phi \equiv \cos\phi\hat{J}_x + \sin\phi\hat{J}_y$ (see Methods). The coherence of the state $|\psi_{\text{kitten}}\rangle$, involving the opposite coherent states $|\pm J\rangle_z$, cannot be probed using a linear spin observable, such as the magnetization, but requires interpreting the detailed structure of the probability distributions $\Pi_m(\phi)$[49]. By expanding the coherent states $|\pm J\rangle_z$ on the eigen-basis $|m\rangle_\phi$ of the spin component $\hat{J}_\phi$, we rewrite the state as

$$|\psi_{\text{kitten}}\rangle = \frac{\mathrm{e}^{\mathrm{i}\pi/4}}{\sqrt{2}}\sum_m \left[\mathrm{e}^{-\mathrm{i}(J\phi+m\pi)} - \mathrm{e}^{\mathrm{i}\left(J\phi+\frac{\pi}{2}\right)}\right] c_m |m\rangle_\phi \tag{5}$$

where the c_m coefficients were introduced in Eq. (2). For the particular angles $\phi = (p + 1/4)\pi/J$ (p integer), the two terms in brackets cancel each other for odd m values. Alternatively, for angles $\phi = (p - 1/4)\pi/J$ we expect destructive interferences for even m[8,49]. This behavior can be revealed in the parity of the spin projection

$$P(\phi) \equiv \sum_m (-1)^m \Pi_m(\phi) = \sin(2J\phi), \tag{6}$$

which oscillates with a period $2\pi/(2J)$.

As shown in Fig. 3a, the experimental probability distributions $\Pi_m(\phi)$ feature strong variations with respect to the angle ϕ. The center of mass of these distributions remains close to zero, consistent with the zero magnetization of the state $|\psi_{\text{kitten}}\rangle$. We furthermore observe high-contrast parity oscillations agreeing with the above discussion and supporting quantum coherence between the $|\pm J\rangle_z$ components (see Fig. 3c).

Information on maximal-order coherences can be unveiled using another measurement protocol, which consists in applying an additional light pulse identical to the one used for the kitten state generation[50]. When performed right after the first pulse, the second pulse brings the state $|\psi_{\text{kitten}}\rangle$ to the polarized state $|J\rangle_z$, which corresponds to the second revival occuring around $\omega t = \pi$ in Fig. 2. An additional wait time between the two pulses allows for a Larmor precession of angle ϕ around z, leading to the expected evolution

$$|\psi(\phi)\rangle = \cos(J\phi)|J\rangle_z + \sin(J\phi)|-J\rangle_z, \tag{7}$$

$$m_z(\phi) = J\cos(2J\phi). \tag{8}$$

We vary the wait time and measure corresponding probability distributions $\Pi_m(\phi)$ (Fig. 3b) and magnetization $m_z(\phi)$ (Fig. 3c) consistent with Eqs. (7) and (8), respectively. This non-linear detection scheme reduces the sensitivity to external perturbations, as it transfers information from high-order quantum coherences onto the magnetization, much less prone to decoherence. It also decreases the requirements on the detection noise[51–55].

A highly sensitive one-atom magnetic probe. The Larmor precession of the atomic spins in small samples of atoms can be used for magnetometry combining high spatial resolution and high sensitivity[56]. While previous developments of atomic magnetometers were based on alkali atoms, multi-electron lanthanides, such as erbium or dysprosium intrinsically provide an increased sensitivity due to their larger magnetic moment, and potentially a substantial quantum enhancement when probing with non-classical spin states[57].

We interpret below the oscillation of the parity $P(\phi)$ discussed in the previous section as the footing of a magnetometer with quantum-enhanced precision, based on the non-classical character of the kitten state. According to generic parameter estimation theory, the Larmor phase ϕ can be estimated by measuring a generic observable $\hat{\mathcal{O}}$ with an uncertainty

$$\Delta\phi = \frac{\Delta\hat{\mathcal{O}}}{\mathrm{d}\langle\hat{\mathcal{O}}\rangle/\mathrm{d}\phi} \tag{9}$$

for a single measurement[58]. Measuring the angle ϕ using coherent spin states (e.g. in a Ramsey experiment) leads to a minimum phase uncertainty $\Delta\phi_{\text{SQL}} = 1/\sqrt{2J}$, corresponding to the standard quantum limit (SQL). For an uncertainty limit on phase measurement $\Delta\phi$ we define the metrological gain compared to the SQL as the ratio $G \equiv (\Delta\phi_{\text{SQL}}/\Delta\phi)^2$, also commonly referred to as the quantum enhancement of measurement precision[5]. In this framework, the parity oscillation $P(\phi)$ expected from Eq. (6) for the state $|\psi_{\text{kitten}}\rangle$ yields a metrological gain $G = 2J$, corresponding to the best precision limit $\Delta\phi = 1/(2J)$ achievable for a spin J—the Heisenberg limit. From the finite contrast $C = 0.74(2)$ of a sine fit of the measured parity oscillation, we deduce a metrological gain $G = 2JC^2 = 8.8(4)$.

A further increase of sensitivity can be achieved using the full information given by the measured probability distributions $\Pi_m(\phi)$ (see Fig. 3a), i.e. without assuming the parity to be the most sensitive observable to measure phase variations[44]. In this more general approach, the phase sensitivity is obtained from the rate of change of the probability distribution $\Pi_m(\phi)$ upon a variation of ϕ, that we quantify using the Hellinger distance $d_{\text{H}}^2(\phi,\phi') \equiv \frac{1}{2}\sum_m \left[\sqrt{\Pi_m(\phi)} - \sqrt{\Pi_m(\phi')}\right]^2$ between the

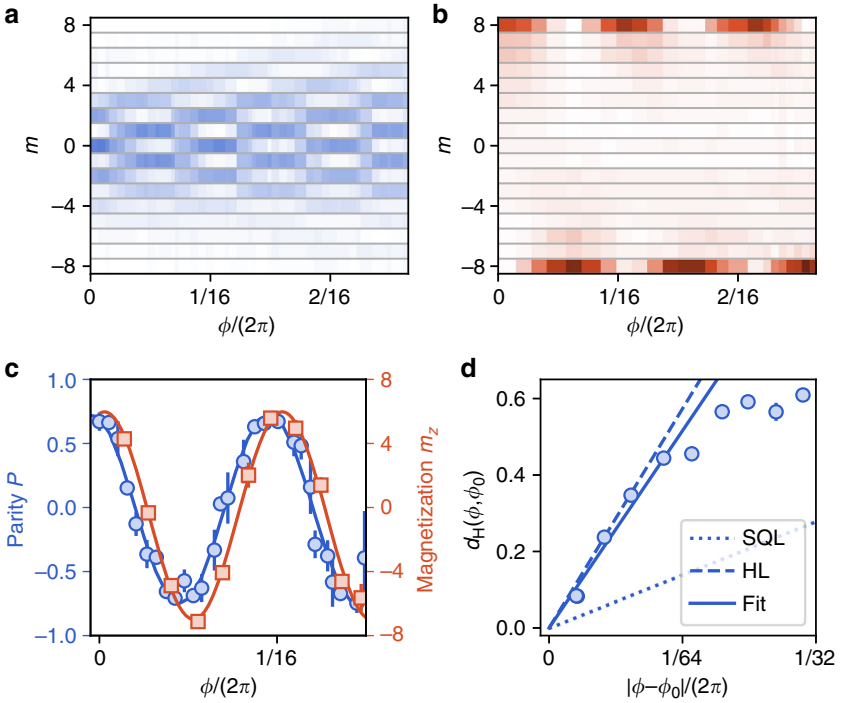

Fig. 3 Probing quantum coherence. **a** Measured spin projection probabilities $\Pi_m(\phi)$ on the equatorial directions of azimutal angle ϕ. **b** Measured spin projection probabilities $\Pi_m(\phi)$ along z, after a Larmor rotation of angle ϕ followed by a light pulse inducing further non-linear spin dynamics. **c** Evolution of the mean parity P (blue circles) and magnetization m_z (red squares) calculated from the probabilities shown in **a** and **b**, respectively. The phase shift between the measured oscillations stems from the phase offset associated with the Larmor rotation around z occurring during the parity measurement sequence. **d** Variation of the Hellinger distance between projection probabilities of angles ϕ and ϕ_0 as a function of the relative angle $\phi-\phi_0$, calculated from the data plotted in a with $\phi_0 = 0.02$. The solid line corresponds to the linear variation for small angle differences fitted to the data. The dotted (dashed) line corresponds to the standard quantum limit (Heisenberg limit). Error bars represent the 1σ statistical error

distributions $\Pi_m(\phi)$ and $\Pi_m(\phi')$. For small angle differences, one expects the scaling behavior $d_{\mathrm{H}}(\phi,\phi') \simeq \sqrt{F/8}|\phi-\phi'|$, where F is the classical Fisher information, which quantifies the measurement sensitivity as $\Delta\phi = 1/\sqrt{F}$[44,58]. For coherent spin states, the Fisher information $F = 2J$ corresponds to a measurement precision at the SQL. More generally, an increase in the slope of the Hellinger distance variation signals a gain in precision compared to the SQL, quantified by the metrological gain $G = F/(2J)$. For the kitten state given by Eq. (5), we expect a metrological gain $G = 2J$ at the Heisenberg limit. We show in Fig. 3d the Hellinger distance computed from the distributions $\Pi_m(\phi)$ shown in Fig. 3a. Its variation for small angle differences yields a metrological gain $G = 13.9(1.1)$. We thus find that using the full information from the probability distributions—rather than using its parity $P(\phi)$ only—increases the phase sensitivity.

For a given quantum state used to measure the Larmor phase, we expect the metrological gain to remain bounded by the value of its spin projection variance, as $G \leq 2\Delta J_z^2/J = 14.3(1)$[58]. As the measured gain coincides with this bound within error bars, we conclude that the phase measurement based on the Hellinger distance is optimum. We also performed a similar Hellinger distance analysis based on the distributions $\Pi_m(\phi)$ shown in Fig. 3b leading to a comparable metrological gain $G = 14.0(9)$ (see the Supplementary Note 3). Further increase of sensitivity would require improving the state preparation.

Tomography of the superposition state. In order to completely characterize the superposition state, we perform a tomographic reconstruction of its density matrix[59]. The latter involves $(2J+1)^2 - 1 = 288$ independent real coefficients, that we determine from a fit of the spin projection probabilities Π_m measured on the z-axis and on a set of directions uniformly sampling the xy equatorial plane[60]. The inferred density matrix is plotted in Fig. 4a. Its strongest elements correspond to populations and coherences involving the coherent states $|\pm J\rangle_z$, as expected for the state $|\psi_{\mathrm{kitten}}\rangle$. We measure a coherence to population ratio $2|\rho_{-J,J}|/(\rho_{-J,-J}+\rho_{J,J}) = 0.92(8)$.

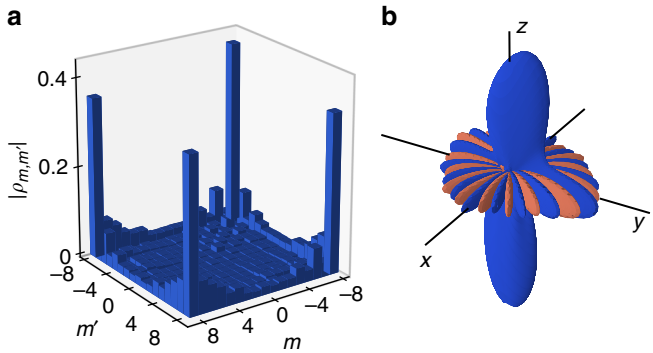

Fig. 4 Tomographic reconstruction of the kitten state. **a** Absolute values of the density matrix coefficients $|\rho_{m,m'}|$ fitted from spin projection measurements performed along z and in the equatorial plane. **b** Angular Wigner function corresponding to the density matrix plotted in **a**. Negative-valued regions are plotted in red

In order to further illustrate the non-classical character of the superposition state, we compute from the density matrix its associated Wigner function $W(\theta,\phi)$[22], defined for a spin over the

spherical angles θ, ϕ as

$$W(\theta,\phi) = \sum_{\ell=0}^{2J}\sum_{m=-\ell}^{\ell} \rho_\ell^m Y_\ell^m(\theta,\phi), \qquad (10)$$

where ρ_ℓ^m is the density matrix component on the spherical harmonics $Y_\ell^m(\theta,\phi)$[61]. The reconstructed Wigner function, plotted in Fig. 4b, exhibits two lobes of positive value around the south and north poles, associated with the population of the states $|\pm J\rangle_z$. It also features interferences around the equatorial plane originating from coherences between these two states, with strongly negative values in a large phase space area. This behavior directly illustrates the highly non-classical character of the kitten state.

Dephasing due to classical noise. We furthermore investigated the environment-induced decay of quantum coherence by following the evolution of density matrices $\rho(t)$ reconstructed after variable wait times t in the 10–100 μs range.

While we do not detect significant evolution of the populations Π_m, we observe a decrease of the extremal coherence $|\rho_{-J,J}|$, of 1/e decay time $\tau = 58 \pm 4$ μs, which we attribute to fluctuations of the ambient magnetic field. To calibrate such a dephasing process, we study the damping of the amplitude $J_\perp(t)$ of a coherent state, initially prepared in the state $|J\rangle_x$ and evolving under the applied magnetic field along z and the ambient magnetic field fluctuations (see Methods). As shown in Fig. 5b, the transverse spin amplitude $J_\perp$ decays on a 1/e timescale $\tau_0 = 740 \pm 80$ μs, consistent with residual magnetic field fluctuations in the mG range. The decoherence rate of the kitten state is thus enhanced by a factor $\tau_0/\tau = 13(2)$ compared to a coherent state, which illustrates the intrinsic fragility of mesoscopic coherent superpositions.

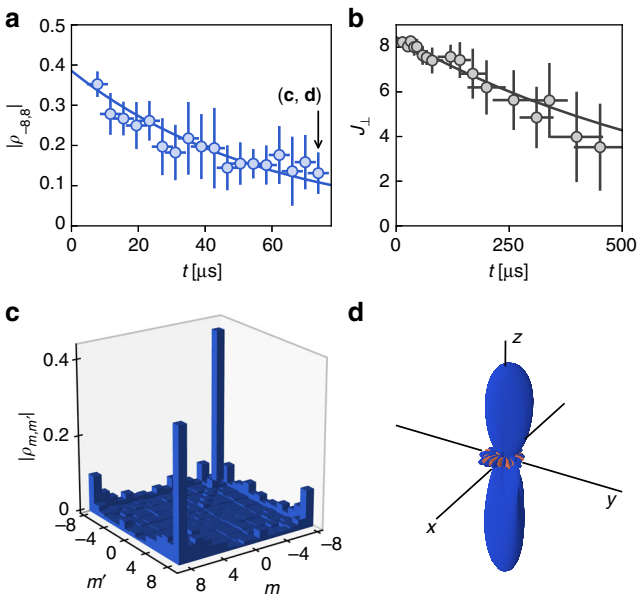

Fig. 5 Dephasing of coherences. **a** Evolution of the modulus of the extremal coherence $|\rho_{-8,8}|$ (blue circles) calculated from the tomography of the superposition state after a wait time t. The horizontal error bars correspond to the standard deviation of the Larmor precession times required for tomography. Vertical error bars are the 1σ statistical error computed using a random-weight bootstrap method. **b** Evolution of the mean transverse spin amplitude $J_\perp$ for an initial state $|J\rangle_x$ in the same magnetic field environment than for the data in **a**. The solid lines in **a** and **b** are exponential fits of the data. **c**, **d** Density matrix and Wigner function reconstructed for $t = 70 \pm 3$ μs, i.e. after a strong damping of coherences

Spin decoherence due to magnetic field fluctuations can be modeled similarly to the T_2^* decay in nuclear magnetic resonance[62] (see the Supplementary Note 4). Using a magnetic probe located close to the atom position, we measure shot-to-shot magnetic field fluctuations on a 0.5-mG range, but their variation on the ~100-μs dephasing timescale remains negligible. In this regime, we expect the dephasing of the state $|\psi_{\text{kitten}}\rangle$ to occur $2J = 16$ times faster than for a coherent state, a value close to our measurement.

Finally, we plot in Fig. 5c, d the reconstructed density matrix and its associated Wigner function for the wait time $t = 70 \pm 3$ μs. The weak amplitude of coherences and the shrinking of the negative regions in the Wigner function illustrate the dynamics towards an incoherent statistical mixture[6].

Discussion

In this work, we use spin-dependent light shifts to drive the electronic spin $J = 8$ of dysprosium atoms under a non-linear one-axis twisting Hamiltonian. The observation of several collapses and revivals of quantum coherence shows that the spin dynamics remains coherent over a full period of the evolution. In particular, the state produced after one quarter of the period consists of a coherent superposition between quasi-classical spin states of opposite orientation, which can be viewed as a mesoscopic instance of Schrödinger cat. While such coherent dynamics could be achieved with individual alkali atoms of smaller spin size[39,40], the realization of large-size coherent superpositions with ensembles of spin-1/2 particles is extremely challenging[9,17]. The high fidelity of our protocol stems from the reduced size $2J + 1$ of the available Hilbert space, that scales linearly with the effective distance $2J$ between the states involved in the superposition. Such scaling contrasts with the exponential scaling in the number of accessible states for ensembles of qubits, which dramatically increases the number of decoherence channels. Similarly, the full tomographic reconstruction of the produced quantum state also crucially relies on this limited size of the Hilbert space. Quantum state tomography of an equivalent 16-qubit ensemble remains inaccessible, unless restricting the Hilbert space to the permutationally invariant subspace[63] or using compressed sensing for almost pure states[64].

We show that our kitten state provides a quantum enhancement of precision of 13.9(1.1), up to 87(2)% of the Heisenberg limit. So far, such a high value could only be reached in ensembles of thousands of qubits based on multiparticle entanglement[25,27–30]. In such systems, while entanglement occurs between a large number of qubits, the quantum enhancement of precision remains small compared to the system size, far from the Heisenberg limit. Our protocol could be extended to prepare kitten states $(|-K\rangle_z - \mathrm{i}|K\rangle_z)/\sqrt{2}$ with $|K| \le J$, by initiating the atoms in $|-K\rangle_z$ before applying a non-linear spin coupling identical to the one used in this work. This would allow us to demonstrate the Heisenberg scaling of measurement sensitivity $\delta\phi \propto 1/K$. We could also implement, using similar techniques, protocols to prepare non-classical states based on adiabatic evolutions[65–67].

Our method could also be applied to systems of larger electronic spin J. Dysprosium being the optimum choice among all atomic elements in the electronic ground state, further improvement would require using highly excited electronic levels, such as Rydberg atomic states[12], or using ultracold molecules[68]. By increasing the atom density, one could also use interactions between N atoms of spin J to act on a collective spin of very large size $\mathcal{J} = NJ$, allowing to explore non-classical states of much larger size.

Methods

Sample preparation and detection. We use samples of about $9(1) \times 10^4$ atoms of ^{164}Dy, cooled to a temperature $T \simeq 2$ μK using laser cooling and subsequent

evaporative cooling in an optical dipole trap[69]. The dipole trap has a wavelength $\lambda = 1064$ nm, resulting in negligible interaction with the atomic spin[70]. The samples are initially spin-polarized in the absolute ground state $|-J\rangle_z$, with a bias field $B_z \simeq 0.5$ G along z, such that the induced Zeeman splitting largely exceeds the thermal energy. Before starting the light-induced spin dynamics, we ramp the bias field down to the final value $B_z = 18.5(3)$ mG in 20 ms. We checked that the promotion to higher spin states (with $m > -J$) due to dipole–dipole interactions remains negligible on this timescale. The optical trapping light is switched off right before the spin dynamics experiments.

After the light-induced spin dynamics, we perform a Stern–Gerlach separation of the various spin components using a transient magnetic field gradient (typically 50 G/cm during 2 ms) with a large bias magnetic field along z. After a 3.5 ms time of flight, the atomic density is structured as 17 separated profiles (see Fig. 1c), allowing to measure the individual spin projection probabilites Π_m using resonant absorption imaging, where m is the spin projection along z. The relative scattering cross-sections between $|m\rangle_z$ sub-levels are calibrated using samples of controlled spin composition.

Spin projection measurements along equatorial directions are based on spin rotations followed by a projective measurement along z. We apply a magnetic field pulse along y, of temporal shape $B_y(t) = B_y^{\max}\sin^2(\pi t/\tau)$, with $\tau = 3$ and $B_y^{\max}$ adjusted to map the z-axis on the equator. Taking into account the static field along z, we expect the pulse to map the equatorial direction of azimutal angle $\phi_i \simeq 0.35$rad on the z-axis. An arbitrary angle $\phi = \phi_i + \phi_L$ can be reached using an additional wait time before the B_y pulse, allowing for a Larmor precession of angle ϕ_L. The calculation of the angle $\phi_L$uses the magnetic field component B_z measured using an external probe, allowing to reduce the effect of shot-to-shot magnetic field fluctuations.

Spin dynamics modeling. Quantitative understanding of the observed spin dynamics requires taking into account experimental imperfections. We include the linear Zeeman coupling induced by the magnetic field applied along z (see Eq.(1)), leading to a small Larmor rotation on the typical timescales used for the light-induced spin dynamics. We also take into account the slight polarization ellipticity expected from the focusing of the laser beam on the atomic sample (beam divergence $\theta = \lambda/(\pi w) \simeq 4$mrad). Finally, we improve the spin dynamics modeling by fitting a small angle mismatch $\simeq 8°$ between the quantization field and the z-axis. More details on this modeling can be found in the Supplementary Note 2.

Quantum state tomography. The density matrix of the kitten state is determined from a least-square fit of the measured spin projection probabilities Π_m along z and $\Pi_m(\phi)$ on equatorial directions[60]. We uniformly sample the equatorial plane using a set of azimutal angles $\phi \in [\phi_0, \phi_0 + \pi]$. The procedure thus requires variable spin rotation durations (on average $\simeq 10$ µs), which limits the quality of the tomography due to dephasing. To reduce its effect, we use the magnetic field values measured for each experiment with an external probe to compensate for part of the dephasing, which increases the quality of the tomography and extents the coherence times by a factor $\simeq 3$. The robustness of the method with respect to measurement noise and finite sampling is tested using a random-weight bootstrap method, from which we define the statistical error bars in Fig. 5.

Calibration of dephasing. To calibrate the dephasing of coherences due to magnetic field fluctuations, we perform a Ramsey experiment using coherent spin states. We start in the ground state $|-J\rangle_z$, that we bring on the equator using a $\pi/2$ magnetic field pulse applied along y. We then let the spin precess around z for a duration t, and subsequently perform a second $\pi/2$ pulse before performing a spin projection measurement along z. We observe Ramsey oscillations of the magnetization $m_z(t) = J_\perp(t)\cos(\omega_L t + \phi)$, where the local oscillation contrast $J_\perp(t)$ corresponds to the transverse spin amplitude shown in Fig. 5b.

Data availability

The datasets generated and analyzed during the current study are available from the corresponding author on request.

Received: 14 June 2018 Accepted: 26 October 2018
Published online: 23 November 2018

References

1. Fröwis, F., Sekatski, P., Dür, W., Gisin, N. & Sangouard, N. Macroscopic quantum states: measures, fragility, and implementations. *Rev. Mod. Phys.* **90**, 025004 (2018).
2. Streltsov, A., Adesso, G. & Plenio, M. B. Colloquium: quantum coherence as a resource. *Rev. Mod. Phys.* **89**, 041003 (2017).
3. Horodecki, R., Horodecki, P., Horodecki, M. & Horodecki, K. Quantum entanglement. *Rev. Mod. Phys.* **81**, 865–942 (2009).
4. Giovannetti, V., Lloyd, S. & Maccone, L. Advances in quantum metrology. *Nat. Photon.* **5**, 222–229 (2011).
5. Pezzè, L., Smerzi, A., Oberthaler, M. K., Schmied, R. & Treutlein, P. Quantum metrology with nonclassical states of atomic ensembles. *Rev. Mod. Phys.* **90**, 035005 (2018).
6. Zurek, W. H. Decoherence, einselection, and the quantum origins of the classical. *Rev. Mod. Phys.* **75**, 715–775 (2003).
7. Haroche, S. & Raimond, J.-M. *Exploring the Quantum: Atoms, Cavities, and Photons* (Oxford University Press, Oxford, 2006).
8. Monroe, C., Meekhof, D., King, B. & Wineland, D. J. A Schrödinger Cat superposition state of an atom. *Science* **272**, 1131–1136 (1996).
9. Monz, T. et al. 14-qubit entanglement: creation and coherence. *Phys. Rev. Lett.* **106**, 130506 (2011).
10. Brune, M. et al. Observing the progressive decoherence of the meter in a quantum measurement. *Phys. Rev. Lett.* **77**, 4887 (1996).
11. Deleglise, S. et al. Reconstruction of non-classical cavity field states with snapshots of their decoherence. *Nature* **455**, 510–514 (2008).
12. Facon, A. et al. A sensitive electrometer based on a Rydberg atom in a Schrödinger-cat state. *Nature* **535**, 262–265 (2016).
13. Friedman, J. R., Patel, V., Chen, W., Tolpygo, S. & Lukens, J. E. Quantum superposition of distinct macroscopic states. *Nature* **406**, 43–46 (2000).
14. Ourjoumtsev, A., Tualle-Brouri, R., Laurat, J. & Grangier, P. Generating optical Schrödinger kittens for quantum information processing. *Science* **312**, 83–86 (2006).
15. Neergaard-Nielsen, J. S., Nielsen, B. M., Hettich, C., Mølmer, K. & Polzik, E. S. Generation of a superposition of odd photon number states for quantum information networks. *Phys. Rev. Lett.* **97**, 083604 (2006).
16. Takahashi, H. et al. Generation of large-amplitude coherent-state superposition via ancilla-assisted photon subtraction. *Phys. Rev. Lett.* **101**, 233605 (2008).
17. Yao, X.-C. et al. Observation of eight-photon entanglement. *Nat. Photon.* **6**, 225–228 (2012).
18. Kirchmair, G. et al. Observation of quantum state collapse and revival due to the single-photon Kerr effect. *Nature* **495**, 205–209 (2013).
19. Vlastakis, B. et al. Deterministically encoding quantum information using 100-photon Schrödinger cat states. *Science* **342**, 607–610 (2013).
20. Estève, J., Gross, C., Weller, A., Giovanazzi, S. & Oberthaler, M. Squeezing and entanglement in a Bose-Einstein condensate. *Nature* **455**, 1216–1219 (2008).
21. Gross, C., Zibold, T., Nicklas, E., Esteve, J. & Oberthaler, M. K. Nonlinear atom interferometer surpasses classical precision limit. *Nature* **464**, 1165–1169 (2010).
22. Riedel, M. F. et al. Atom-chip-based generation of entanglement for quantum metrology. *Nature* **464**, 1170–1173 (2010).
23. Maussang, K. et al. Enhanced and reduced atom number fluctuations in a BEC splitter. *Phys. Rev. Lett.* **105**, 080403 (2010).
24. Lücke, B. et al. Twin matter waves for interferometry beyond the classical limit. *Science* **334**, 773–776 (2011).
25. Hamley, C. D., Gerving, C., Hoang, T., Bookjans, E. & Chapman, M. S. Spin-nematic squeezed vacuum in a quantum gas. *Nat. Phys.* **8**, 305–308 (2012).
26. Berrada, T. et al. Integrated Mach-Zehnder interferometer for Bose-Einstein condensates. *Nat. Commun.* **4**, 2077 (2013).
27. Lücke, B. et al. Detecting multiparticle entanglement of Dicke states. *Phys. Rev. Lett.* **112**, 155304 (2014).
28. Bohnet, J. G. et al. Reduced spin measurement back-action for a phase sensitivity ten times beyond the standard quantum limit. *Nat. Photonics* **8**, 731–736 (2014).
29. Hosten, O., Engelsen, N. J., Krishnakumar, R. & Kasevich, M. A. Measurement noise 100 times lower than the quantum-projection limit using entangled atoms. *Nature* **529**, 505–508 (2016).
30. Cox, K. C., Greve, G. P., Weiner, J. M. & Thompson, J. K. Deterministic squeezed states with collective measurements and feedback. *Phys. Rev. Lett.* **116**, 093602 (2016).
31. Bohnet, J. G. et al. Quantum spin dynamics and entanglement generation with hundreds of trapped ions. *Science* **352**, 1297–1301 (2016).
32. Yurke, B. & Stoler, D. Generating quantum mechanical superpositions of macroscopically distinguishable states via amplitude dispersion. *Phys. Rev. Lett.* **57**, 13 (1986).
33. Arecchi, F. T., Courtens, E., Gilmore, R. & Thomas, H. Atomic coherent states in quantum optics. *Phys. Rev. A* **6**, 2211–2237 (1972).
34. Cirac, J. I., Lewenstein, M., Mølmer, K. & Zoller, P. Quantum superposition states of Bose-Einstein condensates. *Phys. Rev. A* **57**, 1208–1218 (1998).
35. Mølmer, K. & Sørensen, A. Multiparticle entanglement of hot trapped ions. *Phys. Rev. Lett.* **82**, 1835–1838 (1999).
36. Gordon, D. & Savage, C. M. Creating macroscopic quantum superpositions with Bose-Einstein condensates. *Phys. Rev. A.* **59**, 4623–4629 (1999).
37. Castin, Y. Bose–Einstein condensates in atomic gases: simple theoretical results. In *Coherent Atomic Matter Waves* (eds. Kaiser, R., Westbrook, C. & David, F.) 1–136 (Springer, Berlin, Heidelberg, 2001).

38. Smith, G. A., Chaudhury, S., Silberfarb, A., Deutsch, I. H. & Jessen, P. S. Continuous weak measurement and nonlinear dynamics in a cold spin ensemble. *Phys. Rev. Lett.* **93**, 163602 (2004).
39. Chaudhury, S. et al. Quantum control of the hyperfine spin of a Cs atom ensemble. *Phys. Rev. Lett.* **99**, 163002 (2007).
40. Fernholz, T. et al. Spin squeezing of atomic ensembles via nuclear-electronic spin entanglement. *Phys. Rev. Lett.* **101**, 073601 (2008).
41. Smith, A. et al. Quantum control in the Cs $6s_{1/2}$ ground manifold using radio-frequency and microwave magnetic fields. *Phys. Rev. Lett.* **111**, 170502 (2013).
42. Schäfer, F. et al. Experimental realization of quantum zeno dynamics. *Nat. Commun.* **5**, 3194 (2014).
43. Kitagawa, M. & Ueda, M. Squeezed spin states. *Phys. Rev. A.* **47**, 5138–5143 (1993).
44. Strobel, H. et al. Fisher information and entanglement of non-Gaussian spin states. *Science* **345**, 424–427 (2014).
45. Taubes, G. Schizophrenic atom doubles as Schrödinger's cat-or kitten. *Science* **272**, 1101 (1996).
46. Cummings, F. Stimulated emission of radiation in a single mode. *Phys. Rev.* **140**, A1051 (1965).
47. Eberly, J. H., Narozhny, N. & Sanchez-Mondragon, J. Periodic spontaneous collapse and revival in a simple quantum model. *Phys. Rev. Lett.* **44**, 1323 (1980).
48. Rempe, G., Walther, H. & Klein, N. Observation of quantum collapse and revival in a one-atom maser. *Phys. Rev. Lett.* **58**, 353 (1987).
49. Bollinger, J. J., Itano, W. M., Wineland, D. J. & Heinzen, D. Optimal frequency measurements with maximally correlated states. *Phys. Rev. A.* **54**, R4649–R4652 (1996).
50. Leibfried, D. et al. Toward Heisenberg-limited spectroscopy with multiparticle entangled states. *Science* **304**, 1476–1478 (2004).
51. Davis, E., Bentsen, G. & Schleier-Smith, M. Approaching the Heisenberg limit without single-particle detection. *Phys. Rev. Lett.* **116**, 053601 (2016).
52. Friöwis, F., Sekatski, P. & Dür, W. Detecting large quantum Fisher information with finite measurement precision. *Phys. Rev. Lett.* **116**, 090801 (2016).
53. Nolan, S. P., Szigeti, S. S. & Haine, S. A. Optimal and robust quantum metrology using interaction-based readouts. *Phys. Rev. Lett.* **119**, 193601 (2017).
54. Huang, J., Zhuang, M., Lu, B., Ke, Y. & Lee, C. Achieving Heisenberg-limited metrology with spin cat states via interaction-based readout. *Phys. Rev. A.* **98**, 012129 (2018).
55. Fang, R., Sarkar, R. & Shahriar, S. M. Enhancing sensitivity of an atom interferometer to the Heisenberg limit using increased quantum noise. Preprint at http://arxiv.org/abs/1707.08260 (2017).
56. Wildermuth, S. et al. Bose–Einstein condensates: microscopic magnetic-field imaging. *Nature* **435**, 440 (2005).
57. Degen, C. L., Reinhard, F. & Cappellaro, P. Quantum sensing. *Rev. Mod. Phys.* **89**, 035002 (2017).
58. Pezzè, L. & Smerzi, A. Entanglement, nonlinear dynamics, and the Heisenberg limit. *Phys. Rev. Lett.* **102**, 100401 (2009).
59. Lvovsky, A. I. & Raymer, M. G. Continuous-variable optical quantum-state tomography. *Rev. Mod. Phys.* **81**, 299 (2009).
60. Klose, G., Smith, G. & Jessen, P. S. Measuring the quantum state of a large angular momentum. *Phys. Rev. Lett.* **86**, 4721 (2001).
61. Dowling, J. P., Agarwal, G. S. & Schleich, W. P. Wigner distribution of a general angular-momentum state: applications to a collection of two-level atoms. *Phys. Rev. A* **49**, 4101–4109 (1994).
62. Allen, L. & Eberly, J. H. *Optical Resonance and Two-level Atoms*, (Wiley, New York, 1975).
63. Tóth, G. et al. Permutationally invariant quantum tomography. *Phys. Rev. Lett.* **105**, 250403 (2010).
64. Gross, D., Liu, Y.-K., Flammia, S. T., Becker, S. & Eisert, J. Quantum state tomography via compressed sensing. *Phys. Rev. Lett.* **105**, 150401 (2010).
65. Lee, C. Adiabatic Mach–Zehnder interferometry on a quantized bose-josephson junction. *Phys. Rev. Lett.* **97**, 150402 (2006).
66. Zhang, Z. & Duan, L.-M. Generation of massive entanglement through an adiabatic quantum phase transition in a spinor condensate. *Phys. Rev. Lett.* **111**, 180401 (2013).
67. Huang, J., Zhuang, M. & Lee, C. Non-gaussian precision metrology via driving through quantum phase transitions. *Phys. Rev. A.* **97**, 032116 (2018).
68. Frisch, A. et al. Ultracold dipolar molecules composed of strongly magnetic atoms. *Phys. Rev. Lett.* **115**, 203201 (2015).
69. Dreon, D. et al. Optical cooling and trapping of highly magnetic atoms: the benefits of a spontaneous spin polarization. *J. Phys. B* **50**, 065005 (2017).
70. Ravensbergen, C. et al. Accurate determination of the dynamical polarizability of dysprosium. *Phys. Rev. Lett.* **120**, 223001 (2018).

Acknowledgements

This work is supported by PSL University (MAFAG project) and European Union (ERC UQUAM and TOPODY, Marie Curie project 661433). We thank F. Gerbier, R. Lopes, and P. Zoller for fruitful discussions.

Author contributions

T.C., L.S., C.B., A.E., V.M., and D.D. carried out the experiment. J.D. and S.N. supervised the project. All authors contributed to the discussion, analysis of the results, and the writing of the manuscript.

Additional information

Supplementary Information accompanies this paper at https://doi.org/10.1038/s41467-018-07433-1.

Competing interests: The authors declare no competing interests.

Reprints and permission information is available online at http://npg.nature.com/reprintsandpermissions/

Publisher's note: Springer Nature remains neutral with regard to jurisdictional claims in published maps and institutional affiliations.

Open Access This article is licensed under a Creative Commons Attribution 4.0 International License, which permits use, sharing, adaptation, distribution and reproduction in any medium or format, as long as you give appropriate credit to the original author(s) and the source, provide a link to the Creative Commons license, and indicate if changes were made. The images or other third party material in this article are included in the article's Creative Commons license, unless indicated otherwise in a credit line to the material. If material is not included in the article's Creative Commons license and your intended use is not permitted by statutory regulation or exceeds the permitted use, you will need to obtain permission directly from the copyright holder. To view a copy of this license, visit http://creativecommons.org/licenses/by/4.0/.

© The Author(s) 2018

Enhanced Magnetic Sensitivity with Non-Gaussian Quantum Fluctuations

Alexandre Evrard, Vasiliy Makhalov, Thomas Chalopin, Leonid A. Sidorenkov,*
Jean Dalibard, Raphael Lopes, and Sylvain Nascimbene†
Laboratoire Kastler Brossel, Collège de France, CNRS, ENS-PSL University, Sorbonne Université, 11 Place Marcelin Berthelot, 75005 Paris, France

(Received 18 January 2019; published 1 May 2019)

The precision of a quantum sensor can overcome its classical counterpart when its constituents are entangled. In Gaussian squeezed states, quantum correlations lead to a reduction of the quantum projection noise below the shot noise limit. However, the most sensitive states involve complex non-Gaussian quantum fluctuations, making the required measurement protocol challenging. Here we measure the sensitivity of nonclassical states of the electronic spin $J = 8$ of dysprosium atoms, created using light-induced nonlinear spin coupling. Magnetic sublevel resolution enables us to reach the optimal sensitivity of non-Gaussian (oversqueezed) states, well above the capability of squeezed states and about half the Heisenberg limit.

DOI: 10.1103/PhysRevLett.122.173601

The measurement of a physical quantity is fundamentally limited in precision by the quantum nature of the measurement apparatus, via the Heisenberg uncertainty principle [1,2]. Similarly, to the mere averaging of N independent measurements, a measurement device made of N independent quantum probes allows reducing the measurement uncertainty by a factor $\sqrt{N}$ compared to a single realization, leading to the standard quantum limit of precision (SQL). Conversely, a set of correlated quantum probes may reach a better sensitivity [3,4], ultimately up to the Heisenberg limit—a measurement uncertainty reduced by a factor N [5]. However, reaching this precision limit with large-size quantum systems remains challenging, because it requires manipulating highly entangled quantum states, whose increased measurement sensitivity comes together with a higher fragility to environmental perturbations [6].

A quantum sensitivity enhancement has been demonstrated in various experimental settings, including photonic systems [7–9], trapped ions [10–14], Rydberg atoms [15], thermal atomic gases [16–21], or Bose-Einstein condensates [22–31]. In squeezed quantum states described by Gaussian statistics, fluctuations of the mean response of the N probes are reduced below the shot noise limit, thus increasing the measurement precision [3]. In the most common squeezing protocols, the measurement uncertainty is decreased by a factor $N^{2/3}$ intermediate between the SQL and the Heisenberg limit [32,33]. The precision can be further improved using states with non-Gaussian quantum fluctuations, characterized by high-order correlations between all probes [34]. Quantum sensing with such non-Gaussian states has been demonstrated in Refs. [14,30]; yet, the reported spectroscopic enhancement values remain limited, because reaching optimal sensitivity typically requires single-particle resolution [35,36] or nonlinear detection [37–40].

In this Letter, we use ultracold samples of atomic dysprosium to study the magnetic-field sensitivity of Gaussian and non-Gaussian quantum spin states, encoded for each atom in its electronic spin of size $J = 8$—equivalent to a set of precisely $N = 2J = 16$ elementary spin-1/2 particles [41]. We use spin-dependent light shifts to induce nonlinear dynamics described by the one-axis twisting Hamiltonian $\hat{H} = \hbar\chi\hat{J}_x^2$ [32]. These dynamics generate Gaussian squeezed states at short times, before the stretching of spin distribution leads to non-Gaussian "oversqueezed" states. Single magnetic sublevel resolution gives us access to the magnetic sensitivity hidden in non-Gaussian quantum fluctuations, yielding a spectroscopic enhancement of 8.6(6) compared to the SQL, consistent with the maximum sensitivity $J + 1/2$ expected for oversqueezed states and about half the Heisenberg limit. We stress that our method is not based on correlations between different atoms but rather exploits the spin degree of freedom of individual atoms. A clear asset for our procedure robustness is the absence of effective constituents number fluctuations $N = 2J$.

The experimental protocol is pictured in Fig. 1. We first prepare a gas of $1.0(2) \times 10^5$ atoms of ^{162}Dy at a temperature $T = 1.1(2)\ \mu$K, using standard cooling techniques [42]. The atoms are initially spin polarized in the absolute ground state $|m = -J>_z$, under a quantization field $\mathbf{B} = B\hat{\mathbf{z}}$, with $B = 60.6(3)$ mG. We shine on the atoms an off-resonant laser beam inducing spin-dependent light shifts thanks to the proximity to the narrow 626-nm optical transition (natural linewidth $\Gamma \simeq 0.85\ \mu\text{s}^{-1}$). For a linear light polarization along $\hat{\mathbf{x}}$, the light shift reduces (up to a

 © 2019 American Physical Society

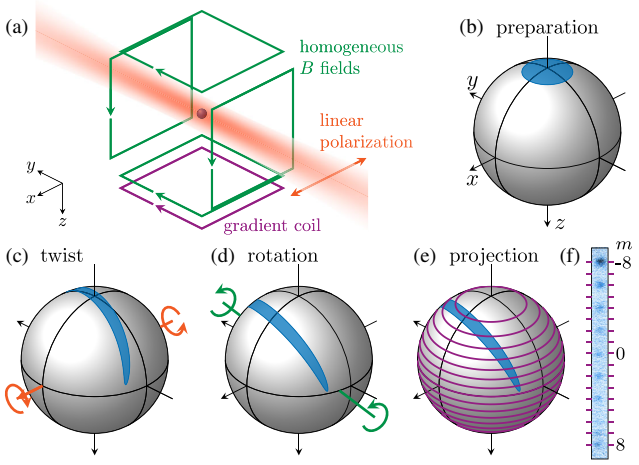

FIG. 1. (a) Scheme of the experimental setup. Starting with a coherent state of the electronic spin of dysprosium atoms aligned with the south pole (b), we induce nonlinear dynamics using an off-resonant laser beam (c). We then perform a spin rotation (d) followed by a projective measurement along z using a magnetic field gradient (e). A typical absorption image is shown in (f).

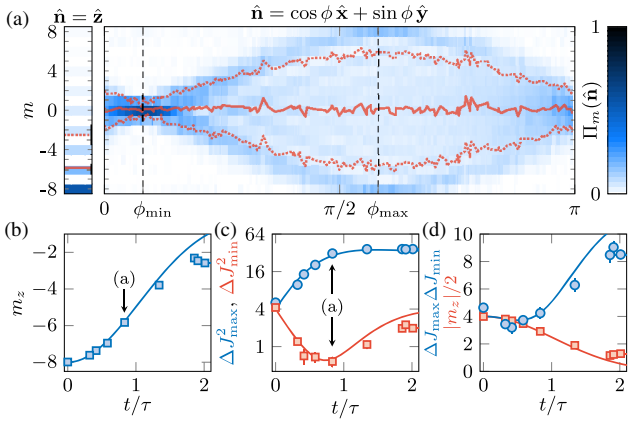

FIG. 2. (a) Projection probabilities $\Pi_m(\hat{\mathbf{n}})$ along $\hat{\mathbf{n}} = \hat{\mathbf{z}}$ and $\hat{\mathbf{n}} \perp \hat{\mathbf{z}}$, for an interaction time $t = 0.83(1)\tau$, with $\tau = (\sqrt{2J}\chi)^{-1}$. The solid (dotted) red line indicates the magnetization $m_{\hat{\mathbf{n}}}$ (values of $m_{\hat{\mathbf{n}}} \pm \Delta J_{\hat{\mathbf{n}}}$). (b) Magnetization m_z as a function of the interaction time t. (c) Maximum and minimum spin projection variances $\Delta J^2_{\max}$ and $\Delta J^2_{\min}$ (blue dots and red squares, respectively). (d) Comparison between the uncertainty product $\Delta J_{\max}\Delta J_{\min}$ and the half mean spin length $|m_z|/2$. The solid lines in (b)–(d) correspond to the one-axis twisting model predictions. In all figures of this Letter error bars represent the 1-σ statistical uncertainty determined using a bootstrap sampling method.

constant) to a coupling $\hbar\chi\hat{J}_x^2$, where the rate χ is proportional to the light intensity (in the range $\chi \sim 1$–$10\ \mu\mathrm{s}^{-1}$) [43,44]. Over the typical pulse duration, $t \sim 100$ ns, the Larmor rotation induced by the quantization magnetic field is $\sim 3°$ only, and we neglect it hereafter. We thus expect the dynamics to be well described solely by the one-axis twisting Hamiltonian [see Fig. 1(c)]. After the nonlinear spin dynamics, we apply time-dependent magnetic fields to rotate the spin along arbitrary directions [see Fig. 1(d)]. We finally perform a projective measurement along z using a magnetic field gradient that spatially separates the $|m>_z$ magnetic sublevels after a free expansion of 2.45 ms [see Figs. 1(e) and 1(f)]. Combining rotation and projective measurement gives us access to the projection probabilities $\Pi_m(\hat{\mathbf{n}})$ $(-J \le m \le J)$ along any direction $\hat{\mathbf{n}}$ [45].

We first characterize the produced spin states by measuring their first and second spin moments. We expect from the symmetry of the one-axis twisting Hamiltonian that the mean spin $\mathbf{m} \equiv \langle\hat{\mathbf{J}}\rangle$ remains oriented along z. An example of populations $\Pi_m(\hat{\mathbf{z}})$ is shown in Fig. 2(a), from which we extract the magnetization m_z. We find that the magnetization decreases with time in absolute value as expected from the one-axis twisting model [see Fig. 2(b)]. We also plot in Fig. 2(a) projection probabilities measured along directions $\hat{\mathbf{n}} \perp \hat{\mathbf{z}}$, from which we extract the minimum (maximum) uncertainty $\Delta J_{\min}$ ($\Delta J_{\max}$), for a projection direction $\hat{\mathbf{n}}_{\min}$ ($\hat{\mathbf{n}}_{\max}$) of azimutal angle $\phi_{\min}$ ($\phi_{\max}$, respectively).

For $t = 0$, the spin is polarized in $|-J\rangle_z$, corresponding to a coherent spin state. This state constitutes the best representation of a classical state magnetized along $-\hat{\mathbf{z}}$, with zero magnetization along x and y, and projection uncertainties $\Delta J_x/J = \Delta J_y/J = 1/\sqrt{2J}$ taking the minimum value allowed for an isotropic distribution in the xy plane [48]. For this state, we find that for all directions $\hat{\mathbf{n}} \perp \hat{\mathbf{z}}$ the population distributions remain identical, and the projection variance $\Delta J^2_{\hat{\mathbf{n}}} = 4.3(2)$, as expected [48]. For $t > 0$, we measure a squeezing of the minimum projection uncertainty down to $\Delta J^2_{\min} = 0.6(1)$, i.e., about seven times smaller than the coherent state value [see Fig. 2(c)]. The maximum spin quadrature $\Delta J^2_{\max}$ increases with t up to a value $\simeq 37(1)$. This behavior is consistent with a semiclassical picture of spin "diffusion" over the entire yz meridian, leading to steady asymptotic values $\Delta J^2_{\min} = \Delta J^2_x = J/2$ and $\Delta J^2_{\max} = \Delta J^2_y = \Delta J^2_z = J(J+\frac{1}{2})/2 = 34$. We find this dynamics to occur on the timescale of the diffusion time $\tau \equiv (\sqrt{2J}\chi)^{-1}$ expected within the one-axis twisting model [32]. We also use these measurements to quantify the Gaussian character of quantum fluctuations, characterized by a saturation of the Heisenberg uncertainty relation $\Delta J_{\max}\Delta J_{\min} \ge |m_z|/2$ [49]. As shown in Fig. 2(d), we find that this inequality is saturated for $t < 0.5\tau$, while non-Gaussian states occur for longer times.

We now discuss magnetic field sensing, i.e., the estimation of small rotation angles ν around an axis $\hat{\mathbf{b}}$. In the most basic scheme, one estimates the angle ν from a measurement of the mean spin projection, giving access to the magnetization m_z up to the projection noise ΔJ_z. The single-shot uncertainty on the estimation of ν then reads $\Delta\nu = \Delta J_z/|dm_z/d\nu|$ [1]. For a set of $N = 2J$ uncorrelated spins 1/2, optimal sensitivity $\Delta\nu_{\mathrm{SQL}} = 1/\sqrt{2J}$ is expected

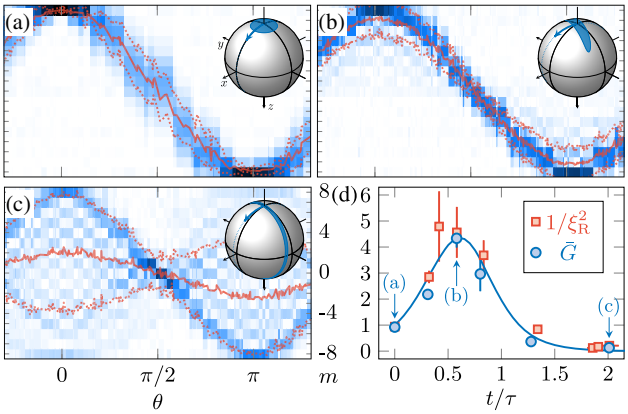

FIG. 3. (a),(b) Evolution of the projection probabilities Π_m upon a Larmor rotation of angle θ around the direction $\hat{\mathbf{n}}_{\max}$ of maximum sensitivity, for a coherent state (a), a squeezed state (b) [interaction time $t = 0.58(2)\tau$] and an oversqueezed state [c, $t = 2.01(1)\tau$]. The solid (dotted) red line corresponds to the magnetization m_z (values of $m_z \pm \Delta J_z$) computed from the Π_m values. (d) Usual metrological gain $\bar{G}$ and value of $1/\xi_R^2$ deduced from the Figs. 2(b) and 2(c) data as a function of the interaction time t. The solid line corresponds to the one-axis twisting model prediction.

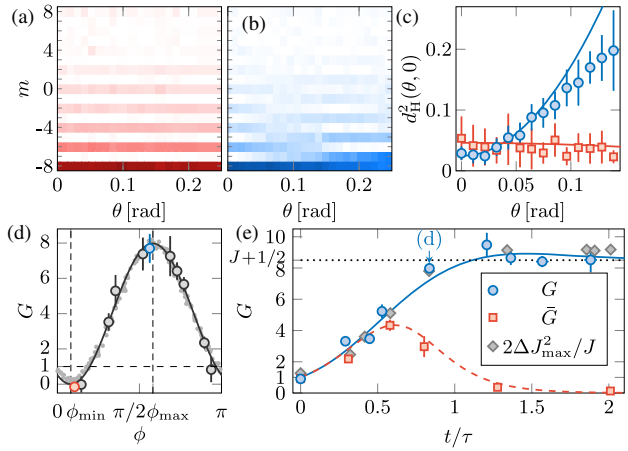

FIG. 4. (a),(b) Projection probabilities Π_m measured for small rotation angles θ around $\hat{\mathbf{b}} = \cos\phi\hat{\mathbf{x}} + \sin\phi\hat{\mathbf{y}}$, with $\phi = 0.10(2)\pi \simeq \phi_{\min}$ and $0.56(2)\pi \simeq \phi_{\max}$, respectively, for an interaction time $t = 0.835(5)\tau$. Each probability is the average of three independent experiments. (c) Hellinger distances $d_H^2(\theta, 0)$ deduced from (a),(b), together with a quadratic fit of the small-θ data. (d) Metrological gain G deduced from the curvature of the Hellinger distance as a function of the azimutal angle ϕ (gray circles). The black line is a sine fit of the data. Gray dots correspond to the upper bound $2\Delta J_{\hat{\mathbf{b}}}^2/J$ extracted from the Fig. 2(a) data. (e) Measured metrological gain G (blue dots) as a function of the interaction time t. The gray diamonds correspond to the upper bound $2\Delta J_{\max}^2/J$ [from Fig. 2(c)], and the red squares are the $\bar{G}$ values from Fig. 3(d). The solid blue and dashed red lines correspond to the gains G and $\bar{G}$ expected from the one-axis twisting model.

when all probes are aligned together, corresponding to a coherent spin state [48], and for a rotation axis $\hat{\mathbf{b}} \perp \mathbf{m}$. To check this behavior, we measure the precession of the coherent state $|m = -J>_z$ around a direction $\hat{\mathbf{b}} \perp \hat{\mathbf{z}}$, parametrized by the angle θ [see Fig. 3(a)]. We estimate the sensitivity of the state obtained after a rotation $\theta_0 = \pi/2$ by evaluating the slope $dm_z/d\nu = -8.01(4)$ at the vicinity of θ_0. We extract, at this angle, a value of $\Delta J_z^2 = 4.3(1)$, leading to $\Delta\nu = 1.04(3)\Delta\nu_{\mathrm{SQL}}$, which validates our procedure.

We extend this measurement to the states produced after nonlinear dynamics. We observe a decrease of the magnetization oscillation amplitude corresponding to the reduction of the mean spin length [see Figs. 3(b) and 3(c)]. The best magnetic sensitivity is achieved for a rotation axis $\hat{\mathbf{b}}$ coinciding with the direction $\hat{\mathbf{n}}_{\max}$ of maximal spin projection variance $\Delta J_{\max}$ and around $\theta = \pi/2$. We quantify the increase of sensitivity with respect to the SQL by the metrological gain $\bar{G} \equiv (\Delta\nu_{\mathrm{SQL}}/\Delta\nu)^2$ [50]. For durations $0 < t < \tau$ we observe a quantum enhancement $\bar{G} > 1$, with a maximum gain $\bar{G} = 4.3(4)$ reached for $t = 0.58(2)\tau$. As shown in Fig. 3(d), our data are in good agreement with the one-axis twisting model predictions [32]. We expect the sensitivity to be related to the minimum spin projection variance $\Delta J_{\min}$, as $\bar{G} = 1/\xi_R^2$, where we introduce the so-called spin squeezing parameter $\xi_R \equiv \sqrt{2J}\Delta J_{\min}/|m_z|$ [4]. We verify this relation in Fig. 3(d), where the ξ_R values are computed from the measured m_z and $\Delta J_{\min}$ data. For $t > \tau$, we observe that the gain $\bar{G}$ drops below unity, as expected from the mean spin length reduction.

To go beyond this "usual" metrological gain $\bar{G}$, we now exploit a key feature of our setup, i.e., the ability to resolve individual sublevels. This allows us to unveil small-scale structures in the measured projection probabilities $\Pi_m(\theta)$ that rapidly vary with θ, suggesting hidden phase sensitivity in higher-order moments of the probability distribution, even when $\bar{G} < 1$. In order to quantify this θ dependence, we introduce the Hellinger distance between probability distributions $d_H^2(\theta, \theta') \equiv \frac{1}{2}\sum_m[\sqrt{\Pi_m(\theta)} - \sqrt{\Pi_m(\theta')}]^2$. The phase sensitivity, expressed in terms of metrological gain, is then related to the curvature of the Hellinger distance as [30,51]

$$G(\theta) = \frac{2}{J}\frac{\partial^2 d_H^2(\theta, \theta+\nu)}{\partial\nu^2}\bigg|_{\nu=0}. \tag{1}$$

This gain coincides with the usual gain $\bar{G}$ for states with Gaussian quantum fluctuations.

We show in Figs. 4(a) and 4(b) the projection probabilities $\Pi_m(\theta)$ measured for an oversqueezed state [interaction time $t = 0.84(1)\tau$]. As theoretically shown in Ref. [40], we expect, for this protocol, optimal sensitivity around $\theta = 0$. We observe strong population variations

when the rotation axis $\hat{\mathbf{b}}$ coincides with the direction $\hat{\mathbf{n}}_{\max}$ of maximal spin projection variance [Fig. 4(b)] and minor variations for $\hat{\mathbf{b}} = \hat{\mathbf{n}}_{\min}$ [Fig. 4(a)]. To extract the metrological gain G, we calculate the Hellinger distances $d_{\mathrm{H}}^2(\theta, \theta')$ from the measured $\Pi_m(\theta)$ data and use a polynomial fit to extract its curvature around $\theta = \theta' = 0$ [45]. We show in Fig. 4(c) examples of cuts $d_{\mathrm{H}}^2(\theta, \theta' = 0)$, together with the corresponding fits. As shown in Fig. 4(d), we find that the measured gain agrees well for all rotation axes $\hat{\mathbf{b}}$ with the quantum Cramér-Rao bound for a pure state—the maximum achievable sensitivity—given by $2\Delta J_{\hat{\mathbf{b}}}^2/J$ [51]. The optimal character of this measurement protocol has been demonstrated theoretically in Ref. [40] and is based on the conservation of parity by the one-axis twisting Hamiltonian.

We repeat this measurement for various interaction times up to $t = 2\tau$ [see Fig. 4(e)]. For $t < 0.5\tau$, the measured gain G remains close to the usual gain $\bar{G}$ deduced from the first two moments, as expected in this regime of Gaussian quantum fluctuations [50]. For longer times, the measured gain G largely exceeds the gain $\bar{G}$, reaching an almost constant value $G = 8.6(6)$ in the oversqueezed regime (average value of $t > \tau$ data). This value is consistent with $G = J + 1/2$ expected for a spin state uniformly spanning the entire yz meridian. The measured sensitivity closely follows the one-axis twisting model prediction, and it remains close to the upper bound $(2/J)\Delta J_{\max}^2$ in the whole considered range of interaction times.

To get more physical insight we characterize the produced quantum states by their phase space representation on the generalized Bloch sphere. We consider in the following two quasiprobability distributions, the Wigner function W and the Husimi function Q [52,53]. The Wigner function, defined for a spin in [54], is an indicator of nonclassical behavior via its negative-value regions. The Husimi function $Q(\hat{\mathbf{n}})$, defined as the squared overlap with a coherent spin state pointing along $\hat{\mathbf{n}}$ [53], corresponds to a Gaussian smoothening of the Wigner function [55]. We compute both functions from the measured probabilities $\Pi_m(\hat{\mathbf{n}})$, using $Q(\hat{\mathbf{n}}) = \Pi_{m=J}(\hat{\mathbf{n}})$ and $W(\hat{\mathbf{n}}) = \sum_m (-1)^{J-m} a_m \Pi_m(\hat{\mathbf{n}})$, with $a_m \equiv \sum_{k=0}^{2J} (2k+1) \langle J, m, J, -m; k, 0\rangle / \sqrt{4\pi}$ [54]. As a reference, we measured the Husimi function of a coherent spin state [see Fig. 5(a)]. We find an almost isotropic Gaussian distribution of rms angular width $\delta\theta = 0.351(2)$, close to the expected value $1/\sqrt{J} \simeq 0.354$. For a short time $t = 0.48(2)\tau$, we reconstruct a twisted Husimi function, well described by an anisotropic Gaussian distribution [see Fig. 5(b)]. For $t = 2.2(1)\tau$, in the oversqueezed regime, the distribution has spread over the full yz meridian [see Fig. 5(c)]. Although semiclassical dynamics would predict diffusion toward a featureless distribution, we observe several small-scale dips that we interpret as the location of zeros of the Husimi function. For a pure quantum state $|\psi\rangle$ of a spin J,

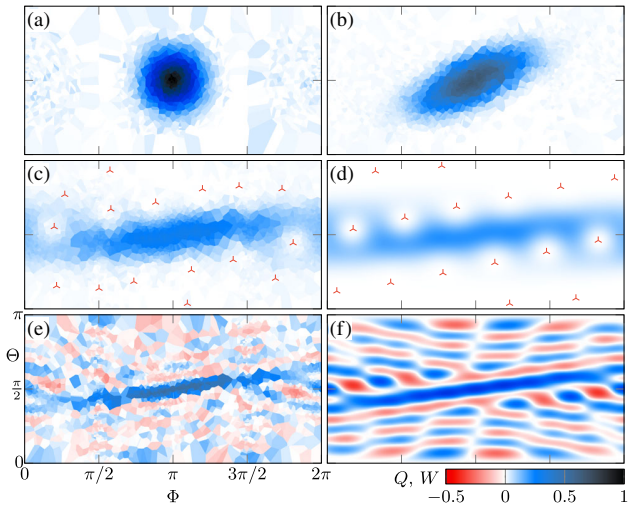

FIG. 5. (a)–(c) Husimi Q function measured for a coherent, squeezed, and oversqueezed spin states (a)–(c), achieved after evolution times $t/\tau = 0$, 0.48(2) and 2.2(1), respectively. The Bloch sphere is parametrized by the spherical angles (Θ, Φ) associated with the frame (y, z, x). The red stars in (c) indicate the fitted zeros of the Husimi function. (d),(f) Husimi (d) and Wigner (f) functions of the quantum state expected from the one-axis twisting model for an interaction time $t = 2.2\tau$. (e) Wigner function reconstructed from the same data used in (c).

we expect the occurrence of $2J$ zeros in the Husimi function, corresponding to the opposite orientations of the $2J$ fictitious spin-1/2 particles composing the spin J—the so-called Majorana stellar representation [56]. Denoting these orientations $\hat{\mathbf{u}}_i$ $(1 \le i \le 2J)$, the Husimi function reads $Q(\hat{\mathbf{n}}) \propto \prod_i (1 + \hat{\mathbf{u}}_i \cdot \hat{\mathbf{n}})$ and vanishes for $\hat{\mathbf{n}} = -\hat{\mathbf{u}}_i$ [57]. Fitting the entire distribution with this ansatz, we obtain the location of all zeros of the Husimi function, in good agreement with the expected positions [see Fig. 5(d)]. We show in Fig. 5(e) the Wigner function reconstructed for the oversqueezed state. It exhibits negative values in a large fraction of phase space, indicating a highly nonclassical character [58]. We also find small-scale oscillations reminiscent of "sub-Planck" structuring of phase space, as expected for metrologically useful quantum states [59]. Although the measured small-scale structures in the Husimi function are not directly linked to the magnetic sensitivity, the oscillations found in the Wigner function imply a fast variation of the state upon rotation, making a direct connection with the high magnetic sensitivity of oversqueezed states [60].

To conclude, we showed that measurements based on single magnetic sublevel resolution allow reaching optimal sensitivity with non-Gaussian states of a quantum spin J. An optimum $G = 8.6(6)$ is reached as soon as the spin distribution is stretched along the full yz meridian. The Heisenberg limit $G = 16$ could in principle be achieved using the maximally entangled N00N state [13,21]; however, the required interaction time $t = \sqrt{\pi^2 J/2}\tau$ is much

longer than τ for $J \gg 1$, making this state more fragile to decoherence [45]. Oversqueezed states thus appear as a compromise for future progress with large atomic ensembles. We also provided a full characterization of nonclassical spin states in phase space in terms of their Majorana stellar representation. The latter could be used to characterize ordering in spinor quantum gases [61], geometric quantum entanglement [62] or chaotic behavior [63].

We thank Chayma Bouazza for contributions in earlier stages of the experiment. This work is supported by PSL University (MAFAG project) and European Union (ERC UQUAM and TOPODY, Marie Curie project Grant No. 661433).

*Present address: LNE-SYRTE, Observatoire de Paris, Université PSL, CNRS, Sorbonne Université, 61 Avenue de l'Observatoire, 75014 Paris, France.
†sylvain.nascimbene@lkb.ens.fr

[1] C. W. Helstrom, J. Stat. Phys. **1**, 231 (1969).
[2] C. L. Degen, F. Reinhard, and P. Cappellaro, Rev. Mod. Phys. **89**, 035002 (2017).
[3] C. M. Caves, Phys. Rev. D **23**, 1693 (1981).
[4] D. J. Wineland, J. J. Bollinger, W. M. Itano, F. L. Moore, and D. J. Heinzen, Phys. Rev. A **46**, R6797 (1992).
[5] V. Giovannetti, S. Lloyd, and L. Maccone, Nat. Photonics **5**, 222 (2011).
[6] R. Demkowicz-Dobrzański, M. Jarzyna, and J. Kołodyński, in *Progress in Optics*, edited by E. Wolf (Elsevier, New York, 2015), Vol. 60, pp. 345–435.
[7] M. J. Holland and K. Burnett, Phys. Rev. Lett. **71**, 1355 (1993).
[8] B. L. Higgins, D. W. Berry, S. D. Bartlett, H. M. Wiseman, and G. J. Pryde, Nature (London) **450**, 393 (2007).
[9] J.-W. Pan, Z.-B. Chen, C.-Y. Lu, H. Weinfurter, A. Zeilinger, and M. Żukowski, Rev. Mod. Phys. **84**, 777 (2012).
[10] V. Meyer, M. A. Rowe, D. Kielpinski, C. A. Sackett, W. M. Itano, C. Monroe, and D. J. Wineland, Phys. Rev. Lett. **86**, 5870 (2001).
[11] D. Leibfried *et al.*, Nature (London) **438**, 639 (2005).
[12] C. F. Roos, M. Chwalla, K. Kim, M. Riebe, and R. Blatt, Nature (London) **443**, 316 (2006).
[13] T. Monz, P. Schindler, J. T. Barreiro, M. Chwalla, D. Nigg, W. A. Coish, M. Harlander, W. Hänsel, M. Hennrich, and R. Blatt, Phys. Rev. Lett. **106**, 130506 (2011).
[14] J. G. Bohnet, B. C. Sawyer, J. W. Britton, M. L. Wall, A. M. Rey, M. Foss-Feig, and J. J. Bollinger, Science **352**, 1297 (2016).
[15] A. Facon, E.-K. Dietsche, D. Grosso, S. Haroche, J.-M. Raimond, M. Brune, and S. Gleyzes, Nature (London) **535**, 262 (2016).
[16] A. Kuzmich, L. Mandel, and N. P. Bigelow, Phys. Rev. Lett. **85**, 1594 (2000).
[17] J. Appel, P. J. Windpassinger, D. Oblak, U. B. Hoff, N. Kjærgaard, and E. S. Polzik, Proc. Natl. Acad. Sci. U.S.A. **106**, 10960 (2009).
[18] I. D. Leroux, M. H. Schleier-Smith, and V. Vuletić, Phys. Rev. Lett. **104**, 073602 (2010).
[19] J. G. Bohnet, K. C. Cox, M. A. Norcia, J. M. Weiner, Z. Chen, and J. K. Thompson, Nat. Photonics **8**, 731 (2014).
[20] O. Hosten, N. J. Engelsen, R. Krishnakumar, and M. A. Kasevich, Nature (London) **529**, 505 (2016).
[21] T. Chalopin, C. Bouazza, A. Evrard, V. Makhalov, D. Dreon, J. Dalibard, L. A. Sidorenkov, and S. Nascimbene, Nat. Commun. **9**, 4955 (2018).
[22] A. Sørensen, L.-M. Duan, J. I. Cirac, and P. Zoller, Nature (London) **409**, 63 (2001).
[23] J. Estève, C. Gross, A. Weller, S. Giovanazzi, and M. K. Oberthaler, Nature (London) **455**, 1216 (2008).
[24] M. F. Riedel, P. Böhi, Y. Li, T. W. Hänsch, A. Sinatra, and P. Treutlein, Nature (London) **464**, 1170 (2010).
[25] J.-C. Jaskula, M. Bonneau, G. B. Partridge, V. Krachmalnicoff, P. Deuar, K. V. Kheruntsyan, A. Aspect, D. Boiron, and C. I. Westbrook, Phys. Rev. Lett. **105**, 190402 (2010).
[26] R. Bücker, J. Grond, S. Manz, T. Berrada, T. Betz, C. Koller, U. Hohenester, T. Schumm, A. Perrin, and J. Schmiedmayer, Nat. Phys. **7**, 608 (2011).
[27] E. M. Bookjans, C. D. Hamley, and M. S. Chapman, Phys. Rev. Lett. **107**, 210406 (2011).
[28] B. Lücke *et al.*, Science **334**, 773 (2011).
[29] C. D. Hamley, C. S. Gerving, T. M. Hoang, E. M. Bookjans, and M. S. Chapman, Nat. Phys. **8**, 305 (2012).
[30] H. Strobel, W. Muessel, D. Linnemann, T. Zibold, D. B. Hume, L. Pezzè, A. Smerzi, and M. K. Oberthaler, Science **345**, 424 (2014).
[31] X.-Y. Luo, Y.-Q. Zou, L.-N. Wu, Q. Liu, M.-F. Han, M. K. Tey, and L. You, Science **355**, 620 (2017).
[32] M. Kitagawa and M. Ueda, Phys. Rev. A **47**, 5138 (1993).
[33] L. Pezzè, A. Smerzi, M. K. Oberthaler, R. Schmied, and P. Treutlein, Rev. Mod. Phys. **90**, 035005 (2018).
[34] M. Gessner, A. Smerzi, and L. Pezzè, Phys. Rev. Lett. **122**, 090503 (2019).
[35] H. Zhang, R. McConnell, S. Ćuk, Q. Lin, M. H. Schleier-Smith, I. D. Leroux, and V. Vuletić, Phys. Rev. Lett. **109**, 133603 (2012).
[36] D. B. Hume, I. Stroescu, M. Joos, W. Muessel, H. Strobel, and M. K. Oberthaler, Phys. Rev. Lett. **111**, 253001 (2013).
[37] B. Yurke, S. L. McCall, and J. R. Klauder, Phys. Rev. A **33**, 4033 (1986).
[38] E. Davis, G. Bentsen, and M. Schleier-Smith, Phys. Rev. Lett. **116**, 053601 (2016).
[39] D. Linnemann, H. Strobel, W. Muessel, J. Schulz, R. J. Lewis-Swan, K. V. Kheruntsyan, and M. K. Oberthaler, Phys. Rev. Lett. **117**, 013001 (2016).
[40] S. P. Nolan, S. S. Szigeti, and S. A. Haine, Phys. Rev. Lett. **119**, 193601 (2017).
[41] L. D. Landau and E. Lifshitz, *Quantum Mechanics, Non-Relativistic Theory* (Pergamon Press, London, 1958).
[42] T. Chalopin *et al.*, Phys. Rev. A **98**, 040502(R) (2018).
[43] G. A. Smith, S. Chaudhury, A. Silberfarb, I. H. Deutsch, and P. S. Jessen, Phys. Rev. Lett. **93**, 163602 (2004).
[44] We estimate relative corrections to this coupling due to imperfect light polarization to remain below 0.05%. Furthermore, the laser detuning $\Delta = -2\pi \times 1.1(1)$ GHz ensures negligible incoherent Raman scattering over the typical light pulse duration $t \sim 100$ ns.

[45] See Supplemental Material at http://link.aps.org/supplemental/10.1103/PhysRevLett.122.173601 for details on the metrological gain in the presence of noise, experiment protocols, additional Hellinger distance data, Husimi and Wigner functions measured and computed for coherent and Gaussian squeezed states, and a discussion on the evaluation of purity of quantum states, which includes Refs. [46,47].
[46] G. M. D'Ariano, L. Maccone, and M. Paini, J. Opt. B **5**, 77 (2003).
[47] S. N. Filippov and V. I. Man'ko, J. Russ. Laser Res. **34**, 14 (2013).
[48] F. T. Arecchi, E. Courtens, R. Gilmore, and H. Thomas, Phys. Rev. A **6**, 2211 (1972).
[49] A. Holevo, in *Probabilistic and Statistical Aspects of Quantum Theory*, edited by A. Holevo, Publications of the Scuola Normale Superiore (Edizioni della Normale, Pisa, 2011), pp. 187–218.
[50] L. Pezzé and A. Smerzi, in *Atom Interferometry*, edited by G. M. Tino and M. A. Kasevich, Proceedings of the International School of Physics "Enrico Fermi"(IOS Press, Amsterdam, 2014), pp. 691–741.
[51] S. L. Braunstein and C. M. Caves, Phys. Rev. Lett. **72**, 3439 (1994).
[52] E. Wigner, Phys. Rev. **40**, 749 (1932).
[53] K. Husimi, J. Phys. Soc. Jpn. **22**, 264 (1940).
[54] J. P. Dowling, G. S. Agarwal, and W. P. Schleich, Phys. Rev. A **49**, 4101 (1994).
[55] M. Hillery, R. F. O'Connell, M. O. Scully, and E. P. Wigner, Phys. Rep. **106**, 121 (1984).
[56] E. Majorana, Nuovo Cimento **9**, 43 (1932).
[57] We also checked that the spin state remains quasipure on this timescale [45].
[58] A. Kenfack and K. Życzkowski, J. Opt. B **6**, 396 (2004).
[59] W. H. Zurek, Nature (London) **412**, 712 (2001).
[60] M. G. A. Paris, Int. J. Quantum. Inform. **07**, 125 (2009).
[61] D. M. Stamper-Kurn and M. Ueda, Rev. Mod. Phys. **85**, 1191 (2013).
[62] H. D. Liu and L. B. Fu, Phys. Rev. Lett. **113**, 240403 (2014).
[63] P. Leboeuf and A. Voros, J. Phys. A **23**, 1765 (1990).

Probing Quantum Criticality and Symmetry Breaking at the Microscopic Level

Vasiliy Makhalov, Tanish Satoor, Alexandre Evrard, Thomas Chalopin, Raphael Lopes, and Sylvain Nascimbene*
Laboratoire Kastler Brossel, Collège de France, CNRS, ENS-PSL University, Sorbonne Université, 11 Place Marcelin Berthelot, 75005 Paris, France

(Received 9 May 2019; published 18 September 2019)

We report on an experimental study of the Lipkin-Meshkov-Glick model of quantum spins interacting at infinite range in a transverse magnetic field, which exhibits a ferromagnetic phase transition in the thermodynamic limit. We use dysprosium atoms of electronic spin $J = 8$, subjected to a quadratic Zeeman light shift, to simulate $2J = 16$ interacting spins $1/2$. We probe the system microscopically using single magnetic sublevel resolution, giving access to the spin projection parity, which is the collective observable characterizing the underlying $\mathbb{Z}_2$ symmetry. We measure the thermodynamic properties and dynamical response of the system, and we study the quantum critical behavior around the transition point. In the ferromagnetic phase, we achieve coherent tunneling between symmetry-broken states, and we test the link between symmetry breaking and the appearance of a finite order parameter.

DOI: 10.1103/PhysRevLett.123.120601

From complex quantum materials such as cuprate superconductors to simple spin models, many-body systems close to a quantum critical point exhibit distinct properties driven by quantum fluctuations [1]. Some features, such as the slowing down of relaxation times, can be probed via macroscopic observables. However, revealing specifically quantum properties (e.g., many-body quantum entanglement [2]) remains challenging. The recent development of highly controlled quantum systems of mesoscopic size (such as ion crystals [3], ultracold gases [4], Rydberg atom arrays [5], or interacting photons [6]) allows for a microscopic characterization of collective quantum properties [7], e.g., the full density matrix [6], entanglement entropy [8], or nonlocal string order [9]. This degree of control could be used to investigate fundamental aspects of quantum phase transitions, such as the link between the breaking of an underlying symmetry and the onset of a nonzero-order parameter [10]. This connection cannot be tested in macroscopic systems because superselection rules forbid large-size quantum superpositions [11], making spontaneous symmetry breaking unavoidable [12].

In this Letter, we experimentally characterize at the microscopic level the Lipkin-Meshkov-Glick model (LMGM) consisting of N quantum spins with infinite-range Ising interactions in a transverse field. This model is applicable to nuclear systems [13,14], large-spin molecules [15], trapped ions [16,17], and two-mode [18–20] or spinor [21] Bose-Einstein condensates. Our study is based on the equivalence between the electronic spin $J = 8$ of dysprosium atoms and a set of $N = 16$ spins $1/2$ symmetric upon exchange [22], with Ising interactions simulated via a light-induced quadratic Zeeman shift [23]. In the thermodynamic limit (TL), the LMGM exhibits a ferromagnetic phase transition (see Fig. 1) characterized by spontaneous breaking of a $\mathbb{Z}_2$ symmetry—the parity of the total z spin projection. We measure a crossover between paramagnetic and ferromagnetic behaviors, which are separated by a quantum critical regime where we observe nonclassical behavior and a minimum of the energy gap [24,25]. A specific asset of our setup is the direct access to the quantum state parity, which is a collective observable

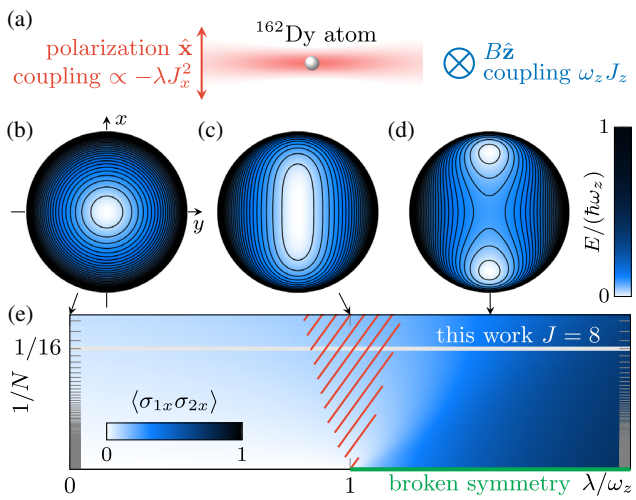

FIG. 1. (a) Scheme of experiment, based on laser-induced dynamics of the electronic spin of dysprosium atoms (quadratic light shift of $\propto -\lambda J_x^2$) in the presence of a magnetic field (Zeeman coupling $\omega_z J_z$). (b), (c), and (d) Classical energy landscapes on the southern hemisphere of the generalized Bloch sphere for $\lambda = 0$, ω_z, and $1.5\omega_z$, respectively. (e) Finite-size phase diagram, showing the spin pair correlator $\langle\sigma_{1x}\sigma_{2x}\rangle$, with a ferromagnetic phase in the thermodynamic limit for $\lambda > \omega_z$ (green line). For a finite N, the phase transition is smoothened over a quantum critical region (dashed red area).

 © 2019 American Physical Society

hidden in macroscopic systems such as large ensembles of spins 1/2. We show that the $\mathbb{Z}_2$ symmetry breaking is directly related to the onset of a nonzero-order parameter.

The LMGM is described by the Hamiltonian

$$H = -\frac{\hbar\lambda}{4(N-1)} \sum_{1\le i\neq j\le N} \sigma_{ix}\sigma_{jx} + \frac{\hbar\omega_z}{2} \sum_{1\le i\le N} \sigma_{iz}. \quad (1)$$

Here, $\hbar\sigma_{iu}/2$ denotes the projection of the spin i along u ($1 \le i \le N$), the factor $1/(N-1)$ ensures extensivity of the energy for large N [26], and we restrict ourselves to ferromagnetic interactions of $\lambda > 0$. Although the exact ground state is not a product state [27], thermodynamic quantities are well described by the classical mean-field theory in the TL because each spin interacts with the sum of all other spins [24]. The corresponding classical energy functionals, parametrized by the mean spin orientation, are shown in Figs. 1(b)–1(d) for $\lambda = 0$, ω_z, and $1.5\omega_z$. They reveal the occurrence of a quantum phase transition between a paramagnetic phase for $\lambda < \omega_z$ and a ferromagnetic phase for $\lambda > \omega_z$, for which the system exhibits two degenerate ground states with nonzero-order parameter $\langle\sigma_{1x}\rangle \neq 0$. Furthermore, the $\mathbb{Z}_2$ symmetry, associated to the conservation of parity,

$$P_z = \prod_{i=1}^{N} \sigma_{i,z},$$

is spontaneously broken at the transition point. Introducing the collective spin

$$\mathbf{J} = \frac{1}{2}\sum_i \boldsymbol{\sigma}_i,$$

the Hamiltonian [Eq. (1)] can be recast (up to an overall energy shift) as

$$H = -\frac{\hbar\lambda}{2J-1} J_x^2 + \hbar\omega_z J_z. \quad (2)$$

For ferromagnetic interactions, its lowest-energy states are permutationally symmetric and their collective spin has the maximal length of $J = N/2$.

In this work, we study the nonlinear dynamics of the electronic spin of $J = 8$ of ^{162}Dy atoms, simulating a ferromagnetic LMGM with $N = 16$ spins 1/2. We use ultracold samples of $1.3(3) \times 10^5$ atoms, which are initially held in an optical dipole trap at a temperature of $T \simeq 1.1(1)$ μK. The atomic spin is initially polarized in the ground state $|-J\rangle_z$, under a magnetic field $\mathbf{B} = B\hat{\mathbf{z}}$ with $B = 114(1)$ mG, corresponding to a Larmor frequency of $\omega_z = 2\pi \times 198(2)$ kHz. In this state, the N elementary spins are antialigned with the magnetic field, corresponding to a paramagnetic state. We then switch off the trap before applying a laser beam close to the 626 nm optical transition, coupling the spin J to an excited electronic state of spin $J' = 9$. Given the transition linewidth of $\Gamma \simeq 0.86$ μs^{-1} and the detuning from resonance of $\simeq$20 GHz, we expect negligible incoherent Rayleigh scattering on the timescale of the experiment. The light is linearly polarized along x, producing a quadratic Zeeman shift proportional to J_x^2 [23], up to a spin-independent energy shift that does not influence the spin dynamics. The laser beam waist of $w = 50$ μm is large enough to ensure uniform intensity over the atomic sample (rms size of $\sigma \simeq 5$ μm). For the maximum available light power ($P \simeq 1$W), we reach a ferromagnetic coupling of $\lambda \simeq 4\omega_z$ deep in the ferromagnetic phase. In the following, the coupling λ is adjusted via the light intensity on the atoms. After a typical evolution time of $t \sim 100$ μs, we switch off the light beam and apply time-dependent magnetic fields to perform arbitrary spin rotations before making a projection measurement along z. Combining rotation and projection gives us access to the spin projection probabilities of $\Pi_m(\hat{\mathbf{n}})$ ($-J \le m \le J$) along any direction $\hat{\mathbf{n}}$ [28].

We first investigate the properties of the ground state of the LMGM. We start with all atoms in the state $|-J\rangle_z$, which is the (paramagnetic) ground state for $\lambda = 0$. We then slowly ramp the light coupling from zero up to a final value λ using a linear ramp of speed $\dot{\lambda} \simeq 0.015\omega_z^2$, for which we expect quasiadiabatic evolution [29]. The measured spin projection probabilities $\Pi_m(\hat{\mathbf{n}})$ ($\hat{\mathbf{n}} = \hat{\mathbf{x}}, \hat{\mathbf{y}}, \hat{\mathbf{z}}$) are shown in Figs. 2(a), 2(c), and 2(e). We first consider the occurrence of a ferromagnetic ground state by measuring the order parameter $\langle\sigma_{1x}\rangle$. We show in Fig. 2(a) the single-shot projections $\Pi_m(\hat{\mathbf{x}})$ measured for various couplings λ. For small λ, we find a single-peak distribution centered on zero, which is consistent with the state $|-J\rangle_z$ projected along $\hat{\mathbf{x}}$. For $\lambda \gtrsim \omega_z$, we observe a bifurcation towards a double-peak distribution, which is consistent with population of the two broken-symmetry states: each with an order parameter of $\langle\sigma_{1x}\rangle \neq 0$. As the distributions remain globally symmetric, the system does not seem to choose a single broken state. With our measurement being averaged over many atoms, we cannot exclude a situation with almost half of the atoms in each broken state, e.g., organized in unresolved spin domains. This scenario is invalidated by a direct measurement of the mean parity $p_z \equiv \langle P_z\rangle$ that remains close to unity for all interaction strengths [see Fig. 2(f)]. Such an absence of symmetry breaking is, in fact, expected for a finite-size system, for which the ground state remains nondegenerate, as will be discussed later. The ground state prepared in the ferromagnetic phase exhibits both a large-spin projection variance along x and a well-defined parity along z, which is characteristic of a mesoscopic quantum superposition that is useful for quantum-enhanced metrology [33,34].

We now characterize the thermodynamic properties that are independent of the symmetry breaking itself. We probe ferromagnetic spin correlations, i.e., the relative alignment

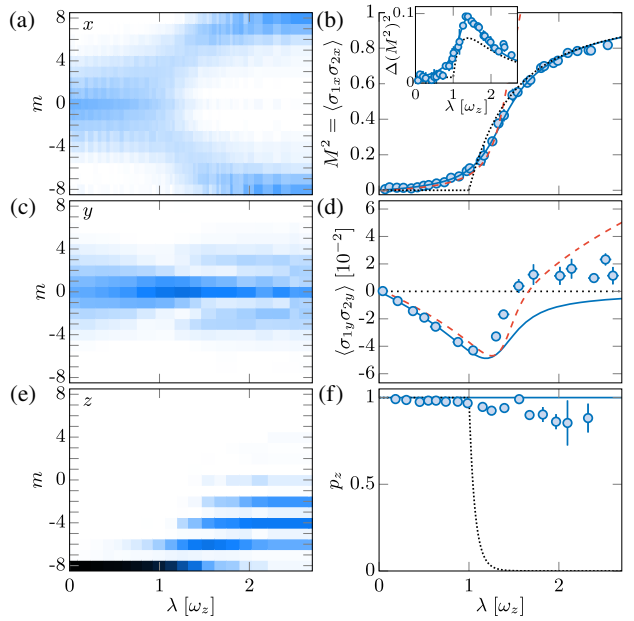

FIG. 2. (a), (c), and (e) Measured projection probabilities $\Pi_m(\hat{\mathbf{n}})$ for $\hat{\mathbf{n}} = \hat{\mathbf{x}}, \hat{\mathbf{y}}$, and $\hat{\mathbf{z}}$ [Figs. 2(a), 2(c), and 2(e), respectively] as a function of the interaction strength λ. (b), (d), and (f) Evolution of the spin pair correlator $\langle\sigma_{1x}\sigma_{2x}\rangle$ [Fig. 2(b)], its variance [inset of Fig. 2(b)], the correlator $\langle\sigma_{1y}\sigma_{2y}\rangle$ [Fig. 2(d)], and the mean parity p_z [Fig. 2(f)]. Solid blue, dotted black, and dashed red lines correspond to the LMGM, the classical mean-field model, and the critical Hamiltonian, respectively. No averaging is performed in Fig. 2(a). In other panels, all data are the averages of about five independent measurements. In all figures, error bars represent the 1-σ statistical uncertainty.

between spins along $\hat{\mathbf{x}}$ quantified by the correlator $M^2 \equiv \langle\sigma_{1x}\sigma_{2x}\rangle$ [24]. We compute it from the second moment of the measured probabilities $\Pi_m(\hat{\mathbf{x}})$ using $N+N(N-1)\langle\sigma_{1\hat{\mathbf{n}}}\sigma_{2\hat{\mathbf{n}}}\rangle = 4\langle J_{\hat{\mathbf{n}}}^2\rangle$ [35]. As shown in Fig. 2(b), we measure a smooth increase of M^2 as a function of λ, which is consistent with a crossover between paramagnetic and ferromagnetic behaviors. We compare our measurements with various theoretical models: namely, the $N = 16$ LMGM (blue lines in Fig. 2), the mean-field model corresponding to the $N \to \infty$ limit (dotted black lines), and its first finite-N correction close to the critical point, as will be discussed below (dashed red lines). As shown in Fig. 2(b), the measured ferromagnetic correlator M^2 agrees with the $N = 16$ LMGM for all couplings λ, and it remains close to the mean-field theory for most values of λ, except around $\lambda = \omega_z$ [29,36]. In the critical regime, the leading $1/N$ finite-size correction can be simply formulated because the quantum ground state remains close to the coherent state $|-J\rangle_z$ such that operators J_x and J_y are almost canonically conjugated variables with $[J_x, J_y] = iJ_z \simeq -iJ$ [37]. This approximation leads to a low-energy "critical" Hamiltonian [29,38,39]

$$\frac{H_c}{\hbar\omega_z} = -\left(J + \frac{1}{2}\right) + \frac{1}{J^{1/3}}\left(\frac{P^2}{2} - \frac{\epsilon X^2}{2} + \frac{X^4}{8}\right), \qquad (3)$$

describing the dynamics of a massive particle in a harmonic plus quartic potential, where $\epsilon = J^{2/3}(\lambda/\omega_z - 1)$, $X = J^{-2/3}J_x$, and $P = -J^{-1/3}J_y$. This description matches the textbook Landau picture of a second-order phase transition evolving from single- to double-well potentials when crossing the critical point at $\epsilon = 0$ [10]. As plotted in Fig. 2(b), the universal Hamiltonian [Eq. (3)] is sufficient to account for the measured deviations to the TL well around $\lambda = \omega_z$ [40].

We also investigated signatures of the phase transition itself in our finite-size system. First, we measured an increase of fluctuations of the ferromagnetic correlator $\Delta(M^2) \equiv \Delta(J_x^2)/[J(J-\frac{1}{2})]^2$ around the critical point of $\lambda = \omega_z$ [see inset of Fig. 2(b)]—a generic feature of continuous phase transitions [41]. More specifically, quantum phase transitions are also associated with the onset of entanglement in the critical region [1]. *A priori*, probing quantum entanglement requires partitioning the electronic spin J, which is forbidden at low energy but could, in principle, be achieved using coherent optical transitions $J \to J'$ [42,43]. Yet, we can indirectly probe entanglement in our system via spin projection correlations. Indeed, separable states that are symmetric upon exchange satisfy $\langle\sigma_{1\hat{\mathbf{n}}}\sigma_{2\hat{\mathbf{n}}}\rangle = \langle\sigma_{1\hat{\mathbf{n}}}\rangle^2$ for all projection directions $\hat{\mathbf{n}}$, and thus can only exhibit positive correlators [35,44]. As shown in Figs. 2(c) and 2(d), we measure the correlator $\langle\sigma_{1y}\sigma_{2y}\rangle$ and show that it assumes negative values in a broad range of interaction strengths [45], which is consistent with entanglement and suggests that the phase transition is driven by quantum (rather than thermal) fluctuations [2,47]. The measured correlator—including its minimum value—is consistent with the LMGM prediction for $\lambda < \omega_z$. In the ferromagnetic phase, the measured correlator significantly exceeds the expected values, which we attribute to shot-to-shot variations of the spin rotation parameters used for the y spin projection due to magnetic field fluctuations.

We now extend our study to the system dynamics by measuring the energy gap of low-lying excitations. Due to the $\mathbb{Z}_2$ symmetry of the LMGM, the eigenstates can be divided into two sectors of even and odd parities. The low-energy dynamics is then governed by two energy gaps, namely, the "parity" gap $\hbar\delta$ between opposite-parity ground states and the "dynamical" gap $\hbar\Delta$ between the lowest two energy levels of even parity. In the effective potential picture, these gaps correspond to the oscillation frequencies of the dipole (δ) and breathing (Δ) modes. To excite the breathing mode, we simply increase the ramp speed $\dot{\lambda}$ used for the state preparation, leading to a diabatic population of the first excited state of even parity while keeping the higher states almost unpopulated. We then measure the time evolution of the second moment $\langle\sigma_{1x}\sigma_{2x}\rangle$,

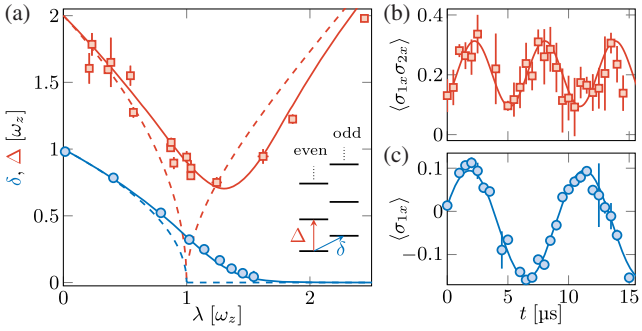

FIG. 3. (a) Parity gap δ between even- and odd-parity sectors, and dynamical gap Δ between the ground and first even-parity states as a function of the coupling λ. Solid (dashed) lines are LMGM (mean-field) predictions. [(a) inset] Energy level scheme of the six lowest eigenstates for $\lambda = 0.5\omega_z$. (b) Breathing mode oscillation performed for $\lambda = 1.04(2)\omega_z$. The solid line is a sine fit of frequency Δ. (c) Dipole mode oscillation performed for $\lambda = 0.79(2)\omega_z$. The solid line is a sine fit of frequency δ.

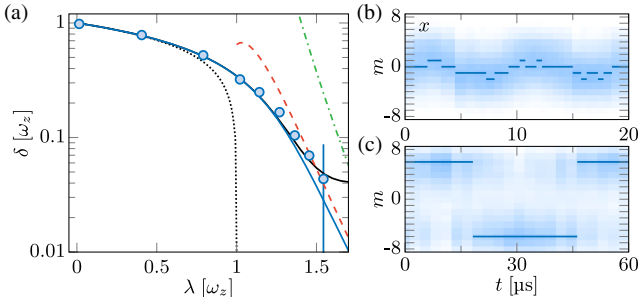

FIG. 4. (a) Parity gap δ as a function of λ (blue dots) compared with LMGM (blue line), mean-field theory (black dotted line), semiclassical tunneling (red dashed line), and perturbation theories (green dash-dotted line). The solid black line is the mean value of δ expected from the LMGM and averaged over magnetic field fluctuations. (b) and (c) Time evolutions of projection probabilities $\Pi_m(\hat{\mathbf{x}})$ during dipole mode oscillation for $\lambda = 0.79(2)\omega_z$ [Fig. 4(b)] and $\lambda = 1.36(2)\omega_z$ [Fig. 4(c)]. The most probable projection m^* is plotted as a blue line.

and we extract its oscillation frequency Δ [see Fig. 3(b)]. To excite the dipole mode, we first prepare the ground state for a given coupling λ, and we apply a parity-breaking perturbation using a pulse of the magnetic field along x of duration $t \simeq 3$ μs, coupling the ground state to the odd-parity sector. The amplitude is chosen small enough to only populate the even- and odd-parity ground states, and the first moment's $\langle\sigma_{1x}\rangle$ oscillation frequency (δ) is extracted [see Fig. 3(c)].

The measured parity and dynamical gaps, reported in Fig. 3(a), agree well with the LMGM. The dynamical gap Δ exhibits a minimum around the critical point, which is reminiscent of the closing of the gap in the TL at the transition point. The parity gap δ decreases when increasing the coupling λ, which is in analogy with the softening of the spin dipole mode in quantum systems close to a ferromagnetic transition [48,49]. In the paramagnetic phase of $\lambda \lesssim 0.5\omega_z$, the dynamical gap Δ remains about twice the parity gap δ, which is consistent with a picture of noninteracting excitation quanta [25,37]. At the critical point, the measured dynamical gap of $\Delta = 0.91(5)\omega_z$ significantly exceeds twice the parity gap of $\delta = 0.33(1)\omega_z$, which is as expected from particle dynamics in a quartic potential [see Eq. (3) for $\epsilon = 0$]. This nonharmonic behavior illustrates the generic behavior of quantum critical systems, for which the low-energy spectra cannot be simply reduced to noninteracting excitation quanta [1]. The gap value for $\lambda = \omega_z$ is also consistent with the leading finite-size correction to the mean field $\Delta/\omega_z \simeq 1.78/J^{1/3} = 0.89$, which is valid for $J \gg 1$ [24,50,51].

We now focus on the dipole oscillation measurements in the ferromagnetic phase, where we measure a strong reduction of the parity gap [see Fig. 4(a)]. The even- and odd-parity ground states thus become almost degenerate, which is a behavior reminiscent of the exact double degeneracy expected in the TL for $\lambda > \omega_z$. We show, in Figs. 4(b) and 4(c), the time evolutions of the probability distributions $\Pi_m(\hat{\mathbf{x}})$ during the dipole oscillation in the paramagnetic [Fig. 4(b)] and ferromagnetic [Fig. 4(c)] phases. In the paramagnetic phase, the distributions always exhibit a single peak for which the center smoothly oscillates around zero. On the contrary, in the ferromagnetic phase, the distributions exhibit two peaks at positive or negative large-$|m|$ values, and the dynamics consists of an oscillation between the peak weights, without significantly populating small-$|m|$ states. This qualitatively different behavior is well illustrated by the evolution of the most probable projection m^*, which only takes two possible values of $m^* = \pm 6$ during the evolution shown in Fig. 4(c). These maximal projection values are close to the collective spin projections of $\langle J_x\rangle = \pm 5.4(5)$ of the two mean-field broken-symmetry states for $\lambda = 1.36(2)\omega_z$. Such a dynamics can be interpreted as a "macroscopic" quantum tunneling regime between broken states—a phenomenon studied extensively in large-spin molecules [15,52–54] and

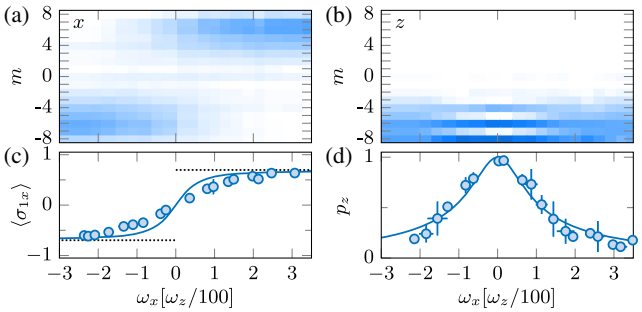

FIG. 5. (a) and (b) Projection probabilities $\Pi_m(\hat{\mathbf{x}})$ [Fig. 5(a)] and $\Pi_m(\hat{\mathbf{z}})$ [Fig. 5(b)] in the ground state as a function of ω_x for $\lambda = 1.40(3)\omega_z$. (c) and (d) Order parameter $\langle\sigma_{1x}\rangle$ and mean parity p_z computed from Figs. 5(a) and 5(b) and compared to the LMGM (solid lines) and the mean-field order parameter values (dotted lines).

superconducting quantum interference device systems [55–57]. Deep in the ferromagnetic phase, the dipole frequencies are consistent with the semiclassical theory of quantum tunneling [58–60]. In the limit $\lambda \gg \omega_z$, the perturbation theory provides a simple picture of this behavior: the two broken states $|\pm J\rangle_x$ being coupled by the z field via a $2J$-order process leads to a high power-law scaling of $\delta/\omega_z \propto (\omega_z/\lambda)^{2J-1}$. For values of $\lambda \gtrsim 1.5\omega_z$, the oscillation contrast decreases and the measured frequency deviates from theory, which we attribute to residual magnetic field fluctuations along x (rms width of $\sigma_B = 0.4$ mG), inducing an offset between the two wells that exceeds the tunnel coupling.

We finally investigate the controlled breaking of parity symmetry by a static magnetic field applied along x, which adds a Zeeman coupling of $-\hbar\omega_x J_x$ mixing the two parity sectors. As shown in Fig. 4, this field simultaneously induces a finite order parameter $\langle\sigma_{1x}\rangle$ and a reduction of the mean parity p_z. For large fields, the order parameter reaches a plateau consistent with the mean-field prediction of $\langle\sigma_{1x}\rangle = \mathrm{sgn}(\omega_x)\sqrt{1-(\omega_z/\lambda)^2}$. This behavior coincides with a cancellation of the mean parity p_z, illustrating the link between broken-symmetry and nonzero order parameter [29]. Besides the controlled symmetry breaking discussed above, spontaneous symmetry breaking also occurs in our system when preparing the ground state in the ferromagnetic phase using very slow ramps of the light coupling of $\dot{\lambda} \simeq 10^{-3}\omega_z^2$. We find that the sign of the spontaneous order parameter $\langle\sigma_{1x}\rangle$ is directly related to the sign of the shot-to-shot magnetic field fluctuation, which is independently recorded. We found no signature of more complex symmetry-breaking mechanisms, e.g., induced by interactions between atoms [61].

In conclusion, we studied the ground state and low-energy spectrum of the LMGM via nonlinear dynamics of the electronic spin of ^{162}Dy atoms. A possible extension of this study would be the nonadiabatic crossing of the critical point, which is a problem related to quantum annealing [62] and the Kibble-Zurek mechanism—for which the relevance for infinitely coordinated systems is debated [63–67]. In the ferromagnetic phase, we have demonstrated the production of the coherent superposition of broken-symmetry states [68] of interest for quantum-enhanced metrology [69]. Our system is also well suited to investigate various spontaneous symmetry-breaking mechanisms at the microscopic level and their connection to decoherence [70,71]. Our work could also be generalized to systems with an internal spin of larger amplitude, such as large-spin molecules [15,72] or Rydberg atoms [73].

We thank J. Dalibard, L. Glazman, and P. Ribeiro for stimulating discussions, as well as J. Beugnon, J. Dalibard, and F. Gerbier for a careful reading of the Letter. This work is supported by PSL University (MAFAG project) and the European Union (ERC UQUAM and TOPODY).

V. M. and T. S. contributed equally to this work.

*sylvain.nascimbene@lkb.ens.fr

[1] S. Sachdev, *Quantum Phase Transitions* (Cambridge University Press, Cambridge, England, 2011).
[2] A. Osterloh, L. Amico, G. Falci, and R. Fazio, Nature (London) **416**, 608 (2002).
[3] R. Blatt and C. F. Roos, Nat. Phys. **8**, 277 (2012).
[4] C. Gross and I. Bloch, Science **357**, 995 (2017).
[5] M. Saffman, J. Phys. B **49**, 202001 (2016).
[6] X.-s. Ma, B. Dakic, W. Naylor, A. Zeilinger, and P. Walther, Nat. Phys. **7**, 399 (2011).
[7] I. M. Georgescu, S. Ashhab, and F. Nori, Rev. Mod. Phys. **86**, 153 (2014).
[8] R. Islam, R. Ma, P. M. Preiss, M. Eric Tai, A. Lukin, M. Rispoli, and M. Greiner, Nature (London) **528**, 77 (2015).
[9] T. A. Hilker, G. Salomon, F. Grusdt, A. Omran, M. Boll, E. Demler, I. Bloch, and C. Gross, Science **357**, 484 (2017).
[10] L. D. Landau, Ukr. J. Phys. **11**, 19 (1937).
[11] S. D. Bartlett, T. Rudolph, and R. W. Spekkens, Rev. Mod. Phys. **79**, 555 (2007).
[12] P. Anderson, *Basic Notions of Condensed Matter Physics* (Benjamin Cummings, San Francisco, 1984).
[13] H. J. Lipkin, N. Meshkov, and A. J. Glick, Nucl. Phys. **62**, 188 (1965).
[14] P. Cejnar, J. Jolie, and R. F. Casten, Rev. Mod. Phys. **82**, 2155 (2010).
[15] D. Gatteschi and R. Sessoli, Angew. Chem., Int. Ed. **42**, 268 (2003).
[16] B. P. Lanyon, C. Hempel, D. Nigg, M. Müller, R. Gerritsma, F. Zähringer, P. Schindler, J. T. Barreiro, M. Rambach, G. Kirchmair, M. Hennrich, P. Zoller, R. Blatt, and C. F. Roos, Science **334**, 57 (2011).
[17] R. Islam, E. E. Edwards, K. Kim, S. Korenblit, C. Noh, H. Carmichael, G.-D. Lin, L.-M. Duan, C.-C. Joseph Wang, J. K. Freericks, and C. Monroe, Nat. Commun. **2**, 377 (2011).
[18] M. Albiez, R. Gati, J. Fölling, S. Hunsmann, M. Cristiani, and M. K. Oberthaler, Phys. Rev. Lett. **95**, 010402 (2005).
[19] S. Levy, E. Lahoud, I. Shomroni, and J. Steinhauer, Nature (London) **449**, 579 (2007).
[20] A. Trenkwalder, G. Spagnolli, G. Semeghini, S. Coop, M. Landini, P. Castilho, L. Pezzè, G. Modugno, M. Inguscio, A. Smerzi, and M. Fattori, Nat. Phys. **12**, 826 (2016).
[21] T. Zibold, E. Nicklas, C. Gross, and M. K. Oberthaler, Phys. Rev. Lett. **105**, 204101 (2010).
[22] L. D. Landau and E. Lifshitz, *Quantum Mechanics, Non-Relativistic Theory* (Pergamon, London, 1958).
[23] G. A. Smith, S. Chaudhury, A. Silberfarb, I. H. Deutsch, and P. S. Jessen, Phys. Rev. Lett. **93**, 163602 (2004).
[24] R. Botet, R. Jullien, and P. Pfeuty, Phys. Rev. Lett. **49**, 478 (1982).
[25] S. Dusuel and J. Vidal, Phys. Rev. Lett. **93**, 237204 (2004).
[26] A. Campa, T. Dauxois, D. Fanelli, and S. Ruffo, *Physics of Long-Range Interacting Systems* (Oxford University, New York, 2014).
[27] R. Orús, S. Dusuel, and J. Vidal, Phys. Rev. Lett. **101**, 025701 (2008).
[28] A. Evrard, V. Makhalov, T. Chalopin, L. A. Sidorenkov, J. Dalibard, R. Lopes, and S. Nascimbene, Phys. Rev. Lett. **122**, 173601 (2019).
[29] See Supplemental Material at http://link.aps.org/supplemental/10.1103/PhysRevLett.123.120601 for a study

of adiabaticity requirements for the ground state preparation, eigenstate spectroscopy at higher energy, a description of the classical mean-field treatment, a derivation of the critical Hamiltonian, and an extensive discussion of parity symmetry breaking by an external magnetic field. It includes Refs. [30–32].

[30] F. T. Hioe, D. MacMillen, and E. W. Montroll, Phys. Rep. **43**, 305 (1978).

[31] F. Leyvraz and W. D. Heiss, Phys. Rev. Lett. **95**, 050402 (2005).

[32] M. Heyl, Rep. Prog. Phys. **81**, 054001 (2018).

[33] J. J. Bollinger, W. M. Itano, D. J. Wineland, and D. J. Heinzen, Phys. Rev. A **54**, R4649 (1996).

[34] C. Lee, Phys. Rev. Lett. **97**, 150402 (2006).

[35] D. Ulam-Orgikh and M. Kitagawa, Phys. Rev. A **64**, 052106 (2001).

[36] L. Landau, L. Pitaevskii, and E. Lifshitz, *Electrodynamics of Continuous Media* (Butterworth, Washington, DC, 1984).

[37] T. Holstein and H. Primakoff, Phys. Rev. **58**, 1098 (1940).

[38] V. V. Ulyanov and O. B. Zaslavskii, Phys. Rep. **216**, 179 (1992).

[39] The Hamiltonian [Eq. (3)] corresponds to a $1/N$ expansion of the LMGM at fixed ϵ, which is expected to be valid in the range $\lambda/\omega_z - 1 \lesssim 1/4$ [29].

[40] It becomes inaccurate in the deep ferromagnetic phase (for $\lambda \gtrsim 1.5\omega_z$, see [29]), where the precise shape of the double-well potential is required to describe quantitatively the quantum tunneling effects [38].

[41] L. Landau and E. Lifshitz, in *Statistical Physics* (Butterworth-Heinemann, Oxford, England, 1980), 3rd ed., pp. 446–516.

[42] O. Gühne and G. Tóth, Phys. Rep. **474**, 1 (2009).

[43] N. Killoran, M. Cramer, and M. B. Plenio, Phys. Rev. Lett. **112**, 150501 (2014).

[44] J. Vidal, Phys. Rev. A **73**, 062318 (2006).

[45] The minimum value $\langle \sigma_{1y}\sigma_{2y}\rangle = -0.040(5)$ for $\lambda \simeq \omega_z$ is about 60% of the minimum correlation $\langle \sigma_{1\hat{\mathbf{n}}}\sigma_{2\hat{\mathbf{n}}}\rangle = -1/(N-1)$ allowed for a set of N spins that are symmetric upon exchange [46].

[46] M. Koashi, V. Bužek, and N. Imoto, Phys. Rev. A **62**, 050302(R) (2000).

[47] X.-Y. Luo, Y.-Q. Zou, L.-N. Wu, Q. Liu, M.-F. Han, M. K. Tey, and L. You, Science **355**, 620 (2017).

[48] A. Sartori, J. Marino, S. Stringari, and A. Recati, New J. Phys. **17**, 093036 (2015).

[49] G. Valtolina, F. Scazza, A. Amico, A. Burchianti, A. Recati, T. Enss, M. Inguscio, M. Zaccanti, and G. Roati, Nat. Phys. **13**, 704 (2017).

[50] S. Dusuel and J. Vidal, Phys. Rev. B **71**, 224420 (2005).

[51] We present in the Supplemental Material [29] measurements of higher-energy levels that confirm this picture on a larger energy range.

[52] S. A. Owerre and M. B. Paranjape, Phys. Rep. **546**, 1 (2015).

[53] J. R. Friedman, M. P. Sarachik, J. Tejada, and R. Ziolo, Phys. Rev. Lett. **76**, 3830 (1996).

[54] L. Thomas, F. Lionti, R. Ballou, D. Gatteschi, R. Sessoli, and B. Barbara, Nature (London) **383**, 145 (1996).

[55] J. R. Friedman, V. Patel, W. Chen, S. K. Tolpygo, and J. E. Lukens, Nature (London) **406**, 43 (2000).

[56] C. H. van der Wal, A. C. J. ter Haar, F. K. Wilhelm, R. N. Schouten, C. J. P. M. Harmans, T. P. Orlando, S. Lloyd, and J. E. Mooij, Science **290**, 773 (2000).

[57] Y. Makhlin, G. Schön, and A. Shnirman, Rev. Mod. Phys. **73**, 357 (2001).

[58] M. Enz and R. Schilling, J. Phys. C **19**, 1765 (1986).

[59] G. Scharf, W. F. Wreszinski, van, and J. L. Hemmen, J. Phys. A **20**, 4309 (1987).

[60] O. B. Zaslavskii, Phys. Lett. A **145**, 471 (1990).

[61] We did not observe a significant reduction of parity when increasing the atomic density (up to $\sim 10^{14}$ cm^{-3}).

[62] V. Bapst and G. Semerjian, J. Stat. Mech. (2012) P06007.

[63] T. Caneva, R. Fazio, and G. E. Santoro, Phys. Rev. B **78**, 104426 (2008).

[64] P. Solinas, P. Ribeiro, and R. Mosseri, Phys. Rev. A **78**, 052329 (2008).

[65] O. L. Acevedo, L. Quiroga, F. J. Rodríguez, and N. F. Johnson, Phys. Rev. Lett. **112**, 030403 (2014).

[66] M.-J. Hwang, R. Puebla, and M. B. Plenio, Phys. Rev. Lett. **115**, 180404 (2015).

[67] N. Defenu, T. Enss, M. Kastner, and G. Morigi, Phys. Rev. Lett. **121**, 240403 (2018).

[68] J. I. Cirac, M. Lewenstein, K. Mølmer, and P. Zoller, Phys. Rev. A **57**, 1208 (1998).

[69] L. Pezzè, A. Smerzi, M. K. Oberthaler, R. Schmied, and P. Treutlein, Rev. Mod. Phys. **90**, 035005 (2018).

[70] M. Lucamarini, S. Paganelli, and S. Mancini, Phys. Rev. A **69**, 062308 (2004).

[71] J. van Wezel, J. van den Brink, and J. Zaanen, Phys. Rev. Lett. **94**, 230401 (2005).

[72] J. Floß, A. Kamalov, I. S. Averbukh, and P. H. Bucksbaum, Phys. Rev. Lett. **115**, 203002 (2015).

[73] A. Facon, E.-K. Dietsche, D. Grosso, S. Haroche, J.-M. Raimond, M. Brune, and S. Gleyzes, Nature (London) **535**, 262 (2016).

arXiv:2001.01664v1 [cond-mat.quant-gas] 6 Jan 2020

Exploring the topology of a quantum Hall system at the microscopic level

Thomas Chalopin,* Tanish Satoor,* Alexandre Evrard, Vasiliy Makhalov, Jean Dalibard, Raphael Lopes, and Sylvain Nascimbene†
Laboratoire Kastler Brossel, Collège de France, CNRS, ENS-PSL University, Sorbonne Université, 11 Place Marcelin Berthelot, 75005 Paris, France
(Dated: January 7, 2020)

Quantum Hall systems are characterized by the quantization of the Hall conductance – a bulk property rooted in the topological structure of the underlying quantum states [1]. In condensed matter devices, material imperfections hinder a direct connection to simple topological models [2, 3], and restrict the existence of fragile topological phases to defect-free samples [4, 5]. Artificial systems, as realized with photonic platforms [6] or cold atomic gases [7], open novel possibilities by enabling specific probes of topology [8–15] or flexible manipulation e.g. using synthetic dimensions encoded in internal degrees of freedom [16–23]. However, the sizes of synthetic dimensions realized so far remain moderate, making the notion of a bulk irrelevant. Here, we realize a quantum Hall system using ultracold dysprosium atoms, in a two-dimensional geometry formed by one spatial dimension and one synthetic dimension encoded in the atomic spin $J = 8$. We demonstrate that the large number, $2J + 1 = 17$, of magnetic sublevels leads to distinct behaviors in the bulk, where motion is inhibited due to a flattened energy band, and along the edges, where the particles are free to move in only one direction. We also show that the low-energy excitations take the form of cyclotron and skipping orbits. Furthermore, we measure the transverse drift induced by a weak force, and find a uniform Hall response in the bulk, reaching 98(5)% of the quantized value expected for a topological system. Our findings pave the way towards the realization of quantum many-body systems with non-trivial topology, such as mean-field Abrikosov vortex lattices or fractional quantum Hall states, as supported by numerical simulations of interacting bosons in our setting.

In two-dimensional electron gases, the quantization of the Hall conductance results from the non-trivial topological structuring of the quantum states of an electron band. For an infinite system, this topological character is described by the Chern number $\mathcal{C}$, a global invariant taking a non-zero integer value that is robust to relatively weak disorder [1]. In a real finite-size system, the non-trivial topology further leads to in-gap excitations delocalized over the edges, characterized by unidirectional motion exempt from backscattering [3]. Such protected edge modes, together with their generalization to topological insulators, topological superconductors or fractional quantum Hall states [4, 5], lie at the heart of possible applications in spintronics [24] or quantum computing [25].

In electronic quantum Hall systems, the topology manifests itself via the spectacular robustness of the Hall conductance quantization to finite-size or disorder effects [26]. Nonetheless, such perturbations typically lead to conducting stripes surrounding insulating domains of localized electrons, making the comparison with simple defect-free models challenging. In topological insulators or fractional quantum Hall systems, topological properties are more fragile, and can only be revealed in very clean samples [4, 5]. Recent experiments with topological quantum systems in photonic or atomic platforms [7, 27] have created new possibilities, from the realization of emblematic models of topological matter [8, 28, 29] to the application of well-controlled edge and disorder potentials. In such systems, internal degrees of freedom can be used to simulate a synthetic dimension of finite size with sharp-edge effects [16–23]. Encoding a synthetic dimension in the time domain can also give access to higher-dimensional physics [30, 31].

In this work, we engineer a topological system with ultracold ^{162}Dy atoms based on coherent light-induced couplings between the atom's motion and the electronic spin $J = 8$, with relevant dynamics along two dimensions – one spatial dimension and a synthetic dimension encoded in the discrete set of $2J + 1 = 17$ magnetic sublevels. These couplings give rise to an artificial magnetic field, such that our system realizes an analog of a quantum Hall ribbon. We characterize the dispersionless bulk modes and chiral edge states of the lowest energy band, and study elementary excitations to higher bands. We also measure the Hall drift induced by an external force, and infer the local Hall response of the band via the local Chern marker, which quantifies topological order in real space [32]. Our experiments show that the synthetic dimension is large enough to allow for a meaningful bulk with robust topological properties.

The atom dynamics is induced by two-photon optical transitions involving counter-propagating laser beams along x (see Fig. 1a), and coupling successive magnetic sublevels m [33, 34]. Here, the integer m ($-J \leq m \leq J$) quantifies the spin projection along the direction z of an external magnetic field. The spin coupling amplitudes then inherit the complex phase Kx of the interference between both lasers, where $K = 4\pi/\lambda$ and $\lambda = 626.1\,\mathrm{nm}$ is the light wavelength (see Fig. 1b). Given the Clebsch-Gordan algebra of atom-light interactions for the domi-

* These two authors contributed equally.
† sylvain.nascimbene@lkb.ens.fr

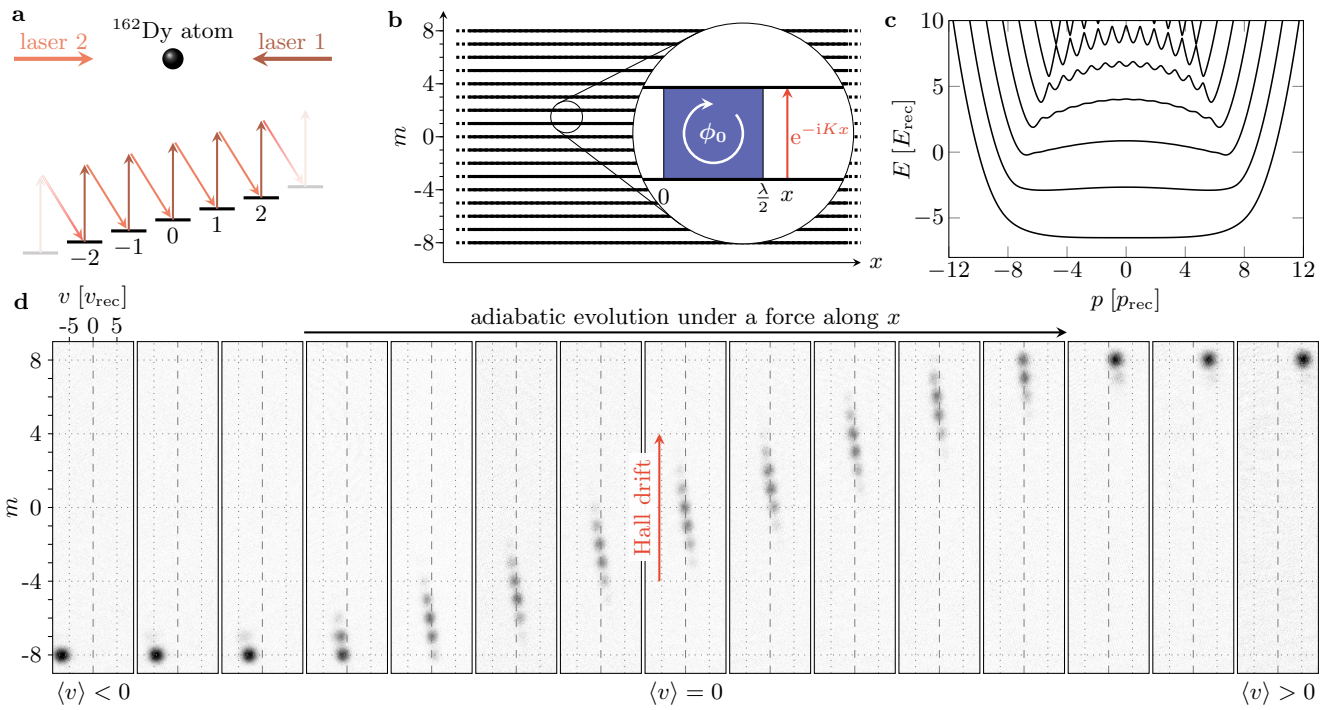

Figure 1. **Synthetic Hall system**. (a) Laser configuration used to couple the magnetic sublevels m of a ^{162}Dy atom (with $-J \leq m \leq J$ and $J = 8$, only a few m values represented). (b) Interpreting the spin projection as a synthetic dimension, the system is mapped to a two-dimensional ribbon of finite width. The photon recoil $p_{\rm rec} = \hbar K$ imparted upon a spin transition leads to complex-valued hopping amplitudes along m, equivalent to the Aharonov-Bohm phase of a charged particle evolving in a magnetic field. The blue area represents a magnetic unit cell pierced by one flux quantum ϕ_0. (c) Dispersion relation describing the quantum level structure, with flattened energy bands reminiscent of Landau levels. (d) The lowest energy band is explored by applying an external force. We probe the velocity and magnetic projection distributions by imaging the atomic gas after an expansion under a magnetic field gradient. We find three types of behavior: free motion with negative (positive) velocity on the bottom edge $m = -J$ (top edge $m = J$) and zero average velocity in the bulk.

nant optical transition, the atom dynamics is described by the Hamiltonian

$$\hat{H} = \frac{1}{2}M\hat{v}^2 - \frac{\hbar\Omega}{2}\left(e^{-iK\hat{x}}\hat{J}_+ + e^{iK\hat{x}}\hat{J}_-\right) + V(\hat{J}_z) \quad (1)$$

where M is the atom mass, $\hat{v}$ is its velocity, $\hat{J}_z$ and $\hat{J}_\pm$ are spin projection and ladder operators. The coupling Ω is proportional to both laser electric fields, and the potential $V(\hat{J}_z) = -\hbar\Omega\hat{J}_z^2/(2J+3)$ stems from rank-2 tensor light shifts (see Methods).

A light-induced spin transition $m \to m+1$ is accompanied by a momentum kick $-p_{\rm rec} \equiv -\hbar K$ along x, such that the canonical momentum $\hat{p} = M\hat{v} + p_{\rm rec}\hat{J}_z$ is a conserved quantity. The dynamics for a given momentum p is then described by the Hamiltonian

$$\hat{H}_p = \frac{(p - p_{\rm rec}\hat{J}_z)^2}{2M} - \hbar\Omega\hat{J}_x + V(\hat{J}_z), \quad (2)$$

which resembles the Landau one,

$$\hat{H}_{\rm Landau} = \frac{(\hat{p}_x - eB\hat{y})^2}{2M} + \frac{\hat{p}_y^2}{2M}, \quad (3)$$

describing the dynamics of an electron evolving in 2D under a perpendicular magnetic field B. The analogy between both systems can be made upon the identifications $\hat{J}_z \leftrightarrow \hat{y}$ and $eB \leftrightarrow p_{\rm rec}$. The term $\hat{J}_x$ in (2) plays the role of the kinetic energy along the synthetic dimension, since it couples neighboring m levels with real positive coefficients, similarly to the discrete form of the Laplacian operator $\propto \hat{p}_y^2$ in (3) (see Methods). The range of magnetic projections being limited, our system maps onto a Hall system in a ribbon geometry bounded by the edge states $m = \pm J$. The relevance of the analogy is confirmed by the structure of energy bands $E_n(p)$ expected for our system, shown in Fig. 1c. The energy dispersion of the first few bands is strongly reduced for $|p| \lesssim Jp_{\rm rec}$, reminiscent of dispersionless Landau levels. A parabolic dispersion is recovered for $|p| \gtrsim Jp_{\rm rec}$, similar to the ballistic edge modes of a quantum Hall ribbon [3].

We first characterize the ground band using quantum states of arbitrary values of momentum p. We begin with an atomic gas spin-polarized in $m = -J$, and with a negative mean velocity $\langle\hat{v}\rangle = -6.5(1)v_{\rm rec}$ (with $v_{\rm rec} \equiv p_{\rm rec}/M$), such that it corresponds to the ground state of (2) with $p = -14.5(1)p_{\rm rec}$. The gas temperature $T =$

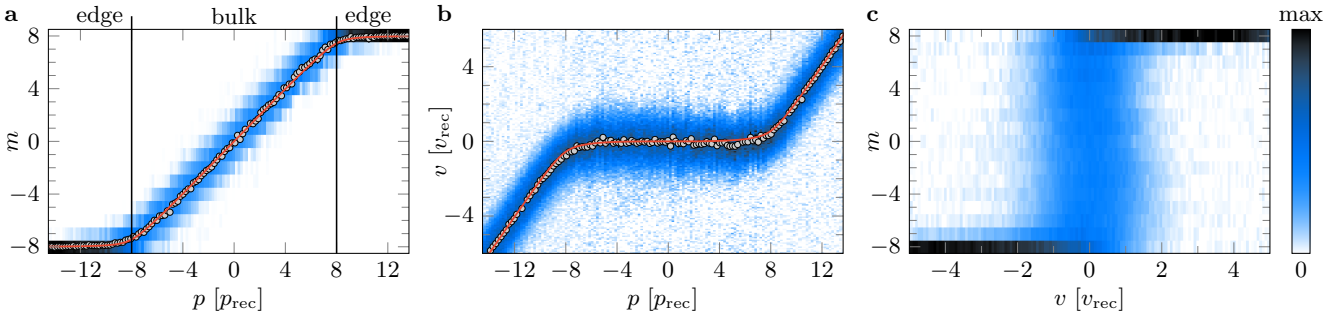

Figure 2. **Ground band characterization**. **a.** Spin projection distribution Π_m as a function of the momentum p, with the mean spin projection $\langle \hat{J}_z \rangle$ (gray dots) and the theoretical prediction $(p - M\partial_p E_0)/p_{\rm rec}$ (red line). **b.** Velocity distribution, together with the mean velocity $\langle \hat{v} \rangle$ (gray dots) and the expected value, given by the derivative of the band dispersion $\partial_p E_0$ (red line). **c.** Local density of states obtained by integrating the measured distributions in (v, m) space over all momenta.

0.55(6) µK is such that the thermal velocity broadening is smaller than the recoil velocity $v_{\rm rec}$. We then slowly ramp up the light intensity up to a coupling $\hbar\Omega = 1.02(6)E_{\rm rec}$, where $E_{\rm rec} \equiv p_{\rm rec}^2/(2M)$ is the natural energy scale in our system. Subsequently, we apply a weak force F_x along x, such that the state adiabatically evolves in the ground energy band with $\dot{p} = F_x$, until the desired momentum is reached. We measure the distribution of velocity v and spin projection m by imaging the atomic gas after a free flight in the presence of a magnetic field gradient.

The main features of Landau level physics are visible in the raw images shown in Fig. 1d. Depending on the momentum p, the system exhibits three types of behaviors. (i) When spin-polarized in $m = -J$, the atoms move with a negative mean velocity $\langle \hat{v} \rangle$, consistent with a left-moving edge mode. (ii) When the velocity approaches zero under the action of the force F_x, the system experiences a series of resonant transitions to higher m sublevels – in other words a transverse Hall drift along the synthetic dimension. In this regime the atom's motion is inhibited along x, as expected for a quasi non-dispersive band. (iii) Once the edge $m = J$ is reached, the velocity $\langle \hat{v} \rangle$ rises again, corresponding to a right-moving edge mode. Overall, while exploring the entire ground band under the action of a force along x, the atoms are pumped from one edge to the other along the synthetic dimension.

To distinguish between bulk and edge modes, we plot in Fig. 2a the spin projection probabilities Π_m as a function of momentum p. We find that the edge probabilities $\Pi_{m=\pm J}$ exceed 1/2 for $|p| > 8.0(1)p_{\rm rec}$, defining the edge mode sectors – with the bulk modes in between. We study the system dynamics via its velocity distribution and mean velocity $\langle \hat{v} \rangle$, shown in Fig. 2b. We observe that the velocity of bulk modes remains close to zero, which shows via the Hellmann-Feynman relation $\langle \hat{v} \rangle = \partial E_0/\partial p$ that the ground band is almost flat. The measured residual mean velocities allow us to infer a dispersion $\Delta E_0^{\rm pk-pk} = 1.2(5)\, E_{\rm rec}$ in the bulk mode region – nearly 2% of the free-particle dispersion expected over the same range of momenta. On the contrary, edge modes are characterized by a velocity $\langle \hat{v} \rangle \simeq (p - p_0)/M$, corresponding to ballistic motion – albeit with the restriction $\langle \hat{v} \rangle < 0$ for edge modes close to $m = -J$, and $\langle \hat{v} \rangle > 0$ at the opposite edge. We also characterize correlations between velocity v and spin projection m over the full band, via the local density of states (LDOS) in (v, m) space, integrated over p. We stress here that the LDOS only involves gauge-independent quantities, and could thus be generalized to more complex geometries lacking translational invariance. As shown in Fig. 2c, it also reveals characteristic quantum Hall behavior, namely inhibited dynamics in the bulk and chiral motion on the edges.

The Landau level structure is characterized by a harmonic energy spacing $\hbar\omega_{\rm c}$, set by the cyclotron frequency $\omega_{\rm c} = eB/M$. We test this behavior in our system by studying elementary excitations above the ground band, via the trajectories of the center of mass following a velocity kick $v_{\rm kick} \simeq v_{\rm rec}$. As shown in Fig. 3 (blue dots), we measure almost-closed trajectories in the bulk, consistent with the periodic cyclotron orbits expected for an infinite Hall system. We checked that this behavior remains valid for larger excitation strengths, until one couples to highly dispersive excited bands (for velocity kicks $v_{\rm kick} \gtrsim 2v_{\rm rec}$, see Methods). Close to the edges, the atoms experience an additional drift and their trajectories are similar to classical skipping orbits bouncing on a hard hall. In particular, the drift orientation only depends on the considered edge, irrespective of the kick direction. We report in the inset of Fig. 3 the frequencies of velocity oscillations, which agree well with the expected cyclotron gap to the first excited band. We find that the gap is almost uniform within the bulk mode sector, with a residual variation in the range $\omega_c = 3.0(1) - 3.8(1)E_{\rm rec}/\hbar$.

We now investigate the key feature of Landau levels, namely their quantized Hall response, which is intrinsically related to their topological nature. In a ribbon geometry, the Hall response of a particle corresponds to the transverse velocity acquired upon applying a potential difference across the edges (see Fig. 4a). In our system, such a potential corresponds to a Zeeman term $-F_m \hat{J}_z$ added to the Hamiltonian (2), which can now be recast

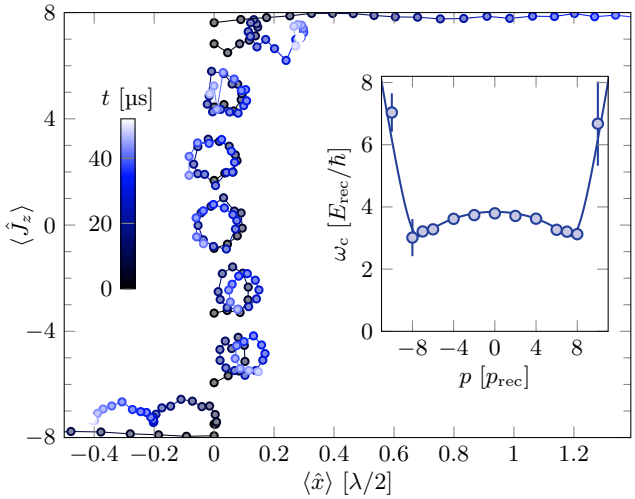

Figure 3. **Cyclotron and skipping orbits**. Trajectories in (x, m) space following a velocity kick $v_{\rm kick} \simeq v_{\rm rec}$, starting at $\langle \hat{x} \rangle = 0$, and for different initial momentum states (blue dots). The color encodes the time evolution. Inset: Frequencies extracted from the velocity dynamics (blue dots), and compared with the expected cyclotron gap for $\hbar\Omega = E_{\rm rec}$ (blue line).

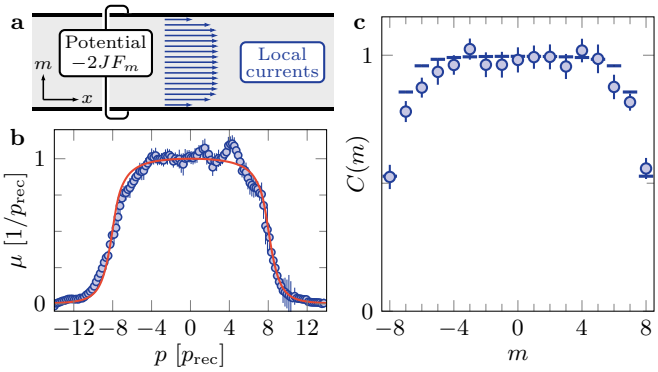

Figure 4. **Hall response**. **a**. We determine the Hall response from the measurement of local currents in the real dimension, that result from the application, in synthetic space, of a potential difference $-2JF_m$ between the edges. **b**. Hall mobility $\mu(p)$ measured for states of momenta p, via their increase of velocity upon a small force F_m along m. **c**. Local Chern marker as a function of m, corresponding to the integrated mobility $\mu(p)$ weighted by the projection probability $\Pi_m(p)$.

as

$$\hat{H}_p - F_m \hat{J}_z = \hat{H}_{p+Mv'} - v'p, \quad \text{with} \quad v' = F_m/p_{\rm rec},$$

such that the force acts as a momentum shift Mv' in the reference frame with velocity v'. In the weak force limit, the perturbed state remains in the ground band, and its mean velocity reads

$$\langle \hat{v} \rangle = \langle \hat{v} \rangle_{F_m=0} - \mu F_m, \quad \text{where} \quad \mu = \frac{1}{p_{\rm rec}} \frac{\partial}{\partial p}(p - M\langle \hat{v} \rangle)$$

is the Hall mobility. We present in Fig. 4b the Hall mobility $\mu(p)$ deduced from the mean velocity shown in Fig. 2b. For bulk modes, it remains close to the value $\mu = 1/p_{\rm rec}$, which corresponds to the classical mobility $\mu = 1/(eB)$ in the equivalent Hall system. The mobility decreases in the edge mode sector, as expected for topologically protected boundary states whose ballistic motion is undisturbed by the magnetic field.

We use the measured drift of individual quantum states to infer the overall Hall response of the ground band. As for any spatially limited sample, our system does not exhibit a gap in the energy spectrum due to the edge mode dispersion. In particular, high-energy edge modes of the ground band are expected to resonantly hybridize with excited bands upon disorder, such that defining the Hall response of the entire ground band is not physically meaningful. We thus only consider the energy branch $E < E^*$, where E^* lies in the middle of the first gap at zero momentum (see Methods). We characterize the (inhomogeneous) Hall response of this branch via the local Chern marker

$$C(m) \equiv 2\pi \, \mathrm{Im} \, \langle m | \, [\hat{P}\hat{x}\hat{P}, \hat{P}\hat{J}_z\hat{P}] \, | m \rangle = \int_{E(p)<E^*} \mathrm{d}p \, \Pi_m(p)\mu(p),$$

where $\hat{P}$ projects on the chosen branch [32, 35]. This local geometrical marker quantifies the adiabatic transverse response in position space, and matches the integer Chern number $\mathcal{C}$ in the bulk of a large, defect-free system. Here, it is given by the integrated mobility $\mu(p)$, weighted by the spin projection probability $\Pi_m(p)$ (see Methods). As shown in Fig. 4c, we identify a plateau in the range $-5 \leq m \leq 5$. There, the average value of the Chern marker, $\overline{C} = 0.98(5)$, is consistent with the integer value $\mathcal{C} = 1$ – the Chern number of an infinite Landau level. This measurement shows that our system is large enough to reproduce a topological Hall response in its bulk. For positions $|m| \geq 6$, we measure a decrease of the Chern marker, that we attribute to non-negligible correlations with the edges.

Such a topological bulk is a prerequisite for the realization of emblematic phases of two-dimensional quantum Hall systems, as we now confirm via numerical simulations of interacting quantum many-body systems. In our system, collisions between atoms *a priori* occur when they are located at the same position x, irrespective of their spin projections m, m', leading to highly anisotropic interactions. While this feature leads to an interesting phenomenology [36], we propose to control the interaction range by spatially separating the different m states using a magnetic field gradient, preventing collisions for $m \neq m'$ (see Fig. 5a). We discuss below the many-body phases expected for bosonic atoms with such short-range interactions, assuming for simplicity repulsive interactions of equal strength for each projection m.

We first consider the case of a large filling fraction $\nu \equiv N_{\rm at}/N_\phi \gg 1$, where N_ϕ is the number of magnetic flux quanta in the area occupied by $N_{\rm at}$ atoms – as realized in previous experiments on rapidly rotating gases [37, 38]. In this regime and at low tempera-

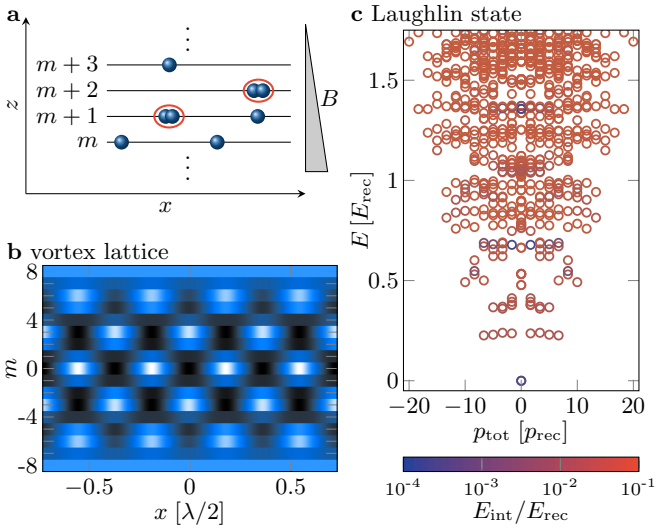

Figure 5. **Simulations of topological many-body systems**. **a**. Proposed scheme to engineer contact interactions along both directions x and m. A magnetic field gradient spatially separates the different m states along z, such that collisions (represented by the red ellipses) only occur for atoms in the same magnetic sublevel m. **b**. Density distribution of a Bose-Einstein condensate, with a chemical potential at $\simeq 2E_{\mathrm{rec}}$ above the single-particle ground state energy. **c**. Many-body spectrum of a system of $N = 5$ interacting atoms, where the color encodes the interaction energy. We use periodic boundary conditions along x, with a circumference $L = 0.6(\lambda/2)$ allowing for $N_{\mathrm{orb}} = 9$ orbitals at low energy, compatible with the Laughlin state. The residual energy dispersion between these orbitals is minimized by using a coupling strength $\Omega = 0.5\, E_{\mathrm{rec}}/\hbar$.

ture, the system forms a Bose-Einstein condensate that spontaneously breaks translational symmetry, leading to a triangular Abrikosov lattice of quantum vortices (see Fig. 5b). Due to the hard-wall boundary along m, one expects phase transitions between vortex lattice configurations when tuning the coupling strength Ω and the chemical potential, similar to the phenomenology of type-II superconductors in confined geometries [39] (see Methods).

For lower filling fractions $\nu \sim 1$, one expects strongly-correlated ground states analogous to fractional quantum Hall states [40]. We present in Fig. 5c a numerical calculation of the many-body spectrum for $N_{\mathrm{at}} = 5$ atoms with periodic boundary conditions along x, corresponding to a cylinder geometry. We choose the circumference such that the number of orbitals $N_{\mathrm{orb}} = 9$ in the bulk region of the lowest band matches the number $N_{\mathrm{orb}} = 2N_{\mathrm{at}} - 1$ required to construct the Laughlin wavefunction. For contact interactions parametrized by a Haldane pseudopotential of amplitude $U = E_{\mathrm{rec}}$, we numerically find a ground state separated by an energy gap $E_{\mathrm{gap}} \simeq 0.23\, E_{\mathrm{rec}} = k_{\mathrm{B}} \times 140\,\mathrm{nK}$ from the rest of the excitations. It also exhibits a very small interaction energy E_{int}, indicating anti-bunching between atoms, which is a hallmark of the Laughlin state.

The realization of a quantum-Hall system based on a large synthetic dimension, as discussed here, is a promising setting for future realizations of topological quantum matter. An important asset of our setup is the large cyclotron energy, measured in the range $\hbar\omega_{\mathrm{c}} \simeq k_{\mathrm{B}} \times 1.8 - 2.3\,\mu\mathrm{K}$, much larger than the typical temperatures of quantum degenerate gases, thus enabling the realization of strongly-correlated states at realistic temperatures. The techniques developed here could give access to complex correlation effects, such as flux attachment via cyclotron orbits [41] or charge fractionalization via center-of-mass Hall response [42].

[1] Thouless, D. J., Kohmoto, M., Nightingale, M. P. & den Nijs, M. Quantized Hall Conductance in a Two-Dimensional Periodic Potential. *Phys. Rev. Lett.* **49**, 405–408 (1982).

[2] Laughlin, R. B. Quantized Hall conductivity in two dimensions. *Phys. Rev. B* **23**, 5632–5633 (1981).

[3] Halperin, B. I. Quantized Hall conductance, current-carrying edge states, and the existence of extended states in a two-dimensional disordered potential. *Phys. Rev. B* **25**, 2185–2190 (1982).

[4] Stormer, H. L., Tsui, D. C. & Gossard, A. C. The fractional quantum Hall effect. *Rev. Mod. Phys.* **71**, S298–S305 (1999).

[5] Hasan, M. Z. & Kane, C. L. Colloquium: Topological insulators. *Rev. Mod. Phys.* **82**, 3045–3067 (2010).

[6] Ozawa, T. *et al.* Topological photonics. *Rev. Mod. Phys.* **91**, 015006 (2019).

[7] Goldman, N., Budich, J. C. & Zoller, P. Topological quantum matter with ultracold gases in optical lattices. *Nat. Phys.* **12**, 639–645 (2016).

[8] Jotzu, G. *et al.* Experimental realization of the topological Haldane model with ultracold fermions. *Nature* **515**, 237–240 (2014).

[9] Aidelsburger, M. *et al.* Measuring the Chern number of Hofstadter bands with ultracold bosonic atoms. *Nat. Phys.* **11**, 162–166 (2015).

[10] Hu, W. *et al.* Measurement of a Topological Edge Invariant in a Microwave Network. *Phys. Rev. X* **5**, 011012 (2015).

[11] Mittal, S., Ganeshan, S., Fan, J., Vaezi, A. & Hafezi, M. Measurement of topological invariants in a 2D photonic system. *Nat. Photonics* **10**, 180–183 (2016).

[12] Wu, Z. *et al.* Realization of two-dimensional spin-orbit coupling for Bose-Einstein condensates. *Science* **354**, 83–88 (2016).

[13] Fläschner, N. *et al.* Experimental reconstruction of the Berry curvature in a Floquet Bloch band. *Science* **352**, 1091–1094 (2016).

[14] Ravets, S. *et al.* Polaron Polaritons in the Integer and Fractional Quantum Hall Regimes. *Phys. Rev. Lett.* **120**, 057401 (2018).

[15] Schine, N., Chalupnik, M., Can, T., Gromov, A. & Si-

mon, J. Electromagnetic and gravitational responses of photonic Landau levels. *Nature* **565**, 173 (2019).

[16] Celi, A. *et al.* Synthetic Gauge Fields in Synthetic Dimensions. *Phys. Rev. Lett.* **112**, 043001 (2014).

[17] Mancini, M. *et al.* Observation of chiral edge states with neutral fermions in synthetic Hall ribbons. *Science* **349**, 1510–1513 (2015).

[18] Stuhl, B. K., Lu, H.-I., Aycock, L. M., Genkina, D. & Spielman, I. B. Visualizing edge states with an atomic Bose gas in the quantum Hall regime. *Science* **349**, 1514–1518 (2015).

[19] Livi, L. F. *et al.* Synthetic Dimensions and Spin-Orbit Coupling with an Optical Clock Transition. *Phys. Rev. Lett.* **117**, 220401 (2016).

[20] Kolkowitz, S. *et al.* Spin–orbit-coupled fermions in an optical lattice clock. *Nature* **542**, 66–70 (2017).

[21] An, F. A., Meier, E. J. & Gadway, B. Direct observation of chiral currents and magnetic reflection in atomic flux lattices. *Sci. Adv.* **3**, e1602685 (2017).

[22] Lustig, E. *et al.* Photonic topological insulator in synthetic dimensions. *Nature* **567**, 356–360 (2019).

[23] Ozawa, T. & Price, H. M. Topological quantum matter in synthetic dimensions. *Nat. Rev. Phys.* **1**, 349 (2019).

[24] Pesin, D. & MacDonald, A. H. Spintronics and pseudospintronics in graphene and topological insulators. *Nature Mater* **11**, 409–416 (2012).

[25] Kitaev, A. Y. Fault-tolerant quantum computation by anyons. *Annals of Physics* **303**, 2–30 (2003).

[26] v. Klitzing, K., Dorda, G. & Pepper, M. New Method for High-Accuracy Determination of the Fine-Structure Constant Based on Quantized Hall Resistance. *Phys. Rev. Lett.* **45**, 494–497 (1980).

[27] Lu, L., Joannopoulos, J. D. & Soljačić, M. Topological photonics. *Nat. Photonics* **8**, 821–829 (2014).

[28] Aidelsburger, M. *et al.* Realization of the Hofstadter Hamiltonian with Ultracold Atoms in Optical Lattices. *Phys. Rev. Lett.* **111**, 185301 (2013).

[29] Miyake, H., Siviloglou, G. A., Kennedy, C. J., Burton, W. C. & Ketterle, W. Realizing the Harper Hamiltonian with Laser-Assisted Tunneling in Optical Lattices. *Phys. Rev. Lett.* **111**, 185302 (2013).

[30] Lohse, M., Schweizer, C., Price, H. M., Zilberberg, O. & Bloch, I. Exploring 4D quantum Hall physics with a 2D topological charge pump. *Nature* **553**, 55–58 (2018).

[31] Zilberberg, O. *et al.* Photonic topological boundary pumping as a probe of 4D quantum Hall physics. *Nature* **553**, 59–62 (2018).

[32] Bianco, R. & Resta, R. Mapping topological order in coordinate space. *Phys. Rev. B* **84**, 241106 (2011).

[33] Lin, Y.-J., Jiménez-García, K. & Spielman, I. B. Spin–orbit-coupled Bose–Einstein condensates. *Nature* **471**, 83–86 (2011).

[34] Cui, X., Lian, B., Ho, T.-L., Lev, B. L. & Zhai, H. Synthetic gauge field with highly magnetic lanthanide atoms. *Phys. Rev. A* **88** (2013).

[35] Kitaev, A. Anyons in an exactly solved model and beyond. *Annals of Physics* **321**, 2–111 (2006).

[36] Barbarino, S., Taddia, L., Rossini, D., Mazza, L. & Fazio, R. Magnetic crystals and helical liquids in alkaline-earth fermionic gases. *Nat Commun* **6**, 1–9 (2015).

[37] Schweikhard, V., Coddington, I., Engels, P., Mogendorff, V. P. & Cornell, E. A. Rapidly Rotating Bose-Einstein Condensates in and near the Lowest Landau Level. *Phys. Rev. Lett.* **92**, 040404 (2004).

[38] Bretin, V., Stock, S., Seurin, Y. & Dalibard, J. Fast Rotation of a Bose-Einstein Condensate. *Phys. Rev. Lett.* **92** (2004).

[39] Abrikosov, A. A. On the magnetic properties of superconductors of the second group. *Sov. Phys. - Jetp* **5**, 1174–1182 (1957).

[40] Kane, C. L., Mukhopadhyay, R. & Lubensky, T. C. Fractional Quantum Hall Effect in an Array of Quantum Wires. *Phys. Rev. Lett.* **88**, 036401 (2002).

[41] Goldman, V. J., Su, B. & Jain, J. K. Detection of composite fermions by magnetic focusing. *Phys. Rev. Lett.* **72**, 2065–2068 (1994).

[42] Taddia, L. *et al.* Topological Fractional Pumping with Alkaline-Earth-Like Atoms in Synthetic Lattices. *Phys. Rev. Lett.* **118**, 230402 (2017).

Acknowledgements

We thank J. Beugnon, N. Cooper, P. Delpace, N. Goldman, L. Mazza, and H. Price for stimulating discussions. We acknowledge funding by the EU under the ERC projects 'UQUAM' and 'TOPODY', and PSL research university under the project 'MAFAG'.

Author contributions

All authors contributed to the setup of the experiment, the data acquisition, its analysis and the writing of the manuscript.

Data availability

The datasets generated and analyzed during the current study are available from the corresponding author on request.

Author Information

Correspondence and requests for materials should be addressed to S.N. (sylvain.nascimbene@lkb.ens.fr).

Bibliography

Abo-Shaeer, J. R., C. Raman, J. M. Vogels, and W. Ketterle (2001). *Observation of Vortex Lattices in Bose-Einstein Condensates*. Science **292** (**5516**), 476–479 (cited on page 148).

Abrikosov, A. A. (1957). *The magnetic properties of superconducting alloys*. Journal of Physics and Chemistry of Solids **2** (**3**), 199–208 (cited on page 151).

Acernese, F., M. Agathos, L. Aiello, A. Allocca, A. Amato, et al. (2019). *Increasing the Astrophysical Reach of the Advanced Virgo Detector via the Application of Squeezed Vacuum States of Light*. Physical Review Letters **123** (**23**), 231108 (cited on page ix).

Aharonov, Y. and D. Bohm (1959). *Significance of Electromagnetic Potentials in the Quantum Theory*. Physical Review **115** (**3**), 485–491 (cited on page 114).

Aidelsburger, M., M. Atala, M. Lohse, J. T. Barreiro, B. Paredes, and I. Bloch (2013). *Realization of the Hofstadter Hamiltonian with Ultracold Atoms in Optical Lattices*. Physical Review Letters **111** (**18**), 185301 (cited on page x).

Aikawa, K., A. Frisch, M. Mark, S. Baier, A. Rietzler, R. Grimm, and F. Ferlaino (2012). *Bose-Einstein Condensation of Erbium*. Physical Review Letters **108** (**21**), 210401 (cited on page viii).

Anderegg, L., B. L. Augenbraun, Y. Bao, S. Burchesky, L. W. Cheuk, W. Ketterle, and J. M. Doyle (2018). *Laser cooling of optically trapped molecules*. Nature Physics **14** (**9**), 890 (cited on page 23).

Anderson, M. H., J. R. Ensher, M. R. Matthews, C. E. Wieman, and E. A. Cornell (1995). *Observation of Bose-Einstein Condensation in a Dilute Atomic Vapor*. Science **269** (**5221**), 198–201 (cited on pages vii, 39, 52).

Appel, J., P. J. Windpassinger, D. Oblak, U. B. Hoff, N. Kjærgaard, and E. S. Polzik (2009). *Mesoscopic atomic entanglement for precision measurements beyond the standard quantum limit*. Proceedings of the National Academy of Sciences **106** (**27**), 10960–10965 (cited on page ix).

Arecchi, F. T., E. Courtens, R. Gilmore, and H. Thomas (1972). *Atomic Coherent States in Quantum Optics*. Physical Review A **6** (**6**), 2211–2237 (cited on page 62).

Atala, M., M. Aidelsburger, M. Lohse, J. T. Barreiro, B. Paredes, and I. Bloch (2014). *Observation of chiral currents with ultracold atoms in bosonic ladders*. Nature Physics **10** (**8**), 588–593 (cited on page 154).

Barbarino, S., L. Taddia, D. Rossini, L. Mazza, and R. Fazio (2015). *Magnetic crystals and helical liquids in alkaline-earth fermionic gases*. Nature Communications **6** (**1**), 1–9 (cited on page 148).

Baumann, K., N. Q. Burdick, M. Lu, and B. L. Lev (2014). *Observation of low-field Fano-Feshbach resonances in ultracold gases of dysprosium*. Physical Review A **89** (**2**), 020701 (cited on page 45).

Becher, J. H., S. Baier, K. Aikawa, M. Lepers, J.-F. Wyart, O. Dulieu, and F. Ferlaino (2018). *Anisotropic polarizability of erbium atoms*. Physical Review A **97** (**1**), 012509 (cited on page 28).

Berry, M. (1984). *Quantal phase factors accompanying adiabatic changes*. Proceedings of the Royal Society of London. A. Mathematical and Physical Sciences **392** (**1802**), 45–57 (cited on page 109).

Bianco, R. and R. Resta (2011). *Mapping topological order in coordinate space*. Physical Review B **84** (**24**), 241106 (cited on pages 110, 163).

Biedenharn, L. C. and J. D. Louck (1984). *Angular momentum in quantum physics: theory and application*. Cambridge University Press (cited on page 61).

Bilitewski, T. and N. R. Cooper (2016). *Synthetic dimensions in the strong-coupling limit: Supersolids and pair superfluids*. Physical Review A **94** (**2**), 023630 (cited on page 148).

Bloch, I., J. Dalibard, and W. Zwerger (2008). *Many-body physics with ultracold gases*. Reviews of Modern Physics **80** (**3**), 885–964 (cited on page vii).

Bloch, I., J. Dalibard, and S. Nascimbène (2012). *Quantum simulations with ultracold quantum gases*. Nature Physics **8** (**4**), 267–276 (cited on page vii).

Bose (1924). *Plancks Gesetz und Lichtquantenhypothese*. Zeitschrift für Physik **26** (**1**), 178–181 (cited on page 39).

Böttcher, F., M. Wenzel, J.-N. Schmidt, M. Guo, T. Langen, et al. (2019a). *Dilute dipolar quantum droplets beyond the extended Gross-Pitaevskii equation*. Physical Review Research **1** (**3**), 033088 (cited on page 45).

Böttcher, F., J.-N. Schmidt, M. Wenzel, J. Hertkorn, M. Guo, T. Langen, and T. Pfau (2019b). *Transient Supersolid Properties in an Array of Dipolar Quantum Droplets*. Physical Review X **9** (**1**), 011051 (cited on pages viii, 45).

Bouazza, C. (2018). *Ultracold dysprosium gas in optical dipole traps: control of interactions between highly magnetic atoms*. PhD Thesis. PSL Research University (cited on pages 6, 9).

Boyd, G. D. and D. A. Kleinman (1968). *Parametric Interaction of Focused Gaussian Light Beams*. Journal of Applied Physics **39** (**8**), 3597–3639 (cited on page 160).

Burdick, N. Q., K. Baumann, Y. Tang, M. Lu, and B. L. Lev (2015). *Fermionic Suppression of Dipolar Relaxation*. Physical Review Letters **114** (**2**), 023201 (cited on page 16).

Burdick, N. Q., Y. Tang, and B. L. Lev (2016). *Long-Lived Spin-Orbit-Coupled Degenerate Dipolar Fermi Gas*. Physical Review X **6** (**3**), 031022 (cited on page xi).

Castin, Y. and R. Dum (1996). *Bose-Einstein Condensates in Time Dependent Traps*. Physical Review Letters **77** (**27**), 5315–5319 (cited on page 52).

Castin, Y., Z. Hadzibabic, S. Stock, J. Dalibard, and S. Stringari (2006). *Quantized Vortices in the Ideal Bose Gas: A Physical Realization of Random Polynomials*. Physical Review Letters **96** (**4**), 040405 (cited on page 151).

Celi, A., P. Massignan, J. Ruseckas, N. Goldman, I. B. Spielman, G. Juzeliūnas, and M. Lewenstein (2014). *Synthetic Gauge Fields in Synthetic Dimensions*. Physical Review Letters **112** (**4**), 043001 (cited on page 113).

Chalony, M., A. Kastberg, B. Klappauf, and D. Wilkowski (2011). *Doppler Cooling to the Quantum Limit*. Physical Review Letters **107** (**24**), 243002 (cited on page 23).

Chalopin, T., V. Makhalov, C. Bouazza, A. Evrard, A. Barker, et al. (2018a). *Anisotropic light shift and magic polarization of the intercombination line of dysprosium atoms in a far-detuned dipole trap*. Physical Review A **98** (**4**), 040502 (cited on page 24).

Chalopin, T., C. Bouazza, A. Evrard, V. Makhalov, D. Dreon, J. Dalibard, L. A. Sidorenkov, and S. Nascimbene (2018b). *Quantum-enhanced sensing using non-classical spin states of a highly magnetic atom*. Nature Communications **9** (**1**), 4955 (cited on page 80).

Chalopin, T., T. Satoor, A. Evrard, V. Makhalov, J. Dalibard, R. Lopes, and S. Nascimbene (2020). *Exploring the topology of a quantum Hall system at the microscopic level*. arXiv.2001.01664 (cited on page 132).

Chevy, F., K. W. Madison, and J. Dalibard (2000). *Measurement of the Angular Momentum of a Rotating Bose-Einstein Condensate*. Physical Review Letters **85** (**11**), 2223–2227 (cited on pages x, 148).

Chin, C., R. Grimm, P. Julienne, and E. Tiesinga (2010). *Feshbach resonances in ultracold gases*. Reviews of Modern Physics **82** (**2**), 1225–1286 (cited on page 45).

Chomaz, L., R. M. W. van Bijnen, D. Petter, G. Faraoni, S. Baier, J. H. Becher, M. J. Mark, F. Wächtler, L. Santos, and F. Ferlaino (2018). *Observation of roton mode population in a dipolar quantum gas*. Nature Physics **14** (**5**), 442 (cited on page viii).

Chomaz, L., D. Petter, P. Ilzhöfer, G. Natale, A. Trautmann, et al. (2019). *Long-Lived and Transient Supersolid Behaviors in Dipolar Quantum Gases*. Physical Review X **9** (**2**), 021012 (cited on pages viii, 45).

Cohen-Tannoudji, C. (1996). *Atomes ultrafroids – Piégeage non dissipatif et refroidissement évaporatif*. Cours du Collège de France (cited on page 48).

— (1997). *Condensation de Bose-Einstein – gaz sans interactions*. Cours du Collège de France (cited on page 40).

Cohen-Tannoudji, C. (1998). *Condensation de Bose-Einstein des gaz atomiques ultra froids – effets des interactions*. Cours du Collège de France (cited on page 40).

Cohen-Tannoudji, C., B. Diu, and F. Laloë (1973). *Mécanique Quantique*. Hermann (cited on page 61).

Cooper, N. R. (2008). *Rapidly rotating atomic gases*. Advances in Physics **57** (**6**), 539–616 (cited on page 155).

Cooper, N. R., J. Dalibard, and I. B. Spielman (2019). *Topological bands for ultracold atoms*. Reviews of Modern Physics **91** (**1**), 015005 (cited on pages x, 102, 110, 111, 114, 139).

Cui, X., B. Lian, T.-L. Ho, B. L. Lev, and H. Zhai (2013). *Synthetic gauge field with highly magnetic lanthanide atoms*. Physical Review A **88** (**1**), 011601 (cited on pages xi, 20).

Dalfovo, F., S. Giorgini, L. P. Pitaevskii, and S. Stringari (1999). *Theory of Bose-Einstein condensation in trapped gases*. Reviews of Modern Physics **71** (**3**), 463–512 (cited on page 40).

Dalibard, J. (2014). *Le magnétisme artificiel pour les gaz d'atomes froids*. Cours du Collège de France (cited on page 102).

— (2018). *La matière topologique et son exploration avec les gaz quantiques*. Cours du Collège de France (cited on page 102).

Dalibard, J., F. Gerbier, G. Juzeliūnas, and P. Öhberg (2011). *Artificial gauge potentials for neutral atoms*. Reviews of Modern Physics **83** (**4**), 1523–1543 (cited on pages x, xi, 102, 113).

Davis, K. B., M. O. Mewes, M. R. Andrews, N. J. van Druten, D. S. Durfee, D. M. Kurn, and W. Ketterle (1995). *Bose-Einstein Condensation in a Gas of Sodium Atoms*. Physical Review Letters **75** (**22**), 3969–3973 (cited on pages vii, 39, 52).

Dietsche, E. K., A. Larrouy, S. Haroche, J. M. Raimond, M. Brune, and S. Gleyzes (2019). *High-sensitivity magnetometry with a single atom in a superposition of two circular Rydberg states*. Nature Physics **15** (**4**), 326–329 (cited on page ix).

Dowling, J. P., G. S. Agarwal, and W. P. Schleich (1994). *Wigner distribution of a general angular-momentum state: Applications to a collection of two-level atoms*. Physical Review A **49** (**5**), 4101–4109 (cited on page 63).

Dreon, D. (2017). *Designing and building an ultracold Dysprosium experiment: a new framework for light-spin interaction*. PhD Thesis. Ecole Normale Supérieure (ENS) ; PSL Research University (cited on pages 6, 10).

Dreon, D., L. A. Sidorenkov, C. Bouazza, W. Maineult, J. Dalibard, and S. Nascimbene (2017). *Optical cooling and trapping of highly magnetic atoms: the benefits of a spontaneous spin polarization*. Journal of Physics B: Atomic, Molecular and Optical Physics **50** (**6**), 065005 (cited on page 7).

Duarte, P. M., R. A. Hart, J. M. Hitchcock, T. A. Corcovilos, T.-L. Yang, A. Reed, and R. G. Hulet (2011). *All-optical production of a lithium quantum gas using narrow-line laser cooling*. Physical Review A **84** (**6**), 061406 (cited on page 26).

Dusuel, S. and J. Vidal (2004). *Finite-Size Scaling Exponents of the Lipkin-Meshkov-Glick Model*. Physical Review Letters **93** (**23**), 237204 (cited on page 119).

Dzuba, V. A., V. V. Flambaum, and B. L. Lev (2011). *Dynamic polarizabilities and magic wavelengths for dysprosium*. Physical Review A **83** (**3**), 032502 (cited on pages 20, 24).

Eberlein, C., S. Giovanazzi, and D. H. J. O'Dell (2005). *Exact solution of the Thomas-Fermi equation for a trapped Bose-Einstein condensate with dipole-dipole interactions*. Physical Review A **71** (**3**), 033618 (cited on page 43).

Einstein, A (1924). *Quantentheorie des einatomigen idealen Gases*. Preuss. Akad. Wiss **261** (cited on page 39).

Engels, P., I. Coddington, P. C. Haljan, V. Schweikhard, and E. A. Cornell (2003). *Observation of Long-Lived Vortex Aggregates in Rapidly Rotating Bose-Einstein Condensates*. Physical Review Letters **90** (**17**), 170405 (cited on pages x, 148).

Estève, J., C. Gross, A. Weller, S. Giovanazzi, and M. K. Oberthaler (2008). *Squeezing and entanglement in a Bose–Einstein condensate*. Nature **455** (**7217**), 1216 (cited on pages ix, 72).

Evrard, A., V. Makhalov, T. Chalopin, L. A. Sidorenkov, J. Dalibard, R. Lopes, and S. Nascimbene (2019). *Enhanced Magnetic Sensitivity with Non-Gaussian Quantum Fluctuations*. Physical Review Letters **122** (**17**), 173601 (cited on page 96).

Facon, A., E.-K. Dietsche, D. Grosso, S. Haroche, J.-M. Raimond, M. Brune, and S. Gleyzes (2016). *A sensitive electrometer based on a Rydberg atom in a Schrödinger-cat state*. Nature **535** (**7611**), 262–265 (cited on page ix).

Ferrier-Barbut, I., H. Kadau, M. Schmitt, M. Wenzel, and T. Pfau (2016). *Observation of Quantum Droplets in a Strongly Dipolar Bose Gas*. Physical Review Letters **116** (**21**), 215301 (cited on pages viii, 55).

Ferrier-Barbut, I., M. Wenzel, F. Böttcher, T. Langen, M. Isoard, S. Stringari, and T. Pfau (2018). *Scissors Mode of Dipolar Quantum Droplets of Dysprosium Atoms*. Physical Review Letters **120** (**16**), 160402 (cited on pages viii, 45).

Fetter, A. L., B. Jackson, and S. Stringari (2005). *Rapid rotation of a Bose-Einstein condensate in a harmonic plus quartic trap*. Physical Review A **71** (**1**), 013605 (cited on pages 148, 151).

Frisch, A., K. Aikawa, M. Mark, A. Rietzler, J. Schindler, E. Zupanič, R. Grimm, and F. Ferlaino (2012). *Narrow-line magneto-optical trap for erbium*. Physical Review A **85** (**5**), 051401 (cited on page viii).

Gammal, A., T. Frederico, and L. Tomio (2001). *Critical number of atoms for attractive Bose-Einstein condensates with cylindrically symmetrical traps*. Physical Review A **64** (**5**), 055602 (cited on page 44).

Gerbier, F. and J. Dalibard (2010). *Gauge fields for ultracold atoms in optical superlattices*. New Journal of Physics **12** (**3**), 033007 (cited on page 26).

Gessner, M., A. Smerzi, and L. Pezzè (2019). *Metrological Nonlinear Squeezing Parameter*. Physical Review Letters **122** (**9**), 090503 (cited on page 71).

Giovanazzi, S., P. Pedri, L. Santos, A. Griesmaier, M. Fattori, T. Koch, J. Stuhler, and T. Pfau (2006). *Expansion dynamics of a dipolar Bose-Einstein condensate*. Physical Review A **74** (**1**), 013621 (cited on page 52).

Giovannetti, V., S. Lloyd, and L. Maccone (2004). *Quantum-Enhanced Measurements: Beating the Standard Quantum Limit*. Science **306** (**5700**), 1330–1336 (cited on page ix).

— (2011). *Advances in quantum metrology*. Nature Photonics **5** (**4**), 222–229 (cited on page vii).

Glaum, K. and A. Pelster (2007). *Bose-Einstein condensation temperature of dipolar gas in anisotropic harmonic trap*. Physical Review A **76** (**2**), 023604 (cited on page 54).

Goldman, N., G. Juzeliūnas, P. Öhberg, and I. B. Spielman (2014). *Light-induced gauge fields for ultracold atoms*. Reports on Progress in Physics **77** (**12**), 126401 (cited on page 112).

Góral, K., L. Santos, and M. Lewenstein (2002). *Quantum Phases of Dipolar Bosons in Optical Lattices*. Physical Review Letters **88** (**17**), 170406 (cited on page ix).

Greenberger, D. M., M. A. Horne, A. Shimony, and A. Zeilinger (1990). *Bell's theorem without inequalities*. American Journal of Physics **58** (**12**), 1131 (cited on page 66).

Greiner, M., O. Mandel, T. Esslinger, T. W. Hänsch, and I. Bloch (2002). *Quantum phase transition from a superfluid to a Mott insulator in a gas of ultracold atoms*. Nature **415** (**6867**), 39 (cited on page vii).

Griesmaier, A., J. Werner, S. Hensler, J. Stuhler, and T. Pfau (2005). *Bose-Einstein Condensation of Chromium*. Physical Review Letters **94** (**16**), 160401 (cited on page viii).

Grimm, R., M. Weidemüller, and Y. B. Ovchinnikov (2000). *Optical Dipole Traps for Neutral Atoms*. Advances In Atomic, Molecular, and Optical Physics. **42**. Academic Press, pp. 95–170 (cited on page 8).

Gross, C., H. Strobel, E. Nicklas, T. Zibold, N. Bar-Gill, G. Kurizki, and M. K. Oberthaler (2011). *Atomic homodyne detection of continuous-variable entangled twin-atom states*. Nature **480** (**7376**), 219–223 (cited on page 70).

Halperin, B. I. (1982). *Quantized Hall conductance, current-carrying edge states, and the existence of extended states in a two-dimensional disordered potential*. Physical Review B **25** (**4**), 2185–2190 (cited on page x).

— (1984). *Statistics of Quasiparticles and the Hierarchy of Fractional Quantized Hall States*. Physical Review Letters **52** (**18**), 1583–1586 (cited on page xi).

Hasan, M. Z. and C. L. Kane (2010). *Colloquium: Topological insulators*. Reviews of Modern Physics **82** (**4**), 3045–3067 (cited on pages x, 108, 110).

Holstein, T. and H. Primakoff (1940). *Field Dependence of the Intrinsic Domain Magnetization of a Ferromagnet*. Physical Review **58** (**12**), 1098–1113 (cited on page 118).

Horodecki, R., P. Horodecki, M. Horodecki, and K. Horodecki (2009). *Quantum entanglement*. Reviews of Modern Physics **81** (**2**), 865–942 (cited on page 64).

Ido, T., Y. Isoya, and H. Katori (2000). *Optical-dipole trapping of Sr atoms at a high phase-space density*. Physical Review A **61** (**6**), 061403 (cited on page 23).

Jaksch, D. and P. Zoller (2003). *Creation of effective magnetic fields in optical lattices: the Hofstadter butterfly for cold neutral atoms*. New Journal of Physics **5** (**1**), 56 (cited on page x).

Jundt, D. H. (1997). *Temperature-dependent Sellmeier equation for the index of refraction, n_e, in congruent lithium niobate*. Optics Letters **22** (**20**), 1553–1555 (cited on page 160).

Kadau, H., M. Schmitt, M. Wenzel, C. Wink, T. Maier, I. Ferrier-Barbut, and T. Pfau (2016). *Observing the Rosensweig instability of a quantum ferrofluid*. Nature **530** (**7589**), 194–197 (cited on pages viii, 55).

Kagan, Y., E. L. Surkov, and G. V. Shlyapnikov (1996). *Evolution of a Bose-condensed gas under variations of the confining potential*. Physical Review A **54** (**3**), R1753–R1756 (cited on page 52).

Kao, W., Y. Tang, N. Q. Burdick, and B. L. Lev (2017). *Anisotropic dependence of tune-out wavelength near Dy 741-nm transition*. Optics Express **25** (**4**), 3411–3419 (cited on page 23).

Kien, F. L., P. Schneeweiss, and A. Rauschenbeutel (2013). *Dynamical polarizability of atoms in arbitrary light fields: general theory and application to cesium*. The European Physical Journal D **67** (**5**), 92 (cited on pages 24, 77).

Kitaev, A. Y. (2001). *Unpaired Majorana fermions in quantum wires*. Physics-Uspekhi **44** (10S), 131 (cited on page xi).

Kitagawa, M. (1993). *Squeezed spin states*. Physical Review A **47** (**6**), 5138–5143 (cited on pages 65, 72, 73).

Klitzing, K. v., G. Dorda, and M. Pepper (1980). *New Method for High-Accuracy Determination of the Fine-Structure Constant Based on Quantized Hall Resistance*. Physical Review Letters **45** (**6**), 494–497 (cited on page 107).

Köhl, M., H. Moritz, T. Stöferle, K. Günter, and T. Esslinger (2005). *Fermionic Atoms in a Three Dimensional Optical Lattice: Observing Fermi Surfaces, Dynamics, and Interactions*. Physical Review Letters **94** (**8**), 080403 (cited on page vii).

Lahaye, T., C. Menotti, L. Santos, M. Lewenstein, and T. Pfau (2009). *The physics of dipolar bosonic quantum gases*. Reports on Progress in Physics **72** (**12**), 126401 (cited on pages viii, 42, 148).

Lahaye, T., T. Koch, B. Fröhlich, M. Fattori, J. Metz, A. Griesmaier, S. Giovanazzi, and T. Pfau (2007). *Strong dipolar effects in a quantum ferrofluid*. Nature **448** (**7154**), 672–675 (cited on page viii).

Larson, D. J., J. C. Bergquist, J. J. Bollinger, W. M. Itano, and D. J. Wineland (1986). *Sympathetic cooling of trapped ions: A laser-cooled two-species nonneutral ion plasma*. Physical Review Letters **57** (**1**), 70–73 (cited on page 32).

Laughlin, R. B. (1983). *Anomalous Quantum Hall Effect: An Incompressible Quantum Fluid with Fractionally Charged Excitations*. Physical Review Letters **50** (**18**), 1395–1398 (cited on pages xi, 155).

Lee, H., P. Kok, and J. P. Dowling (2002). *A quantum Rosetta stone for interferometry*. Journal of Modern Optics **49** (**14-15**), 2325–2338 (cited on page 71).

Lee, T. D., K. Huang, and C. N. Yang (1957). *Eigenvalues and Eigenfunctions of a Bose System of Hard Spheres and Its Low-Temperature Properties*. Physical Review **106** (**6**), 1135–1145 (cited on page 55).

Leibfried, D., M. D. Barrett, T. Schaetz, J. Britton, J. Chiaverini, W. M. Itano, J. D. Jost, C. Langer, and D. J. Wineland (2004). *Toward Heisenberg-Limited Spectroscopy with Multiparticle Entangled States*. Science **304** (**5676**), 1476–1478 (cited on page 71).

Leibfried, D., E. Knill, S. Seidelin, J. Britton, R. B. Blakestad, et al. (2005). *Creation of a six-atom 'Schrödinger cat' state*. Nature **438** (**7068**), 639–642 (cited on page 66).

Lepers, M., J.-F. Wyart, and O. Dulieu (2014). *Anisotropic optical trapping of ultracold erbium atoms*. Physical Review A **89** (**2**), 022505 (cited on page 25).

Li, H., J.-F. Wyart, O. Dulieu, S. Nascimbène, and M. Lepers (2017). *Optical trapping of ultracold dysprosium atoms: transition probabilities, dynamic dipole polarizabilities and van der Waals C6 coefficients*. Journal of Physics B: Atomic, Molecular and Optical Physics **50** (**1**), 014005 (cited on pages 23–25, 31).

Lin, Y.-J., R. L. Compton, K. Jiménez-García, J. V. Porto, and I. B. Spielman (2009). *Synthetic magnetic fields for ultracold neutral atoms*. Nature **462** (**7273**), 628–632 (cited on pages xi, 113).

Lin, Y.-J., K. Jiménez-García, and I. B. Spielman (2011). *Spin–orbit-coupled Bose–Einstein condensates*. Nature **471** (**7336**), 83–86 (cited on pages x, 113).

Lu, M., S. H. Youn, and B. L. Lev (2010). *Trapping Ultracold Dysprosium: A Highly Magnetic Gas for Dipolar Physics*. Physical Review Letters **104** (**6**), 063001 (cited on page viii).

— (2011a). *Spectroscopy of a narrow-line laser-cooling transition in atomic dysprosium*. Physical Review A **83** (**1**), 012510 (cited on page 5).

Lu, M., N. Q. Burdick, S. H. Youn, and B. L. Lev (2011b). *Strongly Dipolar Bose-Einstein Condensate of Dysprosium*. Physical Review Letters **107** (**19**), 190401 (cited on page viii).

Lu, M., N. Q. Burdick, and B. L. Lev (2012). *Quantum Degenerate Dipolar Fermi Gas*. Physical Review Letters **108** (**21**), 215301 (cited on page viii).

Lucioni, E., L. Tanzi, A. Fregosi, J. Catani, S. Gozzini, M. Inguscio, A. Fioretti, C. Gabbanini, and G. Modugno (2018). *Dysprosium dipolar Bose-Einstein condensate with broad Feshbach resonances*. Physical Review A **97** (**6**), 060701 (cited on page viii).

Ludlow, A. D. (2015). *Optical atomic clocks*. Reviews of Modern Physics **87** (**2**), 637–701 (cited on pages vii, ix, 26).

Luiten, O. J., M. W. Reynolds, and J. T. M. Walraven (1996). *Kinetic theory of the evaporative cooling of a trapped gas*. Physical Review A **53** (**1**), 381–389 (cited on page 48).

Ma, R. (2014). *Engineered potentials and dynamics of ultracold quantum gases under the microscope*. PhD Thesis. Harvard University (cited on page 20).

Maier, T., H. Kadau, M. Schmitt, M. Wenzel, I. Ferrier-Barbut, et al. (2015). *Emergence of Chaotic Scattering in Ultracold Er and Dy*. Physical Review X **5** (**4**), 041029 (cited on pages 15, 45).

Maier, T. (2015). *Interactions in a Quantum Gas of Dysprosium Atoms*. PhD Thesis. Universität Stuttgart (cited on page 31).

Makhalov, V., T. Satoor, A. Evrard, T. Chalopin, R. Lopes, and S. Nascimbene (2019). *Probing Quantum Criticality and Symmetry Breaking at the Microscopic Level*. Physical Review Letters **123** (**12**), 120601 (cited on pages 98, 150).

Mancini, M., G. Pagano, G. Cappellini, L. Livi, M. Rider, et al. (2015). *Observation of chiral edge states with neutral fermions in synthetic Hall ribbons*. Science **349** (**6255**), 1510–1513 (cited on page 113).

Martin, W. C., R. Zalubas, and L. Hagan (1978). *Atomic energy levels - the rare-earth elements: the spectra of lanthanum, cerium, praseodymium, neodymium, promethium, samarium, europium, gadolinium, terbium, dysprosium, holmium, erbium, thulium, ytterbium, and lutetium*. In collab. with NIST Research Library. National Bureau of Standards. 434 pp. (cited on page 5).

Miller, J., L. Barsotti, S. Vitale, P. Fritschel, M. Evans, and D. Sigg (2015). *Prospects for doubling the range of Advanced LIGO*. Physical Review D **91** (**6**), 062005 (cited on page ix).

Monz, T., P. Schindler, J. T. Barreiro, M. Chwalla, D. Nigg, W. A. Coish, M. Harlander, W. Hänsel, M. Hennrich, and R. Blatt (2011). *14-Qubit Entanglement: Creation and Coherence*. Physical Review Letters **106** (**13**), 130506 (cited on pages 66, 71).

Nascimbène, S. (2013). *Realizing one-dimensional topological superfluids with ultracold atomic gases*. Journal of Physics B: Atomic, Molecular and Optical Physics **46** (**13**), 134005 (cited on page xi).

Nayak, C., S. H. Simon, A. Stern, M. Freedman, and S. Das Sarma (2008). *Non-Abelian anyons and topological quantum computation*. Reviews of Modern Physics **80** (**3**), 1083–1159 (cited on page xi).

Newbury, N. R., C. J. Myatt, E. A. Cornell, and C. E. Wieman (1995). *Gravitational Sisyphus Cooling of ^{87}Rb in a Magnetic Trap*. Physical Review Letters **74** (**12**), 2196–2199 (cited on page 23).

O'Hara, K. M., M. E. Gehm, S. R. Granade, and J. E. Thomas (2001). *Scaling laws for evaporative cooling in time-dependent optical traps*. Physical Review A **64** (**5**), 051403 (cited on page 49).

Omran, A., H. Levine, A. Keesling, G. Semeghini, T. T. Wang, et al. (2019). *Generation and manipulation of Schrödinger cat states in Rydberg atom arrays*. Science **365** (**6453**), 570–574 (cited on page 66).

Ozawa, T., H. M. Price, A. Amo, N. Goldman, M. Hafezi, et al. (2019). *Topological photonics*. Reviews of Modern Physics **91** (**1**), 015006 (cited on page 102).

Petersen, N., M. Trümper, and P. Windpassinger (2019). *Spectroscopy of the 1001 nm transition in atomic dysprosium*. arXiv.1907.05754 (cited on page 20).

Pezzè, L. and A. Smerzi (2009). *Entanglement, Nonlinear Dynamics, and the Heisenberg Limit*. Physical Review Letters **102** (**10**), 100401 (cited on pages 68, 70).

Pezzè, L., A. Smerzi, M. K. Oberthaler, R. Schmied, and P. Treutlein (2018). *Quantum metrology with nonclassical states of atomic ensembles*. Reviews of Modern Physics **90** (**3**), 035005 (cited on pages 61, 63, 67, 69).

Pitaevskii, L. and S. Stringari (2016). *Bose-Einstein condensation and superfluidity*. Vol. 164. Oxford University Press (cited on page 40).

Qi, X.-L. and S.-C. Zhang (2011). *Topological insulators and superconductors*. Reviews of Modern Physics **83** (**4**), 1057–1110 (cited on page 102).

Radcliffe, J. M. (1971). *Some properties of coherent spin states*. Journal of Physics A: General Physics **4** (**3**), 313 (cited on page 62).

Ravensbergen, C., V. Corre, E. Soave, M. Kreyer, S. Tzanova, E. Kirilov, and R. Grimm (2018a). *Accurate Determination of the Dynamical Polarizability of Dysprosium*. Physical Review Letters **120** (**22**), 223001 (cited on pages 23, 25).

Ravensbergen, C., V. Corre, E. Soave, M. Kreyer, E. Kirilov, and R. Grimm (2018b). *Production of a degenerate Fermi-Fermi mixture of dysprosium and potassium atoms*. Physical Review A **98** (**6**), 063624 (cited on page viii).

Sackett, C. A., D. Kielpinski, B. E. King, C. Langer, V. Meyer, et al. (2000). *Experimental entanglement of four particles*. Nature **404** (**6775**), 256–259 (cited on pages ix, 72).

Saito, H., Y. Kawaguchi, and M. Ueda (2009). *Ferrofluidity in a Two-Component Dipolar Bose-Einstein Condensate*. Physical Review Letters **102** (**23**), 230403 (cited on page 150).

Santos, L., G. V. Shlyapnikov, and M. Lewenstein (2003). *Roton-Maxon Spectrum and Stability of Trapped Dipolar Bose-Einstein Condensates*. Physical Review Letters **90** (**25**), 250403 (cited on page viii).

Schleier-Smith, M. H., I. D. Leroux, and V. Vuletić (2010). *States of an Ensemble of Two-Level Atoms with Reduced Quantum Uncertainty*. Physical Review Letters **104** (**7**), 073604 (cited on page 72).

Schmidt, P. O., S. Hensler, J. Werner, T. Binhammer, A. Görlitz, and T. Pfau (2003). *Doppler cooling of an optically dense cloud of magnetically trapped atoms*. JOSA B **20** (**5**), 960–967 (cited on page 23).

Schmitt, M., E. a. L. Henn, J. Billy, H. Kadau, T. Maier, A. Griesmaier, and T. Pfau (2013). *Spectroscopy of a narrow-line optical pumping transition in atomic dysprosium*. Optics Letters **38** (**5**), 637–639 (cited on page 19).

Shvarchuck, I., C. Buggle, D. S. Petrov, K. Dieckmann, M. Zielonkowski, M. Kemmann, T. G. Tiecke, W. von Klitzing, G. V. Shlyapnikov, and J. T. M. Walraven (2002). *Bose-Einstein Condensation into Nonequilibrium States Studied by Condensate Focusing*. Physical Review Letters **89** (**27**), 270404 (cited on page 154).

Slusher, R. E., L. W. Hollberg, B. Yurke, J. C. Mertz, and J. F. Valley (1985). *Observation of Squeezed States Generated by Four-Wave Mixing in an Optical Cavity*. Physical Review Letters **55** (**22**), 2409–2412 (cited on page ix).

Sørensen, A. S. and K. Mølmer (2001). *Entanglement and Extreme Spin Squeezing*. Physical Review Letters **86** (**20**), 4431–4434 (cited on page 70).

Stamper-Kurn, D. M. and M. Ueda (2013). *Spinor Bose gases: Symmetries, magnetism, and quantum dynamics*. Reviews of Modern Physics **85** (**3**), 1191–1244 (cited on page 149).

Stellmer, S., B. Pasquiou, R. Grimm, and F. Schreck (2013). *Laser Cooling to Quantum Degeneracy*. Physical Review Letters **110** (**26**), 263003 (cited on pages 23, 36).

Strobel, H., W. Muessel, D. Linnemann, T. Zibold, D. B. Hume, L. Pezzè, A. Smerzi, and M. K. Oberthaler (2014). *Fisher information and entanglement of non-Gaussian spin states*. Science **345** (**6195**), 424–427 (cited on page 72).

Stuhl, B. K., H.-I. Lu, L. M. Aycock, D. Genkina, and I. B. Spielman (2015). *Visualizing edge states with an atomic Bose gas in the quantum Hall regime*. Science **349** (**6255**), 1514–1518 (cited on page 113).

Süsstrunk, R. and S. D. Huber (2015). *Observation of phononic helical edge states in a mechanical topological insulator*. Science **349** (**6243**), 47–50 (cited on page 110).

Tammuz, N., R. P. Smith, R. L. D. Campbell, S. Beattie, S. Moulder, J. Dalibard, and Z. Hadzibabic (2011). *Can a Bose Gas Be Saturated?* Physical Review Letters **106** (**23**), 230401 (cited on page 53).

Tanzi, L., E. Lucioni, F. Famà, J. Catani, A. Fioretti, C. Gabbanini, R. N. Bisset, L. Santos, and G. Modugno (2019). *Observation of a Dipolar Quantum Gas with Metastable Supersolid Properties*. Physical Review Letters **122** (**13**), 130405 (cited on page viii).

Thouless, D. J., M. Kohmoto, M. P. Nightingale, and M. den Nijs (1982). *Quantized Hall Conductance in a Two-Dimensional Periodic Potential*. Physical Review Letters **49** (**6**), 405–408 (cited on page 109).

Tong, D. (2016). *Lectures on the Quantum Hall Effect*. arXiv.1606.06687 (cited on page 102).

Townsend, C. G., N. H. Edwards, C. J. Cooper, K. P. Zetie, C. J. Foot, A. M. Steane, P. Szriftgiser, H. Perrin, and J. Dalibard (1995). *Phase-space density in the magneto-optical trap*. Physical Review A **52** (**2**), 1423–1440 (cited on page 41).

Trautmann, A., P. Ilzhöfer, G. Durastante, C. Politi, M. Sohmen, M. J. Mark, and F. Ferlaino (2018). *Dipolar Quantum Mixtures of Erbium and Dysprosium Atoms*. Physical Review Letters **121** (**21**), 213601 (cited on page viii).

Trefzger, C., C. Menotti, B. Capogrosso-Sansone, and M. Lewenstein (2011). *Ultracold dipolar gases in optical lattices*. Journal of Physics B: Atomic, Molecular and Optical Physics **44** (**19**), 193001 (cited on page ix).

Tse, M., H. Yu, N. Kijbunchoo, A. Fernandez-Galiana, P. Dupej, et al. (2019). *Quantum-Enhanced Advanced LIGO Detectors in the Era of Gravitational-Wave Astronomy*. Physical Review Letters **123** (**23**), 231107 (cited on page ix).

Tsui, D. C., H. L. Stormer, and A. C. Gossard (1982). *Two-Dimensional Magnetotransport in the Extreme Quantum Limit*. Physical Review Letters **48** (**22**), 1559–1562 (cited on page 155).

Will, S. A., J. W. Park, Z. Z. Yan, H. Loh, and M. W. Zwierlein (2016). *Coherent Microwave Control of Ultracold $^{23}Na^{40}K$ Molecules*. Physical Review Letters **116** (**22**), 225306 (cited on page ix).

Willett, R., J. P. Eisenstein, H. L. Störmer, D. C. Tsui, A. C. Gossard, and J. H. English (1987). *Observation of an even-denominator quantum number in the fractional quantum Hall effect*. Physical Review Letters **59** (**15**), 1776–1779 (cited on page 155).

Wilson, R. M., C. Ticknor, J. L. Bohn, and E. Timmermans (2012). *Roton immiscibility in a two-component dipolar Bose gas*. Physical Review A **86** (**3**), 033606 (cited on page 150).

Wineland, D. J., J. J. Bollinger, W. M. Itano, F. L. Moore, and D. J. Heinzen (1992). *Spin squeezing and reduced quantum noise in spectroscopy*. Physical Review A **46** (**11**), R6797–R6800 (cited on page 65).

Wootters, W. K. (1981). *Statistical distance and Hilbert space*. Physical Review D **23** (**2**), 357–362 (cited on page 71).

Wu, H., E. Arimondo, and C. J. Foot (1997). *Dynamics of evaporative cooling for Bose-Einstein condensation*. Physical Review A **56** (**1**), 560–569 (cited on page 32).

Wu, Z., L. Zhang, W. Sun, X.-T. Xu, B.-Z. Wang, S.-C. Ji, Y. Deng, S. Chen, X.-J. Liu, and J.-W. Pan (2016). *Realization of two-dimensional spin-orbit coupling for Bose-Einstein condensates*. Science **354** **(6308)**, 83–88 (cited on page x).

Xiao, M., G. Ma, Z. Yang, P. Sheng, Z. Q. Zhang, and C. T. Chan (2015). *Geometric phase and band inversion in periodic acoustic systems*. Nature Physics **11** **(3)**, 240–244 (cited on page 109).

Yao, N. Y., A. V. Gorshkov, C. R. Laumann, A. M. Läuchli, J. Ye, and M. D. Lukin (2013). *Realizing Fractional Chern Insulators in Dipolar Spin Systems*. Physical Review Letters **110** **(18)**, 185302 (cited on page 20).

Yi, W., A. J. Daley, G. Pupillo, and P. Zoller (2008). *State-dependent, addressable subwavelength lattices with cold atoms*. New Journal of Physics **10** **(7)**, 073015 (cited on page 26).

Yoshioka, D. (2002). *The Quantum Hall Effect*. Springer Science (cited on page 107).

Youn, S. H., M. Lu, U. Ray, and B. L. Lev (2010). *Dysprosium magneto-optical traps*. Physical Review A **82** **(4)**, 043425 (cited on page 20).

Yurke, B., S. L. McCall, and J. R. Klauder (1986). *SU(2) and SU(1,1) interferometers*. Physical Review A **33** **(6)**, 4033–4054 (cited on page 69).

Zhai, H. (2015). *Degenerate quantum gases with spin–orbit coupling: a review*. Reports on Progress in Physics **78** **(2)**, 026001 (cited on page 113).

Zhou, X., Y. Li, Z. Cai, and C. Wu (2013). *Unconventional states of bosons with the synthetic spin–orbit coupling*. Journal of Physics B: Atomic, Molecular and Optical Physics **46** **(13)**, 134001 (cited on page 113).

Zurek, W. H. (2001). *Sub-Planck structure in phase space and its relevance for quantum decoherence*. Nature **412** **(6848)**, 712–717 (cited on page 68).